HIGGS BOSON CROSS SECTION MEASUREMENTS IN THE DIPHOTON DECAY CHANNEL IN PROTON-PROTON COLLISIONS AT $\sqrt{s} = 13\,\text{TEV}$ USING THE ATLAS DETECTOR AT THE LHC

By

Ivan Konstantinovich Pogrebnyak

A DISSERTATION

Submitted to
Michigan State University
in partial fulfillment of the requirements
for the degree of

Physics—Doctor of Philosophy

2021

ABSTRACT

HIGGS BOSON CROSS SECTION MEASUREMENTS
IN THE DIPHOTON DECAY CHANNEL
IN PROTON-PROTON COLLISIONS AT $\sqrt{s} = 13\,\text{TEV}$
USING THE ATLAS DETECTOR AT THE LHC

By

Ivan Konstantinovich Pogrebnyak

This dissertation presents ATLAS measurements of the total and differential fiducial cross sections for the process of the Higgs boson production and subsequent decay to two photons. The analyzed dataset of proton-proton collisions at $\sqrt{s} = 13\,\text{TeV}$ has an integrated luminosity of $139\,\text{fb}^{-1}$ and was collected during the Run 2 of the Large Hadron Collider in 2015–2018. The cross sections were measured in a fiducial phase space closely matching the experimental selection, and compared to the Standard Model predictions from the state-of-the-art calculations. The differential cross sections were measured with respect to an array of observables, allowing us to probe the kinematics, jet activity, and spin and CP properties of the Higgs boson interactions. The data were analyzed iteratively, with yearly results from partial datasets presented at conferences and in publications. The inclusive fiducial cross section obtained from the analysis of the full Run 2 dataset is $65.2 \pm 4.5\,(\text{stat.}) \pm 5.6\,(\text{exp.}) \pm 0.3\,(\text{theory})\,\text{fb}$, which is in excellent agreement with the SM prediction of $63.5 \pm 3.3\,\text{fb}$. The results provide the state-of-the-art experimental measurements of the Higgs boson production cross sections, and extend our confidence in the SM in the Higgs sector and QCD, as well as in the computational techniques used to obtain theoretical predictions.

ACKNOWLEDGMENTS

I would like to begin this dissertation by expressing my gratitude to everyone who made this work possible and who had a hand in either setting or guiding me on the course of curiosity, exploration, and pursuit of knowledge.

Firstly, I want to thank my parents, Konstantin Vladimirovich and Svetlana Alekseevna. The fact that I was able to undertake this work is largely a product of their support and encouragement. Through their example, I learned that diligent and judicious attitude is what yields quality results. They taught me to use critical thinking and how to deconstruct problems to find a path to a solution. For all that they have done to make this journey possible for me, I can't thank them enough.

Throughout my life, I've been lucky to have great teachers. From elementary to graduate school, there have always been people who kept my curiosity aflame, either with their knowledge or charisma. The teachers showed me the world of ideas, how the inner workings of complex things can be understood, and how fulfilling the path of discovery can be. I express heartfelt thanks to all the teachers of my home city school, "Лингва – XXI век". You were like a family to the students, and you always made me feel at home at school.

When I was in the third grade, mom had the foresight of signing me up for the Radioengineering club at the local "Pioneers' Palace". Armed with an 80 W soldering iron, I set out to build my first medium-wave radio receiver. I am certain that what Georgiy Sergeevich Kotelnikov taught me resulted in my lifelong love for science and engineering. Under his guidance, I obtained my first experience of writing and presenting a research paper. Georgiy Sergeevich is an extraordinary mentor, and the club is a special place for many former students. Stories were always shared during the celebrations we had on the Radio Day and the

club's birthday. The scents of melting rosin and brewing tea, and the sounds of classical music on vinyl records will always stay in my heart.

While studying at the University of North Carolina at Chapel Hill, I was fortunate to learn from and work with Christian Iliadis. He, very enthusiastically, taught my first quantum mechanics class and later hired me as an undergraduate research assistant. Working in Christian's group, which specialized in nuclear astrophysics, gave me my first research experience in experimental physics and taught me many skills that came useful in graduate school.

I cannot leave my friends without mention, particularly my UNC cohort. I thank Patrick Domico for his incredible capacity for conversation, and being a willing interlocutor in discussions of the finest details of any subject. He did not refrain from endless telephone conversations over English usage concerning this dissertation. I thank Perry Harabin for continually sparking my interest in mathematics and for inspiring me to seek deeper understanding of the fundamental mathematical concepts in field theory and particle physics. I thank Nathan Otterness for providing programming advice that enabled me to develop many tools I used in this work. I thank Andrew Ashley for being a fantastic storyteller and making intellectual pursuits seem all the more wondrous. It would be hard to mention everyone I had the pleasure of counting among my friends at MSU, but I would like to note Anton Efremov, Justin Estee, Sam Marinelli, Garrett Neer, and José Reyes.

Finally, I would like to express my gratitude to my PhD adviser, Joey Huston, for all the opportunities and guidance he provided for me in my graduate career. I had always dreamt of working in a technical and fundamental area of research. Joey helped me realize this aspiration by letting me participate in a number of amazing projects, ranging from the analysis of the diphoton decay channel of the newly discovered Higgs boson to electronics

upgrades for the Tile hadronic calorimeter. With Joey's help, I had the privilege to meet and work with many outstanding people in the field of high energy physics.

I also thank the members of my dissertation committee: Matthew Comstock, Wade Fisher, Scott Pratt, and Chien-Peng Yuan, for providing help and useful comments on my work. I thank Andreas von Manteuffel for proofreading the theory chapter, and Ahmed Tarek for proofreading the analysis chapter. And, of course, my deepest thanks go to the post-docs, who helped me with my projects and made the analysis presented in this dissertation possible, as well as to the scientists and engineers, whose tireless work makes the operation of the LHC and ATLAS a reality.

EPIGRAPH

The labor legislation was being flagrantly ignored, and I began to feel that I had lost all desire to struggle against this law-breaking, because, tonight at twelve o'clock on New Year's Eve, plowing through a blizzard, they came in, these people who had more interest in bringing to a conclusion, or starting anew, a useful undertaking... Here came people who would rather be with each other than anywhere else, who couldn't stand any kind of Sunday, because they were bored on Sunday. They were Magi with a capital M, and their motto was "Monday begins on Saturday." True, they knew an incantation or two, knew how to turn water into wine, and any one of them would not find it difficult to feed a thousand with five loaves. But they weren't magi because of that. That was superficial chaff. They were magi because they knew a lot, so much indeed that quantity had finally been transmuted into quality, and they had come into a different relationship with the world than ordinary people. They worked in an Institute that was dedicated above all to the problems of human happiness and the meaning of human life, and even among them, not one knew exactly what was happiness and what precisely was the meaning of life. So they took it as a working hypothesis that happiness lay in the perpetual gaining of new insights into the unknown and the meaning of life was to be found there as well.

Monday begins on Saturday – Arkadi and Boris Strugatsky

TABLE OF CONTENTS

LIST OF TABLES

LIST OF FIGURES

Chapter 1

Introduction

Throughout the 20th century, physicists developed the modern mathematical theories of the nature's fundamental constituents and their interactions. Two ideas have grown in parallel: quantum mechanics, valid at short distances and high energy scales, and applicable in the realm of particles, and a more classical theory of general relativity, which accurately describes the gravitational interaction over large distances on the cosmic scale. Our Standard Model of particle physics is a theory of the interplay between the universe's elementary constituents. Guided by the principles of symmetry and least action, we formulate the Standard Model by applying quantum mechanics and special relativity to suitably defined abstract fields. The result is a powerful model, containing a description of three of the discovered forces: electromagnetic, weak, and strong. But in as much as the Standard Model is elegant, it is also perplexing, leaving a number of questions unanswered.

Investigating the unanswered questions and testing our current understanding are the primary goals of particle physics research. Studying the universe at the smallest scale requires looking at the interactions at the highest energies.* In order to do this in a controlled environment, modern high energy physics laboratories have become the sites of the largest man-made accelerators, that collide particles at the highest energies attainable with modern technology. The Large Hadron Collider (LHC) at CERN is the flagship experiment of this

*Heuristically, the length scale can be represented by the de Broglie wavelength, inversely proportional to the particle's momentum: $\lambda = h/p$, where h is the Planck constant.

kind, and ATLAS and CMS are its largest detectors, collecting data from proton collisions for frontier research in fundamental physics.

Already, the LHC has helped us resolve a conjecture about the Standard Model that had been unanswered since the 1960s. The Higgs boson, whose field provides an elegant mechanism for electroweak symmetry breaking and giving masses to elementary particles, was discovered in 2012 by both ATLAS [1] and CMS [2] collaborations. With the existence of the Higgs boson firmly established, dedicated analysis groups have concentrated their efforts on improving the measurements of the Higgs properties, such as its couplings and production cross sections. Precision measurements in the Higgs sector are very important for our understanding of the fundamental physics, as the Higgs field plays a central role in the gauge field theory of electromagnetic and weak interactions. The way the Higgs boson couples to the other fields also provides a new way to investigate properties and improve modeling of quantum chromodynamics. The presence of the Higgs field in the Standard Model, as well as the specific values of the parameters associated with it, have implications reaching beyond the explanation of the observed masses of elementary particles, soliciting questions about the physics beyond the Standard Model and stability of the vacuum in the universe.

Presented in this dissertation are the methods and results of the data analysis used to extract the Higgs boson production cross section in the diphoton decay channel from the ATLAS data, collected in the Run 2 of the LHC. The author contributed to different aspects of the analysis since the beginning of Run 2 in 2015. The analysis team produced yearly results using incremental datasets. Consequently, the analysis evolved with the increase in integrated luminosity delivered by the LHC, as well as introduction of new methods. A list of the respective publications is provided in Table 6.1.

The dissertation is organized in the following way. Chapter 1 is the introduction. An overview of the theoretical framework of the Standard Model is given in Chapter 2. Chapter 3 discusses simulation of collision events with the help of Monte Carlo event generators and the theoretical predictions used in the analysis. The LHC and the ATLAS detector are described in Chapter 4. Chapter 5 continues with a discussion of the experimental techniques of object and event reconstruction on the ATLAS detector. The central subject of this dissertation is presented in Chapter 6, which contains the details and results of the Higgs boson cross section analysis in the diphoton decay channel. The main discussion is concluded in Chapter 7.

The appendices describe additional projects the author worked on, which do not directly pertain to the main subject of $H \to \gamma\gamma$ cross section measurements. A discussion of the GoSam ntuples and the studies performed using them can be found in Appendices A and B. Hardware, electronics, and firmware upgrade projects for the ATLAS Tile calorimeter are described in Appendix C. Contribution to the TileCal upgrade efforts earned the author an official membership in the ATLAS collaboration.

Before proceeding, it should be noted that equations given in this document are written using natural units, whereby the speed of light, the Plank constant, and the vacuum permittivity, are all dimensionless and equal to one,

$$c = \hbar = \frac{h}{2\pi} = \varepsilon_0 = 1. \tag{1.1}$$

As will be seen in Chapter 2, this definition is very convenient, reducing the amount of clutter in many equations. For example, the fine structure constant can be written as

$$\alpha = \frac{e^2}{4\pi}, \tag{1.2}$$

where e is the magnitude of the electron charge. This convention is unambiguous, and factors of the constants listed in Eq. (1.1) can always be restored using dimensional analysis. In this natural system, only one fundamental unit survives, and units of length and time are both inversely proportional to the units of momentum and energy. The natural scale for the discussion is on the order of the masses of the weak (W and Z) and Higgs bosons. Thus, most values of energy, momentum, and mass will be quoted in gigaelectronvolts (GeV).

Chapter 2

Theory

Our contemporary model of fundamental interactions is formulated as a relativistic theory of quantized fields. Field theory turns out to be the natural language required to reconcile special relativity with quantum mechanics. This can be seen in several ways. One reason for adopting the field theory approach is to be able to deal with systems of variable particle number. On the one hand, extension of the space of states from Hilbert to Fock naturally leads towards field theory. On the other, relativistic processes cannot be assumed to conserve particle number. Einstein's mass–energy equivalence formula, $E = mc^2$, relates the amount of energy absorbed or released when a massive particle is created or annihilated. And, by the uncertainty principle, $\Delta E \Delta t \geq \hbar/2$, intermediate particles can be produced off the mass shell. Thus, the theory must be able to describe fluctuating numbers of particles of different types. In QFT, particles are interpreted as excitation quanta of the respective fields, and creation and annihilation operators appear similarly to ladder operators.* Furthermore, there are systems, such as lasers, whose description requires superposition of states of definite particle number. Another argument for QFT is that it is the only known relativistic quantum mechanics formalism consistent with Lorentz invariance and causality. In particular, QFT

*Ladder operators appear, in particular, as a consequence of quantization of energy levels in harmonic oscillator problems, a discussion of which can be found in any elementary quantum mechanics book, such as [3]. Many problems, at least in approximation, e.g. in perturbation theory, resemble a harmonic oscillator, because any smooth potential can be modeled near a minimum by a parabola using a Taylor series up to the quadratic terms. Heuristically, a field can be viewed as a collection of enharmonic oscillators labeled by generalized coordinates.

solves the causality problem by producing cancellations between particle and antiparticle propagation amplitudes outside the light cone.*

Our central guiding principle in the development of the fundamental theory of interactions is symmetry. Observations of the invariance of natural laws with respect to the choice of the frame of reference led to ideas of relativity (first Galilean, then special and general). Redundancies in the definitions of fields in electromagnetism and phases in quantum mechanics led to the formulation of the fundamental forces as interactions with gauge fields. Symmetries among the multitude of hadronic particles led to the discovery of the color charge and formulation of quantum chromodynamics (QCD). The duality between continuous symmetries and conservation laws is captured by Noether's theorem.† Three discrete symmetries are identified as fundamental to physical laws: charge conjugation, C, parity inversion, P, and time reversal, T. Individually, all three of these are respected by all interactions except for the weak, which violates them individually, as well as in combinations of two. But, the combination of all three, CPT, is respected in all situations.

2.1 Standard Model

The SM is our current best theory of interactions between all known elementary particles, describing three of the four fundamental interactions (electromagnetic, weak, and strong). It provides the means to calculate cross sections for all experimentally observable processes, and its predictions agree extremely well with the data. The theory also gives a conceptual

*Preservation of causality in a relativistic theory requires that events separated by a spacelike interval cannot influence each other. In QFT, this condition can be expressed by the vanishing commutator, $\left[\phi(x), \phi^\dagger(y)\right] = 0$, for $(x-y)^2 < 0$, which is a condition distinct from $\mathbf{x} \neq \mathbf{y}$ and $x^0 = y^0$. For a detailed discussion, see, for example, chapter 2 of [4].

†Noether's theorem states that existence of continuous symmetry transformations that leave the Lagrangian invariant (up to a divergence) implies existence of respective conserved currents.

framework for explanation of many observed phenomena.

Although hugely successful, the SM has its scope of applicability. It does not account for large scale astrophysical phenomena, namely, the predominance of matter over antimatter, the existence of sufficient dark matter, the cosmological constant (dark energy), or the mechanism of inflation of the universe.* The SM does not include gravity, as there is no self-consistent quantum theory of it. General relativity, as the full theory of spacetime, is not incorporated into the SM, which includes only special relativity. Several phenomena are accommodated within the SM without a mechanism that would generate the respective parameters of the model. These constants, that have to be measured and cannot be derived within the theory, include the values of the masses of the Higgs boson and fermions, the parameters of flavor mixing for quarks and neutrinos, including the CP-violating complex phase,† and the values of the coupling constants.

The fundamental particles of SM are cataloged in Fig. 2.1. Due to their properties, the particles fall into various categories. Thus, we distinguish half-integer spin fermions, representing matter particles, and whole-integer spin bosons, representing mediators of interactions through fundamental forces.

Among fermions there are quarks and leptons. Quarks carry color charge and form strongly interacting hadrons, such as protons and neutrons. Leptons don't interact strongly. There are massive electrically charged leptons (electrons and their heavier cousins muons and tau) and nearly massless uncharged neutrinos. Orthogonally, there are three generations, or flavors, of fermions, with each subsequent generation more massive than the previous, but otherwise possessing identical properties. For each type of fermion there is a distinct

*These are appropriately referred to as the "Four Mysteries of the Cosmos" by James Wells in [5].

†CP violation can be observed in experiments with neutral kaons, which can decay to either 2 or 3 photons.

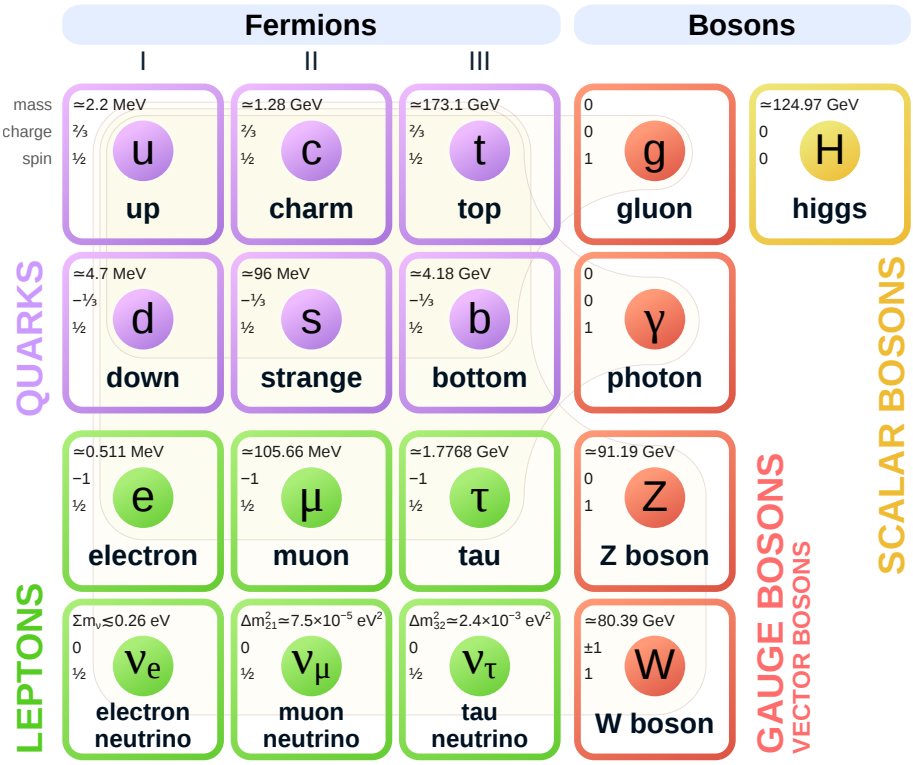

Figure 2.1: Elementary particles of the Standard Model [6].

antiparticle with conjugate charges. All fermions can interact weakly.

Each type of interaction has a corresponding mediator vector boson: photons for electromagnetic, gluons for strong, and W and Z bosons for weak. Photons and gluons are massless, while the weak bosons are massive. W^+ and W^- are electrically charged, while the other bosons are neutral. The scalar Higgs boson, unlike the vector bosons, is not a mediator. However, it plays a central role in the electroweak sector of the SM, allowing the theory to accommodate massive vector bosons, as well as fermions' masses and flavor mixing.

2.2 Quantum Field Theory

The fundamental postulate of mechanics is the principle of least action, whereby the physical dynamics of a system corresponds to the evolution which keeps action, $\mathcal{S}$, stationary

to first order, i.e. $\delta\mathcal{S} = 0$. Action is defined as the integral of the Lagrangian, L, which, in its turn, is a function of generalized coordinates, q, and their time derivatives, $\dot{q}$,

$$\mathcal{S} = \int_{t_1}^{t_2} dt\, L\big(q(t),\, \dot{q}(t),\, t\big). \tag{2.1}$$

Requiring $\delta\mathcal{S} = 0$ then leads to the Euler–Lagrange equations,

$$\frac{\partial L}{\partial q} - \frac{d}{dt}\frac{\partial L}{\partial \dot{q}} = 0, \tag{2.2}$$

which, when applied to a specific Lagrangian, produce equations of motion.

A system of N bodies can be represented by a Lagrangian $L\big(\{q_a\}, \{\dot{q}_a\}, t\big)$, with $a = 1, 2, \ldots, N$. If changes in q_a are small, deviating only slightly from equilibrium, the bodies can be labelled by their position, $q_a(t) \to q(\vec{x}, t)$. In the continuum limit,* the generalized coordinates, q, form a field, which is then customary to instead denote by ϕ. Fields, rather than spacetime coordinates, are the dynamic variables of the Lagrangian. In the setting of field theory, it is more convenient to talk about the Lagrangian density,† $\mathcal{L}$, rather than the Lagrangian, L, with

$$L = \int d^3x\, \mathcal{L}. \tag{2.3}$$

One way to quantize the theory is to promote the dynamic variables, i.e. the fields, to operators and to impose canonical commutation relations,‡

*For an intuitive introduction to QFT, including an analogy between a field and a spring mattress see Chapter 1 in Zee [7].

†In field theory, $\mathcal{L}$ is often simply referred to as the Lagrangian.

‡Canonical (also known as second) quantization is similar to how quantum mechanics was developed. Another way to quantize a relativistic field theory is through path integral formulation. The two approaches yield equivalent results, but the path integral approach is often more convenient for automating calculations.

$$\big[\phi(\mathbf{x}), \pi(\mathbf{y})\big] = i\delta(\mathbf{x}-\mathbf{y}), \qquad \big[\phi(\mathbf{x}), \phi(\mathbf{y})\big] = \big[\pi(\mathbf{x}), \pi(\mathbf{y})\big] = 0, \tag{2.4}$$

where $\pi(\mathbf{x}) \equiv \frac{\partial \mathcal{L}}{\partial \dot{\phi}(\mathbf{x})}$ is the momentum density conjugate to $\phi(\mathbf{x})$. Switching to momentum space via Fourier transformation, one can then formulate creation and annihilation operators, $a^\dagger_{\mathbf{p}}$ and $a_{\mathbf{p}}$, with the appropriate commutation relations. Formally, the states in QFT live in Fock space, which is a space of states of variable or unknown number of identical particles, constructed from a single-particle Hilbert space. The number operator is given by

$$n_i = a^\dagger_i a_i, \tag{2.5}$$

where the index i stands for all labels, including momenta and particle species, implying that creation, annihilation, and number operators, commute for distinct sets of labels.

2.2.1 Types of fields and spin

Fields differ from one another by quantum numbers (or charges) that they carry, by their transformation properties and the symmetries they obey, and by the way they interact with (or couple to) themselves and other fields.

One of the fundamental properties of a field is the way it behaves under Lorentz transformations. This property is intimately related to the notion of spin. Field values can be viewed as elements of a vector space on which elements of the Lorentz Lie group act as transformations. Different types of fields require different representations of the Lorentz group. Associated with these representations are different values of spin.* Mathematically, spin has the same properties as angular momentum, and can be viewed as a fixed intrinsic amount of

*Spin of a relativistic field is determined by the properties of the Wigner's little group, which is defined as the subgroup of homogeneous Lorentz group that leaves the 4-vector of a particle invariant. In particular, the magnitude of spin is determined by the dimensionality of the fundamental representation of the little group.

angular momentum carried by a particle.* However, unlike orbital angular momentum, spin admits half-integer values, with its projection still quantized in integer steps between $-s$ and $+s$. The association between spin and Lorentz transformation properties is as follows: spin-0 fields are scalars, spin-1 are vectors, spin-2 are tensors, etc; spin-$\frac{1}{2}$ fermionic fields are spinors. All elementary particles in the SM have spin of either 0, $\frac{1}{2}$, or 1.

As demonstrated by the spin–statistics theorem, spin also determines the statistical properties of identical particles. Bosons with integer (including zero) spin follow Bose–Einstein statistics and can occupy identical quantum states, while fermions with half-integer spin follow Fermi–Dirac statistics and cannot occupy identical states, which leads to the Pauli exclusion principle. In QFT, this behavior emerges as a consequence of the opposite properties of the two types of wavefunctions under the exchange symmetry. Symmetric bosonic fields are quantized using commutation relations,†

$$\left[a_{\mathbf{p}}, a_{\mathbf{q}}^{\dagger}\right] = a_{\mathbf{p}} a_{\mathbf{q}}^{\dagger} - a_{\mathbf{q}}^{\dagger} a_{\mathbf{p}} = \delta(\mathbf{p} - \mathbf{q}), \tag{2.6}$$

while antisymmetric fermionic fields require anti-commutation relations,

$$\left\{a_{\mathbf{p}}, a_{\mathbf{q}}^{\dagger}\right\} = a_{\mathbf{p}} a_{\mathbf{q}}^{\dagger} + a_{\mathbf{q}}^{\dagger} a_{\mathbf{p}} = \delta(\mathbf{p} - \mathbf{q}). \tag{2.7}$$

The commutator identities allow for repeated application of the creation operator, $a^{\dagger}$, to bosonic states, and thus an arbitrary number of bosons can occupy the same state. But the anticommutator identities imply that repeated application of $a^{\dagger}$ annihilates the state, and

*Spin can be detected in experiments with charged particles in a magnetic field, where it is observed as a magnetic dipole moment. For example, a Stern–Gerlach type of experiment demonstrates separation of particles traveling through a magnetic field into as many bunches as the number of available spin projections.

†Note, that in general, the (anti-)commutation relations for creation and annihilation operators apply only to states at equal time. The commutators must vanish for spacelike separated events to respect causality.

so only one identical fermion per state is allowed. This explains the connection between spin and statistics.

2.2.2 Interactions

The only tangible thing in QFT is the interaction. In fact, a non-interacting field is as good as non-existent, since it is unable to cause any measurable effects. In high energy physics, we describe interactions as scattering or decay processes. Thus, the observables we primarily need to calculate are scattering cross sections, σ, and decay widths, Γ.

To understand why cross section and width are the natural quantities that characterize particle interactions, let's first consider the decay of unstable particles. If we have a set of N particles, each of which has a constant probability Γ of decaying per unit of time, the number of them decaying in a time interval dt is given by $N\Gamma dt$. Therefore,*

$$dN = -\Gamma N dt \quad \Leftrightarrow \quad N = N_0 e^{-\Gamma t}. \tag{2.8}$$

The mean lifetime of a particle is then given by

$$\tau = \langle t \rangle = \frac{\int_0^\infty t p(t) dt}{\int_0^\infty p(t) dt} = \frac{1}{\Gamma}. \tag{2.9}$$

Heuristically, the time-energy uncertainty relationship,

$$\Delta E \Delta t \sim 1, \tag{2.10}$$

*The fact that the probability of still finding an unstable particle, after a given amount of time, decreases exponentially can also be understood by realizing that probabilities are multiplicative. So, to obtain the probability after time t, one needs to take a product integral: $p(t) = \prod_0^t (1 - \Gamma dt) = \exp(-\Gamma t)$.

suggests that an unstable particle with a mean lifetime τ would have an energy uncertainty on the order of

$$\Delta E \sim \frac{1}{\tau} = \Gamma. \tag{2.11}$$

In non-relativistic regime, $\Gamma \ll m$, this can be modeled by adding a complex component to the particle's energy,

$$E = E_0 - i\Gamma/2. \tag{2.12}$$

In the rest frame of the particle, its time-dependent wave function can then be written as

$$\psi(t) = \psi(0)\exp\big(-iEt\big) = \psi(0)\exp\big(-iE_0t\big)\exp\left(-\frac{\Gamma t}{2}\right). \tag{2.13}$$

Therefore, the total probability decays exponentially, as expected,

$$|\psi(t)|^2 = |\psi(0)|^2\, e^{-\Gamma t}. \tag{2.14}$$

To look at the process in the energy space, we take the Fourier transform of Eq. (2.13), which yields

$$\widetilde{\psi}(E) = \frac{i}{\sqrt{2\pi}}\frac{\phi(0)}{(E-E_0)+i\Gamma/2}. \tag{2.15}$$

Squaring the transformed amplitude and normalizing the result, we get the probability for the particle to undergo the transition as a function of energy,

$$p(E) = \frac{1}{2\pi}\frac{\Gamma}{(E-E_0)^2+(\Gamma/2)^2}. \tag{2.16}$$

This is the familiar Breit–Wigner distribution,* with the full width at half maximum

*The Breit–Wigner distribution is also knows as the Lorentzian or the Cauchy distribution.

(FWHM) equal to Γ. The more general relativistic Breit–Wigner distribution,

$$p(E) = \frac{A}{\left(E^2 - m^2\right)^2 + m^2\Gamma^2}, \tag{2.17}$$

which is also valid for $\Gamma \gtrsim m$, can be derived by starting with the propagator for a massive particle in relativistic QFT, whose denominator has the form $p^2 - m^2 + im\Gamma$.

A fundamental quantity characterizing a scattering process is an effective measure of the area of overlap between the interacting objects. Differential scattering cross section, $d\sigma$, represents a portion of this area that results in an outcome within a differential volume $d\Omega$ of the final state phase space. The total scattering cross section, σ, is an integral of $d\sigma/d\Omega$ over the phase space of interest. Naturally, cross section is a function of the impact parameters. In classical mechanics, cross section has a deterministic relationship with the orbits of the interacting bodies. In quantum mechanics, $d\sigma/d\Omega$, essentially, contains a convolution with the probability density of all possible outcomes. Cross section, rather than probability, is typically calculated in particle physics as a quantity that directly relates universally applicable theory to the outcome of a specific experiment. Given the impact parameters, cross section is a universal quantity. However, luminosity, L, which is a measure of the beam intensity, or number of particles in the beam passing through a unit of area in a unit of time, is different for each experiment. The number, N, of interactions of interest one expects to observe in an experiment running for some amount of time, T, is given by

$$N = \int_0^T \sigma L \, dt. \tag{2.18}$$

Or, if the impact parameters are constant,

$$N = \sigma \int L. \tag{2.19}$$

There is also a relationship between scattering cross section and decay width. Eqs. (2.16) and (2.17) describe equally well both decay and production of intermediate states. A process of scattering through an intermediate state can be approximated as a production followed by a decay. In the narrow width approximation, the cross section for producing a final state f from an initial state i through an intermediate state r can be obtained by the Breit-Wigner formula,

$$\sigma_{i\to r\to f} = \frac{4\pi}{k^2}\left[\frac{n_r}{n_i n_f}\right]\frac{\Gamma^2/4}{(E-E_0)^2+(\Gamma/2)^2}B_{r\to i}B_{r\to f}, \tag{2.20}$$

where k is the initial momentum in the center-of-mass frame, n are multiplicity factors due to spin, color, etc., and $B_{r\to x}$ are the branching ratios,* equal to the fraction of times a state r would decay to a state x. The state r is often referred to as a resonance. In a scattering experiment, by varying the center of mass energy, E, one can observe the number of events undergoing the $i \to f$ transition rise sharply around $E = E_0$, which can be interpreted as the mass of the resonant state. In the absence of background, the histogram of observed events would take the shape of the Breit-Wigner distribution.

Ideally, given the Lagrangian, one would solve for eigenvalues and eigenvectors of operators for the relevant observables. Unfortunately, there are no known examples of exactly solvable interacting field theories in more than 2 spacetime dimensions [4]. Fortunately, in many cases of interest, when couplings between fields are small ($g \ll 1$), interactions can be

*Equivalently, Eq. (2.20) can be formulated in terms of partial widths, with $\Gamma_{r\to x} = \Gamma B_{r\to x}$.

treated using perturbation theory.

Given an initial state in the remote past (in) and a final state in the remote future (out), the transition (or scattering) amplitude is the overlap between the states, which can be expressed as

$$ {}_{\text{out}}\langle f|i\rangle_{\text{in}} = \lim_{t\to\infty} \langle f|e^{-iH(-t)} \cdot e^{-iHt}|i\rangle \equiv \langle f|S|i\rangle, \tag{2.21} $$

where t is any common reference time, and S, called the scattering matrix or S-matrix, is a unitary operator relating the initial and final states at the common time. For non-interacting particles, S is simply the identity operator. The interaction part can be separated into the T-matrix,

$$ S = 1 + iT. \tag{2.22} $$

As discovered by Feynman, terms in the perturbative expansion of $\langle f|iT|i\rangle$ have intuitive graphical representations. For example, Fig. 2.2 shows leading-order diagrams for fermion scattering in QED. To make 4-momentum conservation explicit, we define the invariant matrix element or amplitude, $\mathcal{M}$,

$$ \langle f|iT|i\rangle = (2\pi)^4 \delta^{(4)}\left(\sum p_i - \sum p_f\right) \cdot i\mathcal{M}(i \to f). \tag{2.23} $$

Each diagram represents a term in the perturbative expansion of $\mathcal{M}$ for a given channel and order in coupling.

Feynman diagrams are both a bookkeeping and a computational device. They allow a simple visualization of scattering processes and an easy identification of allowed and forbidden channels. The allowed vertices are related to the structure of the Lagrangian, as they correspond to the coupling terms. A Feynman diagram is in itself an expression of a contribu-

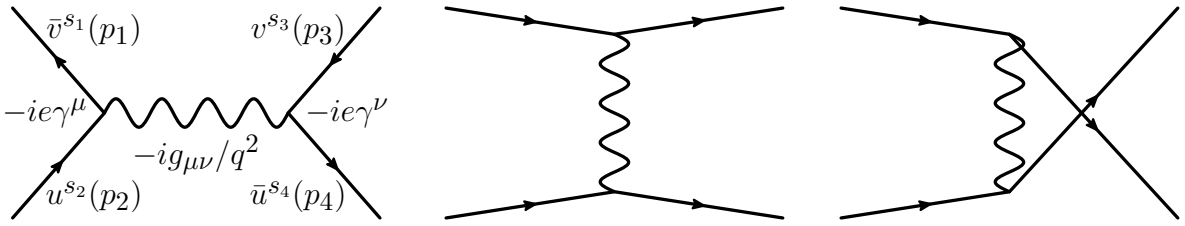

s-channel
$q^2 = s = (p_1 + p_2)^2$

t-channel
$q^2 = t = (p_1 - p_3)^2$

u-channel
$q^2 = u = (p_1 - p_4)^2$

Figure 2.2: Feynman diagrams for e-e scattering in QED, with the spatial dimension drawn vertically, and time horizontally. The three channels are named after the Mandelstam variables, s, t, and u, which, in the respective cases, are equal to the square of the four momentum of the exchanged photon. s and t channels contribute to Bhabha (e^+-e^-) scattering, while t and u channels contribute to Møller (e^--e^-) scattering.

tion to the respective matrix element. The external legs (initial and final states) correspond to free particles, the internal lines (virtual particles) are propagators (or Green's functions) correlating fields at different points in spacetime, and the vertices represent couplings between the interacting fields. The substitutions one makes to obtain amplitude expressions from the diagrams are called Feynman rules.

The prescription for determining the cross section is this: draw all allowed diagrams for the given process up to a sufficient order in coupling and compute the respective matrix elements. The differential cross section for the initial state $\{i\} = \{a, b\}$ and the final state $\{f\}$ is then given by*

$$d\sigma = \frac{1}{2E_a 2E_b \left|v_a - v_b\right|} \left(\prod_f \frac{d^3 p_f}{(2\pi)^3} \frac{1}{2E_f} \right) \left|\mathcal{M}(i \to f)\right|^2 (2\pi)^4 \delta^{(4)} \left(\sum p_i - \sum p_f \right), \quad (2.24)$$

where $|v_a - v_b|$ is the relative velocity of the particles as viewed from the laboratory frame. For identical combinations of initial and final states, one adds amplitudes together; for

*The equation for differential width, $d\Gamma$, has the same structure, except with the prefactor replaced by $1/(2m_a)$, corresponding to the single particle initial state. These expressions are derived in Section 4.5 of [4]. For identical masses in initial and final states, $d\sigma/d\Omega = |\mathcal{M}|^2/(64\pi^2 s)$.

distinct combinations, one adds cross sections.

2.2.3 Gauge fields

One of the great successes of the SM is in the formulation of interactions between elementary particles from principles of symmetry. The recipe consists of requiring the Lagrangian to be *locally* invariant under phase transformations of fermionic fields. This property of the Lagrangian is called gauge invariance. The gauge transformations form continuous symmetry groups, which are related to symmetries observed in the interactions of the respective fermions. Corresponding to each generator of a group, there arises a vector field called the gauge field. When the theory is quantized, the resulting gauge bosons are identified as the mediators of particular interactions.

The gauge symmetry group of the SM can be written as

$$\overbrace{\underbrace{U(1)_Y}_{\substack{\text{Weak}\\ \text{hypercharge}}} \times \underbrace{SU(2)_{\mathrm{L}}}_{\substack{\text{Weak}\\ \text{isospin}}}}^{\text{Electroweak}} \times \overbrace{\underbrace{SU(3)_C}_{\text{Color}}}^{\text{Strong}}, \tag{2.25}$$

with the subscripts denoting the sector of each group. The SM is thus a special case of Yang–Mills gauge theory. To see how the gauge fields appear in the theory,* let us denote the generators of the gauge group as T^a, $a = 1, \ldots, N$. A transformation of a fermion field ψ in the abstract gauge space has the form

$$\delta\psi(x) = igT^a\delta\theta_a(x)\psi(x) \quad \text{or} \quad \psi(x) \to G(x)\psi(x) = \exp\left(ig\,\boldsymbol{T}\cdot\boldsymbol{\theta}\right)\psi(x), \tag{2.26}$$

*A rigorous discussion of gauge theories can be found in Part III of [4].

where g is a coupling constant and $\theta_a(x)$ are spacetime dependent transformation phases. The transformations $G(x)$ form a Lie group, and the generators T^a are elements of the corresponding Lie algebra. For $SU(n)$ groups there are $N = n^2 - 1$ generators, which are $n \times n$ matrices in the fundamental representation. Correspondingly, ψ are $n \times 1$ vectors. Transformations of the form (2.26) are rotations in this vector space.

The kinetic Lagrangian term for a fermionic field has the form

$$\mathcal{L}_{\mathrm{f}} = i\bar{\psi}\not{D}\psi, \tag{2.27}$$

where $\bar{\psi} = \psi^\dagger\gamma^0$, $\not{D} = \gamma^\mu D_\mu$, γ^μ are Dirac matrices, and D_μ is the covariant derivative. In order to maintain gauge invariance of the Lagrangian, the covariant derivative must be defined as follows,

$$D_\mu = \partial_\mu + igT^a A^a_\mu, \tag{2.28}$$

where A^a_μ are new vector fields.* The theory now accounts for interactions between A^a_μ and fermions through the covariant derivative, but to turn A^a_μ into a gauge field, the appropriate kinetic term must be added to the Lagrangian. By analogy with the EM field, we construct a field strength tensor,

$$F_{\mu\nu} = \frac{1}{ig}\big[D_\mu, D_\nu\big] = \partial_\mu A_\nu - \partial_\nu A_\mu + ig\big[A_\mu, A_\nu\big]. \tag{2.29}$$

Introducing the gauge space indices with $A_\mu = T^a A^a_\mu$, we get,

$$F^a_{\mu\nu} = \partial_\mu A^a_\nu - \partial_\nu A^a_\mu - g f^{abc} A^b_\mu A^c_\nu, \tag{2.30}$$

*In the language of differential geometry, a gauge fields is a connection on a principal bundle [8]. The choice of sign in Eq. (2.28) corresponds to the $(+,-,-,-)$ Minkowski metric signature.

where f^{abc} are structure constants of the Lie algebra, given by

$$\left[T^a, T^b\right] = if^{abc}T^c. \tag{2.31}$$

When acting on the gauge fields, T^a are $N \times N$ matrices in the adjoint representation, with matrix elements given by the structure constants,

$$(T^a)_{bc} = -if^{abc}. \tag{2.32}$$

The term in Eq. (2.30) dependent on f^{abc} appears for non-Abelian gauge groups, and produces self-coupling of gauge fields. Within the SM, it is present for weak and strong interactions, but not for EM.

The Lagrangian containing both the fermionic and the gauge field can now be written as

$$\mathcal{L} = -\frac{1}{4}F^a_{\mu\nu}F^{a\mu\nu} + i\bar{\psi}\not{D}\psi. \tag{2.33}$$

As can be shown, Lagrangian mass terms for gauge fields of the form $\frac{1}{2}m^2A_\mu A^\mu$ are not invariant under local gauge transformations. In order to complete the theory and give mass to the weak bosons, a scalar Higgs field is introduced, as discussed in Section 2.3.1.

2.3 Electroweak sector

The electroweak (EW) sector of the SM is a gauge theory unifying electromagnetic and weak interactions. The direct product of two symmetry groups, $U(1)_Y \times SU(2)_\mathrm{L}$, provides the gauge group to produce the interactions of fermions via exchange of the respective gauge

bosons. Consequently, two quantum numbers, corresponding to the charges conserved by the gauge symmetry, are assigned to each fermion: weak hypercharge, Y, and weak isospin, T^3. The EW quantum numbers of SM particles are listed in Table 2.1. To reproduce the experimental observation that the weak interaction involves only left-handed fermions,* so does the gauge transformation under $SU(2)_{\mathrm{L}}$, hence the subscript. A set of generators for the $SU(2)$ Lie group is given by Pauli matrices, and by convention $T^i = \sigma_i/2$. Likewise, there are commutation relations,

$$\left[T^a, T^b\right] = i\epsilon^{abc}T^c, \qquad \left[T^a, Y\right] = 0 \quad \forall\, a. \tag{2.34}$$

Similarly to components of angular momentum or spin, the three components of T are not simultaneously diagonalizable, and T^3 is chosen as the primary component. In the abstract isospin space, since the isospin operators are represented by 2×2 matrices, left-handed fermions are 2×1 vectors, or doublets. The right-handed fermions are singlets, as they don't interact weakly.

Right-handed, rather than left-handed, anti-fermions couple weakly. In fact, the weak interaction famously maximally violates parity and charge conjugation symmetries. This can be readily seen, because P turns left-handed fermions into right-handed fermions, and C turns left-handed fermions into still left-handed anti-fermions.

*Handedness here refers to chirality, which is a Lorentz-invariant concept that applies only to fermions, which are not symmetric under parity transformation. In the Weyl basis, spinors can be written as $\begin{pmatrix}\psi_{\mathrm{L}}\\ \psi_{\mathrm{R}}\end{pmatrix}$, with the components obtained by applying respective chiral projection operators, $P_{\mathrm{L}} = \frac{1}{2}(1-\gamma^5)$ and $P_{\mathrm{R}} = \frac{1}{2}(1+\gamma^5)$. Chirality is not to be confused with helicity, which is the projection of spin onto the momentum direction. For massless fermions, chirality is the same as the sign of helicity, but for massive ones, there always exists a reference frame in which helicity has the opposite sign.

Table 2.1: Electroweak quantum numbers.

	Particles			Y	T^3	Q
Quarks	$\begin{pmatrix} u \\ d \end{pmatrix}_L$	$\begin{pmatrix} c \\ s \end{pmatrix}_L$	$\begin{pmatrix} t \\ b \end{pmatrix}_L$	$1/3$ $1/3$	$1/2$ $-1/2$	$2/3$ $-1/3$
	u_R	c_R	t_R	$4/3$	0	$2/3$
	d_R	s_R	b_R	$-2/3$	0	$-1/3$
Leptons	$\begin{pmatrix} \nu_e \\ e \end{pmatrix}_L$	$\begin{pmatrix} \nu_\mu \\ \mu \end{pmatrix}_L$	$\begin{pmatrix} \nu_\tau \\ \tau \end{pmatrix}_L$	-1 -1	$1/2$ $-1/2$	0 -1
	e_R	μ_R	τ_R	-2	0	-1
Bosons	Photon, γ			0	0	0
	Weak, $W^\pm$			0	±1	±1
	Weak, Z^0			0	0	0
	Higgs, H			1	$-1/2$	0

2.3.1 Higgs mechanism

As discussed in Section 2.2.3, gauge fields are necessarily massless. However, experiments definitively show that W and Z bosons are massive. An elegant idea of spontaneous symmetry breaking allows to reconcile these two facts.* The trick is to add a field that is scalar under Lorentz transformations, but has the same symmetry as the gauge field, and therefore caries the respective charge. The terms the new field brings into the Lagrangian can then be rearranged to form the sought-after longitudinal components of the gauge fields, thus allowing them to have mass without explicitly breaking the gauge symmetry of the Lagrangian. The Lagrangian for the scalar field has the form

$$\mathcal{L} = (D_\mu \Phi)^\dagger (D^\mu \Phi) - V(\Phi), \quad V(\Phi) = \mu^2 \Phi^\dagger \Phi + \lambda (\Phi^\dagger \Phi)^2. \tag{2.35}$$

It is simpler to illustrate the mechanism by first looking at an example with only 2 degrees

*The theory of spontaneous electroweak symmetry breaking was separately developed in 1964 by three independent groups [9–11], and is based on Landau–Ginzburg theory of superconductivity [12].

of freedom.* Consider a $U(1)$ gauge field, A_μ, with the Lagrangian

$$\mathcal{L} = -\frac{1}{4}F_{\mu\nu}F^{\mu\nu}, \quad F_{\mu\nu} = \partial_\mu A_\nu - \partial_\nu A_\mu. \tag{2.36}$$

Naively adding a mass term, $\frac{1}{2}m^2 A_\mu A^\mu$, would break the gauge invariance of the Lagrangian. Instead, add a charged complex scalar field,† ϕ,

$$\mathcal{L} = -\frac{1}{4}F_{\mu\nu}F^{\mu\nu} + (D_\mu\phi)^\dagger(D^\mu\phi) - \mu^2\phi^\dagger\phi - \lambda(\phi^\dagger\phi)^2. \tag{2.37}$$

The scalar field couples to itself via the quartic term and to the gauge field via the covariant derivative, $D_\mu = \partial_\mu - igA_\mu$. The Lagrangian is invariant under the following transformations:

$$\begin{aligned} A_\mu(x) &\to A_\mu(x) - \partial_\mu\alpha(x), \\ \phi(x) &\to \phi(x)e^{-i\alpha(x)}. \end{aligned} \tag{2.38}$$

If $\mu^2 \geq 0$, the state of minimum energy is $\phi = 0$, and the potential preserves the symmetries of the Lagrangian. In this case, the theory is simply that of the two interacting fields. However, if $\mu^2 < 0$, the minimum energy state is no longer $\phi = 0$. The $U(1)$ symmetry will be spontaneously broken, and the scalar field will acquire a non-zero vacuum expectation value, v,

$$\langle\phi\rangle = \sqrt{\frac{\mu^2}{2\lambda}} = \frac{v}{\sqrt{2}}. \tag{2.39}$$

The potential, $V(\phi)$, in this case is colloquially referred to as the Mexican hat potential. The two scenarios are illustrated in Fig. 2.3.

*At least $N = 2$ degree of freedom are required to have a continuous symmetry. $N = 1$ only allows for a discrete reflective symmetry. $N > 2$ is mathematically similar to $N = 1$, but is harder to visualize.

†A complex field has a $U(1)$ symmetry under a phase transformation that rotates one component into the other.

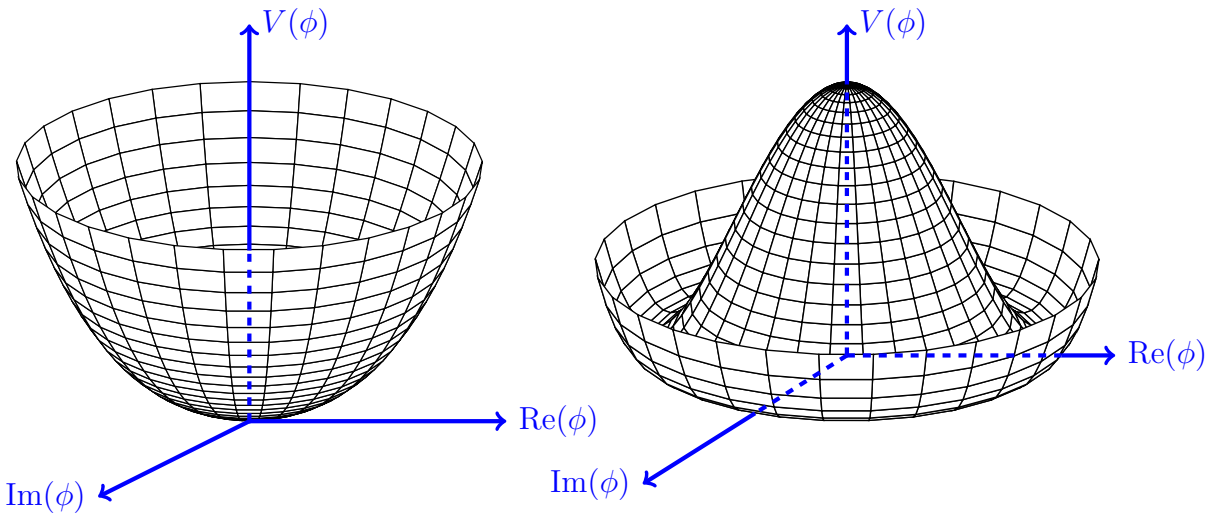

(a) Unbroken vacuum, $\mu^2 \geq 0$, $v = 0$. (b) Broken vacuum, $\mu^2 < 0$, $v \neq 0$.

Figure 2.3: Illustration of spontaneous $U(1)$ symmetry breaking due to non-zero vacuum expectation value of a complex scalar field, ϕ.

We can parametrize ϕ around v in polar coordinates as,

$$\phi = \frac{v+h}{\sqrt{2}}\, e^{i\chi/v}. \tag{2.40}$$

Writing the Lagrangian in terms of the real fields h and χ we get,

$$\begin{aligned}\mathcal{L} = &-\frac{1}{4}F_{\mu\nu}F^{\mu\nu} + \frac{g^2v^2}{2}A_\mu A^\mu - gvA_\mu\partial^\mu\chi + \frac{1}{2}\left(\partial_\mu h\partial^\mu h - 2\mu^2h^2\right) + \frac{1}{2}\partial_\mu\chi\partial^\mu\chi \\ &+ (\text{interaction terms}),\end{aligned} \tag{2.41}$$

which describes a theory with a photon of mass $m_A = gv$, a Higgs boson, h, with mass $m_h = \sqrt{2}\mu = \sqrt{2\lambda}v$, and a massless Goldstone boson, χ. The $gvA_\mu\partial^\mu\chi$ term can be removed by making a global gauge transformation,

$$A_\mu \to B_\mu = A_\mu - \frac{1}{gv}\partial_\mu\chi. \tag{2.42}$$

This is called the unitary gauge. The Goldstone boson then completely disappears from the theory and one says that it has been *eaten* by the now massive photon field, B_μ.

In the SM, the additional scalar field, Φ, has to respect both $U(1)$ weak hypercharge and $SU(2)$ weak isospin symmetries. Therefore, Φ is a complex weak isospin doublet,

$$\Phi = \begin{pmatrix} \phi^+ \\ \phi^0 \end{pmatrix} \quad \text{with} \quad \begin{aligned} \phi^+ &= (\phi_1 + i\phi_2)/\sqrt{2}, \\ \phi^0 &= (\phi_3 + i\phi_4)/\sqrt{2}. \end{aligned} \tag{2.43}$$

Spontaneous symmetry breaking produces three Goldstone bosons, which are eaten by $W^\pm$ and Z, and a Higgs boson with hypercharge $Y = 1$ and isospin $T^3 = -\frac{1}{2}$, which is therefore electrically neutral, since $Q = T^3 + \frac{1}{2}Y$. Going through a similar procedure to the above, and applying the unitary gauge transformation to remove the Goldstone bosons, we get

$$\Phi(x) = \frac{1}{\sqrt{2}} \begin{pmatrix} 0 \\ v + H(x) \end{pmatrix}. \tag{2.44}$$

2.3.2 After symmetry breaking

Following the procedure outlined in Section 2.2.3, we obtain one gauge boson, B with gauge coupling g', from the hypercharge symmetry and three gauge bosons, W^a, $a = 1, 2, 3$ with gauge coupling g, from the isospin symmetry, and the covariant derivative can be written as

$$D_\mu = \partial_\mu - ig'\frac{Y}{2}B_\mu - igT^aW^a_\mu. \tag{2.45}$$

Expanding the kinetic term for Φ and omitting the factors of $\frac{Y}{2}$ and T^a for brevity, we get

$$\begin{aligned}(D_\mu\Phi)^\dagger(D^\mu\Phi) = &\frac{1}{2}(\partial_\mu H)(\partial^\mu H)\\ &+\frac{1}{2}g^2(v+H)^2(W^1_\mu - iW^2_\mu)(W^{1\mu}+iW^{2\mu})\\ &+\frac{1}{2}(v+H)^2(gW^3_\mu - g'B_\mu)^2.\end{aligned} \tag{2.46}$$

From here, we define the physical weak bosons as linear combinations of the original gauge bosons as

$$W^\pm_\mu = \frac{W^1_\mu \mp iW^2_\mu}{\sqrt{2}}, \tag{2.47}$$

$$\begin{aligned}(gW^3_\mu - g'B_\mu) &= \sqrt{g^2+g'^2}\left(\frac{g}{\sqrt{g^2+g'^2}}\,W^3_\mu - \frac{g'}{\sqrt{g^2+g'^2}}\,B_\mu\right)\\ &= \sqrt{g^2+g'^2}\left(c_{\mathrm{W}}W^3_\mu - s_{\mathrm{W}}B_\mu\right)\\ &= \sqrt{g^2+g'^2}Z_\mu,\end{aligned} \tag{2.48}$$

where $s_{\mathrm{W}} = \sin\theta_{\mathrm{W}}$, $c_{\mathrm{W}} = \cos\theta_{\mathrm{W}}$, and θ_{W} is the Weinberg weak mixing angle. The weak bosons' masses are given by

$$M_W = \frac{gv}{2}, \qquad M_Z = \frac{v}{2}\sqrt{g^2+g'^2} = \frac{M_W}{\cos\theta_{\mathrm{W}}}. \tag{2.49}$$

The state orthogonal to Z,

$$A_\mu = \left(s_{\mathrm{W}}W^3_\mu + c_{\mathrm{W}}B_\mu\right), \tag{2.50}$$

does not couple to the Higgs boson,* and so does not acquire mass through the Higgs

*The photon field does couple to the charged component of the Higgs field, but the latter is absent in the unitary gauge.

mechanism. This is in fact the EM photon.

Rewriting the covariant derivative in terms of the physical fields,

$$D_\mu = \partial_\mu - i\frac{g}{\sqrt{2}}\left(W_\mu^+ T^+ + W_\mu^- T^-\right) - iZ_\mu\left(gc_{\mathrm{W}}T^3 - g's_{\mathrm{W}}\frac{Y}{2}\right) - iA_\mu\left(gs_{\mathrm{W}}T^3 + g'c_{\mathrm{W}}\frac{Y}{2}\right), \tag{2.51}$$

we immediately get the respective couplings. We can now define the EM coupling, e, and the electric charge, Q, by examining the photon term,

$$\left(gs_{\mathrm{W}}T^3 + g'c_{\mathrm{W}}\frac{Y}{2}\right) = \frac{gg'}{\sqrt{g^2+g'^2}}\left(T^3 + \frac{Y}{2}\right) = eQ, \tag{2.52}$$

which produces the Gell-Mann–Nishijima formula, $Q = T^3 + Y/2$.

The B-W^3 mixing, in combination with the unitary gauge, allows to explicitly recover $U(1)_{\mathrm{EM}}$ as an unbroken symmetry. This can be verified by applying a local $U(1)$ gauge transformation to a charged fermionic field, with the phase defined as the appropriate combination of the EW phases.

Three parameters can be identified in the EW theory as fundamental:*

- Fine structure constant (EM coupling), $\alpha = \dfrac{e^2}{4\pi} \approx 1/137$,
- Fermi constant (related to weak coupling), $G_{\mathrm{F}} = \dfrac{\sqrt{2}}{8}\dfrac{g^2}{M_W^2} = \dfrac{1}{\sqrt{2}}\,v^{-2}$, $v \approx 246\,\mathrm{GeV}$,
- Weinberg mixing angle, $\sin^2\theta_{\mathrm{W}} \approx 0.23$.

2.3.3 Fermions' masses

In a chirally symmetric theory, fermions can be given mass simply via a Dirac mass term, $m\bar{\psi}\psi$, which, in Weyl basis, separating the left- and right-handed components, can be

*Other choices of fundamental EW parameters are possible, e.g. masses of the gauge bosons. Beyond the LO other choices of input model parameters are possible, which are not fully equivalent.

written as

$$m\bar{\psi}\psi = m(\bar{\psi}_{\mathrm{L}} + \bar{\psi}_{\mathrm{R}})(\psi_{\mathrm{L}} + \psi_{\mathrm{R}}) = m(\bar{\psi}_{\mathrm{L}}\psi_{\mathrm{R}} + \bar{\psi}_{\mathrm{R}}\psi_{\mathrm{L}}). \tag{2.53}$$

Since the isospin symmetry only affects the left-handed fermions, ψ_{L} and ψ_{R} transform differently under $SU(2)_{\mathrm{L}}$, and the bare mass terms, $m\bar{\psi}\psi$, are not gauge invariant in the SM. To fix this problem, the Higgs field can also be attributed responsibility for masses of fermions by adding gauge invariant Yukawa coupling terms to the Lagrangian,*

$$\mathcal{L} = -y\bar{\psi}_{\mathrm{R}}\Phi\psi_{\mathrm{L}} + \mathrm{h.c.} \tag{2.54}$$

After spontaneous symmetry breaking, using Eq. (2.44), we get

$$\mathcal{L} = -\frac{yv}{\sqrt{2}}\bar{\psi}_{\mathrm{R}}\psi_{\mathrm{L}} - \frac{y}{\sqrt{2}}\bar{\psi}_{\mathrm{R}}H\psi_{\mathrm{L}} + \mathrm{h.c.}, \tag{2.55}$$

with the first term being the mass term with $m = yv/\sqrt{2}$, and the second term coupling fermions to the Higgs field proportionally to m/v. It should be noted, that because the Yukawa couplings are arbitrary for all fermions, they do not predict fermion masses, but rather provide a mechanism to accommodate their existence within the SM.

For simplicity, the above equations were written for a single fermionic field, ψ. When more fields are introduced, nothing prohibits addition of mixed terms of the form

$$-\frac{y_{ab}}{\sqrt{2}}\bar{\psi}^{a}_{\mathrm{R}}(v + H)\psi^{b}_{\mathrm{L}} + \mathrm{h.c.}, \tag{2.56}$$

*Mathematically, Yukawa couplings to fermions are not necessary for the EW symmetry breaking. However, attributing both roles to the same field yields a simpler model, and no evidence against it has been observed at the LHC.

where a and b are two species of fermions. In general, then, the fermion mass matrix,

$$M_{ab} = -\frac{y_{ab}v}{\sqrt{2}}, \tag{2.57}$$

is not diagonal, and the mass eigenstates may be distinct from the flavor eigenstates.

The structure of the Lagrangian and the fact that we need to preserve $U(1)_{\text{EM}}$ as an unbroken symmetry impose constraints on M_{ab} being non-diagonal for interactions. In particular, at tree level, only charged currents admit change of fermion flavor, while there are no fundamental flavor-changing neutral currents,* as show in Fig. 2.4. The lack of LO FCNC in the SM is explained by cancellations between Yukawa coupling terms and parts of fermionic kinetic terms involving the gauge fields from the covariant derivative, Eq. (2.45). This cancellation does not occur for charged currents, which only couple to left-handed fermions. The neutral currents do couple to the right-handed fermions because of mixing between B and W^3. FCNC do occur in the SM, but only at NLO and above. Famously, such interactions take place in processes depicted by the so called penguin diagrams, which are important for

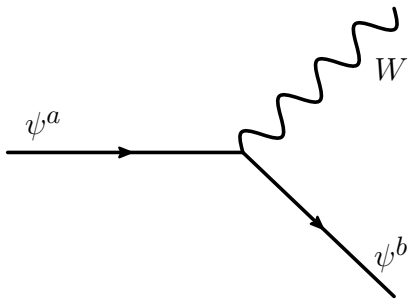

(a) LO interaction. $a \neq b$ is allowed for W, but not for Z or γ.

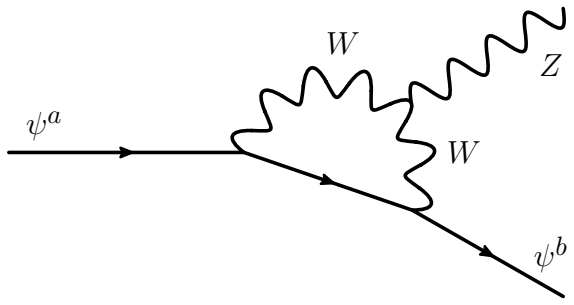

(b) NLO interaction. Same rules apply at the vertices, but the emitted boson can now be Z or γ with $a \neq b$.

Figure 2.4: Flavor-changing interactions. a and b denote fermion generations. The vector bosons are labeled for the case that allows $a \neq b$.

*The observed lack of FCNC supports the assumption that the Higgs is also responsible for fermions' masses.

understanding of CP violation in the SM [13].

The matrix describing quark flavor mixing in charged weak interactions is known as the Cabibbo–Kobayashi–Maskawa (CKM) matrix. In its standard parametrization,* it is expressed as

$$V_{\rm CKM} = \begin{pmatrix} 1 & 0 & 0 \\ 0 & c_{23} & s_{23} \\ 0 & -s_{23} & c_{23} \end{pmatrix} \begin{pmatrix} c_{13} & 0 & s_{13}e^{-\delta_{13}} \\ 0 & 1 & 0 \\ -s_{13}e^{-\delta_{13}} & 0 & c_{13} \end{pmatrix} \begin{pmatrix} c_{12} & s_{12} & 0 \\ -s_{12} & c_{12} & 0 \\ 0 & 0 & 1 \end{pmatrix}. \tag{2.58}$$

The measured values of the parameters are: $\theta_{12} = 0.2276$, $\theta_{13} = 0.0035$, $\theta_{23} = 0.0415$, and $\delta_{13} = 1.20$. θ_{12} is the Cabibbo angle. δ_{13} is the phase responsible for CP violation in flavor changing interactions.† The magnitudes of the CKM matrix elements [14] are

$$\begin{pmatrix} |V_{ud}| & |V_{us}| & |V_{ub}| \\ |V_{cd}| & |V_{cs}| & |V_{cb}| \\ |V_{td}| & |V_{ts}| & |V_{tb}| \end{pmatrix} = \begin{pmatrix} 0.97446(10) & 0.22452(44) & 0.00365(12) \\ 0.22438(44) & 0.97359(11) & 0.04214(76) \\ 0.00896(24) & 0.04133(74) & 0.999105(32) \end{pmatrix}. \tag{2.59}$$

As can be seen, the matrix is nearly diagonal, so the effects of quark flavor mixing are small, but observable.

Technically, neutrino masses can be added to the SM using exactly the same mechanism of Yukawa couplings to the Higgs field. However, that would require addition of undetectable right-handed neutrinos to the model.‡ The PMNS matrix for neutrino mixing has the same

*The CKM matrix lacks components for quark pairs with the same weak isospin, such as uc, because of the absence of FCNC.

†Because $V_{\rm CKM}$ represents a rotation in a 3-dimensional (flavor) space, it can be shown that its irreducible representation requires only 4 parameters: 3 angles and a phase. Extra phases can be absorbed into definitions of the fermionic fields without loss of generality.

‡Another popular model for neutrino masses is the seesaw mechanism.

form of parametrization, but describes mixing of the three neutrino flavors among themselves rather than flavor changing transitions between isospin doublets. Another difference, is that flavor mixing in the quark sector is only relevant for interactions. Quark oscillations are unobservable, because the time scale for hadronization is $\Lambda_{\mathrm{QCD}}^{-1}$, corresponding to a length scale of about 1 fm. The situation with neutrinos is exactly the reverse. Because they are not charged, they can change flavor neither through charged nor neutral currents. There is no $\nu\nu W$ vertex, as it would not conserve charge, and neither $\nu\nu Z$ nor $\nu\ell W$ interactions afford flavor changing. However, because they only interact weakly, neutrinos can travel astronomical distances, over which, the effect of their propagation as mass eigenstates but interaction as flavor eigenstates becomes apparent. Consequently, neutrinos can change flavor only via projection from the flavor state basis to the mass basis, and back. There appears to be no direct flavor mixing among charged leptons.

2.4 Chromodynamics

Quantum Chromodynamics (QCD) is the theory of interactions between color-charged quarks and gluons, describing the zoo of hadrons and the strong interaction between them.* Gluons enter the theory as a non-Abelian gauge field, with the symmetry group $SU(3)_c$, which stands separately from the electroweak sector and is not broken by the Higgs mechanism, thus leaving gluons massless. The gauge group reflects the color symmetry of quarks, which are color triplets — with each quark labelled red, green, or blue, and antiquarks labelled with anti-color. Gluons are color octets, each carrying a color and an anti-color in 8 possible combinations. Bound states of quarks (hadrons) are always color-neutral, and

*A comprehensive contemporary exposition of QCD can be found in [15].

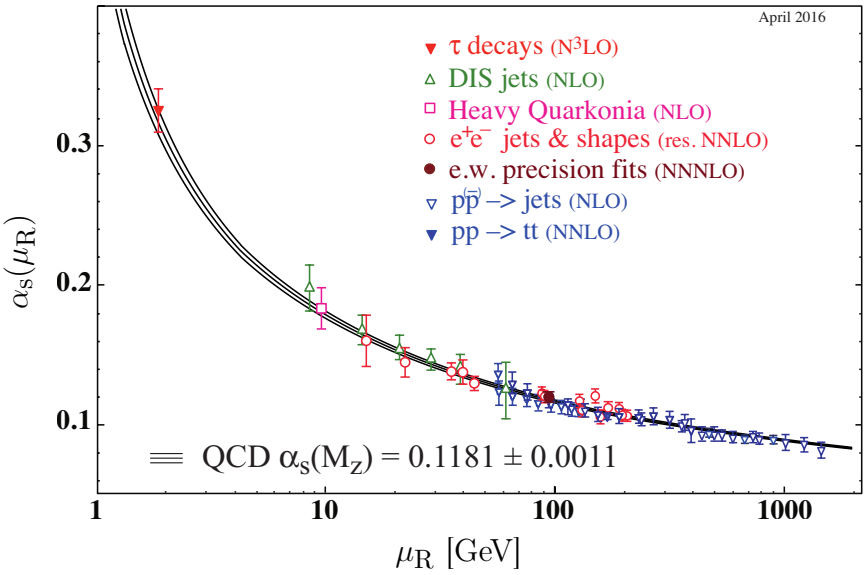

Figure 2.5: The strong coupling constant, α_s, as a function of renormalization scale, μ_R [14]. The solid black lines show theoretically calculated values and their uncertainty. The data points show experimentally obtained values with the corresponding error bars.

can consist of either quark-antiquark pairs of the same color or anti-color (mesons), or three quarks of different colors (baryons).

In fact, only hadrons can be observed directly, but never free quarks, due to the peculiar running* of the strongs coupling α_s, shown in Fig. 2.5. In contrast to the running of the EM α, the strong coupling, α_s, becomes smaller at higher energies — the effect called asymptotic freedom — whereby at short distances and high energies α_s is sufficiently small to apply perturbation theory, while at long distances and low energies the interaction becomes extremely strong, confining quarks, and precluding perturbative calculations. The energy scale at which QCD becomes non-perturbative is $\Lambda_{QCD} \approx 220\,\text{MeV}$. It is often used in calculations in place of the dimensionless coupling constant g. This behavior complicates interpretation of events at hadron colliders, but the challenge is overcome by empirical models for non-perturbative effects.

*Running of couplings is a QFT effect, present because of renormalization of couplings, which makes them dependent on the renormalization scale, μ_R. The effect can be thought of as arising due to different resolution of vacuum polarization effects, i.e. charge screening, at different energy scales.

In general, a QCD process is a combination of short- and long-distance behavior, and as such is not computable directly in perturbation theory [16]. This problem is addressed by the factorization theorem, which makes it possible to decouple non-perturbative processes inside hadrons from the hard scattering process that involves constituent partons and is tractable within perturbation theory. The factorization theorem allows one to write the hadronic cross section as a convolution between the partonic cross section and parton distribution functions (PDF) over the fraction, x, of the hadron's momentum carried by a collinear parton. For example, for a hadron-hadron collision,

$$\sigma = \sum_{ab} \int_0^1 dx_a \int_0^1 dx_b \; f_{a/A}(x_a, \mu_{\mathrm{F}}) \; f_{b/B}(x_b, \mu_{\mathrm{F}}) \; \sigma_{ab}, \tag{2.60}$$

where the sum is taken over all the possible parton combinations that allow for the inclusive final state of interest, and μ_{F} is an introduced parameter called factorization scale.

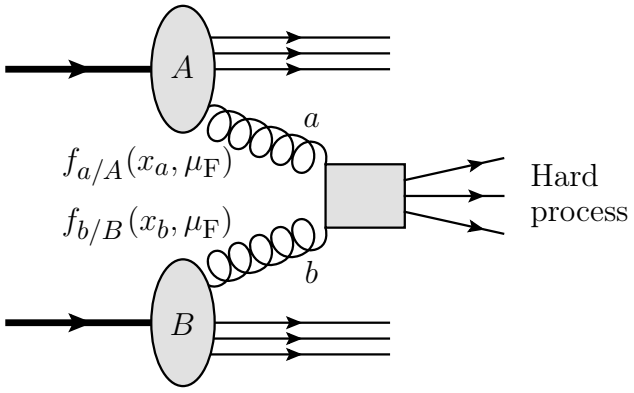

Figure 2.6: Diagramatic representation of the factorization theorem in QCD. Two colliding hadrons (A and B) each contribute a parton (a and b) with probabilities $f_{a/A}$ and $f_{b/B}$ dependent on the momentum fraction, x, and factorization scale, μ_{F}.

The non-perturbative PDF parameters cannot be calculated analytically in QCD. These parameters are determined empirically, by fitting models to deep inelastic scattering and hadron collider data. However, recent advances suggest that it might be possible to predict PDFs using lattice QCD [17–19]. On the other hand, the change of parameters with the

interaction scale can be determined perturbatively. The scale evolution of PDFs is modeled using DGLAP equations [20–22]. Fig. 2.7 shows examples of proton PDFs. As is expected, large momentum fractions are predominantly carried by the valence quarks, with, in the proton case, the probability of finding a u quark at a given value of x larger than that of a d quark. At low momentum fractions, the gluon PDF by far exceeds those of quarks, though the contributions of sea quarks are non-negligible, rising with the energy scale, and are important for obtaining p-p cross sections. In principle, one can also define photon [23] and lepton [24] PDFs through EW corrections to the DGLAP equations.

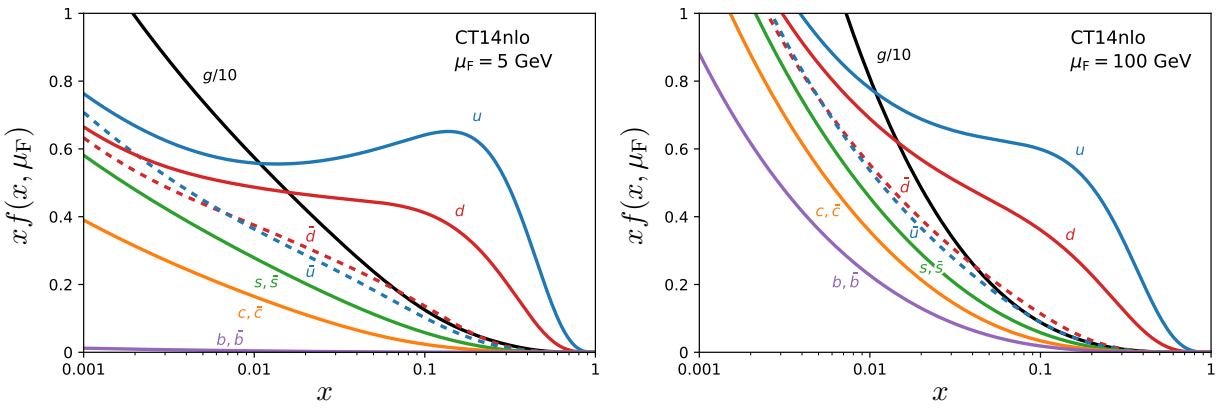

Figure 2.7: CT14nlo proton PDFs at different scales [25].

The situation on the other side of the hard scattering process is reversed, where color-charged quarks and gluons in the final state recombine into color-neutral objects. This process is called hadronization. The process is far from trivial, as non-perturbative effects dominate in this long-distance regime. The result is that, instead of individual partons, detectors see tight cones of many particles, called jets. To produce detector-level predictions, Monte Carlo simulations use various heuristic models of hadronization. These are discussed in Section 3.1. Often, collision events involve multiple jets. Jet clustering algorithms are used to systematically group particles into jets, which can then be identified with partons produced in the hard process. These algorithms are discussed in Section 5.3.

2.5 Higgs phenomenology

From the discussion of Section 2.3, it is clear that the Higgs holds a central role in the SM, like a load-bearing wall, supporting masses of heavy gauge bosons via non-zero vacuum expectation value and masses of fermions (as well as flavor mixing) via Yukawa couplings. The Higgs field provides the means to maintain gauge symmetries of the Lagrangian by balancing effects otherwise incompatible with them. After the successful discovery of the Higgs boson, the experimental agenda is to fully measure its properties and to thoroughly explore the phase space of reactions involving it. In the best case scenario, we may observe deviations from the SM, and obtain clues as to how to advance the theory. In the worst case, we will have confirmed the SM experimentally, as we have up to now, reduced the uncertainty on the SM parameters, and reduced the phase space for potential physics beyond the SM.

The SM Higgs boson directly couples to all massive elementary particles, with the coupling proportional to the mass for fermions, and mass-squared for weak bosons and self-coupling. However, an effective coupling to massless particles is also possible through loop diagrams. In fact, at the LHC, gluon-gluon fusion is the dominant Higgs production channel, due to a combination of large PDFs for gluons and small PDFs for heavy quarks. Fig. 2.8 shows a comparison of inclusive cross sections for Higgs production in pp collisions due to different processes. Archetypal examples of diagrams for the production mechanisms are shown in Fig. 2.9. While the fractions of contribution from different channels vary for different event selection criteria, ggF generally dominates, with VBF attaining a substantial fraction only among Higgs + 2 jets events with high-p_{T} Higgs or large angular separation between the jets.

The discovered Higgs with $m_H = 125$ GeV has an incredibly narrow width of only

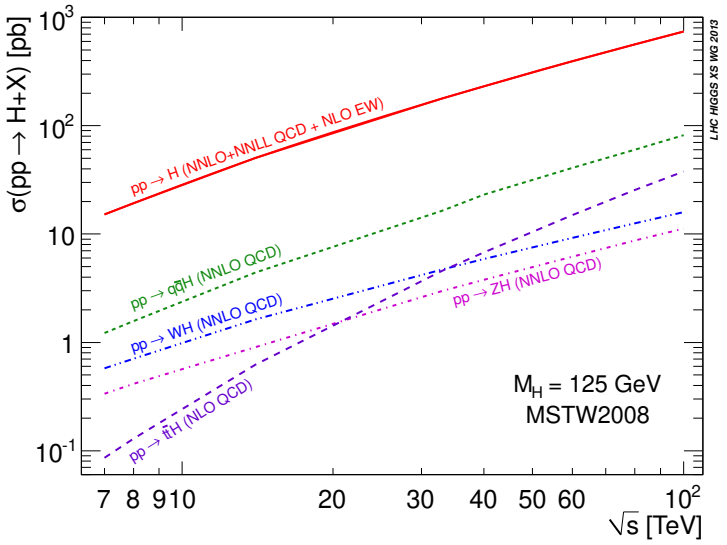

Figure 2.8: The SM Higgs ($m_H = 125\,\text{GeV}$) inclusive production cross sections as functions of $\sqrt{s}$ for different channels in pp collisions [26, 27]. The $pp \to H$ process, which is only possible through gluon-gluon fusion, clearly dominates.

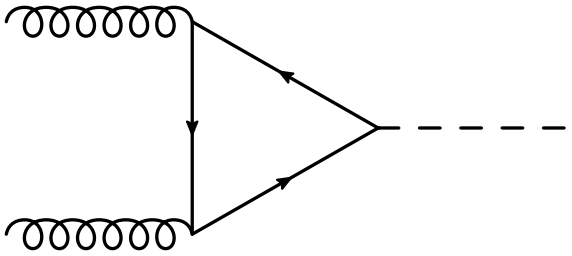

(a) Gluon-gluon Fusion (ggF).

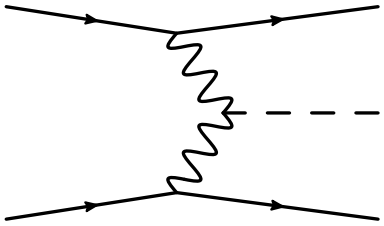

(b) Vector Boson Fusion (VBF).

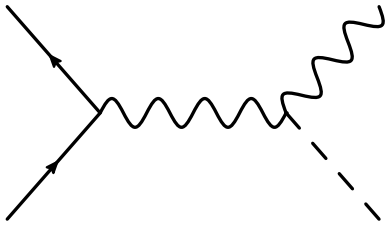

(c) Associated production with weak bosons (WH, ZH).

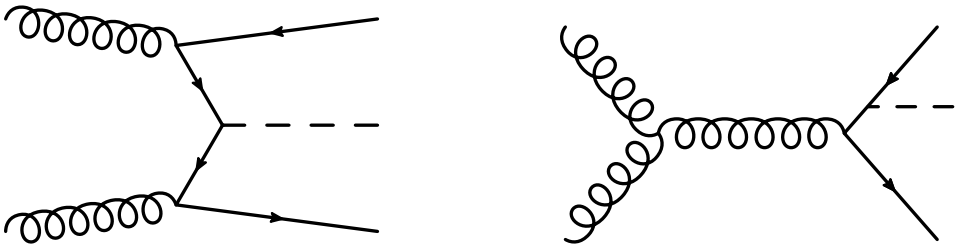

(d) Associated production with heavy quarks (bbH, ttH).

Figure 2.9: Examples of leading-order Feynman diagrams for Higgs production mechanisms.

4 MeV.* The electrically neutral, infinitesimally short-lived Higgs boson can only be studied through its decay products and other final state particles involved in its production processes. Fig. 2.10 shows the Higgs branching ratios as functions of the Higgs mass. What these plots tell us concerning experiment, is that on the one hand, we have an exciting Higgs with many decay channels; on the other hand, most of the largest decay channels are not easily tractable experimentally, due to large backgrounds from other SM processes and hard-to-identify final states. In fact, the golden discovery channels for both ATLAS and CMS, $H \to \gamma\gamma$ and $H \to ZZ^* \to 4\ell$, each have horribly low branching ratios of only about 10^{-3}. However, efforts are now being put forward to harness the $b\bar{b}$ channel, which suffers greatly from both background and selection problems, but offers potential sensitivity in the high-p_{T} region [29].

A detailed account of the phenomenology of the Higgs boson at the LHC can be found in [30].

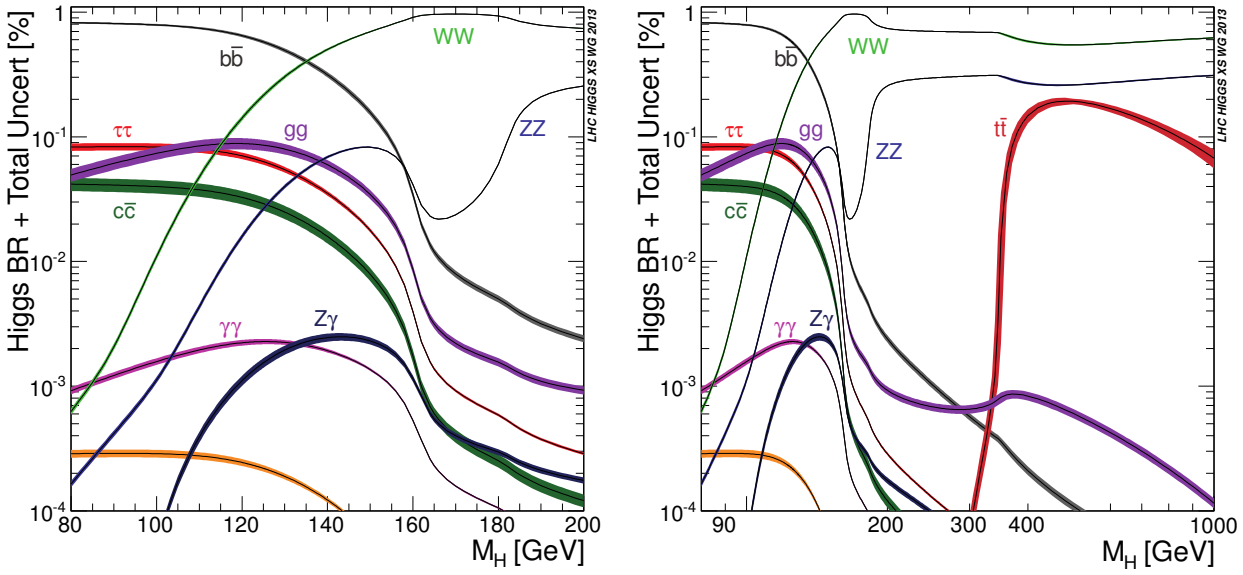

Figure 2.10: Higgs branching ratios and their theoretical uncertainties for the low mass range (left) and an extended mass range (right) [28].

*This is the theoretical width. The experimental width is much larger due to detector effects.

Chapter 3

Theoretical predictions and event simulation

Computer programs for simulating particle collision events are indispensable tools for analyzing LHC data. Simulations provide the means for interpreting the results and comparing them with theoretical predictions. Datasets of generated events allow preparatory studies to be conducted to ascertain the feasibility of new analyses, and to optimize the parameters of the ongoing ones. Such optimizations are carried out for selection cuts on observables characterizing the events, for methodology and parameters of statistical techniques (typically regression models in the form of function fits) used to quantify signal and background, and for subdivision (or binning) of the experimental datasets. Often, simulations are also necessary to derive certain quantities that are required for an analysis, but cannot be obtained directly using data-driven techniques or extrapolated from previous measurements. A typical example is the expected fraction of events due to the background processes. Event simulations are also used to assess detector effects, as generated events can be compared before and after application of the detector simulation and reconstruction algorithms. By this comparison, analysis results can be corrected for the detector effects via unfolding.

The focus of this chapter is on the use of contemporary event generators, their principles of operation, and the relevant theoretical issues. Section 3.6, at the end of this chapter,

contains a discussion of the event samples generated for the $H \to \gamma\gamma$ cross section analysis. Details of the studies conducted in the course of the analysis that relied on the generated event samples can be found in Chapter 6. Additional studies done by the author using GoSam ntuples are presented in Appendices A and B.

3.1 Monte Carlo event generation

Event simulations for hadron colliders can be divided into two categories: the calculation of the hard scattering component of an event, and simulation of the complete proton-proton collision, including the hard scattering. The former are calculations that typically produce the result of a hard interaction at the parton level, for example the production of a Higgs boson and 1, 2, or 3 partons. The latter simulate the entire event and produce final state particles at the hadron level, easier to compare to experimental measurements. In this case, the final state analogous to the above example would consist of a Higgs boson and a set of hadronic jets composed of clusters of particles that develop from the showering and hadronization of the partons produced in the hard process. In addition to the hard component, the soft component, originating from the underlying event, can also be produced. The information about the hard scattering component can be passed from the hard scattering calculation to the full event simulation program. Both types of calculations can be carried out using Monte Carlo methods. Global event simulation programs, such as Sherpa or Pythia, are used in basically every LHC analysis. Theoretical hard scattering calculations, such as GoSam, are typically not directly used by experimenters, due to their complexity, but were used in this analysis and supplementary studies in the form of ntuples.

Event generators can employ the MC method at different steps in the simulation and

for different reasons, but the basic principle is always the same. One of the reasons is that interactions in quantum mechanics are intrinsically probabilistic. Even for precisely stated parameters of the initial configuration, the set of possible final states typically has more than one element with predicted probabilities. Many aspects of the simulations rely on probabilistic models, such as parton distribution functions, splittings in parton showers, or interactions with matter in detector simulations. Another MC application is its use as a method of numerical integration [31]. Integrations required to marginalize probability distributions over certain dimensions of the phase space are often too difficult to perform analytically, either because of the large dimensionality of the phase space,* or because of the presence of experimental cuts, which impose non-trivial boundary conditions. Clustering of hadronic jets is an example of what creates a non-trivial integration problem for theoretical calculations. From the experimental perspective, jet clustering is necessary to match the detected energy deposits to the underlying hard partons; from the theoretical perspective, it provides means to handle infrared and collinear divergences.

One of the challenges of MC simulations is that the probability density function (p.d.f.)† over the phase space cannot in general be sampled directly. The most straightforward way to approach this problem is with the acceptance-rejection method. In its simplest form, the prescription is to use a uniform distribution to randomly choose a phase space point, x, together with an additional uniform random number, u, between zero and the expected maximum of the p.d.f. The p.d.f. at the selected phase space point, $p(x)$, is then evaluated. If $u < p(x)$, the event at x is simulated; otherwise, the phase space point is discarded. This

*This is often referred to as the "curse of dimensionality" because of how fast the number of parameters necessary to map out the phase space, and the number of Feynman diagrams relevant to the calculation, grow with the complexity of the process (i.e. the number of legs) and with the order of the perturbative expansion.

†To avoid confusion between a probability density function and a parton distribution function, they are abbreviated as p.d.f. and PDF respectively.

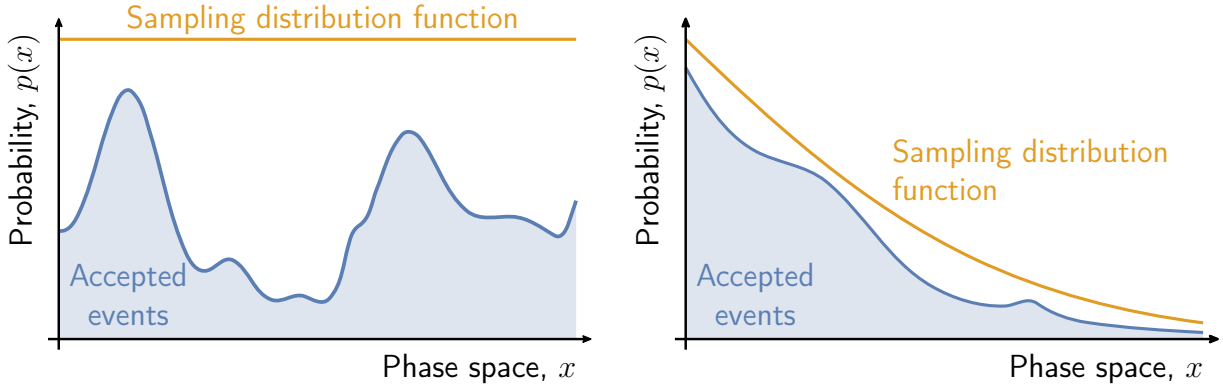

(a) Uniform sampling produces unweighted events.

(b) Non-uniform sampling produces weighted events.

Figure 3.1: Sketches of Monte Carlo sampling approaches for the acceptance-rejection method. The event probability density (blue), proportional to the fully differential cross section, is sampled by generating random numbers with the sampling probability density (orange).

approach is illustrated in Fig. 3.1a. However, often, there exist regions of phase space with much lower event probability. The uniform sampling approach results in poor sampling of such regions. In other words, fractional uncertainty (e.g. estimated with Poisson statistics), in densely populated regions would reach the required precision a lot faster than in the sparsely populated ones. For example, jet kinematics typically yields exponentially falling distributions of jets' transverse momenta. One often needs to explore their distributions on a wide p_{T} range, over which the cross section falls by several orders of magnitude. In this case, uniform sampling can result in oversampling of the lower end of the p_{T} spectrum before reaching the required uncertainty in the upper tail of the distribution.

The oversampling is problematic, because evaluation of each phase space point is a non-negligible operation, so a large fraction of the generator runtime can be spent on computations that don't add the most useful information. The problem can be solved by running multiple simulations, each covering a different region of phase space with a sufficiently flat p.d.f. However, depending on the techniques used in the simulation, this approach may

not correctly account for correlations. An alternative approach, that is used in many MC programs, is to instead define a non-uniform sampling distribution for the phase space, that provides a simplified envelope for the p.d.f., such that it can be sampled directly, i.e. by inverting the c.d.f.* In this case, the random number u is still generated uniformly, but its maximum value is now proportional to the sampling distribution. This approach is illustrated in Fig. 3.1b. By sampling in a way that reflects the varying amplitude of the p.d.f., fractional uncertainty of the observables can converge more uniformly in a different region of the phase space. This may dramatically reduce the total number of events that have to be generated to achieve the required precision. The price one pays for the improved MC efficiency is that the produced events have to be weighted in proportion to the sampling function.

At hadron collider experiments, such as the LHC, strong interactions dominate over electroweak for most processes. The picture of event evolution is thus painted from the QCD perspective, with electroweak processes incorporated mostly as corrections. Generators typically model event evolution as a sequence of processes, relying on factorization of phenomena that take place at different energy scales. These aspects of event simulation, namely the central role of QCD interactions, their sequential evolution, and factorization, can be seen in Fig. 3.2, which schematically illustrates how hadron-hadron collisions are simulated by typical MC generators. The first step in the simulation is the application of the factorization theorem, which determines what partons (quarks or gluons) with what fractions of the initial hadron momenta will participate in the hard process. The hard process is the main interaction of interest in the event, usually associated with the highest energy scale. It is

*The sampling distribution function need not have special properties. It can be discontinuous as long as it covers all the points of the phase space to be sampled. A series of step functions would yield identical results to running multiple simulations, ignoring correlations.

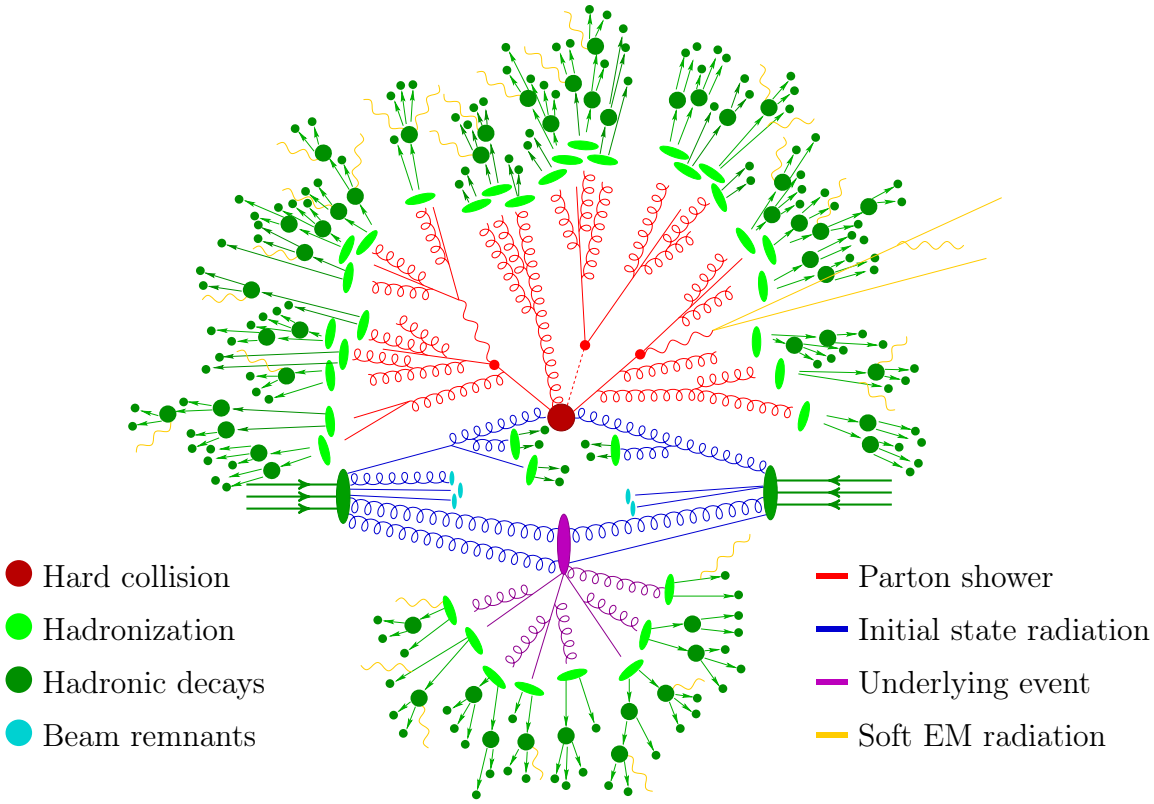

Figure 3.2: Sketch of a hadron-hadron collision as simulated by a Monte Carlo event generator program [32].

described by a matrix element (ME) calculation, typically done to a fixed order in perturbation theory,* which can be expressed as a sum over the Feynman diagrams relevant for the scattering of the two partons. Most initial and final states involve color-charged particles,† that can radiate virtual gluons, which in their turn can split into further gluons or quark-antiquark pairs, forming parton showers (PS) [33]. This pattern of radiation continues until the interaction scale falls and the strong coupling rises sufficiently for the partons to form bound states in the process of hadronization. Many of the formed hadrons are short lived

*Theoretical predictions calculated up to certain terms in a fixed order perturbative expansion are typically referred to as leading order (LO), next-to-leading order (NLO), NNLO, N^{3}LO, etc. By contrast, calculations involving analytic resummation count orders in terms of logarithms and are labeled leading log (LL), next-to-leading log (NLL), NNLL, etc. These can be matched to fixed order calculations.

†A very small fraction of events at a hadron collider involves only color-neutral particles. For example, the hard interaction may be initiated by photons, or the initial color charge may be completely annihilated, in processes such as Higgs boson production with no associated jets.

and undergo subsequent decays. Further corrections may be applied to events, for example to include electroweak interactions that produce EM radiation.*

While the ME accounts for the interaction at the hard scale, the PS describes the subsequent event evolution at lower scales. The branching processes $q \to qg$, $g \to gg$, and $g \to q\bar{q}$ are modeled by the DGLAP equations, with the branching probability given by Sudakov form factors [36]. A shower starts at the hard scale and continues until the scale gradually decreases to several GeV,† which is sufficiently low for formation of color-neutral hadrons. A showering process may be initiated by partons from either the initial or final state of the hard process, resulting in initial (ISR) and final (FSR) state radiation. These are implemented by tracing the splittings forward in time for the FSR, but backward for the ISR, resulting in the FSR being space-like (positive virtuality), and the ISR being time-like (negative virtuality).‡

The PS model has to maintain infrared and collinear (IRC) safety, ensuring that divergences caused by higher order virtual diagrams are canceled by unresolved real infrared emissions. Gluons emitted in a PS are predominantly, though not necessarily, soft and collinear due to the splitting functions. Consequently, branching typically occurs at small angles, with emitted partons carrying only a small fraction of the original momentum. A typical infrared cutoff scale of a parton shower is about 1 GeV. PS models are described in resummation formalism and, therefore, have logarithmic accuracy, not corresponding to a fixed order.** The PS models usually have LL accuracy, although recent advances have

*An overview of event simulation problems and contemporary generator programs can be found in section 4.2 of [34]. Detailed theoretical discussions of the problems of MC event generators and the typical approaches to solve them can be found in [32, 35].

†The hadronization scale is about an order of magnitude higher than the $\Lambda_{\mathrm{QCD}} \approx 220\,\mathrm{MeV}$. The latter is the scale below which the strong coupling, $\alpha_{\mathrm{s}} \gtrsim 1$. However, perturbation theory fails even before that threshold is reached.

‡Virtuality is the square of the sum of the 4-momenta of the two particles after the splitting, i.e. the square of the invariant mass of the system of virtual particles.

**Resummation is a method of regularizing series divergences, in this context, typically infrared and collinear. It effectively rearranges the original perturbative expansion into a new one that has different convergence properties.

allowed to produce PS at NLL [37, 38]. Care has to be taken in matching the fixed-order ME at the hard scale with the resummed PS at the much lower cutoff scale, especially for higher order calculations. This problem is further discussed in Section 3.3.

Multiple parton interactions (MPI) can occur in a single event, generally at scales lower than that of the hard process. The participating partons come from the remnants of the two incoming hadrons that provided the partons that initiated the hard process. Products of these additional interactions form the underlying event.

After the PS terminates at the cutoff scale, hadronization confines color-charged partons into observable color-neutral hadrons. The process can be viewed from the perspective of connection and reconnection of the color charge lines, which, besides the hard scatter, may also have contributions from MPI and the beam remnants. The length scale of these process is larger than the proton radius, corresponding to the non-perturbative regime. The two most commonly used hadronization models are the Lund model [39, 40], implemented in Pythia and Sherpa, and the cluster model [41–43], implemented in Herwig.

Depending on the application, such as analysis optimization studies or unfolding, showered and hadronized MC events may be passed through a detector simulation to incorporate effects of interactions of the particles with the detector material, as well as to account for experimental sensitivity and resolution. This is typically carried out using a dedicated program capable of simulating the material interactions of particles, such as Geant4 [44]. In addition to this, effects of pileup can be simulated by overlaying randomly sampled minimum bias events.* After detector simulation, generated events can be reconstructed in the same

*"Most of the time the color exchange between partons in the beam hadrons occurs through a soft interaction and the two beam hadrons 'ooze' through each other producing lots of soft particles with a uniform distribution in rapidity. Min-bias (MB) is a generic term which refers to events that are selected with a 'loose' trigger that accepts a large fraction of the overall inelastic cross section." [45] In this sense, MB events are not biased by the kinematics of a hard scattering process.

manner as the experimental data, using the techniques discussed in Chapter 5.

It is worth noting that event simulations do not rely on a complete theoretical description of all processes involved in the physical events they model. The simulations "are our best guess of what can happen at the LHC, but we cannot take them as absolute truth. Additionally, we can only generate specific (known) physics processes (with limited accuracy), so simulation is not always expected to describe the data." [34]

3.2 Event generation at NLO

At the momentum scales typical at the LHC, the strong coupling becomes relatively small, $\alpha_s \approx 0.1$.* This allows for a perturbative series expansion of the cross section in terms of the coupling,

$$\sigma = c_0 + c_1\alpha_s + c_2\alpha_s^2 + \dots \tag{3.1}$$

With this approach, increasingly more accurate predictions can be obtained by calculating higher order terms in the series.† Higher order calculations are important for providing accurate predictions for data analyses during planning and preparation, as model inputs, for unfolding, and as comparisons to measured observables. As higher luminosity LHC datasets push the precision frontier from the experimental side, the theoretical predictions strive to maintain a competitive degree of precision.

Naively, one would expect each higher order fractional correction to be on the order of α_s, or about 10%. However, practice shows that this is seldom true for going from LO to NLO.

*At the scale of Z boson mass, $m_Z = 91.19\,\text{GeV}$, $\alpha_s = 0.1181(11)$ [14].

†Strictly speaking, series expansions of observables in QCD in terms of α_s are asymptotic, with convergence only expected up to a certain order. However, this has not been a practical problem because, so far, techniques have been developed that enable only limited order calculations, which agree extremely well with measurements. Convergence problems are expected at arise near order $1/\alpha_s \approx 10$.

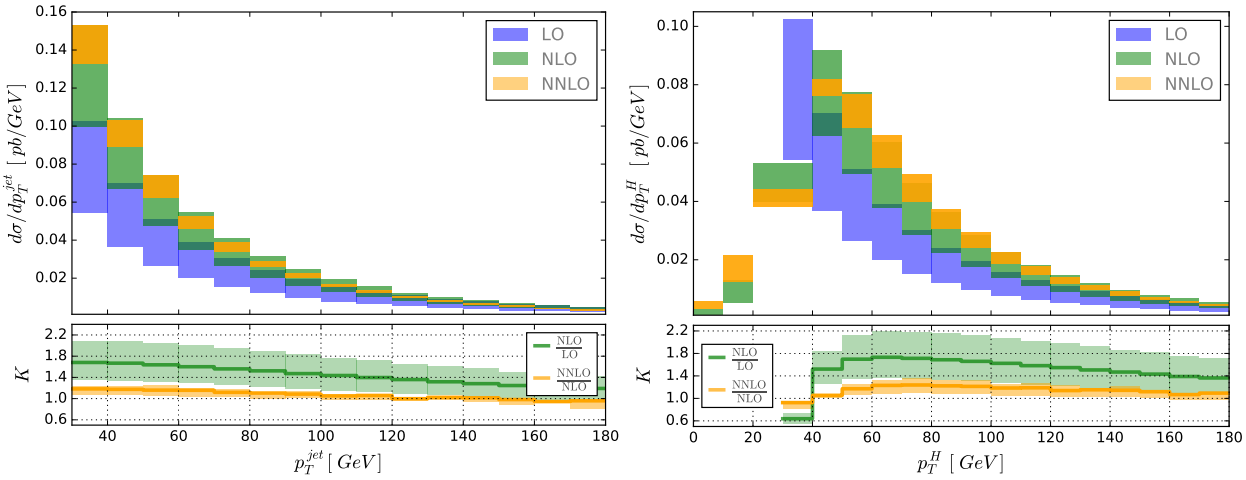

Figure 3.3: The transverse momentum of the leading jet (left) and the Higgs boson (right) calculated using jettiness subtraction technique at LO, NLO, and NNLO in the strong coupling constant for $\sqrt{s} = 8\,\text{TeV}$. The lower panels show the ratios (K-factors) of NLO over LO cross sections, and NNLO over NLO cross sections. The large NLO K-factors are apparent. The shaded regions indicate scale variation errors [46].

For a number of processes, including Higgs production, the NLO/LO ratio, or the K-factor, can be as large as 2, as can be seen in Fig. 3.3. One way to understand this is that higher order Feynman diagrams introduce additional processes into the calculation, which are not present in the lower order diagrams. Another, albeit heuristic, explanation for the large NLO K-factor in Higgs production is color cancellation. The dominant Higgs production mechanism at the LHC is gluon-gluon fusion, having two color octets in the initial state. At the LO, Higgs is produced with no additional radiation, requiring the initial state color charges to cancel out. Real NLO corrections provide a way to retain residual color charge and thus open up the phase space. In practice, virtual corrections can also play an important role in contributing to the large K-factors.

Going to the next higher order can be far from straightforward. Fortunately, in the early 2000s, coinciding with the beginning of data collection at the LHC, a number of advances was made in the automation of NLO calculations, often referred to as the NLO revolution [47–49].

Doing higher order calculations in the fixed order approach involves calculating virtual and real corrections. The virtual corrections come from diagrams containing additional loops. The real corrections appear due to the presence of unresolved phase space, and consist of diagrams with additional external legs corresponding to soft and collinear emissions. Examples of NLO correction diagrams for the gluon-gluon fusion Higgs boson production are shown in Fig. 3.4.

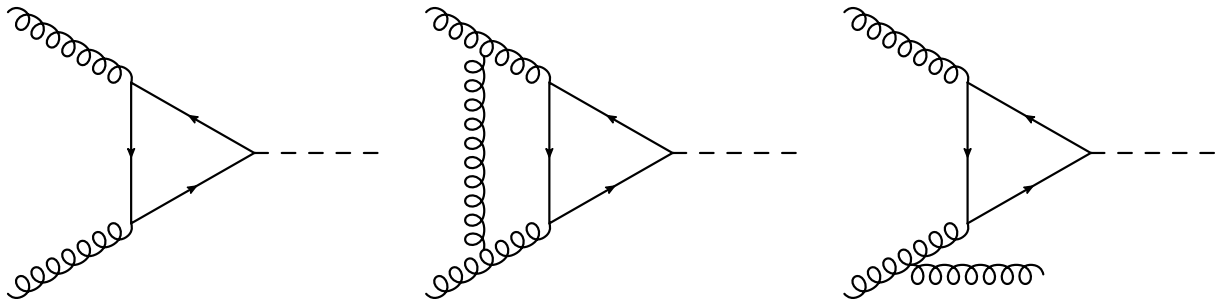

(a) A leading-order diagram (b) A virtual correction (c) A real correction

Figure 3.4: Examples of Feynman diagrams contributing at NLO to the process of Higgs boson production via gluon-gluon fusion.

The difficulty of higher order calculations partially comes from the fact that the number of correction diagrams grows rapidly with the correction order as well as the number of external legs in the process of interest. But, besides the "mere" problem of calculating a large number of increasingly more complex diagrams, additional complications arise due to infrared and collinear divergences associated with real corrections, and infrared and ultraviolet divergences associated with virtual corrections.* The soft and collinear divergences of real corrections appear from the structure of the matrix elements. The divergences of the virtual corrections can be interpreted as the result of addition of a new integration variable – the 4-momentum in the loop, which is unconstrained by overall 4-momentum conservation or on-shell conditions,

*An in-depth discussion of the problems and methodology of NLO QCD calculations can be found in chapter 3 of [15].

and can thus approach zero or infinity. These divergences have to be regularized, which is nowadays typically done with dimensional regularization as the method of choice.* The method consists in performing the integration in $D = 4-2\varepsilon$ spacetime dimensions, instead of the usual 4. Analytic continuation for the function of D can then be found, and the value of the integral can be assigned by taking the limit $\varepsilon \to 0$. This allows divergences to be identified as single, $1/\varepsilon$, or double, $1/\varepsilon^2$, poles for NLO calculations. Infrared divergences from real and virtual terms have to cancel each other out for physical observables. The divergences in the real terms are explicit and cancel with the poles of the virtual corrections. Application of jet clustering algorithms and imposition of cuts, such as on minimum transverse momentum and maximum rapidity for jets, allow physical observables to be defined for QCD final states and soft and collinear divergences to be avoided. Other divergences are renormalized through a suitable, scheme-dependent redefinition of the Lagrangian involving addition of suitable counterterms [15].

However, there is a practical problem with cancellation of the divergences. Real and virtual divergences originate from two different integrals taken over n- and $(n + 1)$-body final state phase spaces, respectively. If the respective integrals could be taken analytically in D dimensions, the infrared divergences from both contributions would cancel out, and finite values for observables could be obtained directly. But in presence of kinematic cuts, integration over dimensionally-regularized unresolved real emission phase space becomes intractable analytically. On the other hand, numerical integration in D dimensions makes it hard to extract singularities, and more importantly, the underlying finite terms. Instead, the real emission contribution can be separated into two parts: a simple part, containing

*Other common approaches to regularization are the cut-off method and the Pauli–Villars method. Advantages of dimensional regularization are that it can guarantee Lorentz and gauge invariance, and is applicable to a wide range of situations.

all singularities, to be integrated analytically in D dimensions; and a remainder, with finite numerical integral over the complete phase space. The universality of the singular limits of the matrix elements makes this possible. The most common approach is to add and subtract an approximation to the real emission squared matrix element that captures all of its divergent collinear and soft limits, and yet is simple enough to be integrated analytically over the unresolved phase space. This manipulation is summarized in Eq. (3.2), and is known as the dipole subtraction method, the most widely used version of which is Catani–Seymour subtraction [50, 51].

$$\begin{aligned}\frac{d\sigma^{\mathrm{NLO}}}{dv} &= \int \left(d\hat{\sigma}_n^{\mathrm{Born}} + d\hat{\sigma}_n^{\mathrm{virt}}\right)\delta_v + \int d\hat{\sigma}_{n+1}^{\mathrm{real}}\,\delta_v \\ &= \int d\hat{\sigma}_n^{\mathrm{Born}}\,\delta_v + \int \left(d\hat{\sigma}_n^{\mathrm{virt}} + d\hat{\sigma}_n^{\mathrm{int}}\right)\delta_v + \int \left(d\hat{\sigma}_{n+1}^{\mathrm{real}} - d\hat{\sigma}_{n+1}^{\mathrm{sub}}\right)\delta_v \\ &= \int d\hat{\sigma}_n^{\mathrm{Born}}\,\delta_v + \int d\hat{\sigma}_n^{\mathrm{fin.\,virt}}\,\delta_v + \int d\hat{\sigma}_n^{\mathrm{fin.\,int}}\,\delta_v + \int \left(d\hat{\sigma}_{n+1}^{\mathrm{real}} - d\hat{\sigma}_{n+1}^{\mathrm{sub}}\right)\delta_v\end{aligned} \tag{3.2}$$

The addition and subtraction of equal $d\hat{\sigma}_n^{\mathrm{int}}$ and $d\hat{\sigma}_{n+1}^{\mathrm{sub}}$ terms that, however, pertain to different multiplicity phase spaces, is what allows reconciliation of the respective divergences. This is the method used in Sherpa and GoSam calculations. There also exist other subtraction techniques, such as the Frixione–Kunszt–Signer method [52, 53]. The subtraction methods lie at the heart of what enables automation of NLO calculations. The rearranged terms in Eq. (3.2) are usually referred to as Born (B), virtual (V), integrated subtraction (I), and real-subtraction (RS) contributions to the NLO calculation.

It should be noted that separation of the expression for the cross section into contributions at NLO using the subtraction methods typically implies that MC generators produce separate sets of events for each contribution. For example, GoSam ntuples are split into the 4 sets: B, V, I, and RS. The subtraction formalism requires that the I events, and a fraction of the

RS events, have negative weights. The cancellation between positive and negative weights represents the remaining cancellation between the regularized divergences. For sufficiently inclusive regions of phase space, positively weighted events are expected to outweigh the negatively weighted ones, so that binned distributions of observables are positively valued.

The presence of negative weights introduces complications. For example, arbitrary binning may result in the positive and negative counterterms populating different bins, or the counterterm events not passing fiducial selection criteria. In the worst case scenario, this may result in negatively valued predicted distributions. Thus, when NLO subtraction methods are used, care has to be taken a priori to generate events in a way that minimizes the possibility of such situations, e.g. by generating with comparable fiducial cuts to the ones expected, and by setting scales of the calculation to values that accurately reflect the simulated process.

An alternative is to use a different formalism, designed to produce only positively weighted events, for example, such as implemented in POWHEG (POsitive Weight Hardest Emission Generator) [54]. The drawback is that this approach requires adoption and tuning of somewhat ad hoc parameters, which makes the method less reliable for completely new predictions. However, for well understood processes, values of these parameters can be determined to give the correct results and produce positively weighted events, which reduce subtlety and are easier to use for experimental studies and non-experts.

The purpose of programs such as GoSam is to provide theoretical calculations of the hard scattering at the parton level. The MC technique is a convenient method to carry these calculations out. The events produced by GoSam have a wide range of weights, which, as mentioned earlier, can be positive or negative. Events with negative weights are relatively easy to handle in the GoSam calculations. Hard scattering information with

negative weights is more difficult to deal with, when that information is used in a full event simulation. Various techniques, such as MC@NLO [55, 56], have been developed to produce full events with both positive and negative weights.

3.3 Matrix element and parton shower matching

In order to provide a complete description of a proton-proton collision, global event simulation programs have to merge the matrix element (ME) calculation of the hard process with the parton shower (PS) simulation. This is not a trivial task, especially because the ME calculation is usually done to a fixed order, while the PS is simulated as a stochastic process and has a logarithmic accuracy from the PS resummation, and therefore effectively contains partial contributions from all orders. The problem becomes even more complicated for higher order ME calculations, which involve contributions from phase spaces with different numbers of particles, i.e. due to real emission, and contain kinematic features not present at LO. But the two calculations are complementary, in that the ME provides a more precise description of the hard process, while the PS more accurately simulates the internal evolution of jets.

A PS cannot be run directly on top of a ME calculation, as that would result in double counting of jets. For example, in a Higgs + jets event, a jet may develop either from a parton originating from the ME of the hard interaction or from QCD radiation in the PS. To avoid double counting, a matching procedure has to be defined in a way that makes the best use of either calculation in its respective domain. The simplest approach is to define a matching scale below which the PS will be used, and above which — the ME. The scale is typically dynamic and is defined in terms of the p_{T} of the jets. Several of the commonly used ME+PS matching schemes are: MLM (Michaelangelo Luigi Mangano) [57], CKKW

(Catani–Krauss–Kuhn–Webber) [58, 59], and CKKW–L (CKKW–Lönneblad) [60].

To combine an NLO calculation with a parton shower, it is essential to ensure that the result inherits the total cross section from the fixed-order (NLO) calculation, and that the radiation pattern to first order follows the real emission part of the calculation. In addition, from a parton shower point of view, it is also important to maintain its intrinsic logarithmic accuracy, which is substantially harder to achieve and to prove. [15]

For NLO ME, an additional phase space has to be subtracted from the PS. There are two commonly used methods. In the MC@NLO method, negative weights are assigned to certain PS configurations that contain radiation already accounted for at the NLO calculation. In the POWHEG method [54], all PS emissions harder than the hardest one from the ME are vetoed. The correct normalization is attained by applying a multiplicative correction to the event weights. An additional damping parameter, D, for real emission is used to suppress overly weighting production at high p_{T}.

$$D = \left(1 + \left(\frac{p_{\mathrm{T}}}{h}\right)^2\right)^{-1}, \quad 0 \leq D \leq 1. \tag{3.3}$$

Here, the p_{T} sets the hard scale, and the h-factor* is a tunable parameter corresponding to the resummation scale. [34]

3.4 Scale dependence

Though, fundamentally, the quantum field theory is scale invariant, perturbative calculations require introduction of scale parameters in order to obtain useful series expansions

*The h-factor is so named because it was first used in calculations of Higgs boson production.

to calculate the observables.* If the full series could be calculated, the dependence on the values of the scales would cancel out, but because only a certain number of terms in the expansion can be computed, the answer retains some scale dependence. Formally, for an observable calculated at a given order in perturbative QFT, its scale dependence is of the next highest order. Typically, scale dependence is expected to decrease for higher order calculations. Scale variations can be used to estimate the expected magnitude of the next order corrections, and to assess the uncertainty of the calculation.

Ultimately, only heuristic decisions can be made for the values of the scales. But arguments can be presented for natural scale choices, which usually correspond to some measure of magnitudes of momentum transfer involved in the process. For example, the value of a scale can be given by, or depend on, the masses of electroweak bosons or combinations of transverse momenta of hadronic jets. While a number of scales can be introduced, with different values for different parts of the process (for example at every vertex), the scheme can be simplified to just two scales, corresponding to factorization (μ_{F}) and renormalization (μ_{R}). Variation of the factorization and renormalization scales is a common way to assess the uncertainty of QCD predictions. The rule of thumb is to vary both scales by a factor of 2 up and down. This is usually simplified to a 7-point variation scheme,

$$(\mu_{\mathrm{F}}/\mu_0, \mu_{\mathrm{R}}/\mu_0) \in \big\{(1,1), (0.5,0.5), (1,0.5), (0.5,1), (2,1), (1,2), (2,2)\big\}, \tag{3.4}$$

in which the ratio between the two scales is kept at a factor of 2 or less. The uncertainty of the calculation is then estimated by the envelope of the values of the observables obtained for each pair of the scales' values.

*Another way to express the meaning of scale parameters is that they appear from the necessity to factorize parts of processes that occur at different energy, or inversely distance and time, scales.

As discussed in Section 2.4, the factorization theorem allows a decoupling of the interaction of the parton that participates in the hard process (at a high energy scale) from the non-perturbative (low energy scale) interactions within the hadron. Large momentum transfers are involved in the hard process, which therefore can be approached with perturbation theory. The non-perturbative effects are accounted for by the parton distribution functions (PDFs), which determine the probability of interaction with a given type of parton carrying a given fraction of the hadron's initial momentum at a given energy (factorization) scale.*

The scale of momentum transfers taking place in an interaction is inversely proportional to the scale of spatial resolution of the structure of the interacting particles. This property is reflected in the scale dependence of the PDFs. As can be seen in Fig. 2.7, the fractions of proton momentum carried by gluons and sea quarks increase at larger factorization scales. In other words, interactions at higher energies reveal a more complex, finer scale structure of a proton, than just a combination of the 3 valence quarks. In fact, in high transverse momentum processes at the LHC, about 40% of the momentum of the proton is observed to be carried by gluons. The large gluon PDF luminosity, in the kinematic range needed for Higgs boson production, results in gluon-gluon fusion being the dominant production mechanism for the Higgs boson at the LHC.

The renormalization scale can also be viewed as a parameter describing the resolution of finer structure at higher energies, but in this case, the structure is that of the vacuum rather than of a composite particle. Higher order perturbative corrections in the quantum field theories of both electroweak and strong interactions in the SM contain divergent loop diagrams. Using the conservation laws, virtual loop momenta cannot be fully constrained

*As discussed in Section 2.4, PDFs cannot be calculated perturbatively, but their evolution with the factorization scale can be, using DGLAP equations.

by the external momenta. So, naively, the contributions of the loop diagrams are given by integrals over all possible loop momenta, from zero to infinity, giving infinite corrections to the observables calculated at tree level. Conceptually, these infinities come from including contributions from arbitrarily large energy scales, corresponding to arbitrarily short wavelengths. However, it is reasonable to expect that a process occurring at a relatively low scale should not be affected by the physics of an arbitrarily high energy regime, nor, in principle, that such a regime can be correctly described by the same low-energy theory.

The crucial idea in renormalization is that the divergences can be absorbed in the effective behavior of particles. In the dynamic picture of Feynman diagrams, a particle continuously undergoes interactions with all the fields to which it can couple. This results in self-energy diagrams, such as the ones shown in Fig. 3.5. In principle, any propagator would contain an infinite number of such diagrams to all orders. These diagrams involving free fields represent infinite corrections to the parameters of the theory due to vacuum polarization. The idea behind renormalization is that the *bare* parameters are immaterial. What is measured

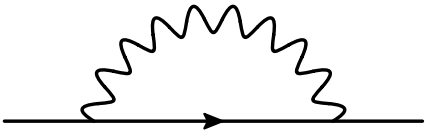

(a) A fermion self-energy diagram.

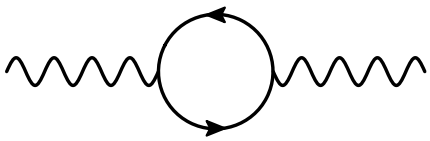

(b) A boson self-energy diagram.

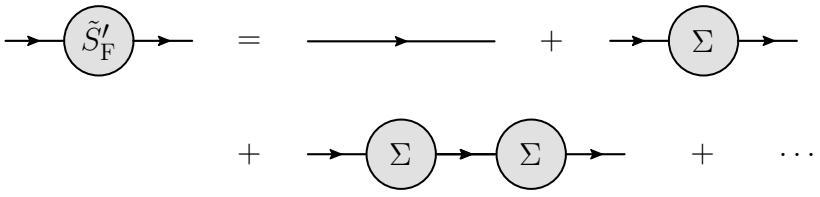

(c) The complete propagator, $\tilde{S}'_{\mathrm{F}}$, is the sum over one-particle irreducible graphs, Σ, arranged along a chain. [61]

Figure 3.5: Examples of self-energy diagrams and their combination into a physical propagator after renormalization.

in a laboratory are the physical parameters, which already include the effects of vacuum polarization. The divergences in the higher order calculations can, in this way, be absorbed into the definitions of the parameters. In the SM, renormalization of 3 kinds of things is necessary: masses, charges, and the fields themselves. In particular, this results in the running of couplings mentioned in Section 2.4.

Depending on the scheme, the renormalization scale parameter introduced can represent a cutoff on the loop momentum or some other measure of the maximum energy scale of integration. The scheme most commonly used in event generators is called the modified minimal subtraction scheme, or $\overline{\text{MS}}$ [62, 63]. In fully renormalizable theories, including the SM, the renormalization scale is not a physical quantity, and any physical prediction, if calculated to all orders, should be scale-independent. The scale simply determines the balance between the tree-level and loop diagrams' contributions. To reduce the effect of higher-order corrections, the scale is typically chosen to be on the order of the magnitude of momentum transfers involved in the process of interest.

Experience at the Tevatron indicated that a good choice of factorization and renormalization scales for calculations of boson production processes is the mass of the boson. But this heuristic was inadequate for processes involving multiple jets in the final state or boson production at high p_{T}. Later, at the LHC, this became especially apparent for the Higgs production. It was soon realized that, as an integral part of the process, QCD radiation has to be accounted for in the scale choice. As mentioned above, gluon-gluon fusion is the dominant process for Higgs boson production at the LHC. While the gluons are color-octets, the Higgs boson is color-neutral, resulting in a situation where a massive colorless particle is produced from an initial state with a "large amount" of color charge. This results in a large probability of gluon radiation, that provides means to dissipate the color, at momentum

scales not dissimilar to the mass of the Higgs. Hence, dynamic scales were introduced, which depend not only on the mass of the gauge boson, but also on the momenta of the jets. Using such dynamic scales, event generators assign different scale values event-by-event, which can effectively account for the varying numbers of vertices with large amounts of momentum transfers.

Studies of the cross section scale dependence have resulted in several improved definitions of dynamic scales for Higgs + jets production, proposed by the GoSam authors. These scales are variations of H_{T} — the scalar sum of the transverse momenta of the jets and the boson. Two commonly used variations are:

$$\hat{H}'_{\mathrm{T}}/2 = \frac{1}{2}\left(\sqrt{p^2_{\mathrm{T},H} + m^2_H} + \sum_{j\in\mathrm{jets}} p_{\mathrm{T},j}\right), \tag{3.5}$$

and

$$\hat{H}''_{\mathrm{T}} = m_H + \frac{1}{2}\left(p_{\mathrm{T},H} + \sum_{j\in\mathrm{jets}} p_{\mathrm{T},j}\right). \tag{3.6}$$

Figs. 3.6 and 3.7 demonstrate the dependence of the Higgs + jets cross section on the factorization and renormalization scales using these dynamic scale definitions. As can be seen in Fig. 3.6a, the NLO cross section exhibits a characteristic saddle point in the $\log\mu_{\mathrm{F}}$-$\log\mu_{\mathrm{R}}$ space [64, 65], and a reduced scale dependence compared to the LO cross section. The studies of scale dependence were done by the author using the GoSam ntuples.

3.5 PDF uncertainty

As has already been discussed, the short-range behavior of partons comprising a hadron is decoupled from the long-range inelastic scattering process by the factorization theorem,

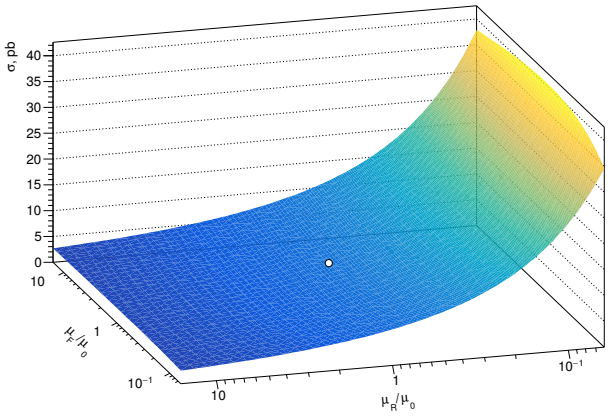

(a) Higgs + 1 jet, $\mu_0 = \hat{H}'_{\mathrm{T}}/2$, $\sigma_0 = 8.06\,\mathrm{pb}$

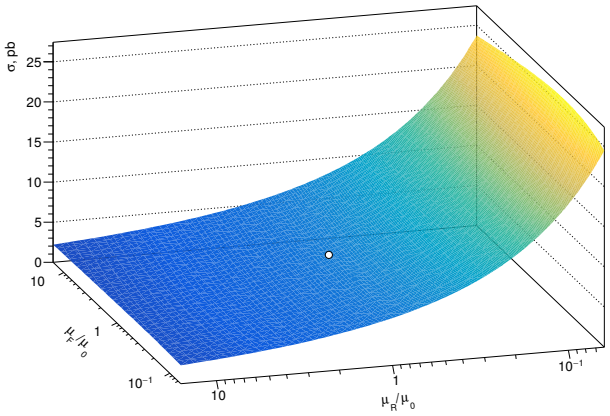

(b) Higgs + 1 jet, $\mu_0 = \hat{H}''_{\mathrm{T}}$, $\sigma_0 = 6.20\,\mathrm{pb}$

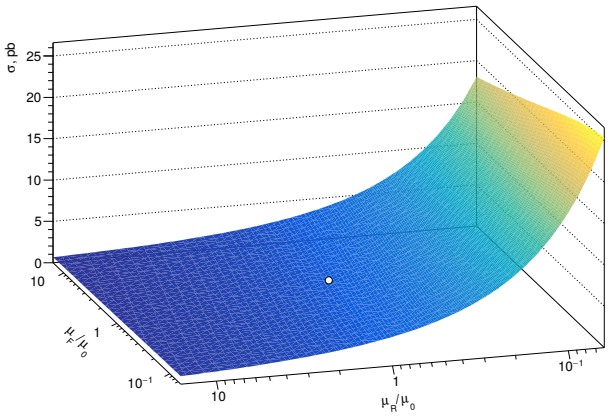

(c) Higgs + 2 jets, $\mu_0 = \hat{H}'_{\mathrm{T}}/2$, $\sigma_0 = 2.99\,\mathrm{pb}$

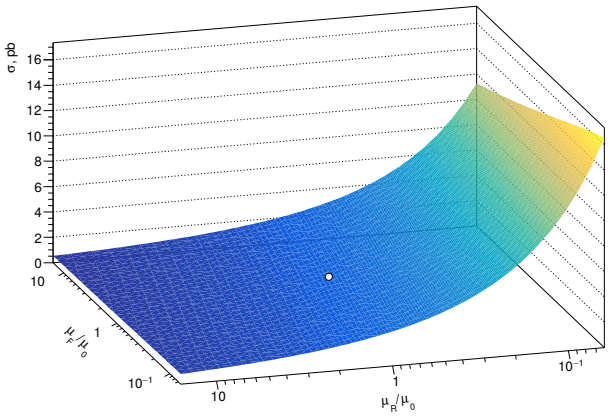

(d) Higgs + 2 jets, $\mu_0 = \hat{H}''_{\mathrm{T}}$, $\sigma_0 = 2.24\,\mathrm{pb}$

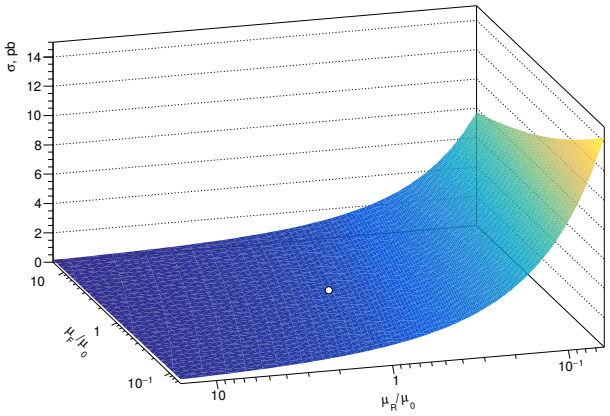

(e) Higgs + 3 jets, $\mu_0 = \hat{H}'_{\mathrm{T}}/2$, $\sigma_0 = 0.98\,\mathrm{pb}$

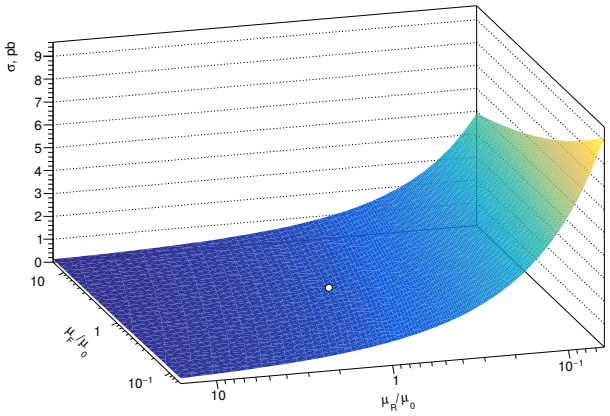

(f) Higgs + 3 jets, $\mu_0 = \hat{H}''_{\mathrm{T}}$, $\sigma_0 = 0.73\,\mathrm{pb}$

Figure 3.6: LO dependence of $pp \to H +$ jets cross section on factorization and renormalization scales at $\sqrt{s} = 13\,\mathrm{TeV}$ for two different choices of dynamic scales, computed using GoSam ntuples. MC events were reweighted using CT14nlo PDFs. Typical jet cuts of $p_{\mathrm{T}} > 30\,\mathrm{GeV}$ and $|\eta| < 4.4$ are applied. The white dot indicates the location of the central scale, $\mu_{\mathrm{F}} = \mu_{\mathrm{R}} = \mu_0$.

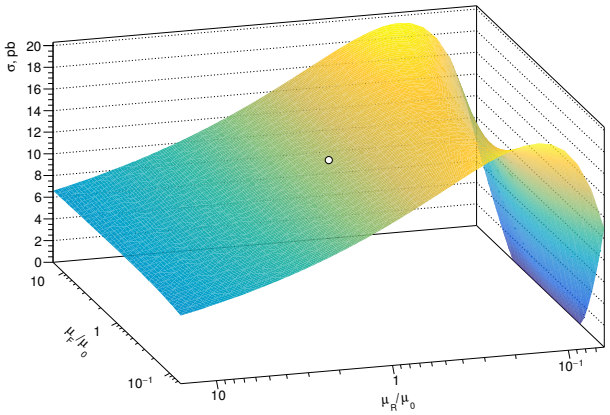

(a) Higgs + 1 jet, $\mu_0 = \hat{H}'_{\mathrm{T}}/2$, $\sigma_0 = 13.34\,\mathrm{pb}$

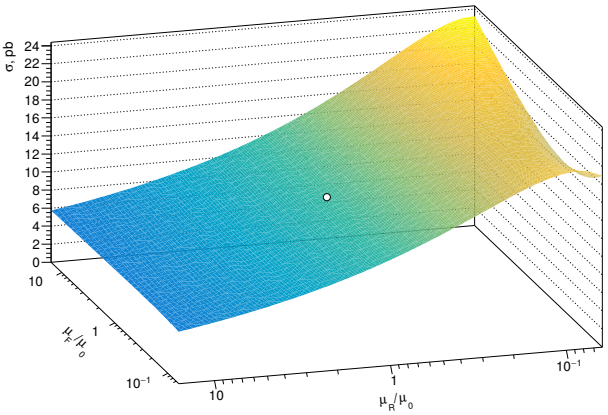

(b) Higgs + 1 jet, $\mu_0 = \hat{H}''_{\mathrm{T}}$, $\sigma_0 = 11.91\,\mathrm{pb}$

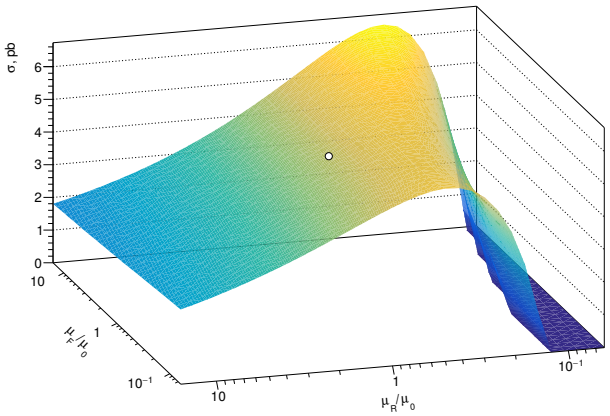

(c) Higgs + 2 jets, $\mu_0 = \hat{H}'_{\mathrm{T}}/2$, $\sigma_0 = 4.55\,\mathrm{pb}$

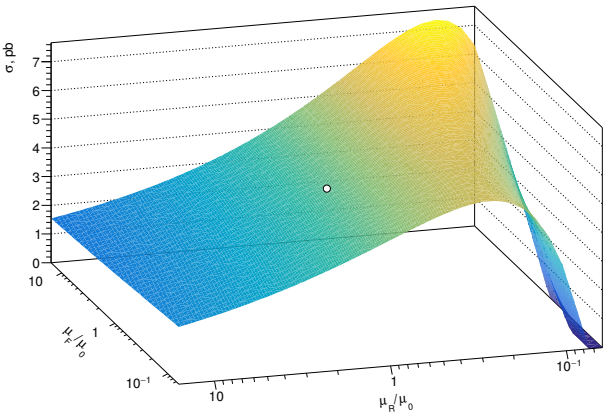

(d) Higgs + 2 jets, $\mu_0 = \hat{H}''_{\mathrm{T}}$, $\sigma_0 = 4.06\,\mathrm{pb}$

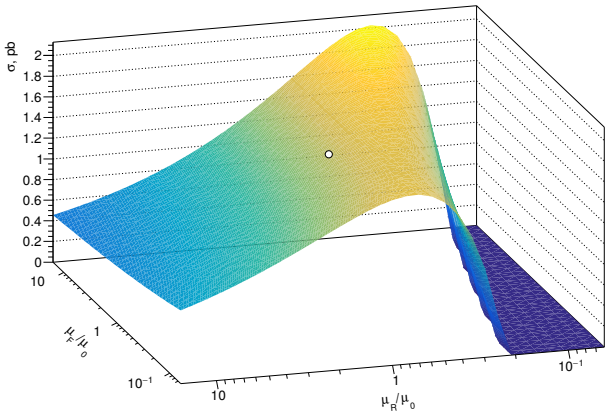

(e) Higgs + 3 jets, $\mu_0 = \hat{H}'_{\mathrm{T}}/2$, $\sigma_0 = 1.46\,\mathrm{pb}$

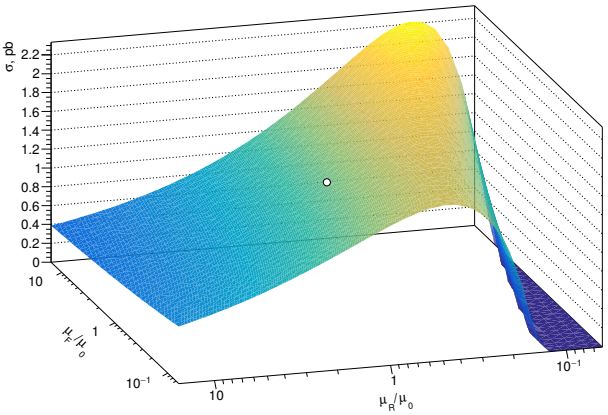

(f) Higgs + 3 jets, $\mu_0 = \hat{H}''_{\mathrm{T}}$, $\sigma_0 = 1.30\,\mathrm{pb}$

Figure 3.7: NLO dependence of $pp \to H +$ jets cross section on factorization and renormalization scales at $\sqrt{s} = 13\,\mathrm{TeV}$ for two different choices of dynamic scales, computed using GoSam ntuples. MC events were reweighted using CT14nlo PDFs. Typical jet cuts of $p_{\mathrm{T}} > 30\,\mathrm{GeV}$ and $|\eta| < 4.4$ are applied. The white dot indicates the location of the central scale, $\mu_{\mathrm{F}} = \mu_{\mathrm{R}} = \mu_0$.

with the non-perturbative short-range description of the hadron contained in the parton distribution functions (PDFs). A number of different methods to determine PDFs from fits to data has been developed over the years, ranging from functional models, such as used by the CTEQ collaboration [25, 66, 67], to the use of neural networks [68, 69]. Regardless of the approach, PDFs are described by a regression model that is fit to the data, and therefore have uncertainties associated with them. The precision of both theoretical predictions and experimental analyses depends on the PDF uncertainties.

A PDF set contains estimates of the probability of interaction, $f(x, Q)$, with a given parton inside a hadron as a function of longitudinal momentum fraction, x, at an energy scale, $Q = \mu_{\mathrm{F}}$. This data is typically stored as a grid of $xf(x, Q)$ values for points in the x-Q space. The PDF values at all possible x and Q values are obtained by grid interpolation. To enable the propagation of PDF uncertainties, a number of error sets is stored in addition to the nominal. A common way to choose the error sets is the Hessian eigenvector method [70–72]. The Hessian matrix elements are second derivatives of the χ^2 function with respect to the PDF fitting parameters, which give the coefficients of the quadratic approximation of the χ^2 near the minimum. The method consists in defining the eigenvector PDF sets using the values of the parameters from the eigenvectors of the Hessian matrix. Principal component analysis can be used to reduce the number of eigenvectors necessary to adequately characterize PDF uncertainties. The uncertainty can then be estimated by the root mean square value of the deviations of the predictions using the eigenvector PDFs from the nominal optimized PDF for both up and down deviations. For predictions of MC event generators, PDF uncertainties are estimated by reweighting the events using the error PDF sets and then taking the root mean square of the deviations of the observables from the nominal value.

`LHAPDF` [73] provides the standard library and repository of parton distribution functions.

Its `C++` and `Python` libraries implement a standard interface for accessing all major PDF sets created in the HEP community. The PDF sets are made available for download from a centralized repository. The programming libraries provide functions to calculate PDF values and uncertainties. An example of PDF uncertainties, produced using `LHAPDF6`, is show in Fig. 3.8.

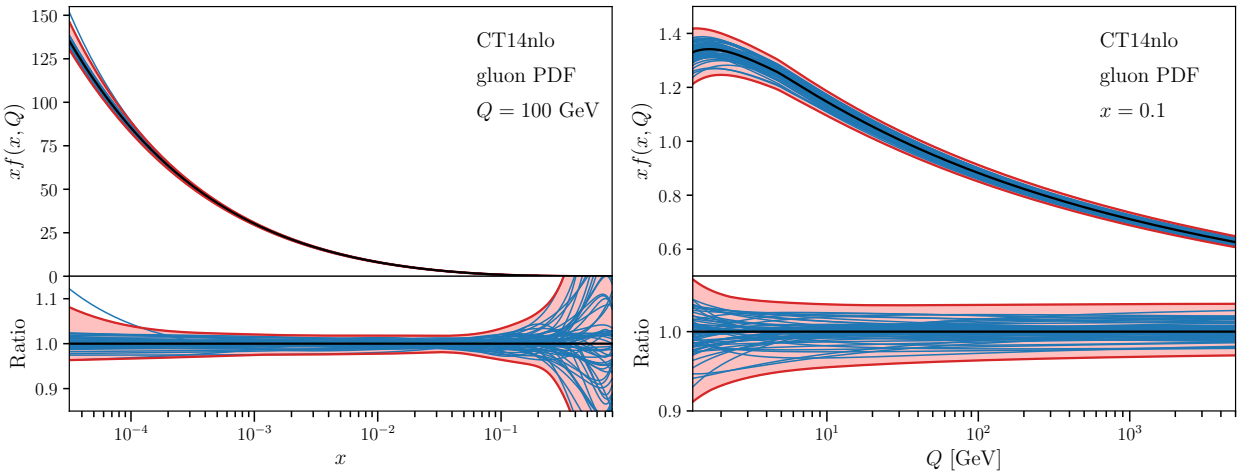

Figure 3.8: Gluon density distributions and Hessian uncertainties from the CT14nlo PDF set for proton. Left: for $Q = 100\,\text{GeV}$ as a function of x. Right: for $x = 0.1$ as a function of Q. The nominal function is shown in black, the error functions in blue, and the uncertainty in red.

3.6 Predictions used in the analysis

Simulated MC event samples are produced for signal and background processes, as listed in Table 3.1. These are used for the derivation of correction factors, the binning of differential distributions, the signal model shape parameters optimization, the background function selection, the estimation of several systematic uncertainties, and the validation of the analysis procedure.

Table 3.1: List of Monte Carlo signal and background samples used in the analysis.

Process	Generator	PS	PDF	ME order	Normalisation order	$\sigma \times$ BR, fb
ggF	Powheg NNLOPS	Pythia8	PDF4LHC15	NNLO + NLL(QCD)	N^3LO(QCD) + NLO(EW)	110
VBF	Powheg-Box	Pythia8	PDF4LHC15	NLO(QCD)	approx. NNLO(QCD) + NLO(EW)	8.58
W^+H	Powheg-Box	Pythia8	PDF4LHC15	NLO(QCD)	NNLO(QCD) + NLO(EW)	1.90
W^-H	Powheg-Box	Pythia8	PDF4LHC15	NLO(QCD)	NNLO(QCD) + NLO(EW)	1.21
$q\bar{q} \to ZH$	Powheg-Box	Pythia8	PDF4LHC15	NLO(QCD)	NNLO(QCD) + NLO(EW)	1.73
$gg \to ZH$	Powheg-Box	Pythia8	PDF4LHC15	LO(QCD)	NLO(QCD) + NLO(EW)	0.28
$t\bar{t}H$	Powheg-Box	Pythia8	PDF4LHC15	NLO(QCD)	NLO(QCD) + NLO(EW)	1.15
$b\bar{b}H$	Powheg-Box	Pythia8	PDF4LHC15	NLO(QCD)	5FS (NNLO), 4FS (NLO)	1.10
WtH	aMC@NLO	Pythia8	CT10 NLO	NLO(QCD)	4FS(LO)	0.034
tHq	aMC@NLO	Pythia8	CT10 NLO	NLO(QCD)	5FS(NLO)	0.169
$\gamma\gamma$	Sherpa	Sherpa	CT10	NLO(QCD)	NLO(QCD)	19.2×10^3

The production of MC samples starts with a matrix element (ME) generator, which generates hard process events at parton level. These are then converted to particle level* events via a parton showering (PS) program that simulates the formation of jets from final state quarks and gluons. Subsequently, the events are passed through a detector simulation, to account for detector effects and to obtain events in the form similar to that observed in the detector [74]. These events are finally processed with the same algorithms as the collected data. This is referred to as the reconstruction level. Simulated events are corrected to reflect photon and jet energy scale and resolution, as well as the trigger, identification, and isolation efficiencies observed in data. As theoretical calculations can typically be performed to higher order for integrated than for differential cross sections, simulated events are reweighted to normalize their integrated cross section to the best known theoretical result.

The effects of multiple interactions occurring withing the same or neighboring bunch crossings, i.e. pileup, are modeled by overlaying inelastic pp, also known as minimum-bias, events generated with PYTHIA 8, using NNPDF2.3LO PDF set [75] and the A3 tune [76], over the original hard-scattering events. Events in the MC simulation are reweighted to reproduce the pileup μ distribution observed in data. The number of pileup events included is obtained by sampling a Poisson distribution with a mean of μ. Minimum-bias simulations are run before data taking is complete and the actual pileup conditions are known. Therefore, each sample is generated with a broad range of values of μ, in order to encompass all possible pileup conditions that may be experienced during data taking. The MC pileup distribution is then corrected by reweighting when the actual conditions become available. Out-of-time pileup is included by adding detector signals from previous bunch crossings, also using PYTHIA 8 minimum-bias events. The frequency of these signals is modeled on the nominal bunch

*The particle level in MC simulations is also colloquially referred to as the truth level.

structure used by the LHC.

Several reweighting corrections are applied to the MC samples. The correction factors are different for samples produced with full and fast detector simulations. Distributions of the following quantities in MC are matched to the data:

- pileup, as discussed above;
- z distribution of the primary vertex;
- photon energy spectrum is smeared to match the observed resolution;
- photon identification and (track and calorimeter) isolation efficiencies.

Additional MC samples and theory calculations were produced to provide comparisons for measured cross sections to the state-of-the-art theoretical predictions. These samples were produced only at parton or particle level, without detector simulation. They were only used for comparison with the results of the analysis, and are discussed in Section 3.6.3.

3.6.1 Signal Monte Carlo

Signal MC samples are generated for all main Higgs production mechanisms discussed in Chapter 2: gluon fusion (ggF), vector boson fusion (VBF), associated production with vector bosons (WH and ZH), and associated production with heavy quarks ($t\bar{t}H$ and $b\bar{b}H$). The relative contribution of each process to the fiducial cross section as a function of diphoton transverse momentum is shown in Fig. 3.9. All samples are generated with the Higgs boson mass of $m_H = 125\,\text{GeV}$ and width of $\Gamma_H = 4.07\,\text{MeV}$ [28]. The hard scattering process leading to the production of the Higgs boson is generated using POWHEG [54, 77–79] with the PDF4LHC15 PDF set [80]. The Higgs boson decay to two photons, as well as the effects of the underlying event, parton showering, and hadronization, are modeled by interfacing the output of the parton level generation with PYTHIA 8 [81], using the AZNLO set of parameters

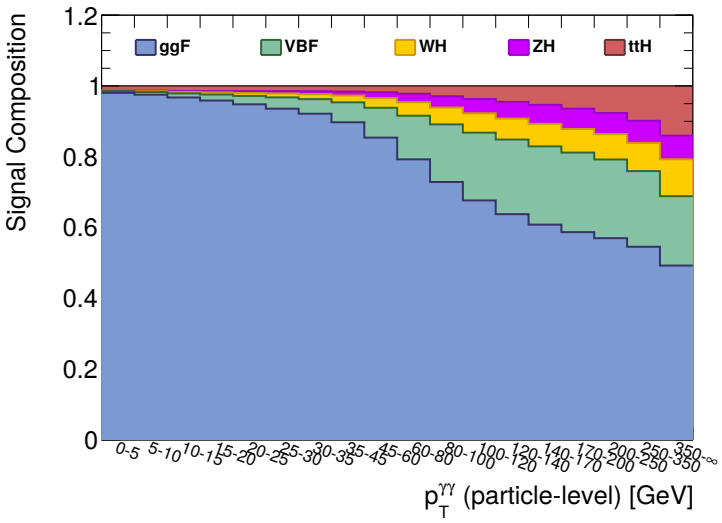

Figure 3.9: Fractional signal composition in terms of the Higgs production processes as a function of diphoton transverse momentum determined from the signal MC samples.

that are tuned to data [82].

The particle level signal MC events are processed with the full Geant4 ATLAS detector simulation [44] and the same reconstruction algorithms as those used for data. The event weights are normalized to the most accurate theoretical calculations for the inclusive cross section in the corresponding production channel, and multiplied by the $H \to \gamma\gamma$ branching ratio of 0.227% calculated with `HDECAY` [83–86] and `PROPHECY4F` [87–89] for the Higgs boson mass of 125.09 GeV.

3.6.1.1 Gluon Fusion

Samples for the ggF process are generated with NNLOPS [90], a state of the art generator based on MiNLO HJ [91] and the Powheg method with NNLO + NNLL accuracy for Higgs p_{T} and rapidity distributions. This is achieved by applying a correction based on the HNNLO(y) program and checking the result against the HqT program [92]. The ggF sample is normalized to a calculation at $\mathrm{N^3LO}$ (QCD) with additional NLO electroweak correc-

tions [28], accounting also for the treatment of the quark mass effects through a correction factor for the total cross.

3.6.1.2 Vector Boson Fusion

VBF samples are generated with PowhegBox [93] and showered with Pythia 8. Powheg is accurate to NLO and is tuned to match calculations with effects due to finite fermion masses and soft-gluon resummation up to NNLL. The VBF sample is normalized to a calculation at NLO (QCD) with additional NLO (EW) corrections, with an approximate NNLO QCD correction.

3.6.1.3 Associated production with vector bosons

WH and ZH samples are generated with NLO parton shower matched matrix elements, except for the $ggZH$ sample, which is generated at LO.

3.6.1.4 Associated production with single top quark

WtH and tHq samples are generated with aMC@NLO, which implements a LO matrix element matched to the parton shower. The samples are produced using the CT10 NLO PDF set and the `CTEQ6L1-UE-EE-5` generator tune.

3.6.2 Background Monte Carlo

The main background to the resonant $pp \to H \to \gamma\gamma$ process is the non-resonant SM diphoton production. This background is irreducible, because events constituting it have an identical signature to the events with the diphoton originating from the Higgs. Background $\gamma\gamma$ samples were generated using Sherpa 2.2.4 [94] and merged with the Sherpa parton

shower [95] according to the ME+PS@NLO prescription [96–99]. The PDF set used is NNPDF3.0 NNLO [68].

The background samples are passed through a fast parametric simulation of the ATLAS detector [74]. A large number, on the order of 100 million, of background events needs to be simulated, given the diphoton cross section of 19.2 nb. Use of the fast, rather than full, detector simulation allows the precessing of these events in a timely manner.

Due to the possibility of the misreconstruction of jets as photons, a reducible background component is also present, consisting of γj and jj events. Because of computational limitations, no dedicated γj or jj samples are generated. Instead, a 2×2D sideband method is used to reweight $\gamma\gamma$ samples to match the shape of the $m_{\gamma\gamma}$ distribution to that in data control regions. This procedure is further discussed in Section 6.5.2 on background modeling. After the fractional contribution of the reducible background is estimated, the total MC weight is normalized to match the number of events observed in the data sidebands.

3.6.3 Predictions compared to the analysis results

Fiducial cross section measurements are designed to be as minimally model dependent as possible, allowing them to be compared to many different theoretical predictions. All of the obtained differential measurements were compared to the SM predictions derived from the default signal MC, discussed in Section 3.6.1. The measured distributions for select observables were compared to an array of state-of-the-art theoretical predictions described below. These predictions were made for the dominant gluon fusion production channel of the Higgs boson, and were therefore combined with the default predictions for the other channels. The theoretical predictions are presented with the analysis results in Section 6.8.2.

Correction factors were applied to the predictions that did not include the fiducial selec-

tion defined by cuts on the photons' transverse momenta and pseudorapidities, and the jets' transverse momenta and rapidities. To most predictions, an additional correction was applied to account for the effect of the photon isolation criteria. Both of these corrections were derived from NNLOPS [90]. Non-perturbative corrections were applied for all predictions not interfaced with a parton shower.

Predictions which did not include the Higgs to diphoton decay were scaled by the corresponding branching ratio of $2.27^{+0.066}_{-0.064} \times 10^{-3}$ [30]. The branching ratio uncertainty was added in quadrature.

Most predictions, unless explicitly stated, used the NNLO PDF set following the PDF4LHC recommendations [80].

3.6.3.1 Sherpa

For the SHERPA [100] predictions, NLO matrix element calculations were merged with the parton shower [95] using the MEPS@NLO multijet techniques [101–103]. They have an accuracy of NLO_n for jet multiplicities of $n = 0, 1, 2, 3$. The 1-loop corrections are generated internally in SHERPA for $H + \geq 1$ jet and externally, using MCFM [104] for $H + \geq 2$ jets and GOSAM [105, 106] for $H + \geq 3$ jets. The calculations make use of the effective field theory in the $m_t \to \infty$ approximation. The effects of the finite top quark mass are taken into account by reweighting the EFT predictions by the ratio of finite m_t to infinite m_t predictions calculated at 1-loop, but in this case, the loop is that of the top quark. AMEGIC [107] and COMIX [108] are used as matrix element generators. The predictions use the NNPDF3.0 NNLO PDF set with $\alpha_s(m_Z) = 0.118$. The calculation is done at particle level, i.e. it also includes multiple interactions, hadronization, hadron decays and electroweak corrections. Photon and jet fiducial cuts are included, as well as photon isolation. The perturbative un-

certainties are estimated by varying the renormalization and factorization scales. Variations in the merging scale and the parton shower starting scale are known to be much smaller. The SHERPA predictions are shown for the jet multiplicity and for all distributions in the phase space with at least 2 jets.

3.6.3.2 GoSam

The GOSAM [100, 106, 109] predictions were prepared by the author of this dissertation, using the GOSAM ntuples, discussed in Appendix A. The predictions have a fixed-order NLO$_n$ accuracy, and are available for jet multiplicities $n = 1, 2, 3$. $\hat{H}'_{\mathrm{T}}/2$, defined in Eq. (3.5), was used as the dynamic renormalization and factorization scale. The perturbative uncertainties were estimated using the 7-point scale variation scheme. The predictions use the `PDF4LHC15_30` NLO PDF set. The PDF uncertainties were calculated using the respective PDF error set. Photon and jet fiducial cuts are included. The GOSAM predictions are shown for the jet multiplicity measurement and for all distributions in the phase space with at least 2 jets.

3.6.3.3 HRes

HRes [110, 111] provides predictions differential in $p_{\mathrm{T}}^{\gamma\gamma}$ at NNLO$_0$ with p_{T}^{H} resummation at NNLL. Finite masses of t, b, and c quarks are included at NLO accuracy. The scale choices are $\frac{1}{2}\sqrt{m_H^2 + p_{\mathrm{T},H}^2}$ for renormalization and factorization, and m_H and $2m_b$ for resummation. Uncertainties are estimated from variations of the renormalization, factorization, and resummation scales. Photon and jet fiducial cuts are included. The HRes predictions are shown for p_{T}^{H} and p_{Tt}^{H}.

3.6.3.4 NNLOjet

NNLOJET [112] provides fixed-order NNLO prediction for inclusive $H+1$ jet production. The renormalization and factorization scales are taken to be $\sqrt{m_H^2 + \sum p_{\mathrm{T},j}^2}$. Uncertainties are estimated using the 7-point scale variation scheme. The predictions use the CT14NNLO PDF set. Photon and jet fiducial cuts are included.

3.6.3.5 RadISH + NNLOjet

RadISH [113] provides predictions with p_{T}^H resummation at NNLL, matched to the NNLO_1 differential spectrum from NNLOjet [114]. Predictions using effective Higgs coupling in the limit $m_t \to \infty$, as well as taking into account finite top quark mass are available. In the latter, the mass effects are exact up to LO, while NLO and NNLO (in the spectrum, i.e. NLO_0, NNLO_0, and $\mathrm{N^3LO}_0$, respectively) corrections are computed in the large m_t approximation. Mass effects are also included in the resummation up to NNLL. Quark masses are renormalized in the on-shell scheme. The effects of fiducial cuts were approximated by a correction factor.

3.6.3.6 SCETlib

The provided predictions for $\left|y_{\gamma\gamma}\right|$, $\left|\Delta y_{\gamma\gamma}\right|$, and $\left|\cos\theta^*\right|$ at $\mathrm{NNLO}_0 + \mathrm{NNLL}'_\phi$ accuracy include a resummation of the virtual corrections to the gluon form factors [115, 116]. The underlying NNLO predictions are obtained using MCFM8 with τ_0 subtraction [117, 118]. They are derived in the fiducial volume defined by the photons' transverse momenta and pseudorapidities. The perturbative uncertainties contain both fixed-order and resummation uncertainties estimated as described in [115].

Predictions for $p_{\mathrm{T}}^{j_1}$ at $\mathrm{NNLL}' + \mathrm{NNLO}_0$ accuracy were derived applying a resummation

in $p_{\mathrm{T}}^{j_1}$ [116, 119]. The perturbative uncertainties contain both fixed-order and resummation uncertainties estimated as described in [119].

Photon and jet fiducial cuts are included for both predictions.

3.6.3.7 SCET + NNLOJET

SCET + NNLOJET provides predictions for $p_{\mathrm{T}}^{\gamma\gamma}$ using a N^{3}LL resummation matched to a NNLO fixed-order calculation in the heavy top quark limit [120].

3.6.3.8 STWZ–BLPTW

The STWZ–BLPTW predictions [119, 121] are a NNLL$'$ + NNLO resummation for the p_{T} of the leading jet, combined with a NLL$'$ + NLO resummation for the subleading jet. The numerical predictions for $\sqrt{s} = 13\,\mathrm{TeV}$ are taken from [30]. In comparison to the SCETlib predictions, decribed in Section 3.6.3.6, these predictions include an improved resummation for the total cross section, with accuracy comparable to N^{3}LO. The effects of fiducial cuts were approximated by a correction factor. The STWZ–BLPTW predictions are shown for the jet multiplicity distribution.

3.6.3.9 JVE + N^{3}LO

The JVE + N^{3}LO predictions [122] include NNLL resummation of the p_{T} of the leading jet with small-R resummation and are matched to the N^{3}LO total cross section. The effects of fiducial cuts were approximated by a correction factor. The JVE + N^{3}LO predictions are shown for the jet multiplicity distribution.

3.6.3.10 MG5_aMC@NLO

The MG5_aMC@NLO prediction [123, 124] includes up to two jets at NLO accuracy using the FxFx merging scheme. The central merging scale is taken to be 30 GeV. Top quark mass effects are included through reweighting, and b quark mass effects are included in the Higgs + 0 jets corrections. Resummation scales are chosen following the prescription in [125]. The predictions are showered with PYTHIA 8. The effects of fiducial cuts were approximated by a correction factor. The MG5_aMC@NLO predictions are shown for the jet multiplicity. Uncertainties are estimated by varying the merging scale between 20 and 50 GeV.

Chapter 4

The LHC and ATLAS

The Large Hadron Collider (LHC) [126] is the world's largest and most powerful particle accelerator. It is the flagship facility at CERN,* an international high energy physics research center, located on the border between France and Switzerland near Geneva. With the highest achieved center-of-mass energy for proton-proton collisions of $\sqrt{s} = 13$ TeV, LHC stands at the frontier of experimental particle physics. Seven experiments collect data at the LHC from proton-proton, as well as heavy ion, collisions:

- ATLAS (A Toroidal LHC Apparatus) [127] is a giant, hermetic, general purpose detector, designed to cover a wide range of physics studies in the highest energy regime that can be created in a laboratory environment. The main goals of its program are to discover and measure the properties of the Higgs boson, and to search for physics beyond the Standard Model.
- CMS (Compact Muon Solenoid) [128] is a sibling detector of ATLAS with similar physics goals. It uses some different detector technologies and is more optimized for measurements of muons.
- LHCb (Large Hadron Collider beauty experiment) [129] is a single-arm forward spectrometer, primarily designed to measure the parameters of CP violation in the interactions of bottom quark hadrons.

*The full name of CERN is European Organization for Nuclear Research (French: Organisation européenne pour la recherche nucléaire). The acronym is derived from Conseil européen pour la recherche nucléaire.

- ALICE (A Large Ion Collier Experiment) [130] is a detector optimized for the heavy-ion collision studies. It is designed to address the physics of strongly interacting matter and the quark-gluon plasma.
- TOTEM (TOTal Elastic and diffractive cross section Measurement) [131] measures the total cross section and luminosity, using a device called a Roman Pot. It shares the interaction point with CMS.
- LHCf (Large Hadron Collider forward experiment) [132] is dedicated to the measurement of neutral particles emitted in the very forward region, with the goal of providing data for calibrating hadron interaction models that are used in studies of Extremely High-Energy Cosmic-Rays. It shares the interaction point with ATLAS.
- MoEDAL (Monopole and Exotics Detector at the LHC) [133] is an experiment designed to search for magnetic monopoles. It shares the cavern with LHCb.

This chapter discusses technical details of the LHC accelerator complex and the ATLAS detector.

4.1 CERN accelerator complex

The LHC is a superconducting hadron synchrotron accelerator and collider [126, 137–139]. Its main ring has a circumference of 26.7 km, with two beam pipes circulating protons (or heavy ions) in opposite directions. It is located in a 3.7 m wide underground tunnel, at the depth between 45 m and 170 m below the surface, containing 8 straight sections and 8 arcs, with the plane of the tunnel inclined at 0.8° towards Lake Geneva. The LHC is installed in the old LEP tunnel, constructed in 1984–1989. LEP was dismantled in 2001, and the LHC construction was finished in 2008. Run 1 of the LHC started in 2010. Most of

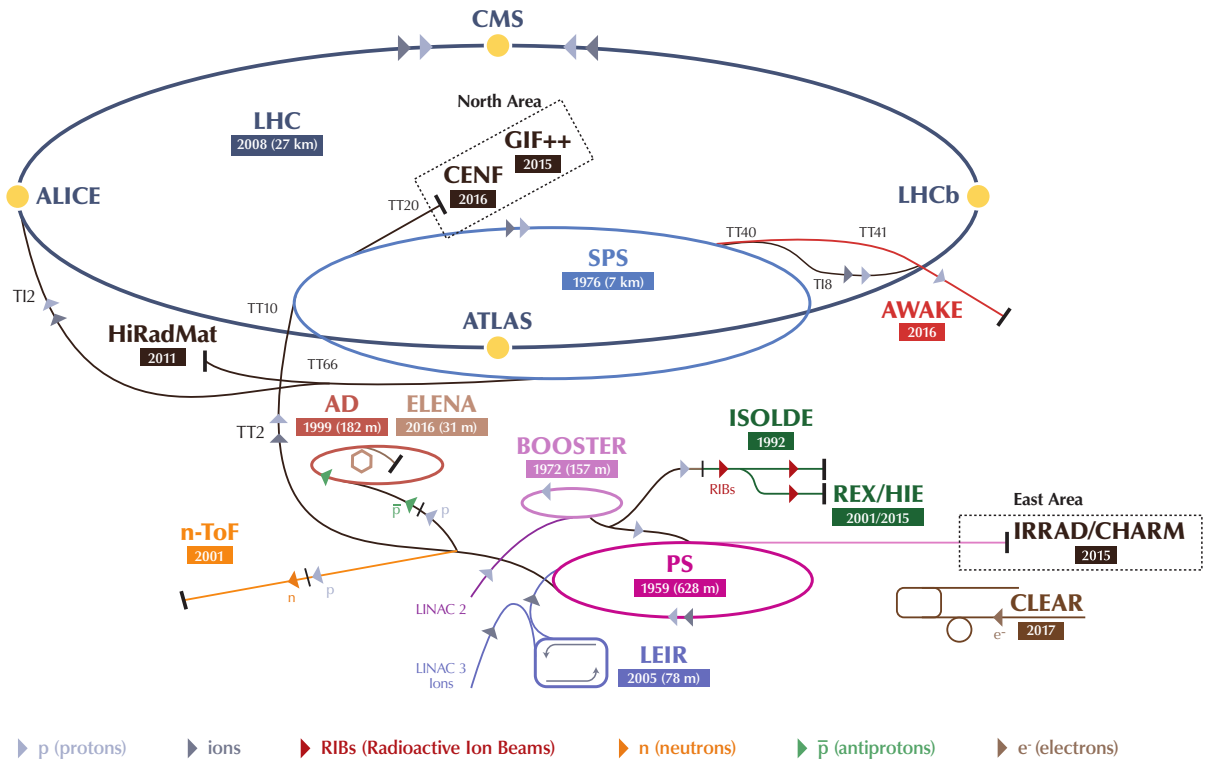

LHC - Large Hadron Collider // **SPS** - Super Proton Synchrotron // **PS** - Proton Synchrotron // **AD** - Antiproton Decelerator // **CLEAR** - CERN Linear Electron Accelerator for Research // **AWAKE** - Advanced WAKefield Experiment // **ISOLDE** - Isotope Separator OnLine // **REX/HIE** - Radioactive EXperiment/High Intensity and Energy ISOLDE // **LEIR** - Low Energy Ion Ring // **LINAC** - LINear ACcelerator // **n-ToF** - Neutrons Time Of Flight // **HiRadMat** - High-Radiation to Materials // **CHARM** - Cern High energy AcceleRator Mixed field facility // **IRRAD** - proton IRRADiation facility // **GIF++** - Gamma Irradiation Facility // **CENF** - CErn Neutrino platForm

Figure 4.1: CERN accelerator complex [134].

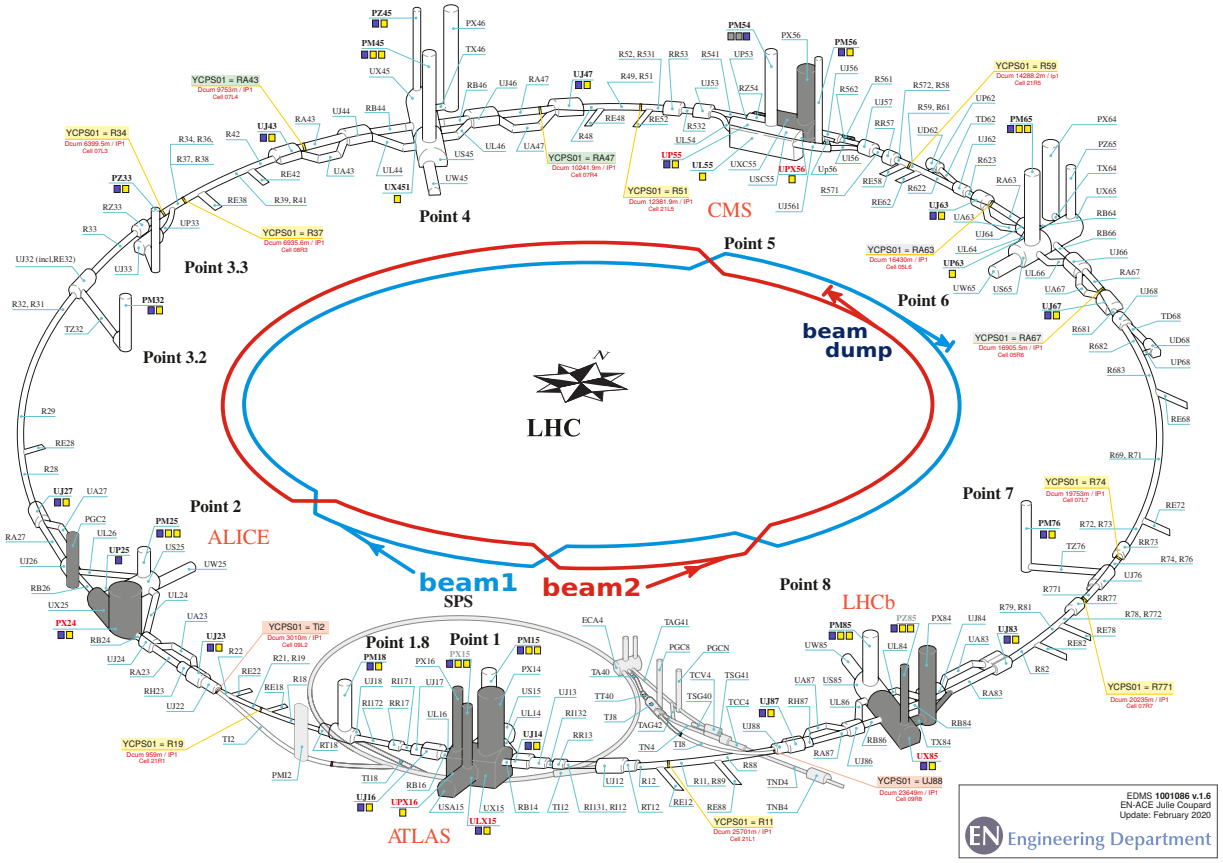

Figure 4.2: Detailed view of the underground LHC facilities, showing the locations of the experiments and beam intersection points [135, 136]. The locations of the four major LHC experiments: ATLAS, CMS, LHCb, and ALICE are highlighted in gray.

the $\sqrt{s} = 7\,\text{TeV}$ data was collected in 2011, and the $\sqrt{s} = 8\,\text{TeV}$ data was collected in 2012. Run 2, in which the $\sqrt{s} = 13\,\text{TeV}$ data used in this dissertation was collected, took place in 2015–2018.

The acceleration of particles is done using a strong electric field generated inside superconducting radiofrequency (RF) cavities. The shape of the RF cavities is design to sustain electromagnetic waves of a given resonance frequency. The frequency is tuned precisely, so that when a charged particle travels through an RF cavity segment it feels a repelling force from behind and an attractive one from the front. This is illustrated in Fig. 4.3. This also produces the effect of protons in each bunch arranging themselves into RF buckets. The protons in the middle of the bucket are given the optimal amount of energy, while those at the ends are accelerated more or less depending on whether they are behind or ahead, thus bringing them closer to the middle. This maintains the integrity of the bunches. The RF cavities bring the protons from the injection energy up to the collision energy, as well as mitigate the energy loss due to synchrotron radiation. The LHC has 16 RF cavities housed in four cryomodules. Each cavity is driven by a high-power klystron, which creates 400 MHz EM waves using intensity-modulated electron beams. The cavities operate at 4.5 K.

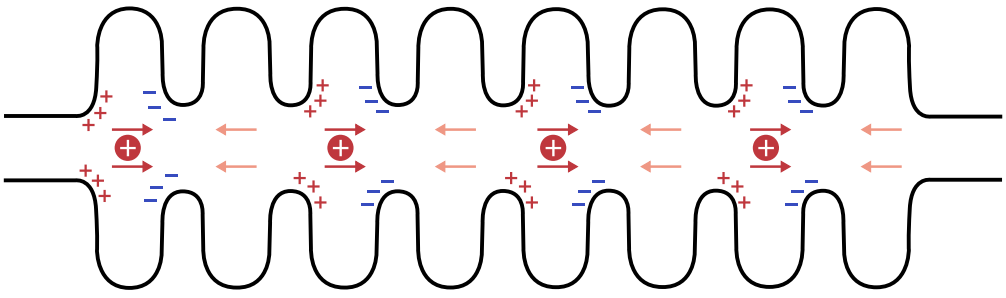

Figure 4.3: An RF cavity diagram [140]. The charge induced at either end of a cavity segment accelerates protons forward. The field in the cavity oscillates at 400 MHz, resulting in the induced charge switching polarity, so that the protons never feel a force in the backward direction. The LHC uses 8 cavities per beam, delivering 2 MV accelerating potential (5 MV/m field). Every proton passing through an RF cavity experiences a total potential difference of $2 \times 8 = 16\,\text{MV}$, gaining 16 MeV of kinetic energy.

A key parameter for a synchrotron is the magnetic field produced by the bending magnets. For a back-of-the-envelope estimate, consider a charged particle moving perpendicularly to a uniform magnetic field. The particle experiences a Lorentz force, and therefore, for relativistic speeds,

$$\vec{F} = q\left(\vec{E} + \vec{v} \times \vec{B}\right) \quad \Rightarrow \quad \gamma m a = \frac{\gamma m v^2}{R} = qvB \quad \Rightarrow \quad E \approx p = \gamma m v = qBR. \tag{4.1}$$

Thus, a storage ring can contain particles with energy directly proportional to the available magnetic field strength and the bending radius.* Clearly, the use of the strongest available magnets is paramount to reducing the accelerator size. The LHC relies on superconducting magnets that are at the edge of present technology. Classical NbTi superconductors are used, but are operated at 2 K temperature† and 8.3 T magnetic field. Special "two-in-one" or "twin-bore" design magnets are used, due to space limitations in the tunnel, allowing to accommodate the windings for the two beam channels in a common coldmass and cryostat. 1232 dipole magnets installed along the LHC ring help bend the particle beam. 392 quadropoles and higher order multipole magnets are used to focus and shape the beam.

The proton accelerator chain for *pp* collision at the LHC consists of the linear accelerator Linac2,‡ Proton Synchrotron Booster (PSB), Proton Synchrotron (PS), Super Proton Synchrotron (SPS), and finally the Large Hadron Collider (LHC). The sequence of injections resulting in a new LHC beam is called a fill. A fill starts with releasing hydrogen gas from a tank into a duoplasmatron, where it is dissociated and ionized, and the protons are given an initial acceleration to 90 keV. This is a part of the RFQ2 pre-injector [145]. The Linac2

*$E\,[\text{TeV}] \approx 0.3 \times B\,[\text{T}] \times R\,[\text{km}]$. The bending radius for the LHC is 2.8 km, which is 1.5 times smaller than the ring average, because the dipole magnets don't cover the whole circumference [137, 141].

†Magnet cooling to maintain superconductivity requires circulation of 100 tons of liquid helium.

‡After Long Shutdown 2, Linac2 will be superseded by Linac4 [142].

Table 4.1: Summary of the LHC injection stages with their normal operation parameters [139, 143, 144].

	Linac2	PSB	PS	SPS	LHC
Output proton energy, GeV	0.05	1.4	25	450	6500
Length or circumference, m	33	157	628	6900	26700
Harmonic number,* h	—	1	7, 21, 84	84	35640
Bunches when full	—	1/ring	6, 18, 72	243	2808
Batches to fill next machine	3	2	3	2×12	—
Repetition time, s	—	1.2	3.6	54	1200

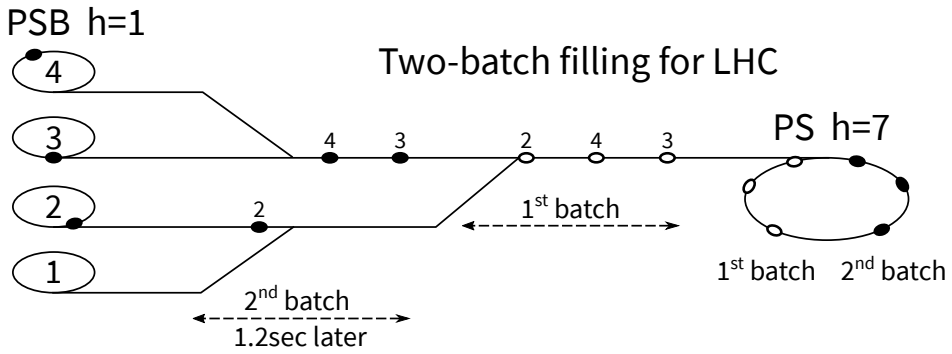

Figure 4.4: PSB-PS transfer: two-batch filling for the LHC [139].

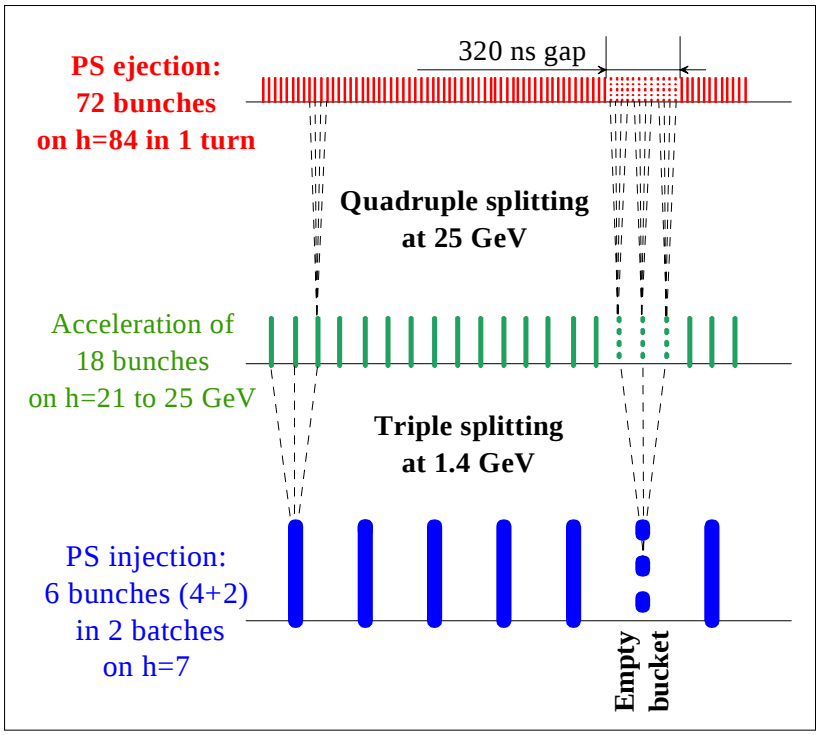

Figure 4.5: PS bunch splitting for a nominal 25 ns LHC bunch train [139].

*Harmonic number is the ratio of the particle revolution period to the period of the accelerating RF voltage changes.

accelerates protons to 50 MeV and delivers them to the first synchrotron preaccelerator — PSB. Here, the incoming beam is split, with each bunch entering one of the four stacked PSB rings, and the protons are accelerated to 1.4 GeV. PS is filled from PSB using a two-batch filling scheme, whereby bunches from three PSB rings are transferred to PS two times, resulting in 6 equally spaced bunches leaving through one beam pipe, as shown in Fig. 4.4. The PS accelerates the protons to 25 GeV, and splits the bunches, giving them the 25 ns spacing needed for the LHC. This splitting scheme is illustrated in Fig. 4.5. As the protons gain energy, the harmonic number is increased by a factor of 3 and then 4, splitting each bunch into 12. Since initially 6 bunches are injected at $h = 7$, a 320 ns gap is formed in the bunch train to accommodate the rise-time of the ejection kicker. The SPS raises the proton energy to 450 GeV. The single beam coming out of the SPS is split into two, by injecting alternating bunches into one of the two LHC rings. Table 4.1 gives a summary of the beam preparation stages. The fill scheme described here is closest to the standard, but other schemes are also possible.

The LHC filling scheme depends on the operation mode [146]. The Standard Physics filling scheme in 2018 was `25ns_2556b_2544_2215_2332_144bpi_20inj`, which means 25 ns bunch spacing, 2556 bunches per beam, 2544 collisions at Point 1 (ATLAS) and Point 5 (CMS), 2215 collisions at Point 2 (ALICE), 2332 collisions at Point 8 (LHCb), 144 bunches in the longest train, and 20 injections per beam [147].

Beams circulating in the LHC deteriorate over time, as their transverse profile disperses after many round trips in the magnetic field. One of the main concerns for the stable operation of the LHC is prevention of frequent quenches of the superconducting magnets. If too many particles stray from the beam and hit the magnets, the magnets may be heated over their critical temperature and lose their superconductivity, and if the energy stored in

a magnet is not diverted, the magnet can be destroyed by resistive heating. While typical quenches can be handled by the safety system, which releases the current from the affected magnets, the number of quenches has to be kept to a reasonable minimum for efficient operation of the LHC. After a quench, or as a result of a safety measure, the circulating LHC beams need to be dumped, before new ones can be injected. For this purpose, there exists a dedicated beam dump facility, located at Point 6. LHC beams are always injected with empty bunches, which, in case of a dump, provide time for the kicker magnets to turn on and steer the beam out of the ring. After ejection, the beam is dispersed by dilutor magnets, which reduce its density by a factor of $\sim 10^5$. The diluted beam is disposed of by colliding it with a beam stop, whose main component is a graphite composite cylinder, 8 m long and 1 m in diameter, which is necessary to stop a beam carrying up to 360 MJ.* The typical lifetime of an LHC beam as on the order of 10 hours. [137, 148]

The quantity that measures the ability of a particle accelerator to produce bunch crossings for particle collisions is called luminosity. It is the proportionality factor between the number of events per unit of time, dN/dt, and the interaction cross section, σ:

$$\frac{dN}{dt} = L\,\sigma. \tag{4.2}$$

Luminosity, rather than collision rate, is used as the measure of collider performance, because luminosity does not factor in the probability of particle interaction, and is thus a direct measure of the machine's ability to create the environment in which particle collisions can

*The 360 MJ energy of a single LHC beam is comparable to the kinetic energy of a passenger train.

take place.* For two beams colliding head-on, luminosity can be expressed as

$$L = \frac{N_1 N_2 f_b}{A_{\text{eff}}}, \tag{4.3}$$

where N_1 and N_2 are the numbers of particles per bunch in the respective beams, f_b is the frequency of bunch crossings, and A_{eff} is the effective area of the overlap of the beams.

Integrated luminosity,† $\int L\,dt$, is often quoted as the amount of data collected in a particular LHC run. Fig. 4.6 shows the integrated luminosity as a function of time for Run 2, which amounts to all the data collected at $\sqrt{s} = 13\,\text{TeV}$ between 2015 and 2018. The analysis presented in this dissertation utilized $139\,\text{fb}^{-1}$ of ATLAS data.

Fig. 4.7 shows the total pp cross section as a function of center of mass energy. Given

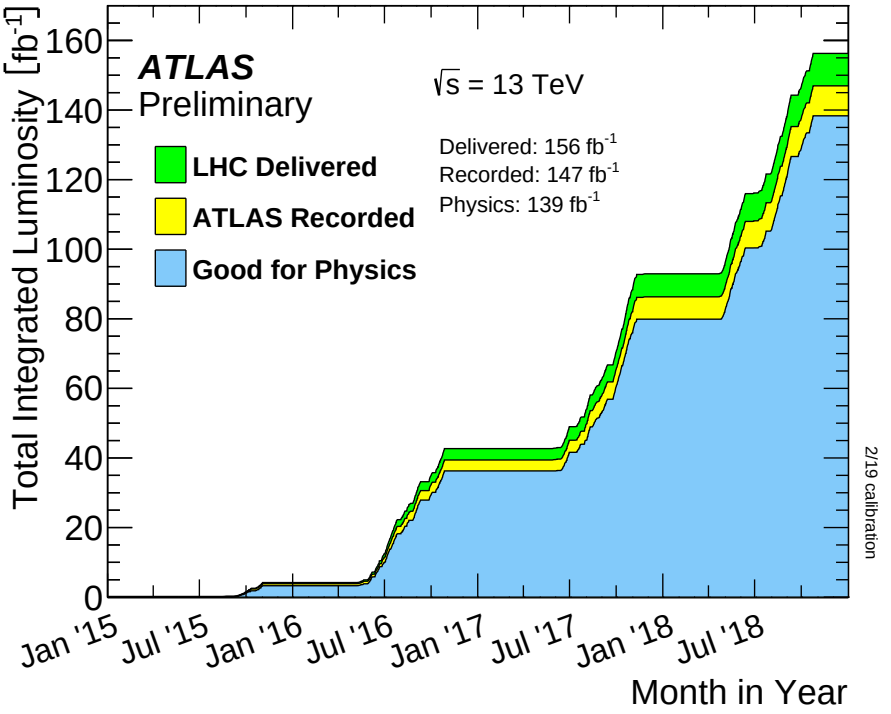

Figure 4.6: The integrated luminosity for $\sqrt{s} = 13\,\text{TeV}$ data delivered by the LHC, recorded by the ATLAS detector, and deemed good for physics analyses during Run 2. [150].

*For a primer on concept of luminosity see [149].

†To disambiguate luminosity from integrated luminosity, the former is often referred to as instantaneous luminosity.

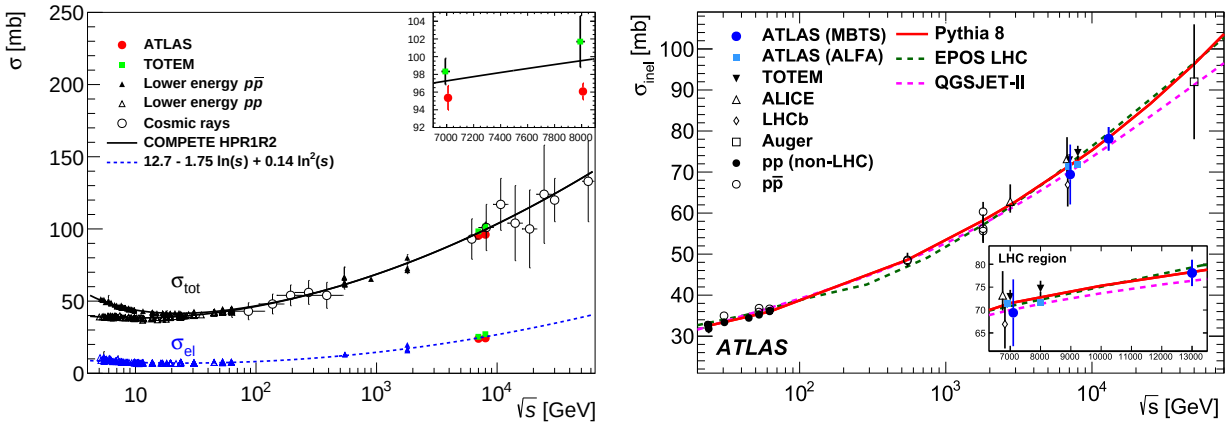

Figure 4.7: Left: Comparison of the total and elastic pp cross section measurements, including measurements form ATLAS and TOTEM at 7 and 8 TeV [151]. Right: The inelastic pp cross section as a function of $\sqrt{s}$, including measurements at $\sqrt{s} = 13\,\text{TeV}$ [152].

the nominal LHC peak luminosity of $L \approx 10^{34}\,\text{cm}^{-2}\text{s}^{-1} = 10\,\text{nb}^{-1}\text{s}^{-1}$, for $\sigma_{pp} \approx 100\,\text{mb}$ at $\sqrt{s} = 13\,\text{TeV}$, one would expect the corresponding total interaction rate of up to 1 GHz for continuously colliding beams. This large interaction rate implies that multiple interactions occur per bunch crossing. With the beams partitioned into bunches with 25 ns spacing, colliding at 40 MHz rate, the 1 GHz expected interaction rate implies the average number of interactions per bunch crossing, $\langle\mu\rangle$, on the order of 25. This is referred to as in-time pileup. Fig. 4.8 shows the distributions of observed numbers of interactions per bunch crossing for the subsets of Run 2 data collected in different years. Due to finite signal integration time for various parts of the detectors, products of interactions within the preceding bunch crossing may appear as a part of the events from following crossing. This is known as out-of-time pileup. Effects of pileup are a major source of experimental uncertainty for data analyses. This will become especially significant for the High Luminosity LHC.

Even though higher luminosity results in increased pileup, raising the luminosity is desired for efficient data collection. Studies of extremely rare processes require enormous numbers of interactions, out of which only a few will result in the process of interest. Effects of

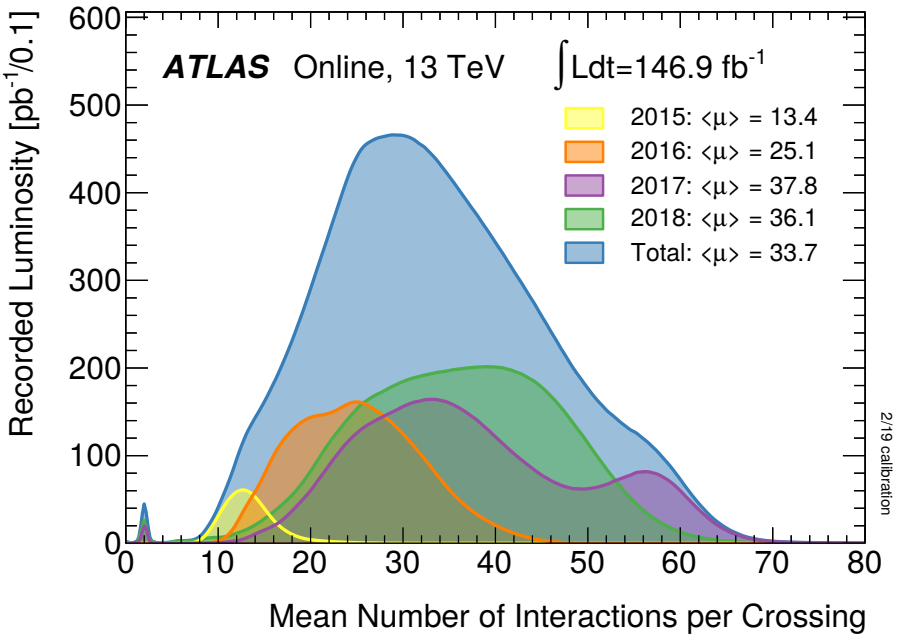

Figure 4.8: The luminosity-weighted distribution of the mean number of interactions per bunch crossing during Run 2. The mean number of interactions corresponds to the mean of the Poisson distribution of the number of interactions per crossing calculated for each bunch. In this calculation the σ_{inel} is taken to be 80 mb for $\sqrt{s} = 13$ TeV [150].

pileup can be addressed using primary vertex identification algorithms for in-time pileup, and application of correction factors obtained through Monte Carlo simulation studies for out-of-time pileup.

4.2 Laboratory coordinates

The ATLAS detector uses a right-handed coordinate system whose origin lies at the nominal interaction point (IP) at the center of the detector. The x axis points towards the center of the LHC ring, the y axis points upwards, and the z axis points along the beam line. Either of the directions parallel to the z axis are refered to as forward. The cylindrical radial coordinate, r, is measured in the x-y plane. Two angular coordinates are also defined. ϕ measures the azimuthal angle in the plane perpendicular to the z axis, such that $\phi = 0$

direction is parallel to the x axis. The detector is essentially symmetric with respect to ϕ. θ is the polar angle, measured such that $\theta = 0$ and $\theta = \pi$ directions are along the positive and negative z axis directions respectively.

Since the two colliding LHC beams have equal energies and opposite momenta, the resulting events have no preferential orientations within the detector. Due to the axial symmetry of the experiment, $\Delta\phi$ is invariant with respect to the event rotation around the z axis. However, this is not true for $\Delta\theta$. For this reason, the polar angle of an object is typically given in terms pseudorapidity.

Rapidity, is a measure of relativistic velocity, or boost, between two reference frames. Unlike velocity, $v = \beta c$, rapidity, $y = \tanh^{-1}\beta$, is additive for one-dimensional motion, which makes differences in rapidity relativistic invariants, and therefore, convenient quantities in relativistic physics. Since,

$$E = m\gamma \quad \text{and} \quad p = m\gamma\beta, \tag{4.4}$$

the rapidity of an object can also be calculated from its energy and momentum,

$$y = \frac{1}{2}\log\frac{E+p}{E-p}. \tag{4.5}$$

For a fixed interaction point, rapidity in the z direction maps out the polar angle. However, the mapping is dependent on the object's mass, m. To avoid this dependence, we define pseudorapidity,

$$\eta = \frac{1}{2}\log\frac{p+p_z}{p-p_z} = \tanh^{-1}\frac{p_z}{p} = -\log\tan\frac{\theta}{2}. \tag{4.6}$$

With this definition, $\eta \to y$ for $E \gg m$, with $\eta = y$ for $m = 0$. Since this condition is largely satisfied for the objects produces in the LHC collisions, differences in pseudorapidity, $\Delta\eta$,

are nearly invariant with respect to the forward or central direction of the vectors within the detector, and are much more useful measures of the polar angle separations than $\Delta\theta$, equal values of which correspond to smaller separations in the central region, and larger separations in the forward regions.

Most of the event information useful for physics analyses is contained in the angular quantities, energies, and masses of the final state objects, with the radial information mostly only important for event reconstruction. Since events can have arbitrary orientation, it is often important to talk about angular separation in the η-ϕ plane,

$$\Delta R = \sqrt{\Delta\eta^2 + \Delta\phi^2}. \tag{4.7}$$

For instance, the ΔR quantity is important in the jet clustering algorithms.

4.3 ATLAS experiment

ATLAS is the largest ever built general purpose particle detector. Located at Point 1 along the LHC accelerator ring, 92 meters underground, it's a cylindrical construct, 25 meters in diameter and 44 meters long, weighing approximately 7,000 tons, as illustrated in Fig. 4.9. The function of the detector is to identify and precisely measure energies and momenta of particles originating from proton-proton collisions that take place at its very center. The primary goal of ATLAS and the LHC program is to fully investigate physics in a new energy regime. The first part of that is the discovery of the Higgs boson and measurements of its properties [1]. But an even larger, long-term agenda consists of precision physics measurements and searches for physics beyond the Standard Model.

The physics goals impose a range of requirements to allow for detection of the events of

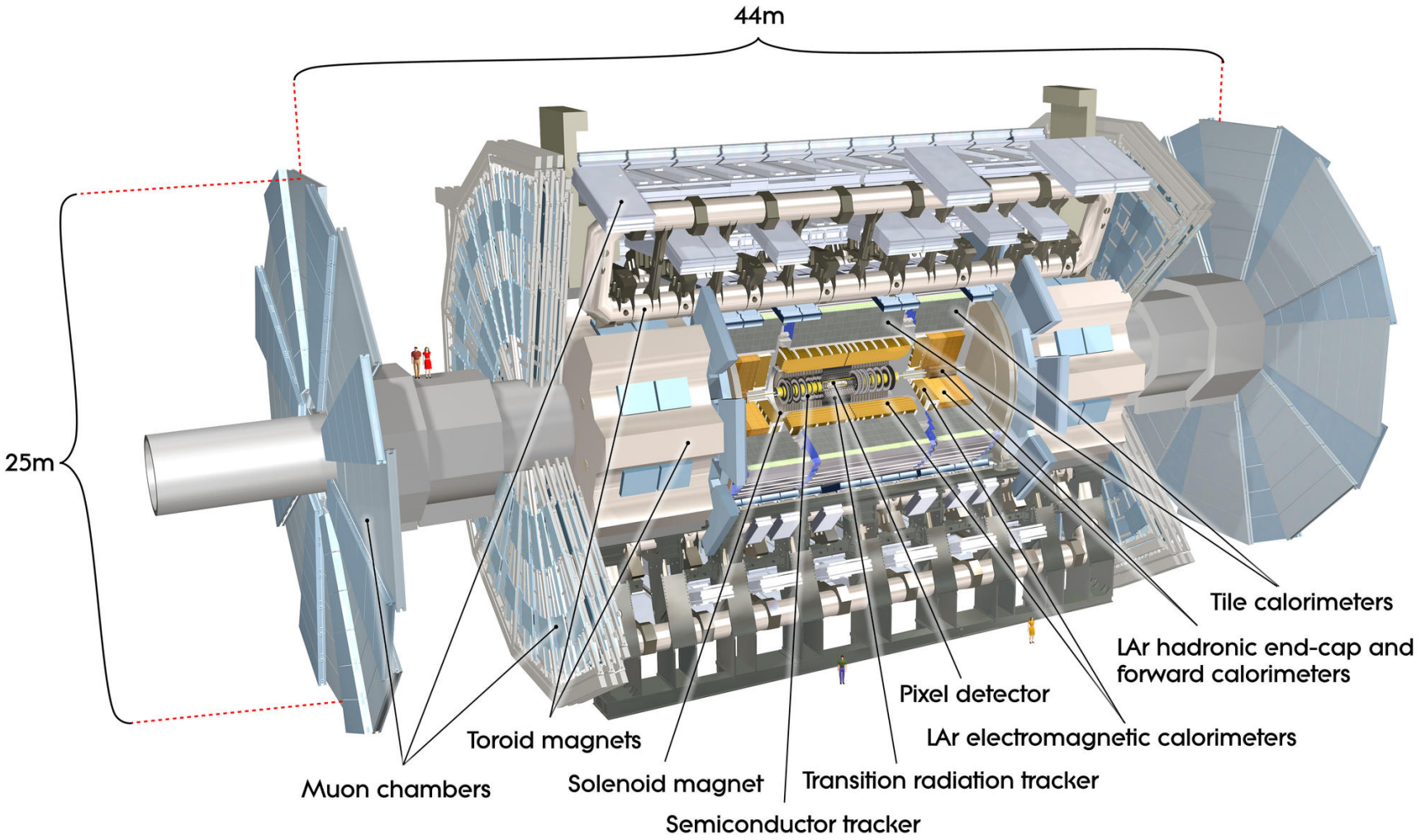

Figure 4.9: Computer generated image of the ATLAS detector indicating all of its major systems [153].

interest. These requirements include:

- **Hermeticity.** In order to fully reconstruct a collision event, it is important to not let particles escape undetected. There are three primary ways for particles to avoid interaction with the active detector elements. Rapidity coverage needs to be optimized in order to detect particles in the forward region, close to the beam pipe. However, at a certain point, returns are diminishing, as good forward rapidity resolution is hard to achieve, because on the one hand, smaller angles correspond to larger changes in rapidity, and on the other, forward objects tend to be more collimated. It is also difficult to provide good particle measurements close to the beam pipe. Secondly, different particles at different energies have different interaction lengths. It is important to have sufficiently thick sub-detector systems in order to fully capture the particles' energy. The third factor that reduces hermeticity is the unavoidable need to leave room between active elements for structural components and cables providing power and communication. Sufficient hermeticity is also required to reduce uncertainty on the missing transverse energy measurements.
- **Speed of response.** With the LHC collisions happening every 25 ns, the detector systems have only a few nanoseconds to measure an event, to leave time for the triggers to process it. Fast response also reduces out-of-time pileup effects.
- **Granularity and spacial resolution.** Accurate position and momentum measurement and particle identification require fine spacial resolution. High granularity also reduces electronics and pileup noise, and improves speed of response [154].
- **Radiation tolerance.** The large number of high-energy LHC collisions results in high intensity radiation near the interaction points. Consequently, active detector elements and on-detector electronics must comply with radiation tolerance require-

ments [155, 156]. This is especially important due to the need to operate the detector for a year or more without full access to its internal components.

Designed as a general purpose detector, ATLAS can be used to study a wide variety of event topologies, with its subsystems dedicated to specific collision products. These include either individual particles, e.g. photons, electrons, muons, or composite objects, like hadronic jets. Methods used for reconstruction of these objects are discussed in Chapter 5.

The innermost part of the detector, located closest to the beam pipe and inside the solenoid magnet, consists of tracking subsystems. Their purpose is to map out charged particles' tracks curved by the field of the solenoid magnet, which allows for determination of the particles' momenta. Situated outside the solenoid magnet are electromagnetic and hadronic calorimeters, which are designed to measure energy of electrons, photons, tau leptons, and hadronic jets. The outermost sub-detector system is the Muon Spectrometer, which measures momenta of muons, which penetrate through the inner detector and the calorimeters. Principles of design and operation of the ATLAS detector systems are discussed in the rest of this chapter.

4.4 Inner tracking detector

The primary goal of the inner detector (ID) [158] is to provide capabilities for reconstruction of paths of charged particles, or tracks. The ID is contained inside the 2 T magnetic field of solenoid magnet, to allow measurement of the particles' charge and momenta from the curvature of the particles' tracks. Prevision measurements can be achieved in p_{T} range between 0.5 GeV (in certain cases as low as 0.1 GeV) and 150 GeV. Using track reconstruction, particles can be traced to primary or secondary interaction vertices. Identification of

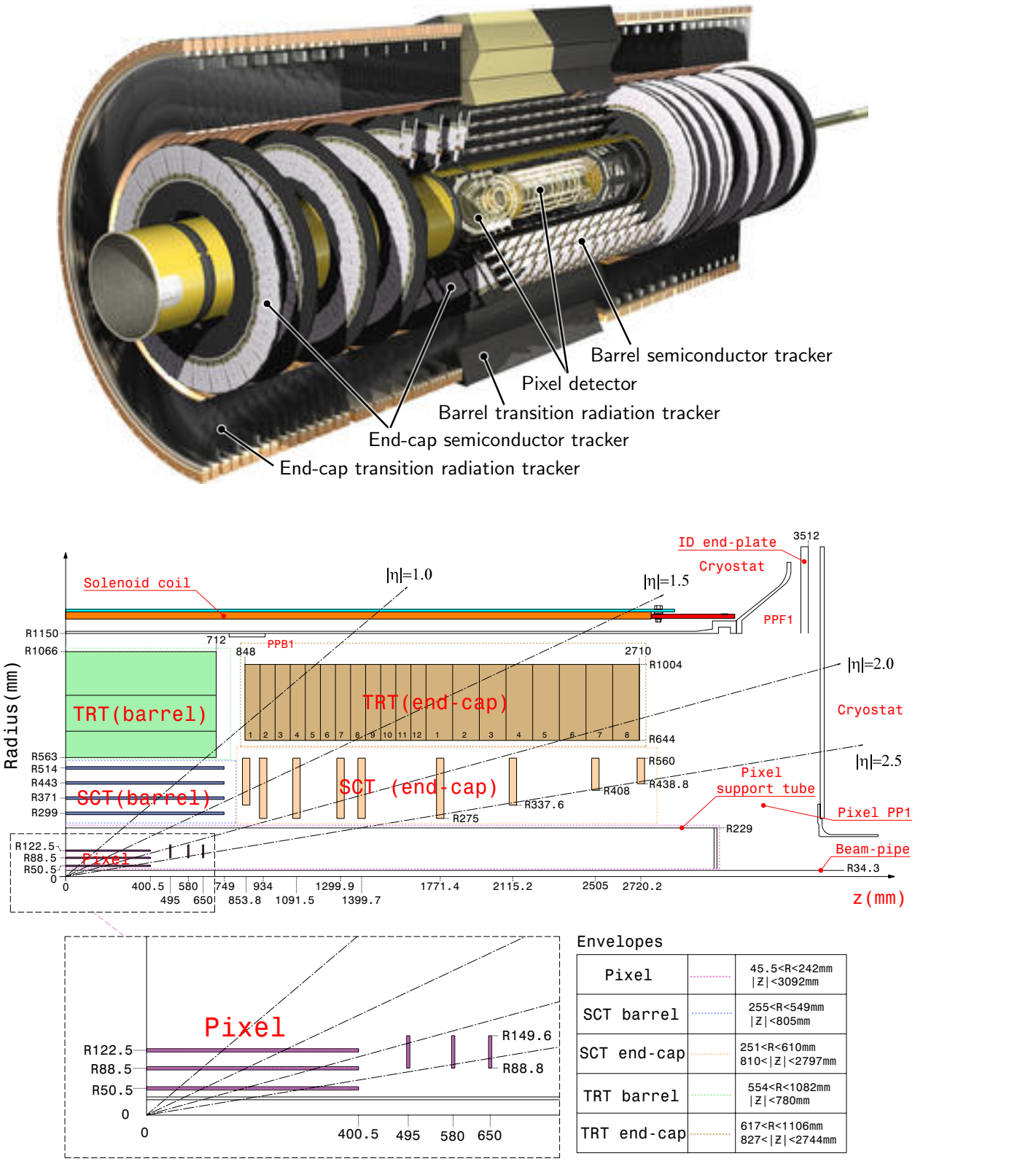

Figure 4.10: ATLAS inner detector. Top: 3D rendered image [157]. Bottom: Schematic view of a quarter-section showing each of the major detector elements and dimensions [127].

primary vertices allows to separate and properly assign products of multiple events occurring within the same bunch crossing, i.e. to distinguish products of an interesting event from pileup. Identification of secondary vertices allows to tag events, e.g. b-tagging.

Three subsystems comprise the ID, enclosing the collision point as concentric cylindrical shells. In order of proximity to the beam line they are: the Pixel detector, the Semiconductor Tracker (SCT), and the Transition Radiation Tracker (TRT). The ID covers the pseudorapidity of $|\eta| < 2.5$ and extends radially to 1.15 m. It is illustrated in Fig. 4.10. Due to the geometric arrangement of the detector elements, ID subsystems are separated into the central barrel and end-cap portions. The Pixel detector is wholly contained in the barrel region of SCT and TRT, but still has an end-cap section.

4.4.1 Pixel detector

The Pixel detector [159–161] is composed of solid state ionizing radiation sensors. A sensor is an array of bipolar diodes (pixels) implanted into a silicon wafer, with the p-n junctions operating under reverse bias. Charged particles from beam collisions are detected when they pass through the sensors, where they excite electrons in the Si lattice, creating electron-hole pairs, which drift between the pixels' anode and cathode, producing measurable electric signal on top of the reverse leakage current.

A pixel sensor consists of a 256 µm thick Si n-bulk. The bulk contains n^+ implants on the read-out side and a p-n junction on the back side. Each $24.4 \times 63.4\,\text{mm}^2$ sensor tile contains 47232 pixels arranged in 144 columns and 328 rows. Individual pixels have a size of $30 \times 382.5\,\mu\text{m}^2$, occupying an area of $50 \times 400\,\mu\text{m}^2$ including spacing. Each tile is attached to 16 front end (FE) chips using flip chip (or bump bonding) technology. The FEs, which amplify the pixel currents, communicate with the detector control system via on-module

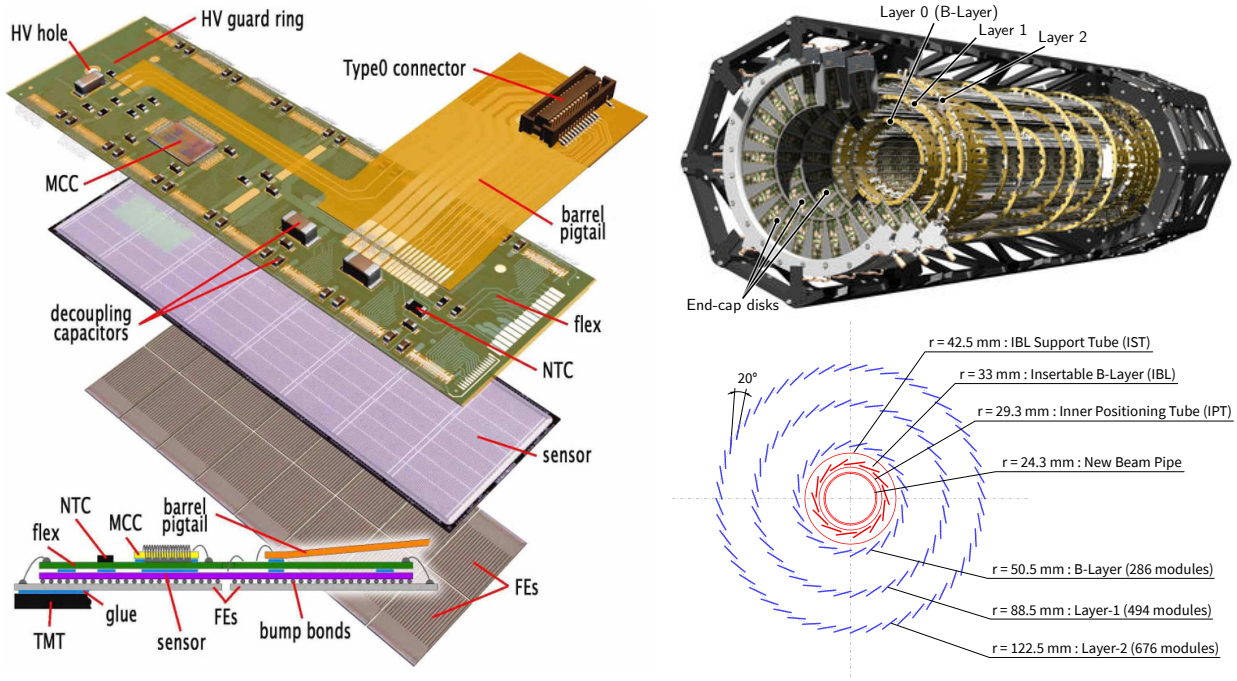

Figure 4.11: Left: Pixel detector module [162]. Top-right: 3D rendered image of the pixel detector [163]. Bottom-right: Diagram of a transverse slice of the pixel layers [164].

Module Control Chips (MCC), which handle data compression and transmission through fiber optics. Fig. 4.11 shows the module design and their arrangement in the detector.

The Pixel detector is made of 1744 modules arranged in 3 coaxial central barrels and 3 end-cap disks. This brings the number of the Pixel detector readout channels to over 80 million, constituting about 50% of the ATLAS total. 3 layers are necessary in order to provide at least 3 hits per track, required for effective reconstruction. In 2014, a fouth layer, called the Insertable B-Layer (IBL), was installed at the radius of 33 mm with $50 \times 250\,\mu\text{m}^2$ pixels [165]. The IBL improves the reconstruction of secondary vertices.

Located centimeters away from the collision point, pixel sensors need to be incredibly resilient to radiation damage. Oxygen impurities are introduced in the bulk Si to increase its tolerance to damage by charged hadrons. To reduce leakage current, sensors are operated at the temperature between $-5\,^{\circ}\text{C}$ and $-10\,^{\circ}\text{C}$. The special design of semiconductor implants

is used to allow operation even after extensive radiation damage has been received.

4.4.2 Semi-Conductor Tracker (SCT)

SCT [166, 167] uses similar technology to the Pixel detector. The primary difference is that instead of pixels, SCT sensors contain strips. To provide two-dimensional resolution in the η-ϕ plane, each module is composed of two sensors, glued back-to-back around a thermally conductive spine, with one rotated by 40 mrad with respect to the other in the same plane.* This construction is illustrated in Fig. 4.12. The shear shift allows the SCT to achieve resolution of 16 µm in ϕ and 580 µm in z.

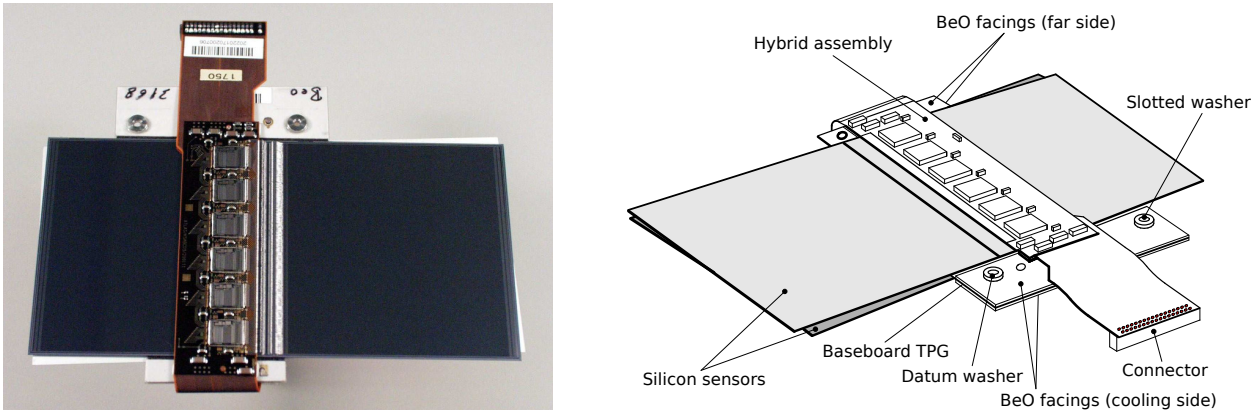

Figure 4.12: Photograph (left) and drawing (right) showing the main components of a SCT barrel module [127].

The SCT consists of four concentric barrels (containing 2112 modules) and two end-caps of nine disks each (containing 988 modules per end-cap). Like the pixel modules, the SCT modules are cooled down to $-7\,^{\circ}\mathrm{C}$. Each SCT module has 1536 channels, with the sensor strips pitched 80 µm apart. A module is read out via the attached hybrid assembly containing front-end ASICs, providing binary readout.

*All modules except the inner modules in the forward region actually contain two sensors on each side.

4.4.3 Transition Radiation Tracker (TRT)

The basic elements of TRT [168–171] are gas-filled drift tubes, or straws, which detect ionization of the gas due to passing charged particles. The straws are made from Aluminum tubes, 4 mm in diameter and 40–150 cm long depending on their location, covered with Kapton film reinforced with carbon fiber bundles. A 30 µm thick, gold plated tungsten wire is under tension inside each tube. The tubes are filled with a 70% Xe, 26% CO_2, 3% O_2 gas mixture, at an overpressure of 5–10 mbar. The wire (anode) and the tube (cathode) are held at a potential difference of 1530 V. When a charged particle passes through a straw, it ionizes the gas, producing electrons which drift to the anode wire. Their current is amplified and read out by the electronics, recording a hit for track reconstruction.

Besides aiding in tracking, the TRT also helps with particle identification, using its namesake phenomenon, transition radiation. Transition radiation (TR) is emitted when a relativistic charged particle traverses a boundary between two materials with different dielectric constants. To produce TR the space between TRT straws is filled with sheets of loosely packed polypropylene-polyethylene fiber. The intensity of emitted TR is logarithmically proportional to the Lorentz factor of the particle. Consequently, lighter particles are much more likely to produce TR. This allows the TRT to distinguish electrons from charged pions,* by optimizing the radiator material so that principally only electrons emit TR. TR in the TRT comes in the form of soft X-rays, which also ionize the gas in the straws. This produces signals with higher amplitude, referred to as "high threshold" hits, which signify TR from electrons.

The TRT consists of a central barrel and two forward end-caps. The straws are oriented

*Other hadrons are heavier than pions, and so have even smaller probability of emitting transition radiation. Both electrons and positrons emit TR.

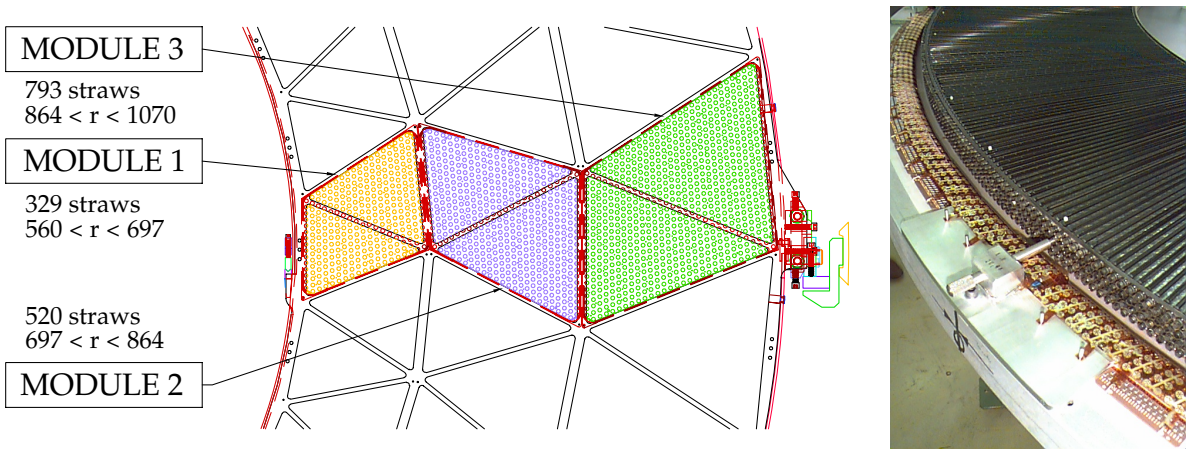

Figure 4.13: Left: Schematic drawing of the TRT barrel showing module and straw positions [127]. Right: Photograph of a TRT wheel module [172].

parallel to the beam pipe in the barrel, and perpendicularly in the end-caps. The barrel, shown in Fig. 4.13, is assembled from 3 cylindrical layers, or rings, of modules and has pseudorapidity coverage of $|\eta| \lesssim 1$. Each ring contains 32 modules. The barrel provides tracking information only in the transverse plane, with resolution of 130 µm. A TRT end-cap consists of 20 wheels, each containing 8 layers of straws with 768 straws per layer. This provides position measurement accuracy of 30–50 µm and covers the region of $1 < |\eta| < 2$. The TRT records, on average, 36 hits for each charged tracks with $p_{\mathrm{T}} > 0.5\,\mathrm{GeV}$ and $|\eta| < 2.0$, except in the barrel/end-cap transition regions, $0.8 < |\eta| < 1.0$, where on average 22 hit are recorded. The TRT operates at a temperature of approximately 20 °C.

4.5 Calorimeters

Calorimeters are detectors that measure energy. Segmentation of calorimeters' active components allows to also use them for position measurements. Calorimeters supplement tracker measurements providing additional information about energetic charged leptons and hadrons, as well as neutral particles invisible to the trackers. The principle of operation of

a calorimeter relies on making incident high-energy particles undergo multiple interactions, which produce cascades, or showers, of secondary, lower energy particles. The lower energy particles are absorbed by the calorimeter, which results in a quantifiable process (e.g. ionization or scintillation) that allows to measure the deposited energy. Relying on scattering and absorption for their operation gives calorimeters the ability to see neutral particles, e.g. photons and neutrons. Calorimeters allow to distinguish electromagnetic and hadronic particles by the shapes, lengths, and locations of their showers. They are crucial for jet reconstruction and provide indirect measurements of $E_{\mathrm{T}}^{\mathrm{miss}}$, which is computed by balancing the sum of observed objects' momenta.

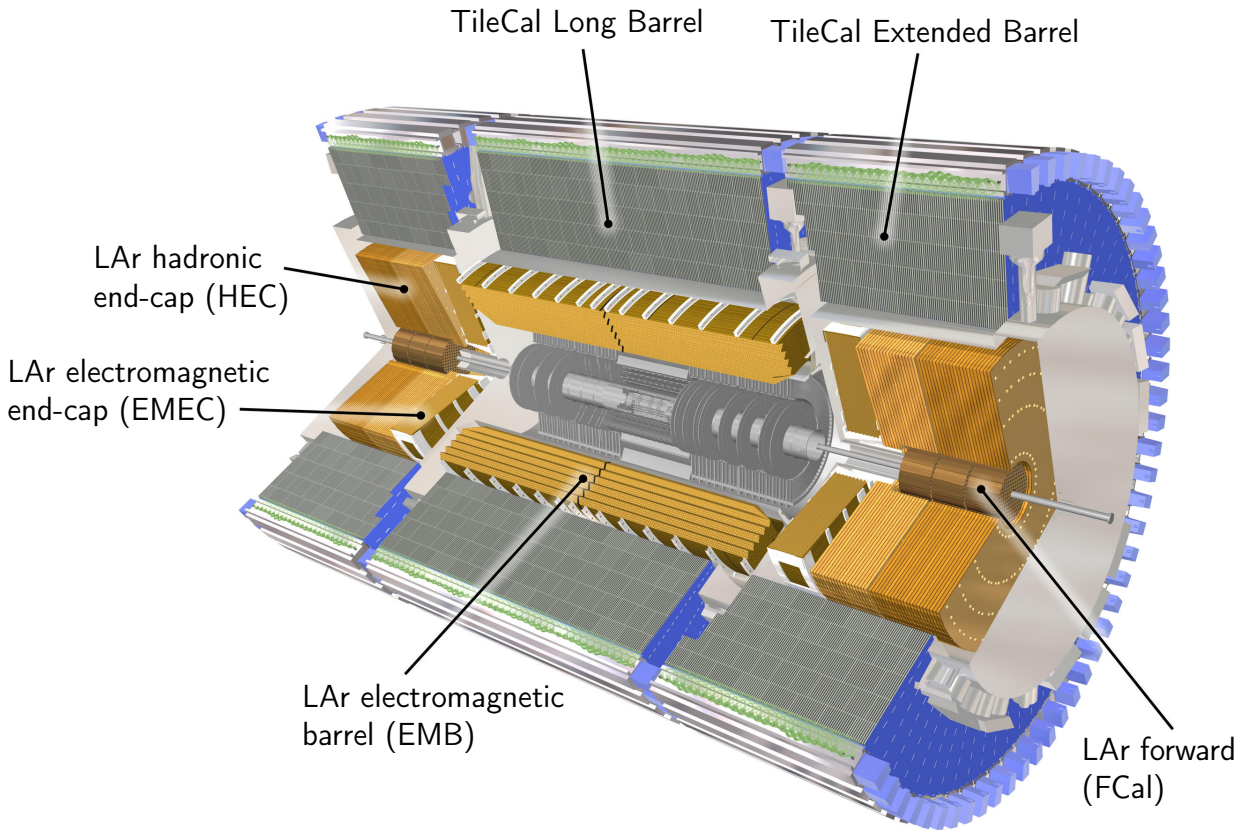

Figure 4.14: Cutaway computer generated image of the ATLAS calorimeter systems [173].

ATLAS contains a number of calorimeter systems, which can be grouped together differently according to the purpose, principle of operation, and structural connection. Thus, we

distinguish electromagnetic (more inner) and hadronic (more outer) systems; liquid argon (LAr) ionization detector and plastic tile (TileCal) scintillator systems; barrel and forward end-cap systems. Table 4.2 gives a concise summary of the ATLAS calorimeter systems.

Table 4.2: ATLAS calorimeter systems.

Name	Purpose	Active material	Absorber	Location
EMB	EM	LAr	Pb	Barrel
EMEC	EM	LAr	Pb	End-cap
HEC	Hadronic	LAr	Cu	End-cap
TileCal	Hadronic	Plastic	Steel	Barrel
FCal	EM, Hadronic	LAr	Cu, W	End-cap

Inelastic scattering due to electromagnetic (EM) and strong interactions produce distinct types of showers. These are illustrated in Fig. 4.15. The primary modes of interaction producing EM showers are bremsstrahlung for charged particles (electrons) and pair production for photons. The shower grows with the two processes alternating until the energy of the photons falls below the electron pair production threshold of $2m_e$ and the energy of electrons falls below the critical energy of the material, E_c, at which point energy losses due to bremsstrahlung and ionization become equal. Once ionization becomes the dominant process, the shower begins to die out. Materials with higher atomic number have lower critical energy. The ionization radiation in the active medium is what creates signal in the LAr EM

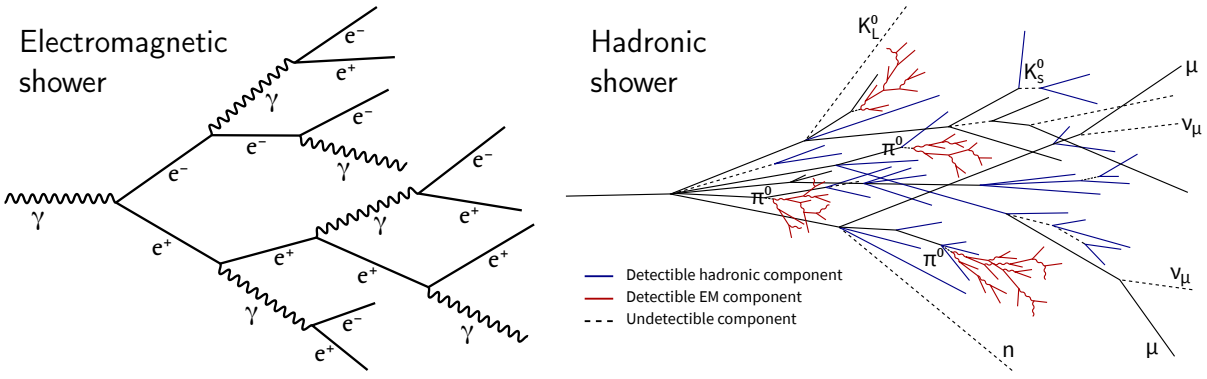

Figure 4.15: Sketches of electromagnetic (left) and hadronic (right) showers.

calorimeter. Shower profiles are determined by two parameters: radiation length, X_0, and Molière radius, R_{M}. The radiation length is the mean distance a particle travels before its energy is reduced by a factor of $1/e$, and determines the length of the shower. X_0 is typically on the order of 1 cm. The Molière radius is the radius that contains 90% of the shower's energy, and the transverse spread of the shower. Its value is proportional to the radiation length and inversely proportional to the critical energy,

$$R_{\mathrm{M}} \propto \frac{X_0}{E_{\mathrm{c}}}. \tag{4.8}$$

Hadronic showers develop due to strong interaction with matter, primarily through secondary hadron production, nuclear deexcitation, and decays to pions and muons. The process continues until the hadrons fall below the pion production energy threshold. Longitudinal propagation of hadronic showers is characterized by the material's nuclear interaction length, λ_{int}, which is the mean free path a hadron travels between subsequent interactions with the material's nuclei. Pions are the main intermediate constituents of a hadronic shower. On average, 1/3 of those are neutral pions, which decay to pairs of photons, resulting in large a fraction of a hadronic shower converting to electromagnetic. This fraction increases with increasing hadron energy. Decays to neutrinos and muons results in undetectable or hard to contain components of the shower. Due to the mixed nature of hadronic showers their modeling is important for calorimeter design.

EM showers are usually shorter and narrower than hadronic ones due to the interaction length typically being an order of magnitude larger than the radiation length. This allows to separate the roles of detection of EM and hadronic showers between two calorimeters, with the EM calorimeter placed closer to the collision point, and the hadronic one positioned be-

hind it. Careful choice of materials allows EM showers to be fully contained in the respective calorimeter, while allowing hadronic showers to only deposit a small fraction of their energy in the EM system and to mostly develop and be contained within the hadronic calorimeter. Other factors in the choice of materials are reduction in the transverse dispersion of showers to improve spacial resolution, as well as cost and radiation tolerance. In order to achieve good energy resolution, it is important to make calorimeters sufficiently thick to contain showers as fully as possible. ATLAS EM calorimeters provide about $22\,X_0$ and the hadronic ones provide about $10\,\lambda_{\text{int}}$.

Depending on whether the active material of a calorimeter is the same as the absorber or not, distinguishes between homogeneous and sampling calorimeters respectively. All calorimeters on ATLAS are of the sampling type. The materials used in them are listed in Table 4.2. Typically, a calorimeter has a higher response to the EM than to hadronic shower component. This is usually expressed as $e/h > 1$. A calorimeter that is designed to have $e/h \approx 1$ is called a compensating calorimeter. ATLAS calorimeters are non-compensating.

Energy resolution of a sampling calorimeter is modeled by Eq. (4.9),

$$\frac{\sigma}{E} = \frac{a}{E} \oplus \frac{b}{\sqrt{E}} \oplus c, \tag{4.9}$$

with the terms corresponding to noise, sampling or stochastic, and constant contributions respectively. The noise term represents electronic noise of the readout system. Scintillator calorimeters generally have lower noise than those using ionization radiation due to the use of photomultiplier tubes (PMTs). The stochastic term represents shower fluctuations and is dependent on the choice of active and absorber materials and the number of absorber layers and their thickness. The constant term does not depend on the shower energy and

represents effects due to calorimeter geometry and non-uniformities. With increasing shower energy, the relative importance of the terms increases from noise, to stochastic, to constant. Table 4.3 lists design goals and test-beam measurements of the energy resolution of the ATLAS calorimeters.

Table 4.3: Energy resolution parameters of ATLAS calorimeter systems measured at test beam [174–178].

Calorimeter	Beam type	Stochastic, %	Constant, %
EM Barrel	electron	10.1 ± 0.1	0.17 ± 0.04
EM End-cap	electron	10 to 12.5	0.6
HEC	pion	70.6 ± 1.5	5.8 ± 0.2
TileCal	pion	56.4 ± 0.4	5.5 ± 0.1
FCal EM	electron	28.5 ± 1.0	3.5 ± 0.1
FCal Hadronic	pion	94.2 ± 1.6	7.5 ± 0.4

4.5.1 Electromagnetic calorimeter

The ATLAS electromagnetic calorimeter (ECal) [179–181] consists of a barrel (EMB) and two end-cap (EMEC) parts, all using liquid argon (LAr) technology, and each housed in its own cryostat. To reduce the amount of material in front of the calorimeter, the same vacuum vessel is shared between EMB and the central solenoid magnet, thereby eliminating two vacuum walls. EMB covers the $|\eta| < 1.475$ region with two half-barrels separated by a 4 mm gap at $\eta = 0$, and EMEC covers the $1.375 < |\eta| < 3.2$ region. Each end-cap calorimeter is structurally divided into an outer wheel, $1.375 < |\eta| < 2.5$, and an inner wheel, $2.5 < |\eta| < 3.2$. A thin presampler layer [182] is located between the cryostat and EMEC, covering the region $|\eta| < 1.8$. It provides a measurement of the energy lost in front of the EM calorimeters. FCal provides forward-most EM coverage on $3.1 < |\eta| < 4.9$.

The design of the main part of the electromagnetic calorimeter, EMB, is illustrated in

Fig. 4.16. Its interesting accordion geometry is motivated by the desire to eliminate projective azimuthal cracks* that contribute to the constant term of the electromagnetic energy resolution (see Eq. (4.9)). As an ionization detector, its principle of operation relies on incident particles ionizing the active medium, LAr. The electrons and ions then drift between the Cu-Kapton electrodes, producing a current proportional to the number of ionization interactions. To create the motion of charges, the electrodes are biased at 2000 V [183]. Liquid argon was chosen for its linear behaviour, stability of response over time, and radiation-hardness [127]. To keep the argon liquid, the cryostats maintain the temperature of 89.3 K through liquid nitrogen cooling.

As the top diagram of Fig. 4.16 show, the EM barrel is made up of three radial layers of decreasing granularity. Spacial resolution and thickness of the layers is summarized in Table 4.4. The presampler is also referred to as Layer 0. The lateral segmentation of the LAr detector allows it to distinguish photons, γ, from neutral pions, π^0. The pions almost always decay to two photons, which up to a certain p_{T} threshold can be resolved.

Table 4.4: EMB layer segmentation dimensions.

	$\Delta\eta$	$\Delta\phi$	Thickness, X_0
Layer 1	0.003	0.1	4.3
Layer 2	0.025	0.025	16
Layer 3	0.05	0.025	2

EMEC is different from EMB in that its inner wheel has only 2 layers. Otherwise, it utilizes the same accordion geometry and also uses lead as the absorber material. The EM part of FCal uses Cu as the absorber and LAr filled drift tubes [184].

*The accordion geometry reclaims azimuthal (ϕ) coverage because the accordion layers are stacked in ϕ.

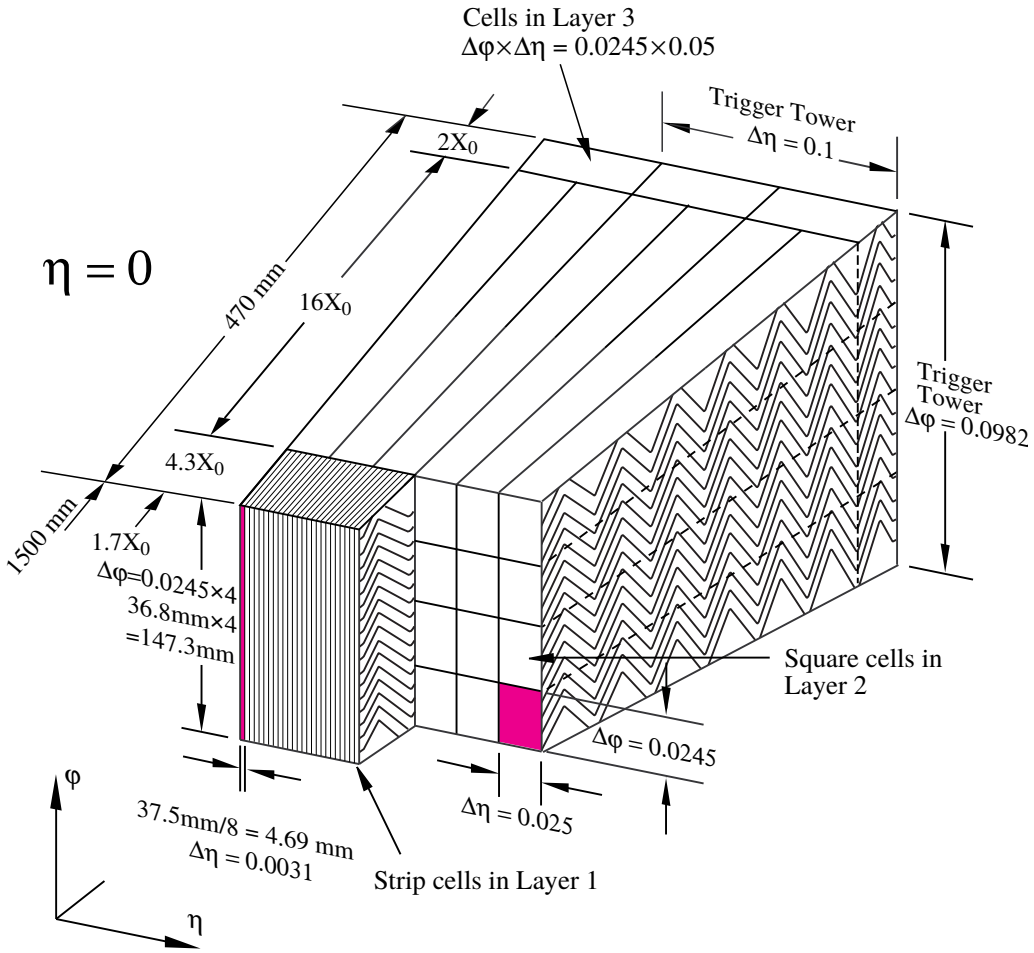

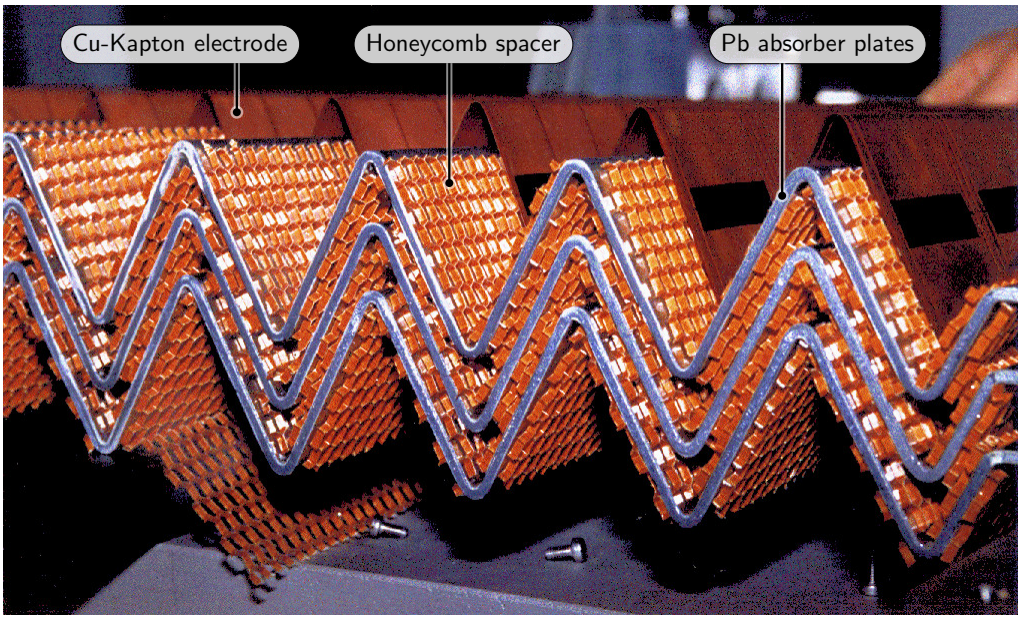

Figure 4.16: Structure of the ATLAS electromagnetic calorimeter. Top: Schematic drawing of an EMB segment showing layers and ganuarity [127]. Bottom: Photograph of an open EMB cell showing its accordion structure [180].

4.5.2 Hadronic calorimeter

The hadronic calorimeter system on ATLAS is comprised of the large scintillator tile barrel calorimeter (TileCal), two liquid argon end-cap calorimeters (HEC), and parts of the liquid argon forward calorimeter (FCal).

4.5.2.1 Tile Calorimeter

In contrast to the ionization detectors described in the previous sections, which detect a current of electrons created in a medium ionized by incident particles, scintillators emit light when their electrons are deexcited, following excitation by radiation absorption. Light in a particular wavelength range is emitted, depending on the available electron states of the scintillator material. The measured energy can be calibrated to the observed light intensity. Transparent scintillator material is required for propagation of light from the bulk to the surface, where the light can be detected using photomultiplier tubes (PMTs).

The primary purpose of the TileCal [185–189] is to extend the ATLAS calorimetry to fully contain and measure hadronic activity in the form of jets. It is a sampling barrel calorimeter, with plastic scintillator active medium and steel absorbers. Its angular coverage is $|\eta| < 1.7$. A TileCal module is illustrated in Fig. 4.17. The bulk of a module consists of an array of scintillator tiles interleaved with steel absorber plates. The fraction of materials is approximately 4.7:1 by volume. The steel plates induce the hadronic showering process, iron having a large cross section for hadronic interactions, limit the particles' interaction length, reducing the required calorimeter thickness, and provide structural support for the scintillators.

An interesting aspect of the design is that the tiles are oriented perpendicularly to the beam axis, i.e. in direction largely parallel to that of the incident particles. This choice is

justified by the fact that the resolution of a sampling hadronic calorimeter is not critically dependent on the orientation of the active medium, since at the end of a hadronic shower, low energy particles have nearly isotropic velocities. Note also, that the LAr calorimeter provides 2λ of interaction length before the TileCal. The parallel orientation of the tiles allows for a more hermetic design, by routing the optical fibers in the radial direction within small slots in the absorber. To prevent particles from traveling for too long inside a single tile, the tiles are made small and are arranged in a staggered pattern [190].

The base material of the TileCal plastic scintillator is polystyrene. The scintillator produces ultraviolet light, which is converted to visible blue light by wavelength-shifting fluors added to the plastic. The light is collected at the edges of each tile using wavelength-shifting fibers. The fibers are also polystyrene-based and further increase the light's wavelength to 476 nm. Each fiber collects light from tiles located at one or two radial depths, and each tile is read out by two fibers, one on each side, providing double readout. At the interface with the PMTs, fibers are bundled together, with a single PMT reading signals from many tiles. This grouping splits a module into cells, approximately projective in pseudorapidity, as shown in the bottom half of Fig. 4.17. A steel girder is located at the outer end of every module. The girders function to support the calorimeter, which also supports the solenoid magnet and the inner detector, as well house the on-detector TileCal electronics and PMTs, and provide flux return for the solenoid magnetic field.

Modules are shaped like wedges for arrangement into barrels: two halves of the central long barrel (LBA, LBC) and two extended barrels (EBA, EBC). 64 modules form a barrel, with each module subtending 5.625° in azimuth. The barrels have inner and outer radii of 2.28 m and 4.25 m, including structural components. The modules are radially segmented into three regions, corresponding to 1.5, 4.1, and 1.8 λ_{int} in the central barrel and 1.5, 2.6,

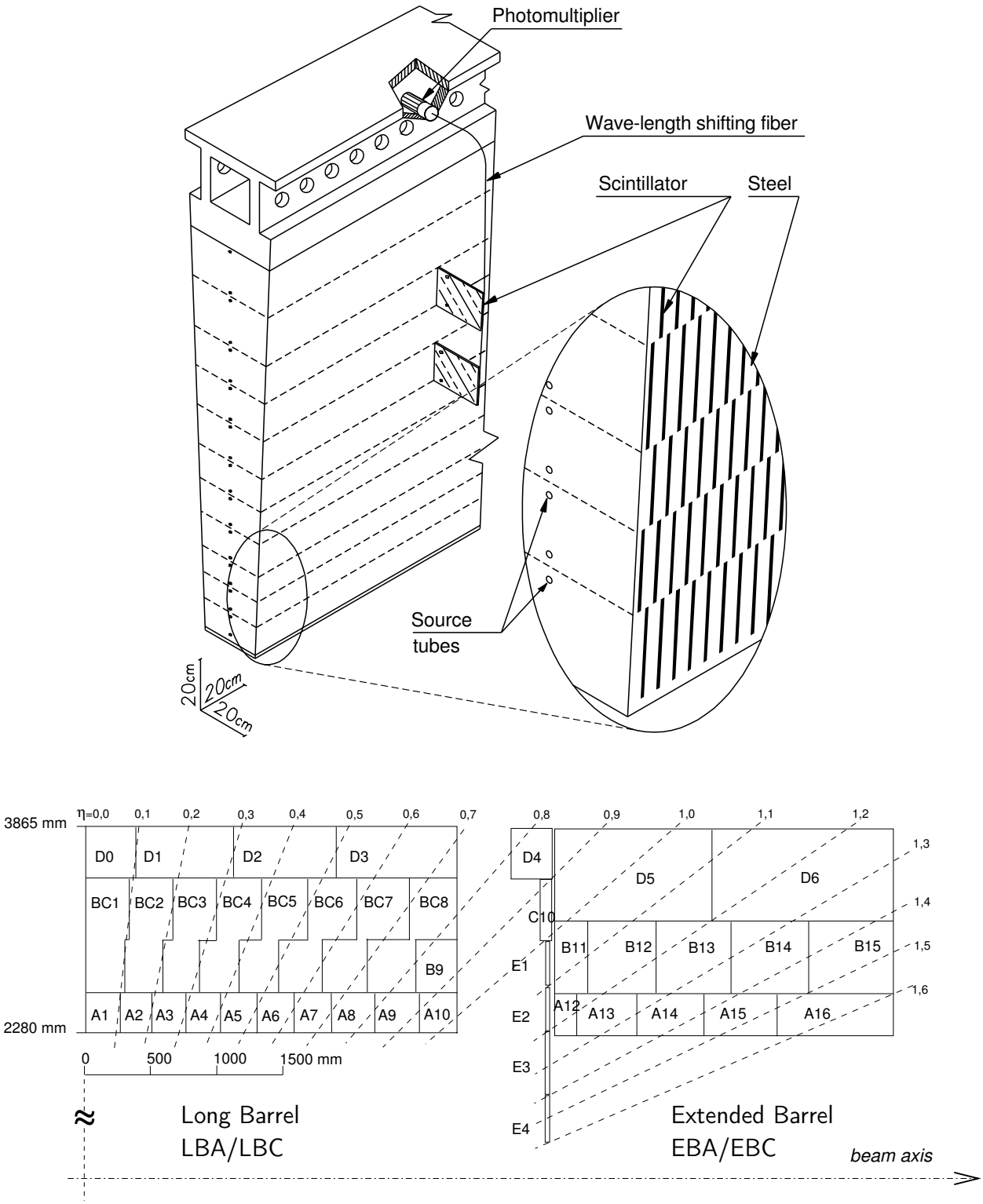

Figure 4.17: A diagram illustrating a TileCal module (top) and the positioning of cells within the central and extended barrels (bottom) [127]. Cells D4 and C10 and refered to as the Plug tile calorimeter, E1 and E2 as the Gap scintillator, and E3 and E4 as the Cryostat scintillator.

and 3.3 λ_{int} in the extended barrel. The LB modules contain 307 tiles per row for a total of 3377. The EB module have between 140 and 157 tiles per row and a total of 1591.

Further discussion of TileCal, its electronic components, their planned upgrades, and my involvement in relevant projects can be found in Appendix C.

4.5.2.2 Hadronic End-Cap calorimeter

The Hadronic End-Cap calorimeter (HEC) [179, 191] is a copper/liquid-argon sampling calorimeter with a flat-plate design, which covers the range $1.5 < |\eta| < 3.2$. HEC shares the end-cap cryostats with EMEC and FCal. It consists of two wheels in each end-cap: a front wheel (HEC1) and a rear wheel (HEC2), each with two longitudinal sections. Each wheel is comprised of 32 identical wedge-shaped modules, sketched in Fig. 4.18. The modules of HEC1(2) are made of 24(16) copper plates, each 25(50) mm thick, and a 12.5(25) mm thick front plate. 8.5 mm gaps separate the plates. The space between the electrodes is maintained using honeycomb sheets. Three electrodes divide the gaps into four separate 1.8 mm wide

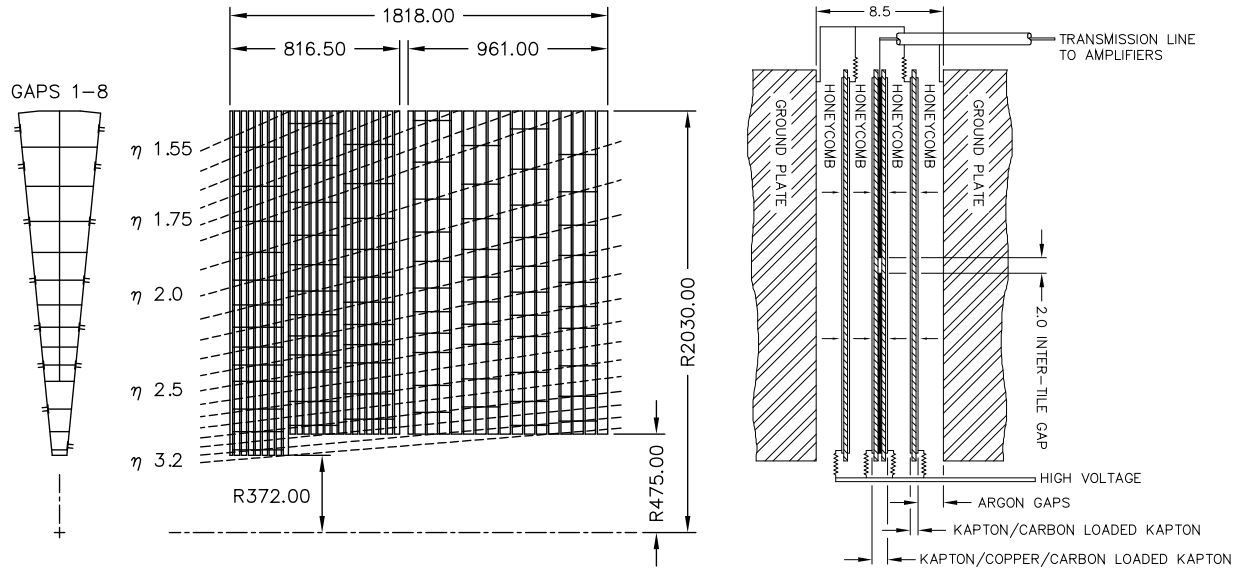

Figure 4.18: HEC module diagrams [127]. Left: r-ϕ and r-z views of a module. Right: Structure of the inter-plate gap.

LAr drift zones. The middle electrode is a 3-layer printed circuit that serves for readout, while the other two electrodes have 2 layers and serve only to carry high voltage (1800 V). This configuration allows to use lower voltage as well as reduces problems with ion build-up. The typical drift time for electrons in the drift zone is 430 ns.

4.5.3 Forward calorimeter

The forward calorimeter (FCal) provides coverage in the forward-most region of $3.1 < |\eta| < 4.9$, at either end of ATLAS, and shares the cryostat with the end-cap calorimeters. Located at such high rapidity, FCal modules are exposed to a very high flux of particles. The FCal was designed with increased density to handle this flux and to limit radiation exposure of the muon system behind it. To further limit downstream flux, a copper alloy shielding plug is mounted behind FCal.

FCal is a liquid argon ionization detector using drift tubes. Its design is shown in Fig. 4.19. Three modules compose FCal: one electromagnetic (FCal1), using copper for absorber, and two hadronic (FCal2 and FCal3), using tungsten. W has a shorter λ_{int} than Cu and was chosen in order to better contain hadronic showers and limit their lateral dispersion. Each module consists of an absorber of stacked thick plates with a matrix of drilled holes housing

Table 4.5: Parameters of FCal modules [127].

	FCal1	FCal2	FCal3
Function	EM	Hadronic	Hadronic
Module mass, kg	2119	3826	3695
Absorber material	Cu	W	W
LAr gap width, mm	0.269	0.376	0.508
Radiation length, X_0	27.6	91.3	89.2
Absorption length, λ_{int}	2.66	3.68	3.60
Number of electrodes	12260	10200	8224
Number of readout channels	1008	500	254

electrodes insulated from the bulk. An electrode consists of a Cu tube and a coaxial rod of the same material as the bulk, separated by a precision, radiation-hard plastic fiber wound around the rod. The LAr gaps in FCal are a lot smaller than the 2 mm ones in EMB to avoid ion build-up and to provide the highest possible density. Table 4.5 lists the main parameters of FCal modules.

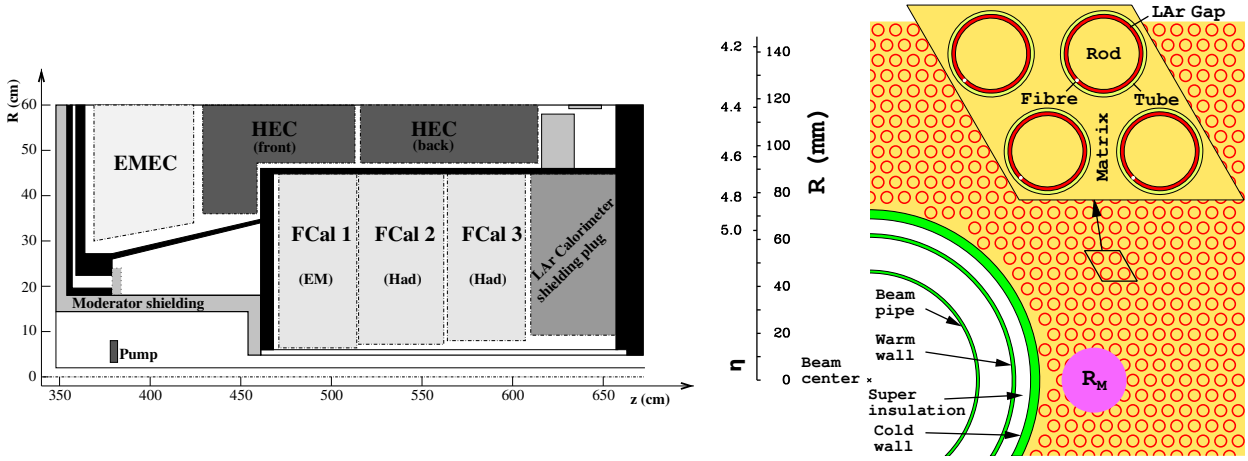

Figure 4.19: Left: Diagram showing FCal modules located in the end-cap cryostat. The black regions are structural parts of the cryostat. Right: Electrode structure of FCal1. The other two modules are similar. The Molière radius, R_{M}, is indicated by the solid circle. [127]

4.6 Muon Spectrometer

Muons are rather special particles from the experimental point of view. Their mass is large enough to significantly reduce bremsstrahlung in comparison to electrons, but not large enough to open up hadronic decay channels, as is the case for tau. Decaying exclusively through the weak interaction, muon have a very long mean lifetime of 2.2 µs in their rest frame, which is made even longer in the laboratory frame by relativistic time dilation. The decay amplitude is further reduced by the small difference in mass between a muon and its decay products, limiting the available phase space. The long lifetime in combination with

reduced probability of interaction give muons much larger penetration depth than any other collision products (aside from neutrinos). Because of this, they demand a dedicated system surrounding the rest of the detector.

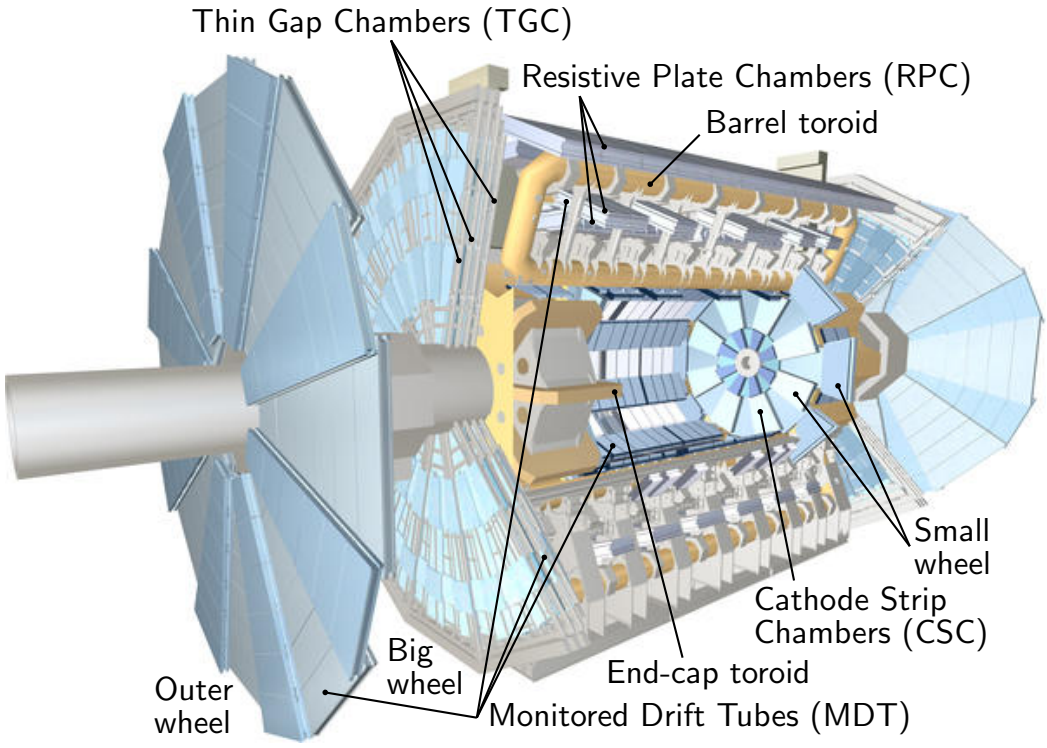

Figure 4.20: Cutaway computer generated image of the ATLAS muon system [192].

The ATLAS Muon Spectrometer [193, 194], illustrated in Fig. 4.20, is a detector comprised of four types of components: Monitored Drift Tubes (MDT) and Cathode Strip Chambers (CSC) are used for precision tracking but are too slow for triggering, while Resistive Plate Chambers (RPC) and Thin Gap Chambers (TGC) provide prompt signals for triggering on the order of 10 ns. Four different components were necessary because a single approach would have to compromise on either resolution or response time. All four, however, are similar in using gas ionization detection as their principle of operation.

Measurements of muon momenta are highly dependent on uncertainty of the position of the Muon Spectrometer components. A 1 TeV muon has a sagitta of 500 µm, thus requiring a

50 µm sagitta resolution to achieve 10% resolution on the momentum, which requires knowing positions of the detector components to 30 µm. To achieve this precision, a sophisticated laser alignment system is installed on the detector [195].

The muon detector elements are interspersed with the ATLAS toroidal magnets, which provide the magnetic field enabling momentum measurements in the Muon Spectrometer. This system allows to measure muon momenta between 3 GeV and 1 TeV and provides resolution better than 10% for 1 TeV tracks.

Monitored Drift Tubes (MDT) [196, 197] provide most of the precision tracking information. They are located in the barrel and outer wheels and cover the pseudorapidity range $|\eta| < 2.7$. The basic element of the MDT is a pressurized drift tube, 29.970 mm in diameter, filled with 93% Ar, 7% CO_2 gas at 3 bar. The electrons resulting from ionization are collected at the central W-Re wire, 50 µm in diameter, at a potential of 3.08 kV. Regular MDT modules, or chambers, consist of two groups of tube layers, called multi-layers, separated by a mechanical spacer (Fig. 4.21). Each multi-layer contains 3 to 4 layers of drift tubes. Due to the Muon Spectrometer sharing space with the toroidal magnets, there are also irregular MDT modules, containing at least 3 layers of tubes. The overall layout of the MDT's is projective, with the layer dimensions and the chamber sizes increasing in proportion to their distance from the interaction point. There are 1088 MDT chambers of 18 main types, covering a total area of 5500 m^2.

Cathode Strip Chambers (CSC) are located in the small wheels and provide coverage in the forward region of $2.0 < |\eta| < 2.7$, where flux of particles and density of tracks is much higher. Each small wheel is made up of two discs, one composed of 8 small chambers and the other of 8 large chambers. The two discs are rotated with respect to each other by $\pi/8$ in ϕ, with their modules slightly overlapping. The chambers are installed inclined

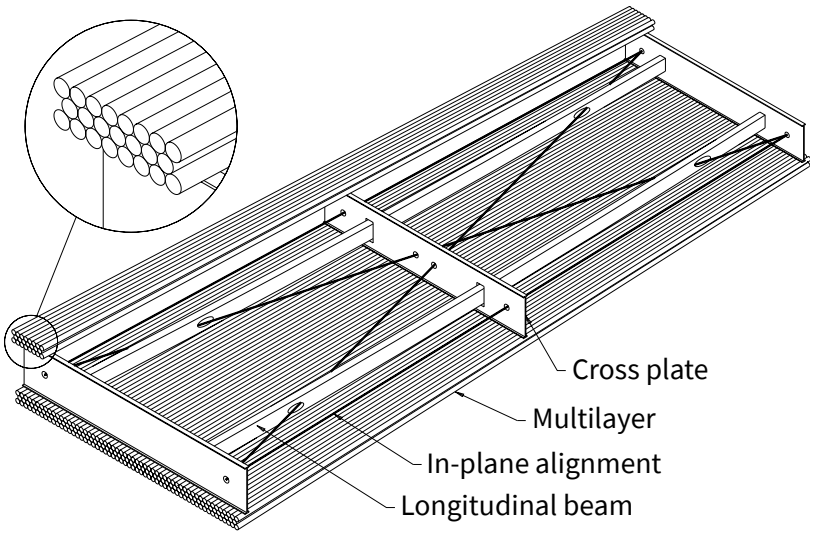

Figure 4.21: Schematic drawing of a regular (2×3) MDT chamber [193].

towards the interaction point by 11.59° with respect to the z axis. CSCs are multi-wire proportion chambers operating with a gas mixture of 80% Ar and 20% CO_2 and potential difference of 1.9 kV. The central wire in each CSC is oriented radially with the other wires parallel to it and pitched at 2.5 mm. Each plane of anode wires lies between two segmented cathode planes separated from it by 2.5 mm. One cathode is segmented perpendicularly to the anodes, providing precision coordinate in the bending plane with 60 µm resolution. The other cathode is segmented parallel to the anodes, and provides a courser transverse coordinate with 5 mm resolution. This scheme allows to distinguish more than one track at a time. The timing resolution of CSC is 7 ns.

Resistive Plate Chambers (RPC) provide measurements for muon triggers in the barrel region, $|\eta| < 1.05$. They are arranged in three cylindrical layers and are attached to one or both sides of MDTs in the one outer or two inner layers respectively. Each RPC consists of two parallel resistive plates, which are separated by a 2 mm gap, filled with $C_2H_2F_4/C_4H_{10}/SF_6$ (94.7/5/0.3) gas, and are kept at 9.8 kV potential difference. There are no wires between the plates, and the signal is read out via capacitive coupling to metallic

strips mounted on the outer faces of the resistive plates. With this design, the signal width can be limited to 5 ns. The resistance of the allows for discharges to be spatially localized, providing $10 \times 10\,\mathrm{mm}^2$ resolution in the ϕ-z plane. Since both sides of the plates can be read out, the RPC provides 6 measurements in η and ϕ per track. This redundancy in track measurements allows the use of coincidence discrimination to reduce the fake trigger rate. The RPC can trigger on muons in the range of 6–35 GeV.

Thin Gap Chambers (TGCs) are multi-wire proportional chambers, with many wires enclosed between two plates. The plates contain cathode strips oriented perpendicularly to the anode wires. The wires, 50 µm in diameter, are pitched 1.8 mm apart and are aligned in a plane 1.4 mm from the cathodes, and operate at potential difference of 2.9 kV. The space between the plates is filled with 55% CO_2, 45% C_5H_{12} gas. The TGCs provide information for muon triggers in the end-cap region, $1.05 < |\eta| < 2.4$ and are installed in the big wheel. The TGCs have a resolution of 2–6 mm in the r direction and 3–7 mm in the ϕ direction, and are able to supplement the ϕ measurements from MDTs. The middle layer of the MDTs in the end-cap is accompanied by seven layers of TGCs, while the inner layer is accompanied by only two layers.

4.7 Magnet system

A strong magnetic field throughout the detector is important to enable measurement of the momentum of electrically charged particles. As the particles traverse the magnetic field, they feel the Lorentz force perpendicular to the direction of their motion and the field, $\vec{B}$. This makes the particles travel along curved trajectories, with the radius of curvature proportional to the momentum and the direction of curvature determined by the sign of the

charge. This makes the strength of the field particularly important for muons, as their energy is not completely measured by the calorimeters. For this purpose, ATLAS features a system of superconducting magnets [198] illustrated in Fig. 4.22. It includes a central solenoid, a barrel toroid, and two end-cap toroids. Their main parameters are listed in Table 4.6. The superconducting material used is aluminum stabilized NbTi/Cu.

The solenoid magnet creates a nearly uniform 2 T field for the inner tracking detector. The field is parallel to the beam axis, resulting in tracks curved in the transverse plane. It occupies the space between the inner detector and the calorimeters. In order to minimise the amount of material in front of the electromagnetic calorimeter, the solenoid magnet shares the cryostat vessel with the EMB, avoiding the need for two extra vacuum walls. This allows the solenoid to contribute only 0.66 radiation lengths at normal incidence.

The 8 barrel toroids provide magnetic field for the central part of the muon detector. The toroidal field is nearly circular about the z axis, and makes the particle tracks curve in the r-z plane. This field is less uniform than that of the solenoid, and varies between 0.5 T near the center of a loop and the 3.9 T peak value. The large spacing between the toroidal coils also contributes to the non-uniformity of the field. Due to these complications, the field must be carefully mapped to accurately track muons. Both the barrel and the end-cap toroids have air cores. The ability of these magnets to create a strong field without a dense core material, e.g. iron, allows a reduction of the effects of multiple scattering on the muon spectrometer resolution.

In order to provide magnetic field for the forward part of the muon detector, and at the same time to allow access to the inner detector, the field in the forward region is created by separate end-cap toroids. The strength of their field varies between approximately 1 and 4.1 T. The coils of the end-cap toroids are offset by $\pi/8$ in ϕ with respect to those of the

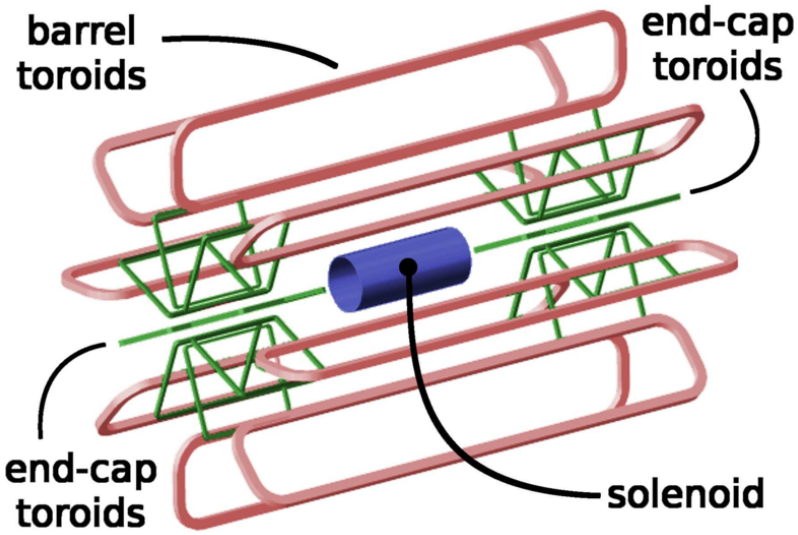

Figure 4.22: 3D view of the bare windings of the ATLAS magnet system [199].

Table 4.6: Main parameters of the ATLAS magnet system [198].

	Property	Central Solenoid	Barrel Toroid	End-Cap Toroid (one)
Overall dimensions:	Inner diameter, m	2.44	9.4	1.65
	Outer diameter, m	2.63	20.1	10.7
	Axial length, m	5.3	25.3	5
	Number of coils	1	8	8
Weight:	Conductor, t	3.8	118	20.5
	Cold mass, t	5.4	370	160
	Total assembly, t	5.7	830	239
Coils:	Number of turns per coil	1173	120	116
	Operating current, kA	7.6	20.5	20
	Stored energy, MJ	38	1080	206
	Central field [127], T	2.0	0.5	1.0
	Peak field, T	2.6	3.9	4.1
Conductors:	Overall size, mm^2	30×4.25	57×12	41×12
	Ratio Al : Cu : NbTi	15.6 : 0.9 : 1	28 : 1.3 : 1	19 : 1.3 : 1
	Number of strands in Rutherford cable	12	33	40
	Strand diameter, mm	1.22	1.3	1.3
	Critical current (at 5 T, 4.2 K), kA	20.4	47.5	55.5
	Total length, km	9.1	56	12.8
Cooling power:	at 4.5 K, W	100	990	329
	at 60-80 K, W	500	7400	1700

barrel toroids in order to provide radial overlap and to optimise the bending power in the transition region.

4.8 Trigger and data acquisition system

To make the data available for physics, calibration, and performance analyses, signals from the detector components have to be read out, digitized, consolidated, and written to tape storage, where they can be later accessed for offline processing. The trigger and data acquisition (TDAQ) system [200] serves as a bridge between the detector components and the permanent data storage.

The DAQ communicates directly with the front-end electronics located on the detector. It provides an interface for both controlling the detector (for example, turning its components on/off and setting their calibration parameters) and reading out the detected signals. Each sub-detector system has dedicated DAQ components, whose output data streams converge into a combined readout system.

The readout dataflow is curated by the trigger systems [201, 202]. Considering that the LHC bunch crossings occur at the rate of 40 MHz, and that every detector system has thousands of readout channels, the amount of data coming from the detector can neither all be saved or fully processed at the rate of collision events. As shown in Fig. 4.23, the upstream data rate at the level of DAQ is approximately 60 TB/s. The triggers make real-time decisions to discard uninteresting events in order to reduce the data rate and give time to slower downstream system that perform more thorough event processing and record the events to permanent storage. Efficiency of the triggers is carefully studied, as it has to be corrected for in data analyses and contributes to the measurements' uncertainty [204, 205].

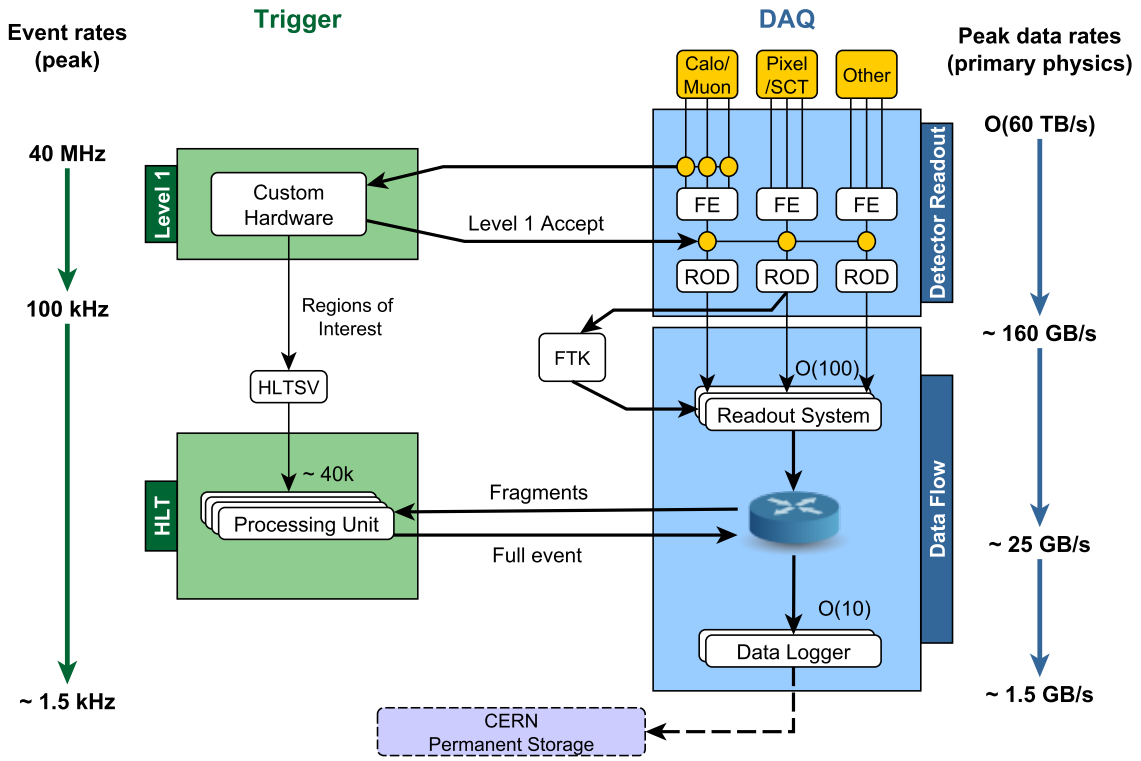

Figure 4.23: Schematic diagram of the ATLAS trigger and data acquisition (TDAQ) systems [203].

The ATLAS trigger system consists of two tiers: a hardware first-level (L1) trigger, and a software high-level trigger (HLT).

The L1 trigger [206] is implemented with fast custom-made electronics. The system consists of the L1 calorimeter triggers (L1Calo) [207], the L1 muon triggers (L1Muon) [208], the L1 topological trigger modules (L1Topo) [209, 210], and the Central Trigger Processors (CTP) [211]. The primary task of the L1 system is to find regions of interest (RoIs) using coarse calorimeter and muon information. A 2.5 µs latency is allowed for identification of RoIs, while the event that is being processed is stored in the temporary pipeline memory. Based on this information, the CTP makes the decision of whether to discard or accept the event. Accepted events are buffered in the Read-Out System (ROS) and sent to the HTL for further processing.

The HLT [212] reduces the L1 trigger output data rate from 100 kHz to about 1.5 kHz. At this level, the available event processing time is increased to about 200 ms. This allows the HLT to be implemented in software and to run much more complex algorithms than the L1 triggers. The LHT runs on 40 000 processor cores of a dedicated computer farm. In addition to the RoIs identified at L1, the HLT is able to utilize full-detector information, including finer-granularity calorimeter information, precision measurements from the MS, and tracking information from the ID. In order to optimize the processing, most HLT triggers follow a two-stage approach, with a fast first-pass reconstruction followed by a slower precision reconstruction of the remaining events. Events accepted by the HLT are transferred to the CERN computing center, and are stored in the RAW byte stream data format on magnetic tapes. Only about one in a million ATLAS events is saved for offline analyses.

Chapter 5

Event reconstruction

Before physics analyses can be performed on the collected ATLAS data, physics objects (photons, leptons, jets, and missing transverse momentum) have to be reconstructed from the signals recorded by the trigger and data acquisition (TDAQ) system. The methods and algorithms of object reconstruction are discussed in this chapter. The same reconstruction methods are applied to the output of the detector simulation to provide for comparability between data and MC.

As discussed in Chapter 4, the ATLAS detector consists of many radially layered detector systems, with different response to different types of particles. This is illustrated in Fig. 5.1. The principle of operation of most of these systems relies on detecting electric pulses produced by ionizing radiation. The ionization strips electrons from atoms of the active medium. The electrons than drift in the electric field created by high voltage, and are collected by conductors, resulting in electric pulses that propagate to the DAQ circuits, which amplify and record them. The TileCal relies on scintillation that produces light rather than electric charge, but the light signals are ultimately converted to electric ones by the PMTs.

The information obtained from the inner detector systems is used to reconstruct tracks of charged particles, with the Muon Spectrometer providing additional tracking measurements for muons. The particles' trajectories within the detector are bent by magnetic fields, so the curvature of their tracks provides accurate measurements of momentum. The tracking

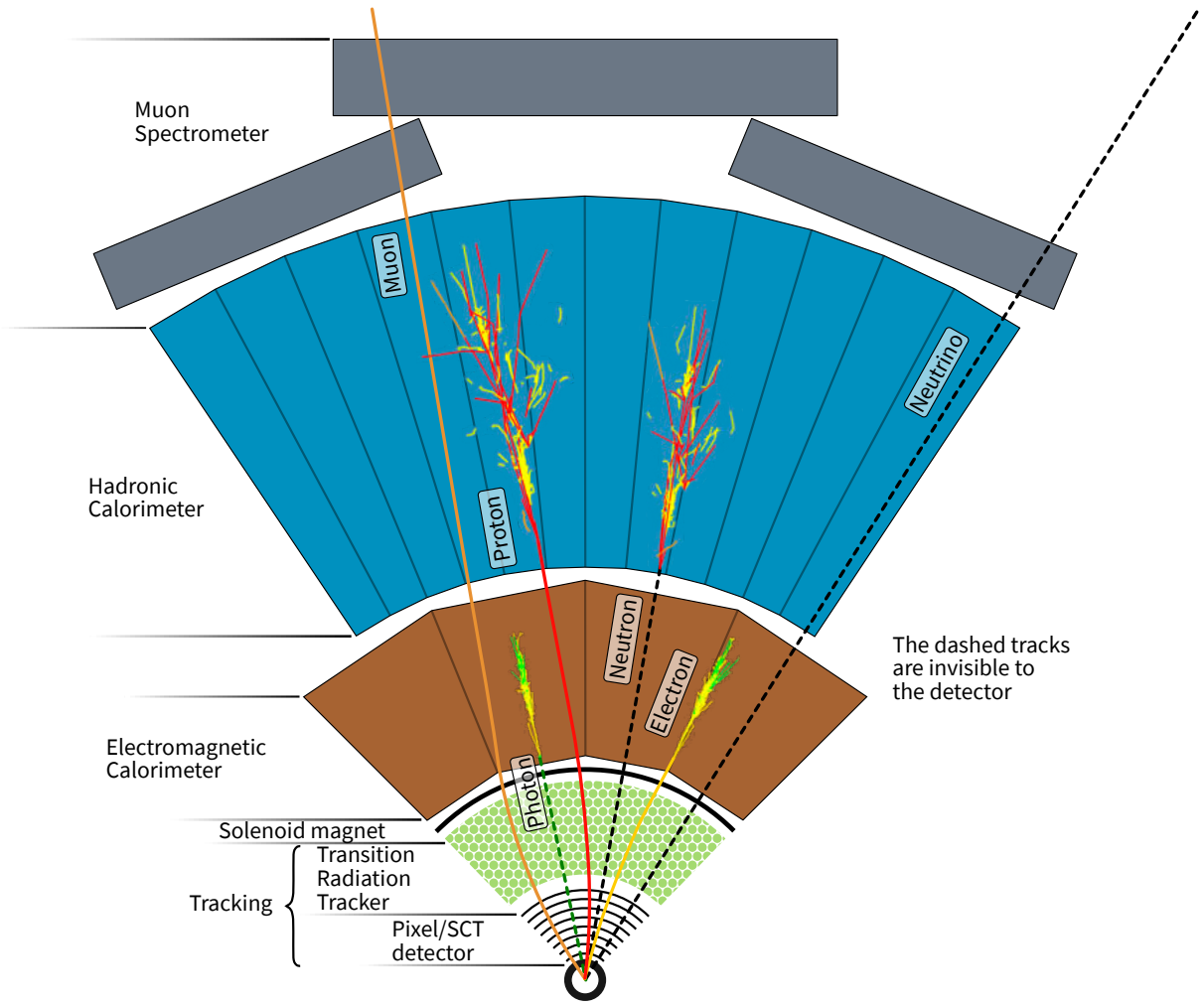

Figure 5.1: A schematic diagram showing interaction of different ATLAS detector systems with various types of collision products [213, 214]. The Inner Detector maps out tracks of charged particles; the Electromagnetic Calorimeter absorbs and measures the energy of photons and electrons; the Hadronic Calorimeter performs the same function for jets formed by e.g. protons or neutrons; and the Muon Spectrometer provides tracking information for muons. The relative layer sizes are not drawn to scale.

information is also used for coordination with the measurements from other detector systems, for example, in reconstructing jets with particle flow algorithms. Track reconstruction is also necessary for identification of primary and secondary interaction vertices, which are important for describing event topology and removing pileup.

The electromagnetic and hadronic calorimeters provide energy measurements and aid in reconstruction of the respective types of particles. Unlike the trackers, calorimeters are able to detect neutral particles, including photons and neutrons. However, ATLAS calorimeters cannot detect neutrinos, as those only interact weakly. The analyses that look for neutrinos, or other hypothetical neutral particles that would escape the detector, rely on calibration of missing transverse energy.

Algorithms and qualitative descriptions of reconstruction procedures are presented in this chapter. Details of object reconstruction methods and their performance relevant to the $H \to \gamma\gamma$ analysis can be found in [215].

5.1 Tracks and vertices

An essential part of the reconstruction of charged particles is reconstruction of their tracks. The tracks are assembled from hits, which are points at which particles have interacted within the active detector elements. The hit points, in their turn, are reconstructed directly from the recorded signals. The ATLAS inner detector can provide 3, 4, and 36 hits from the pixel, SCT, and TRT respectively.*

As discussed in Chapter 4, each detector system has a different structure and segmentation of the active elements, which determine their resolution. The inner detector silicon

*Fewer or more hits can be recorded if a track of a low momentum particle curls in the magnetic field, or strictly fewer if the track ends due to decay or complete absorption, or starts from a secondary vertex.

pixels are segmented in both ϕ and η dimensions, with r-layers providing 3-dimensional coordinates of hits. The SCT is made using longitudinally oriented silicon strips rather than pixels. Every SCT module contains two layers of the strip sensors, slightly rotated with respect to one another, so that the z coordinates of the SCT hits can be obtained from the intersection of the triggered strips. The TRT contains many more elements in the radial direction than either the ID or the SCT, but lacks resolution in the longitudinal (transverse) dimension in the barrel (end-cap), as it consists of parallel drift tubes.*

Tracks are reconstructed from hits using an iterative fitting method employing the Kalman filter algorithm [217, 218]. The procedure begins with the identification of "silicon spacepoints", which are centers of pixel clusters in the pixel detector. The spacepoints are combined into seeds of 2 or 3 hits using a seed-finding algorithm. Tracks are extrapolated from the seeds to the next layer of the inner detector and the Kalman filter algorithm is applied to determine which hits, if any, are suitable for incorporation into the tracks. Tracks to which a hit point was successfully added are then re-fitted and the procedure is repeated iteratively until all inner detector layers have been inspected. Track fitting is done with a χ^2 algorithm [219].

Track extrapolation is performed by applying electromagnetic transport functions, which require an accurate map of the magnetic field inside the detector [220, 221]. A perigee† parametrization of tracks is used for calculations. This parametrization is illustrated in Fig. 5.2 and consists of the following 5 parameters:

*In addition to positioning information, timing information from the TRT can also be used. While it is not typically used for vertex reconstruction, the measured time over threshold is correlated with the amount of ionization within the straws, and can be used to better distinguish between electrons and pions based on their expected dE/dx. Similar discriminators can be used to distinguish between other types of particles, such as protons, kaons, or hypothetical highly ionizing exotic particles. [216]

†In this context, the perigee is the point on the track that is the closest to the beam axis.

- q/p – charge-to-momentum ratio;
- ϕ_0 – the angle between the transverse momentum vector and the x axis in the x-y plane;
- θ_0 – the angle between the transverse momentum vector and the z axis in the r-z plane;
- z_0 – the longitudinal coordinate of the perigee;
- d_0 – the transverse coordinate of the perigee, given as a signed quantity, $d_0 = (\vec{x}_0 \times \hat{p}) \cdot \hat{z}$.

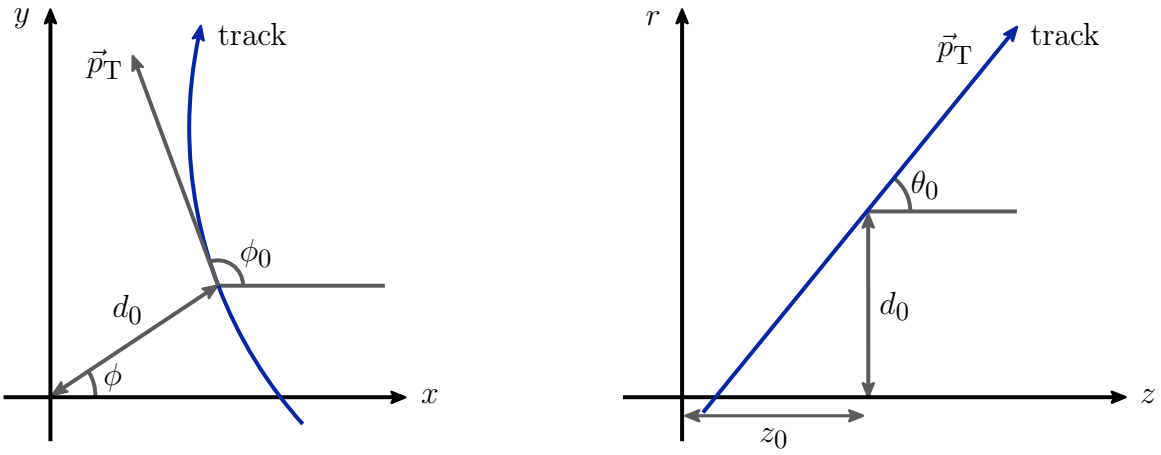

Figure 5.2: Perigee parametrization of a track trajectory.

Transport calculations take into account the quasi-helical motion of the charged particles within the inhomogeneous magnetic field, as well as interactions with detector material, including scattering and energy loss due to ionization, bremsstrahlung, Compton scattering, and hadronic interactions with atomic nuclei.

Many of the potential track candidates share hits, are incomplete, or are fake tracks, i.e. tracks where the majority of associated measurements do not originate from one single particle [218]. Ambiguities in track reconstruction are resolved by assigning a score to each track depending on the track fit χ^2, the number of hits, and the detector the hits originated from [222]. The high-precision pixel detector hits have a higher score than those from the SCT. Low-scoring track candidates are discarded. The ambiguities have to be resolved before the extension into the outer TRT can be done. An example of an ambiguity in track

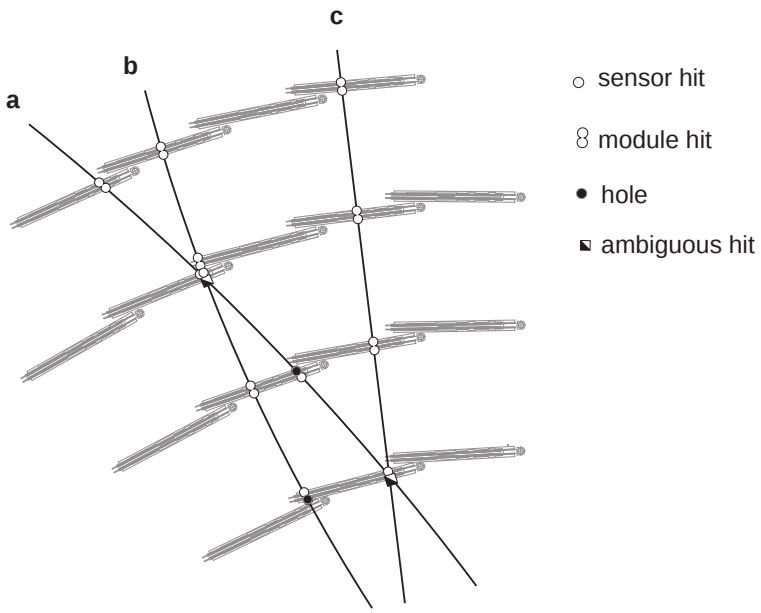

Figure 5.3: A simplified example of ambiguity inherent in track reconstruction [218]. Tracks in the SCT barrel (a, b, c) share several hits. The ambiguity is resolved by assigning a higher score to a track containing hits on both sides of the SCT strips.

reconstruction is shown in Fig. 5.3.

The procedure defined thus far is referred to as the "inside-out" strategy, as it follows the particles' natural trajectory direction, starting in the inner-most layers of the detector. However, not all tracks can be reconstructed in this manner. Tracks originating from secondary vertices may not contain a sufficient number of hits in the silicon detector to be properly seeded or to survive ambiguity resolution. The "outside-in" strategy remedies this by applying the procedure in the reverse direction, starting with hits in the TRT and propagating inwards. Hits already assigned to tracks by the "inside-out" strategy are not considered by the "outside-in" strategy.

After track reconstruction for the event has been completed, vertex finding algorithms [223] are used to assign tracks to their respective vertices. In addition to the primary hard-scatter vertex, event tracks can originate from secondary, or conversion, vertices from decays of intermediate states, or additional primary vertices present because of pileup. Ver-

tex reconstruction starts by forming vertex seeds out of bunches of tracks in close proximity located tracks. The algorithm proceeds iteratively, forming new seeds using tracks that were not compatible with the seeds in the previous iteration, and continues until every track is matched with at most one vertex. Reconstructed vertices are required have at least two associated tracks. The vertex with the highest value of $\sum p_{\mathrm{T}}^2$ is normally chosen as the primary one. However, for the $H \to \gamma\gamma$ analysis, the primary vertex is identified as the one compatible with the origin of the diphoton system. Matching of the photons to their primary vertex is done using dedicated neural network algorithms, which use the photon pointing information, and are trained on the $gg \to H \to \gamma\gamma$ MC event samples [215].

5.2 Photons and electrons

Both photons and electrons are reconstructed using measurements of energy deposited by them in the EM calorimeter cells. The main difference between the two types of particles is that, additionally, tracking information is available for electrons, which are distinguished by successfully matching calorimeter deposits to the inner detector tracks. A sketch of the detector components involved is show in Fig. 5.4.

Detection of a particle in the EM calorimeter is defined by the presence of a group, or cluster, of adjacent cells that have energy deposited by the EM shower, which developed as the particle propagated through the detector material. The showering process is mainly initiated by an absorber material of high atomic number, deliberately installed for this purpose. Two primary algorithms exist for reconstruction of the EM clusters: the sliding window algorithm and the dynamical topological algorithm. Historically, the fixed-sized sliding window algorithm was used, as the computational power necessary for calibration

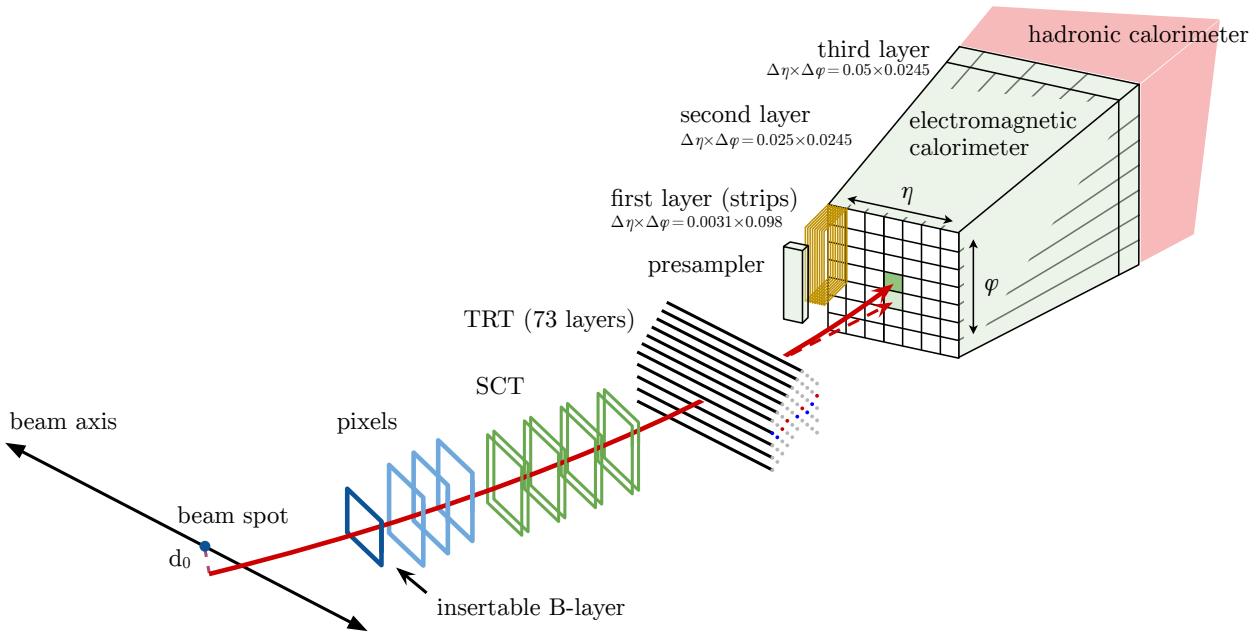

Figure 5.4: Sketch of the ATLAS detector systems used to perform electron reconstruction and identification. [224].

with a more sophisticated algorithm was not available. The dynamical topological algorithm was introduced on ATLAS in 2017 [225]. It relies on multivariate techniques. The energy of the calorimeter cells and clusters is calibrated using a multivariate algorithm [226] trained on a large sample of single-electron fully reconstructed MC events.

For the sliding window clustering algorithm [227], the calorimeter is divided in the η-ϕ plane into a grid of 200×256 elements known as towers, 0.025×0.025 in size. The towers are built by summing the energy from all the overlapping cells stacked in the normal, i.e. radial, direction. A scan is then performed of all 3×5 tower windows on the grid, selecting the ones with total energy above 2.5 GeV as seeds. Clusters are then built by merging cells within windows of 3×7 or 5×5, in the barrel or the end-cap, around the energy-weighted centers of the seeds.

The dynamical topological algorithm [225] forms clusters in a way that more closely resembles spatial signal-significance patterns produced by particle showers. The main ad-

vantage of the algorithm is its ability to recover low-energy deposits from bremsstrahlung photons and associate them to the electron clusters, forming so-called superclusters. Seeding and growth of topo-clusters is governed by the cell significance, $\varsigma_{\text{cell}}^{\text{EM}}$, defined as

$$\varsigma_{\text{cell}}^{\text{EM}} = \left| \frac{E_{\text{cell}}^{\text{EM}}}{\sigma_{\text{cell noise}}^{\text{EM}}} \right|. \tag{5.1}$$

where $E_{\text{cell}}^{\text{EM}}$ is the absolute cell energy at the EM scale and $\sigma_{\text{cell noise}}^{\text{EM}}$ is the expected cell noise. The algorithms proceeds as follows. First, proto-cluster seeds from calorimeter cells with $\varsigma_{\text{cell}}^{\text{EM}} \geq 4$ are selected. Then, all cells with $\varsigma_{\text{cell}}^{\text{EM}} \geq 2$ adjacent to a proto-cluster are added to it. Finally, all neighboring cells are added to the cluster regardless of their significance. Because of the threshold values, the clusters are often referred to as "4-2-0" topo-clusters.

5.2.1 Electrons

Electron candidate tracks are reconstructed using a procedure,* consisting of pattern recognition and track fitting, that allows energy loss from bremsstrahlung to be taken into account, thereby improving reconstruction accuracy. Initially, the particle is assumed to be a pion, and the energy loss is estimated accordingly. Using the pion hypothesis, track seeds are formed by the pattern recognition algorithm. The seeds consist of 3 hits in the silicon pixel detector and must have $p_{\text{T}} > 1\,\text{GeV}$. If a track candidate cannot be extended to a full track with at least 7 hits, including the TRT, the pattern recognition step is redone using the electron hypothesis instead, which allows for up to 30% energy loss at each material surface, to account for bremsstrahlung. The tracks are fitted using the ATLAS global χ^2 track fitter [219], assuming the particle hypothesis from the previous step. If the fitting fails

*The electron reconstruction procedure is based on the default one discussed in Section 5.1, but involves methods for accommodating energy loss due to bremsstrahlung.

using the pion hypothesis, it is redone assuming an electron, which involves an extra term to account for bremsstrahlung.

The reconstructed tracks are matched with the ECal clusters by extrapolating the tracks into the calorimeter. The distance between the track and the EM cluster must be within $\Delta\eta < 0.05$ and $\Delta\phi < 0.2$ (0.05) for a cluster that the track bends towards (away from). These criteria may be satisfied before or after rescaling of the track momentum to the cluster energy. In the second case, the $\Delta\phi$ threshold is reduced from 0.2 to 0.1, but the overall requirement is looser, and allows for matching in cases of significant energy loss before the calorimeter. The matched tracks are re-evaluated using the Gaussian Sum Filter (GSF) [228]. Multiple tracks may be associate with a single cluster. All tracks are kept after reconstruction; but the primary track is chosen based on proximity to the cluster energy-weighted center as well as on the track weight, determined by the number as detector location of the hits. The primary track is used to determine momentum, charge, and electron identification of the candidate.

5.2.2 Electron–photon identification

Based on the outcome of the matching of tracks with clusters, candidate particles are identified as one of the three types:

- **Electrons**, for well matched track-cluster pairs with tracks originating from vertices found in the beam interaction region.
- **Converted photons**, for clusters matched with tracks originating from secondary vertices.
- **Unconverted photons**, for clusters not matched with tracks.

Before these objects can be used in offline analyses, a set of further quality criteria is ap-

plied to select a pure sample of prompt* electrons and photons. The identification criteria require that the longitudinal and transverse shower profiles of the candidates are consistent with those expected for EM showers induced by such particles. Table 5.1 summarizes the discriminating variables, which reflect a number of shower shape parameters.

5.2.3 Photons

As photons are not electrically charged, and so are not themselves detectable by the tracking detector systems, they are mainly reconstructed from the 3D distributions of energy deposits they leave in the EM calorimeter. However, interactions with the inner detector material can lead the showering process to start before a photon enters the calorimeter. The identification criteria, described in Section 5.2.2, can still identify such objects as converted photons. In this case, the collimated electron tracks associated with the calorimeter cluster can be used to aid in reconstruction of the 4-momentum of the photon. The discriminating variables pertaining to photon identification are illustrated in Fig. 5.5. For example, the variables using the EM strip layer of ECal play an important role in rejecting π^0 decays into two collimated photons.

Three working points are chosen for the photon identification: loose, medium and tight. The loose working point is typically used for the single and diphoton triggers. It is defined using the R_{had}, $R_{\text{had}\,1}$, R_{η}, and $w_{\eta\,2}$ shower shape variables. The medium working point includes an additional cut on E_{ratio} and is used mainly for triggering in high pileup conditions. The tight selection is the primary photon working point used in offline analyses. It exploits the full granularity of the calorimeter, including the fine segmentation of the first

*Prompt photons and electrons are those coming from the hard scattering vertex rather than from a showering process.

Table 5.1: Discriminating variables used for electron and photon identification [229–231].

Category	Description	Name	Usage
Hadronic leakage	Ratio of E_{T} in the first sampling of the hadronic calorimeter to the E_{T} of the EM cluster (used over the ranges $\lvert\eta\rvert < 0.8$ and $\lvert\eta\rvert > 1.37$).	$R_{\mathrm{had\,1}}$	e, γ
	Ratio of the E_{T} in the hadronic calorimeter to E_{T} of the EM cluster (used over the range $0.8 < \lvert\eta\rvert < 1.37$).	R_{had}	e, γ
EM third layer	Ratio of the energy in the third layer to the total energy in the EM calorimeter.	f_3	e
EM middle layer	Ratio between the sum of the energies of the cells contained in a 3×7 η-ϕ rectangle (measured in cell units) and the sum of the cell energies in a 7×7 rectangle, both centered around the most energetic cell.	R_η	e, γ
	Lateral shower width, $\sqrt{(\sum E_i\eta_i^2)/(\sum E_i) - ((\sum E_i\eta_i)/(\sum E_i))^2}$, where E_i is the energy and η_i is the pseudorapidity of cell i and the sum is calculated within a window of 3×5 cells.	$w_{\eta\,2}$	e, γ
	Ratio between the sum of the energies of the cells contained in a 3×3 η-ϕ rectangle (measured in cell units) and the sum of the cell energies in a 3×7 rectangle, both centered around the most energetic cell.	R_ϕ	e, γ
EM strip layer	Lateral shower width, $\sqrt{(\sum E_i(i - i_{\max})^2)/(\sum E_i)}$, where i runs over all strips in a window of 3 strips around the highest-energy strip, with index $i_{\max}$.	$w_{s\,3}$	γ
	Total lateral shower width, $\sqrt{(\sum E_i(i - i_{\max})^2)/(\sum E_i)}$, where i runs over all strips in a window of $\Delta\eta \approx 0.0625$ and $i_{\max}$ the index of the highest-energy strip.	$w_{s\,\mathrm{tot}}$	e, γ
	Fraction of energy outside core of three central strips but within seven strips.	f_{side}	γ
	Difference between the energy of the strip associated with the second maximum in the strip layer and the energy reconstructed in the strip with the minimal value found between the first and second maxima.	ΔE_s	γ
	Ratio of the energy difference between the maximum energy deposit and the energy deposit in the second maximum in the cluster to the sum of these energies.	E_{ratio}	e, γ
	Ratio of the energy measured in the first sampling of the electromagnetic calorimeter to the total energy of the EM cluster.	f_1	e, γ
Track conditions	Number of hits in the innermost pixel layer.	$n_{\mathrm{innermost}}$	e
	Number of hits in the pixel detector.	n_{Pixel}	e
	Total number of hits in the pixel and SCT detectors.	n_{Si}	e
	Transverse impact parameter relative to the beam-line.	d_0	e
	Significance of transverse impact parameter defined as the ratio of d_0 to its uncertainty.	$\lvert d_0/\sigma(d_0)\rvert$	e
	Momentum lost by the track between the perigee and the last measurement point divided by the momentum at perigee.	$\Delta p/p$	e
	Likelihood probability based on transition radiation in the TRT.	`eProbabilityHT`	e
Track–cluster matching	$\Delta\eta$ between the cluster position in the first layer of the EM calorimeter and the extrapolated track.	$\Delta\eta_1$	e
	$\Delta\phi$ between the cluster position in the second layer of the EM calorimeter and the momentum-rescaled track, extrapolated from the perigee, times the charge q.	$\Delta\phi_{\mathrm{res}}$	e
	Ratio of the cluster energy to the track momentum.	E/p	e

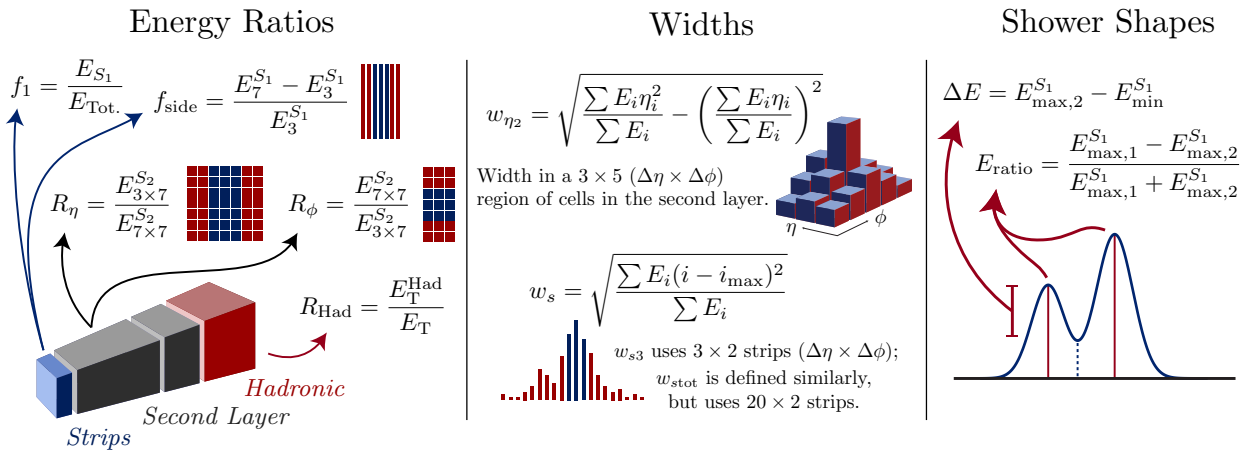

Figure 5.5: Illustration of the shower shape discriminating variables used for photon identification [229, 232].

sampling layer. The tight selection is optimized using a multivariate algorithm, and is performed separately for converted and unconverted photons (loose and medium identification are the same for converted and unconverted). The main differences in the shower shapes of converted and unconverted photons are due to the opening angle of the e^+e^- conversion pair, which is amplified by the magnetic field, and due to the additional interaction of the conversion pair with the material upstream of the calorimeter [231].

5.3 Hadronic jets

Due to color confinement exhibited by the strong interaction, as discussed in Section 2.4, final state quarks and gluons quickly hadronize, producing streams of color-neutral particles called jets. Due to the multiplicity of constituent particles, many of which are soft, it is generally not possible or important to identify them individually. Rather, a whole jet is typically reconstructed as a single object, although, in recent years, characterization of jet substructure has become an important tool for many physics analyses at the LHC [233–235].

Jets are reconstructed from energy deposits recorded in calorimeter cells. The cells are

grouped together based on how their properties compare to those of the neighboring cells. Most ATLAS analyses use topological clustering algorithms [227, 236], which rely only on calorimeter information. However, tracking information can be used to guide clustering the of calorimeter cells with the help of particle flow algorithms [237]. The cell clusters are further combined using jet clustering algorithms. Many such algorithms exist [238]; however the anti-k_t [239] algorithm is the de facto standard at the LHC. The $H \to \gamma\gamma$ analysis presented in this dissertation used jets reconstructed from topological clusters using the AntiKt algorithm with the radius parameter of 0.4 [215]. However, the final Run 2 iteration of the analysis will make use of a particle flow algorithm.

5.3.1 Topological clustering algorithm

Topological clusters, or topo-clusters for short, are groups of adjacent electromagnetic and hadronic calorimeter cells, merged based on the relative amount of signal-to-noise ratio of the cells and their neighbors. The algorithm is similar to that described for electron and photon reconstruction described in Section 5.2. The noise has contributions from the calorimeter electronics, measured with the beam off, and from pileup, estimated from MC simulations.

The first step of the algorithm is to identify seed cells by locating the cells with the signal-to-noise ratio above the threshold of t_{seed}. The default ATLAS value of the seed threshold is 4. The second step is to check whether the cells directly neighboring the seed cells have the ratio above a lower threshold of t_{neighbor} (ATLAS default is 2). The cells that do are then merged with the seeds to form clusters. Clusters sharing eligible neighbor cells are also merged. In the third step, the cells on the clusters' perimeter are merged into the clusters, if their ratio is greater than t_{cell}. The ATLAS default, however, is 0, so all perimeter cells

with any signal are merged. Technically, a final pruning step exists, in which clusters with the total deposited amount of energy below E_{cut} are dropped, though the default ATLAS value is $E_{\text{cut}} = 0$. Because of the default threshold values, this noise suppression algorithm is often referred to as the 4-2-0 scheme. This default scheme is used in the presented analysis.

Ideally, the clusters would be well isolated from each other. Because this is not always the case, cluster splitting is used to keep individual clusters from growing too large and including energy deposits from multiple jets. Local energy maxima are identified to split large clusters into smaller ones.

5.3.2 Particle flow algorithm

Unlike the traditional topological clustering method, the particle flow approach to reconstruction of hadronic jets allows a combination of tracker and calorimeter information. The key idea behind the algorithm is to reconstruct charged particles comprising jets using the tracker and to fall back on the calorimeter clusters for neutral particles. This requires careful single-particle matching between tracks and calorimeter deposits. The ability to accurately subtract all of a single particle's energy, without removing any energy deposited by any other particle, forms the key performance criterion upon which the algorithm is optimized [237].

The particle flow approach provides several advantages:

- The tracking detector resolution for transverse momentum is much better than the calorimeter energy resolution [240]. On the one hand, this implies improved resolution of momentum reconstruction. On the other hand, the detector acceptance can be extended for softer jets, as tracks are reconstructed for charged particles with a minimum transverse momentum of $p_{\text{T}} > 400\,\text{MeV}$, while the respective energy deposits often do not pass the noise thresholds required to seed topo-clusters [241].

- The angular resolution of a single charged particle, reconstructed using the tracker is much better than that using the calorimeter.
- Low-p_{T} charged particles originating within a jet are swept out of the jet's cone by the magnetic field by the time they reach the calorimeter. Using momenta reconstructed from tracks allows to correctly cluster the soft charged particles into the respective jet.
- Because tracks can be accurately associated with vertices, affects of in-time pileup can be mitigated by rejecting particles originating from the pileup vertices.

5.3.3 Generalized k_t algorithm

From the experimental perspective, the function of a jet clustering algorithm is to provide a reliable means of conversion between calorimeter information and the final state objects relevant to an interaction process of interest. Combining fragmentary calorimeter measurements reduces the dimensionality of the problem, as the final state can be described as composed of conceptually simple objects, i.e. jets, directly identifiable with outgoing partons in Feynman diagrams. The desired properties of the algorithm are, thus

- Robustness – similar arrangements of calorimeter clusters should be reconstructed as similar sets of jets;
- Stability – presence of additional jets must not strongly influence the results of reconstruction of individual jets;
- Computational efficiency – with millions of events in the LHC data, each containing multiple jets, their reconstruction must be computationally tractable.

From the theoretical point of view, a jet 4-momentum must be a safe observable with respect to soft (infrared) and collinear contributions. Otherwise, stable predictions cannot be made using perturbation theory. In fact, one of the primary purposes of a jet algorithm is

to provide a mapping between theoretical predictions and experimental observations in the face of soft and collinear divergences present in perturbative QCD.

Sequential recombination algorithms possess all of these required properties. The most widely used class of these algorithms goes under the name of a generalized k_t algorithm, of which k_t, anti-k_t, and Cambridge–Aachen are specific cases [239, 242–244]. The algorithm proceeds by iterating over the following steps:

1. Calculate the pairwise distance, d_{ij}, and the distance to the beam, $d_{i\mathrm{B}}$, for all jet candidates.
2. Find the smallest distance. If d_{ij} is the smallest, merge jet candidates i and j. If instead $d_{i\mathrm{B}}$ is the smallest, identify candidate i as a complete jet and remove it from consideration in subsequent iterations.
3. Repeat until all candidate are clustered into jets.

Here, the term jet candidate refers to any jet constituent at any step of iteration, which are summed as the algorithm proceeds. The term pseudo-jet is used by the popular FastJet library [245], which implements most jet clustering algorithms found in use. The input jet constituents may be 4-momenta of partons or hadrons in MC or calorimeter clusters in detector data. Computational techniques can be used to reduce the algorithm's complexity from $\mathcal{O}(N^3)$ to $\mathcal{O}(N^2)$ or $\mathcal{O}(N \log N)$ [246].

The distance measures d_{ij} and $d_{i\mathrm{B}}$ are defined as following:

$$d_{ij} = \min\left(k_{ti}^{2p}, k_{tj}^{2p}\right) \frac{R_{ij}^2}{R^2}, \tag{5.2}$$

$$d_{i\mathrm{B}} = k_{ti}^{2p}, \tag{5.3}$$

where k_{ti} is the transverse momentum of the i^{th} particle, p is the power constant that

depends on the scheme ($p = -1$ for anti-k_t, $p = 1$ for k_t, and $p = 0$ for Cambridge–Aachen), R is a constant parameter that determines the radius of a typical jet, and R_{ij} is the distance between the two particles given by

$$R_{ij}^2 = (y_i - y_j)^2 + (\phi_i - \phi_j)^2, \tag{5.4}$$

where y is the rapidity and ϕ is the azimuthal angle. Fig. 5.6 demonstrates characteristic shapes of jets reconstructed by commonly used algorithms. Note that the anti-k_t algorithm tends to produce the most cone-like jets.

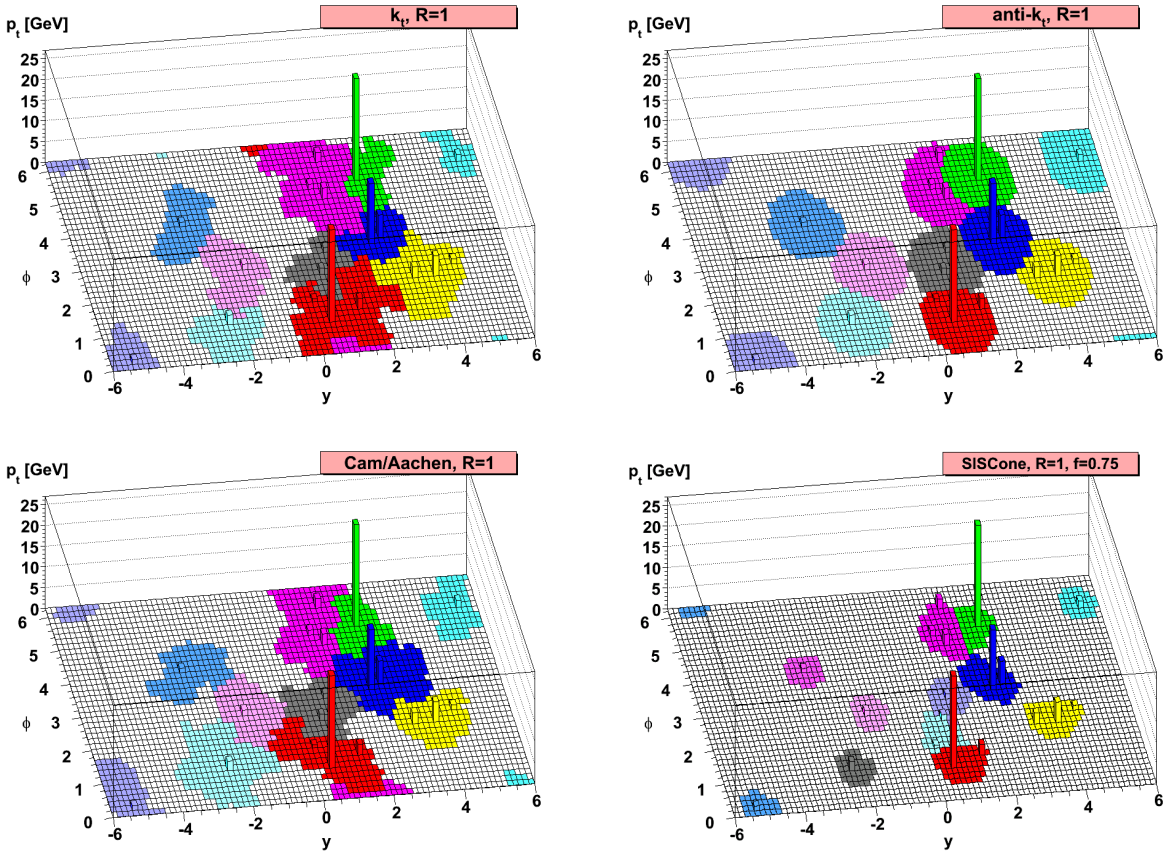

Figure 5.6: Comparison of jet shapes produced by commonly used clustering algorithms [239].

Most ATLAS analyses, as well as the one presented in this dissertation, use the anti-k_t

algorithm with $R = 0.4$, also referred to as AntiKt4. Analyses interested in jet substructure information often use a larger value of R to first identify large jets, followed by reclustering of subjets with a smaller R within the large jets.

5.3.4 Jet correction and calibration

ATLAS calorimeter systems are sampling, meaning that not all energy of jets and showers is deposited into the active medium and recorded. Consequently, in general, energy and position dependent corrections must be applied to the calorimeter measurements.

A local cluster weighting (LCW) is applied to the topo-clusters to correct for the non-compensating nature of the detector.* The LCW classifies clusters as electromagnetic or hadronic and applies the respective corrections. The weighting also takes into account energy loss due to non-instrumented regions of the calorimeters and noise suppression [247, 248]. The correction is determined using MC simulations of calorimeter response to charged and neutral pions.

The directions of the 4-vectors of the calorimeter clusters are corrected assuming that jets originate from the primary vertex. Only the trajectory origin is corrected, leaving the energy unchanged.

The p_{T} of the jets is corrected for pileup with an area-based subtraction method [247], according to the equation

$$p_{\mathrm{T}j}^{\mathrm{corr}} = p_{\mathrm{T}j}^{\mathrm{orig}} - \rho A_j - \alpha(N_{\mathrm{PV}} - 1) - \beta\langle\mu\rangle, \tag{5.5}$$

where $p_{\mathrm{T}}^{\mathrm{orig}}$ and $p_{\mathrm{T}}^{\mathrm{corr}}$ are transverse momenta of a jet before and after the correction, A is

*Compensating calorimeters have equal response to electromagnetic (electrons and photons) particles and hadrons.

the area of the jet in the η-ϕ plane, ρ is the average energy density of all jets in the event, dominated by soft pileup jets, N_{PV} is the number of primary vertices identified in the event, $\langle\mu\rangle$ is the average number of interactions per bunch crossing, and α and β are parameters determined from MC. A is determined using an active area algorithm, in which jets are reclustered after a uniform distribution of "ghost" particles with infinitesimal momentum is added to the event. The number of the "ghosts" clustered into a jet gives the measure of its area. The energy density for each jet is give by $\rho_j = p_{\mathrm{T}j}/A_j$, so $\rho = \mathrm{median}(\rho_j)$.

A jet energy scale (JES) correction is applied to jets. This is a correction factor on the jet energy derived from MC as the ratio of jet energy before and after reconstruction. The factor is obtained using an inclusive MC sample of isolated jets with the origin and pileup corrections applied. The JES correction is rapidity-dependent [249].

The calorimeter response is sensitive to the composition of particles and the energy distribution within jets, which depend on the initiating parton energy and type. Quark jets often include hadrons with high fraction of the total jet p_{T} that penetrate further into the calorimeter, while gluon jets typically contain many soft particles, leading to a lower calorimeter response and a wider transverse profile of jets. A global sequential calibration (GSC) is applied to account for these effects and improve the jet energy resolution (JER) [249, 250]. Five stages of corrections based on the following variables are applied.

1. The energy fraction deposited in the first layer of the tile calorimeter.
2. The energy fraction deposited in the third layer of the EM calorimeter.
3. The number of tracks with $p_{\mathrm{T}} > 1\,\mathrm{GeV}$ associated with the jet.
4. The p_{T}-weighted transverse width of the jet, measured using associated tracks with $p_{\mathrm{T}} > 1\,\mathrm{GeV}$.
5. The amount of jet activity measured in the muon spectrometer.

For each observable, an independent jet four-momentum correction is derived as a function of p_{T} and $|\eta|$ by inverting the jet reconstruction response matrix obtained from MC.

5.3.5 Jet Vertex Tagger

Heavy pileup conditions at the LHC provide a challenging environment for jet reconstruction. In one way, this problem is mitigated by using discriminating variables that allow to distinguish hard-scatter (HS) jets, originating from the primary interaction of interest, from pileup (PU) jets, which are reconstructed from particles originating from the extraneous interactions of the many protons comprising the colliding beams. As most PU jets are relatively soft, it is particularly important to have discriminating power for jets with $p_{\mathrm{T}} < 50\,\mathrm{GeV}$.

Previously, a variable called Jet Vertex Fraction (JVF) was used for this purpose [251]. The JVF discriminating variable is defined as

$$\mathrm{JVF} = \frac{\sum_t p_{\mathrm{T}}^t(\mathrm{PV}_0)}{\sum_t p_{\mathrm{T}}^t(\mathrm{PV}_0) + \sum_{n\geq 1}\sum_t p_{\mathrm{T}}^t(\mathrm{PV}_n)}, \tag{5.6}$$

where $p_{\mathrm{T}}^t(\mathrm{PV}_n)$ is the transverse momentum of the track t associated with the primary vertex PV_n, with the hard-scatter vertex labeled PV_0, and the sums are scalar.

The Jet Vertex Tagger (JVT) [252, 253] is a successor of the JVF. The JVT discriminant is constructed as a 2-dimensional likelihood in the space of the two variables, called corrJVF and $R_{p\mathrm{T}}$. corrJVF is a pileup corrected FJV variable,

$$\mathrm{corrJVF} = \frac{\sum_t p_{\mathrm{T}}^t(\mathrm{PV}_0)}{\sum_t p_{\mathrm{T}}^t(\mathrm{PV}_0) + \frac{\sum_{n\geq 1}\sum_t p_{\mathrm{T}}^t(\mathrm{PV}_n)}{k\, n_{\mathrm{trk}}^{\mathrm{PU}}}}. \tag{5.7}$$

The scalar sum of the p_{T} of the associated tracks originating from PU vertices, $p_{\mathrm{T}}^{\mathrm{PU}} = \sum_{n\geq 1}\sum_t p_{\mathrm{T}}^t(\mathrm{PV}_n)$, on average, tends to grow linearly with respect to the total number of pileup tracks per event, $n_{\mathrm{trk}}^{\mathrm{PU}}$. Thus, dividing $p_{\mathrm{T}}^{\mathrm{PU}}$ by $n_{\mathrm{trk}}^{\mathrm{PU}}$ corrects for this growth. $k = 0.01$ is an empirical factor introduced to make the shape of the corrJVF distributions for HS and PU jets similar to the respective JVF ones. $R_{p\mathrm{T}}$ is defined as the scalar sum of the transverse momentum of the tracks associated with the jet, that originate from the HS vertex, relative to the fully calibrated jet p_{T}, which includes a pileup subtraction,

$$R_{p\mathrm{T}} = \frac{\sum_t p_{\mathrm{T}}^t(\mathrm{PV}_0)}{p_{\mathrm{T}}^{\mathrm{jet}}}. \tag{5.8}$$

$R_{p\mathrm{T}}$ combines both calorimeter and tracking information. The distributions of the two variables are shown in Fig. 5.7.

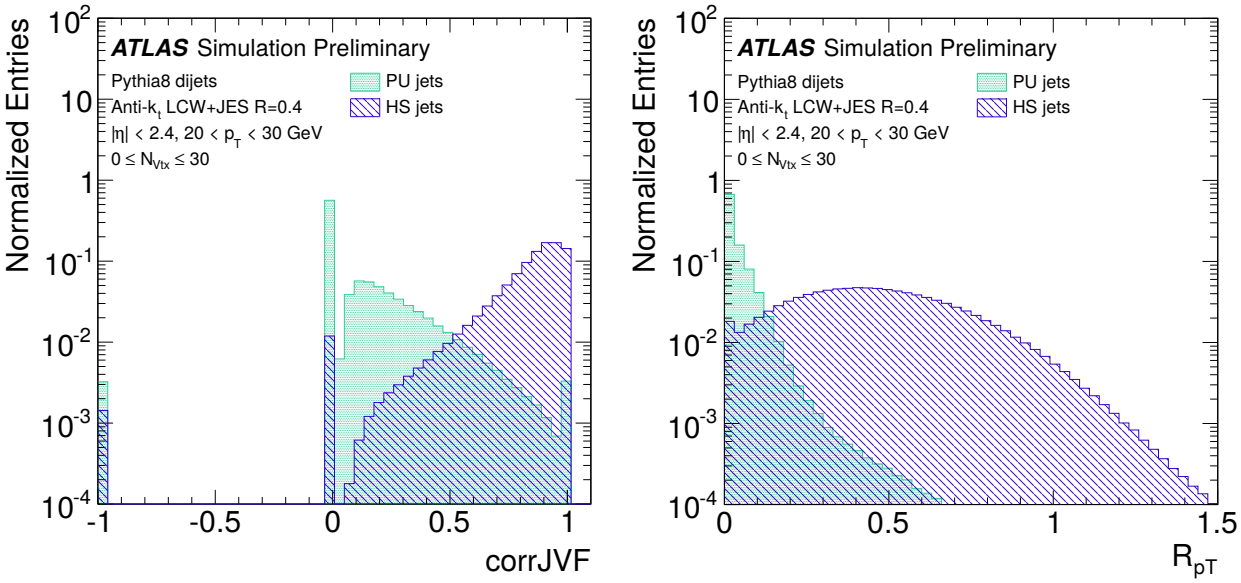

Figure 5.7: Distributions of corrJVF (left) and $R_{p\mathrm{T}}$ (right) for hard-scatter and pileup jets obtained from simulated dijet events [252, 253]. Jets with no associated tracks are assigned corrJVF $= -1$.

The JVT discriminant is obtained using a k-nearest neighbor (kNN) algorithm. For each

point in the two-dimensional corrJVF-$R_{p\mathrm{T}}$ plane, the probability for a jet at that point to be of the signal type is estimated by the ratio of the number of HS jets to the number of HS+PU jets, found in a local neighborhood around the point, using a training sample of both types of jets with $20 < p_{\mathrm{T}} < 50\,\mathrm{GeV}$ and $|\eta| < 2.4$. The JVT likelihood function and the distribution of its values are shown in Fig. 5.8.

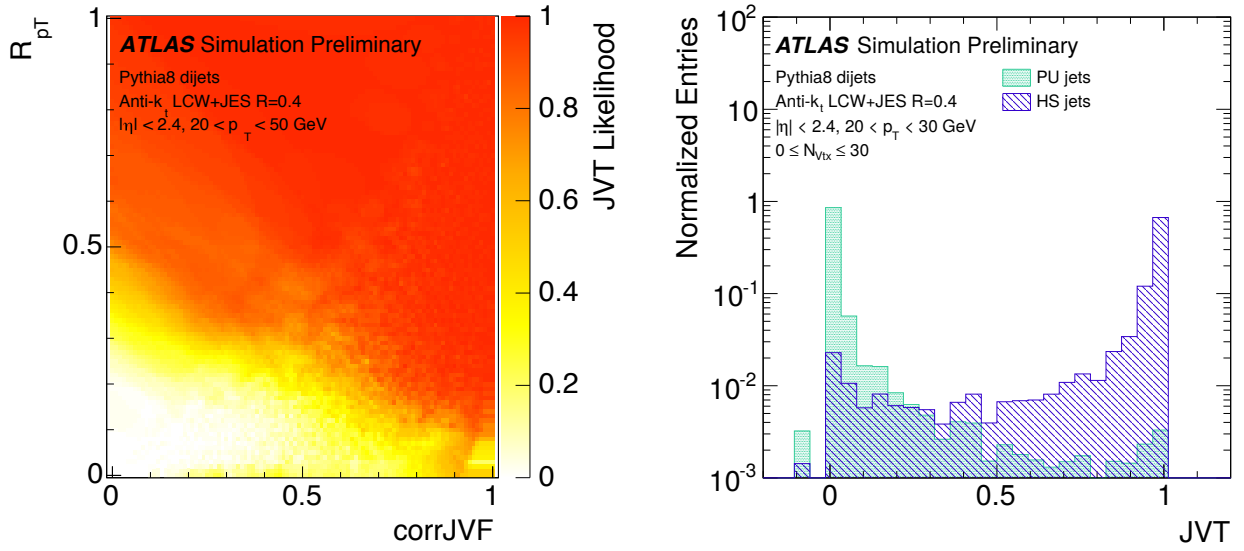

Figure 5.8: Left: JVT likelihood as a function of corrJVF and $R_{p\mathrm{T}}$. Right: Distribution of the JVT likelihood for low-p_{T} central pileup and hard-scatter jets. Both figures from [252].

Because of the limited forward coverage of the tracker, which extends only to $|\eta| < 2.4$, JVT selection can only be applied to central jets. To reduce contamination from PU jets in the forward region, a forward Jet Vertex Tagger (fJVT) was later introduced [254–256]. Using discriminants relying on calorimeter information where tracking is not available, fJVT extends pileup jet rejection range to $2.5 < |\eta| < 4.5$. Timing information and shape analysis are used to reduce the stochastic contribution from out-of-time pileup jets. Jet timing is given by the energy weighted average of the timing of the jet constituents. The principal discriminating feature of the out-of-time pileup jets is their lack of a denser energy core.

For QCD jets from in-time pileup, which are prevalent in the forward region, the two

characteristics mentioned above do not provide effective discriminating power. Instead, an fJVT discriminant is defined as follows,

$$\mathrm{fJVT} = \max(\mathrm{fJVT}_i), \quad \mathrm{fJVT}_i = \frac{\left\langle \mathbf{p}_{\mathrm{T}i}^{\mathrm{miss}} \right\rangle \cdot \mathbf{p}^{\mathrm{fj}}}{\left|\mathbf{p}^{\mathrm{fj}}\right|^2}, \tag{5.9}$$

where $\mathbf{p}^{\mathrm{fj}}$ is the transverse momentum of the forward jet, and $\left\langle \mathbf{p}_{\mathrm{T}i}^{\mathrm{miss}} \right\rangle$ is the average of the weighted vector sum of the transverse momenta of jets and tracks originating from a primary vertex PV_i,

$$\left\langle \mathbf{p}_{\mathrm{T}i}^{\mathrm{miss}} \right\rangle = -\frac{1}{2}\left(k \sum_{\substack{\text{tracks} \\ \in \mathrm{PV}_i}} \mathbf{p}_{\mathrm{T}}^{\mathrm{track}} + \sum_{\substack{\text{jets} \\ \in \mathrm{PV}_i}} \mathbf{p}_{\mathrm{T}}^{\mathrm{jet}} \right). \tag{5.10}$$

An empirical value of $k = 2.5$ is chosen to optimize the overall rejection of forward pileup jets. The fJVT_i values are computed for all combinations of primary vertices i (excluding the hard-scatter vertex) and forward jets, and the maximum value is taken as the discriminant. A forward jet is tagged as pileup if its fJVT value is above a threshold. The fJVT distribution tends to fall more steeply for HS than for QCD PU jets, as shown in Fig. 5.9.

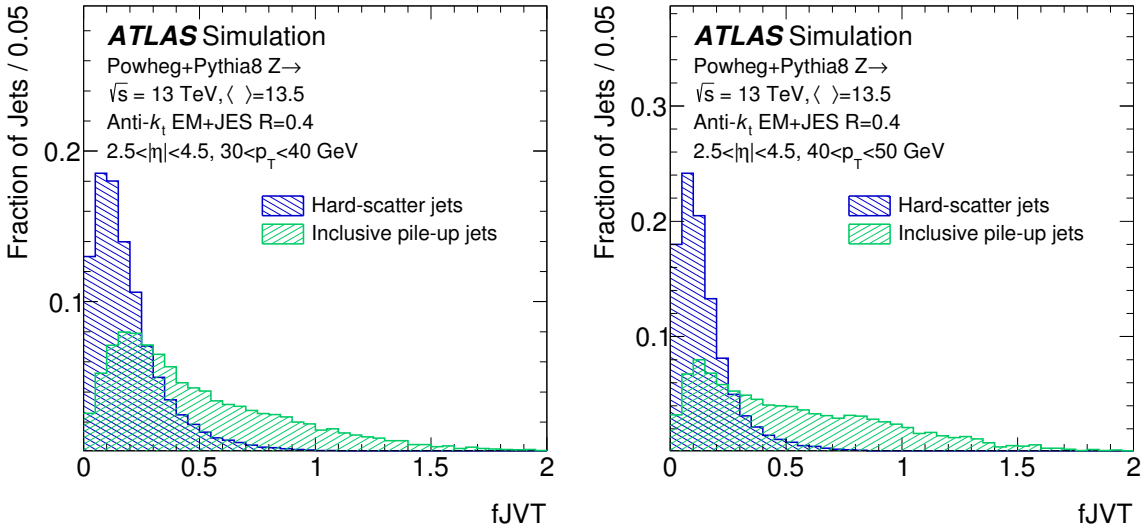

Figure 5.9: The fJVT distribution for hard-scatter (blue) and pileup (green) forward jets in simulated Z + jets events with at least one forward jet with $30 < p_{\mathrm{T}} < 40\,\mathrm{GeV}$ (left) or $40 < p_{\mathrm{T}} < 50\,\mathrm{GeV}$ (right) [254].

5.4 Muons

As discussed in Section 4.6, muons have a far greater penetration depth than any other charged particles. A muon's mass is 200 times larger than that of an electron. This drastically reduces the rate at which muons can lose energy via bremsstrahlung. At the same time, their mass is not large enough to allow hadronic decays, which are available for tau. Both electrons and taus are detected in the calorimeters, while muons require additional tracking outside the calorimeters. In fact, the majority of tracks outside the calorimeters belong to muons. To provide the additional measurements of muon tracks, ATLAS is equipped with the Muon Spectrometer (MS). The MS is used in combination with the inner detector (ID) to fully reconstruct muons, using tracking techniques similar to the ones already described for electrons and other charged articles [219].

Initially, muon tracks are reconstructed separately in the ID and MS. Reconstruction in the MS begins with searching for hit patterns inside each muon chamber to form track segments, which are then connected using different algorithms [257, 258]. MS tracks can be combined with the information from the ID or the calorimeters. Depending on how this is done, the final muon objects are grouped into four categories:

1. Stand-alone (SA) muons are reconstructed only in MS. Their trajectories are extrapolated to the interaction point, taking into account energy loss in the calorimeters. The ID only covers the region of $|\eta| < 2.5$, and SA muons can be used to extend forward acceptance to $|\eta| < 2.7$.
2. Combined (CB) muons are formed by successful combination of MS and ID tracks. These have the highest purity among the different categories.
3. Segment-tagged (ST) muons consist of an ID track identified as a muon and matched

with at least one segment in the precision chambers of the MS but not with a whole MS track.

4. Calorimeter tagged (CT) muons do not have MS track and are instead tagged using calorimeter energy deposits. CT muons have the lowest purity, but can be used to gain statistics in regions not covered by MS.

Muon candidates are required to pass identification and isolation criteria optimized using data from $Z \to \mu\mu$ and $J/\psi \to \mu\mu$ decays [257], similarly to electrons and photons.

5.5 Missing transverse momentum

The momentum fractions carried by interacting partons in any particular collision of hadrons cannot be measured or predicted. But because LHC proton beams are precisely aligned at the collision point inside the ATLAS detector, the initial state has no net transverse momentum, and only the net forward component of the initial momentum vector is unknown. The total transverse momentum of the measured final state, however, is not necessarily zero, because some momentum may be carried by undetected particles, or be absent or present as a result of a mismeasurement. Such undetected particles may be neutrinos, any particles falling outside of the fiducial volume of the detector, or hypothetical BSM particles, such as dark matter candidates. The amount of momentum required to balance the measured total transverse momentum vector is referred to as missing transverse energy and is denoted $E_{\mathrm{T}}^{\mathrm{miss}}$. It is defined as the sum of all calibrated photons, electrons, muons, jets, and also soft terms comprised of the remaining low energy tracks and calorimeter deposits [259]. Accurate measurements of $E_{\mathrm{T}}^{\mathrm{miss}}$ are difficult and require precise calibration. The estimated ATLAS resolution $E_{\mathrm{T}}^{\mathrm{miss}}$ in is to be between 5 and 30 GeV, depending on conditions such as the numbers of jets, neutrinos, and primary vertices [260, 261].

Chapter 6

$H \to \gamma\gamma$ cross section analysis

6.1 Introduction

This chapter describes the Higgs boson cross section measurements in the diphoton channel, conducted on the ATLAS detector in the Run 2 of the LHC. The analysis is a part of a larger program, aimed to extract as much of the information about the Higgs boson as possible from the events produced at the LHC, with parallel efforts conducted by ATLAS and CMS teams. The approach to the problem has naturally evolved over time, as more and more data has been collected. Following the discovery of the Higgs [1, 2], in the independently analyzed $H \to \gamma\gamma$ and $H \to 4\ell$ channels, the studies shifted focus to characterizing the Higgs properties. The first of these studies compared the ratios of the total Higgs production rate to the SM expectations, i.e. signal strength [262]. Subsequent studies differentiated between measurements of cross sections and coupling strengths, the latter using the so-called κ-framework [263]. In Run 1, these studies assumed SM Higgs production mechanisms and kinematics, and thus were not model independent.

With the analyses of the Run 1 data having strongly established the existence of the Higgs boson, and its behavior observed to be in good agreement with that predicted by the SM, the Run 2 analyses evolved their approach to reduce assumptions based on specific physics models. This is accomplished by using empirical signal and background models that

do not strongly rely on SM predictions for signal extraction (see Section 6.5).

Differential measurements of the Higgs properties were introduced towards the end of Run 1, when a sufficient amount of data was collected to subdivide the phase space. Systematic approaches were developed for defining the respective event categories. These are discussed in Section 6.4 for the presented cross section analysis. The couplings analyses refer to the simplified template cross section (STXS) framework [264] for definitions of their event categories.

The presented analysis also provides fiducial* cross section measurements. The fiducial, rather than total, cross section is measured in order to reduce dependence on the detector model, as well as on the theory predictions. The definition of the fiducial volume (see Section 6.3) is designed to match the phase space accessible by the detector as closely as possible to reduce the systematic uncertainty. The measured cross section is given by

$$\sigma_i = \frac{\nu_i^{\text{sig}}}{c_i \times L}, \tag{6.1}$$

where σ_i is the cross section for a given event category i, ν_i^{sig} is the number of extracted signal events, c_i is a correction factor, introduced to account for detector effects such as finite resolution and efficiency, as discussed in Section 6.6, and L is the integrated luminosity of the dataset.

The inclusive fiducial phase space region is further subdivided into finer event categories, described in Section 6.4. The primary goal of the analysis is to present the cross section of the $pp \to H \to \gamma\gamma$ process as a function of various variables that characterize the interaction kinematics. In other words, the analysis provides measurements of differential distributions

*Fiducial refers to the fact that the phase space of interest comprises only a part of the full phase space, excluding the phase space unobservable by the detector.

for a set of differential variables. A distribution for each variable is formed by histogramming events into contiguous bins, whose union spans the whole fiducial volume. Signal extraction from the diphoton invariant mass distribution, discussed in Section 6.5.3, is then performed for each bin.

The analysis strategy is summarized in Fig. 6.1. The details are discussed in the following sections of this chapter, but broadly the procedure can be summarized as following:

1. Events corresponding to the fiducial volume are selected from the ATLAS data.
2. Preliminary studies are performed to choose functional forms and parameters of the signal and background models.
3. Systematic uncertainties are assessed.
4. Events are grouped into categories and fits are performed to extract signal yields.
5. Signal yields are corrected for detector effects, i.e. unfolded, to obtain particle-level cross sections.

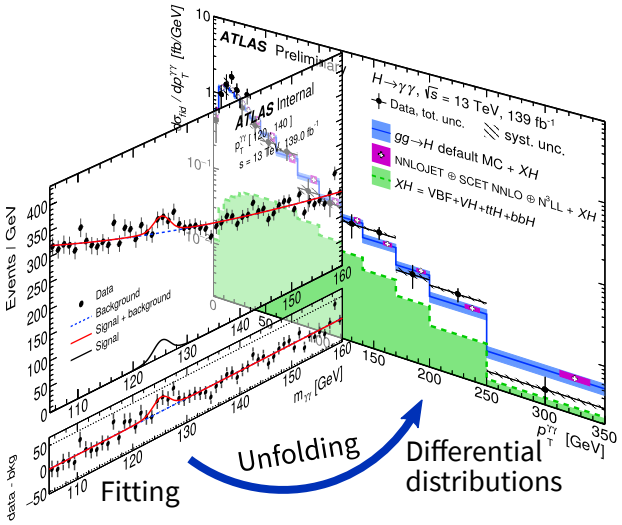

(a) Signal yield is extracted for every event category and bin of differential distributions by fitting signal+background model to the $m_{\gamma\gamma}$ spectrum. Detector level yields obtained from fitting are converted to particle level cross sections by unfolding.

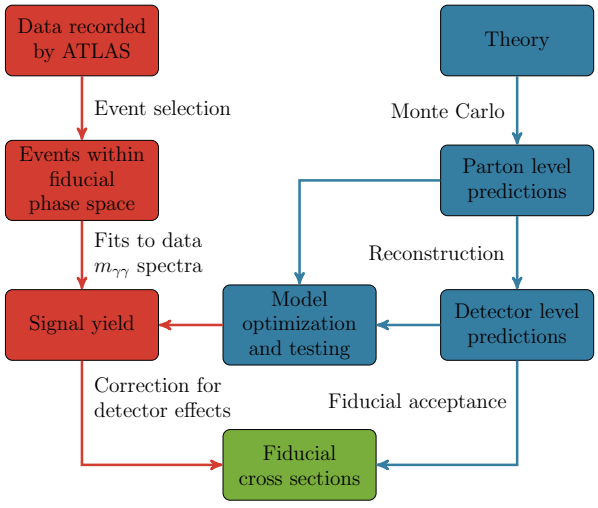

(b) Flowshart of the structure of the analysis.

Figure 6.1: Schematic summary of the analysis strategy.

Analysis is performed on the events with the diphoton invariant mass within the range of $105\,\text{GeV} < m_{\gamma\gamma} < 160\,\text{GeV}$. The $[121, 129]\,\text{GeV}$ region, 4 GeV on either side of the Higgs mass at 125 GeV, is designated as the signal region, and is blinded* until all preliminary studies are complete and signal extraction is ready to proceed. The two $(105, 121)\,\text{GeV}$ and $(129, 160)\,\text{GeV}$ regions are referred to as sidebands, and are used for binning optimization (Section 6.4.3) and background model F-tests (Section 6.5.2.2). Preliminary studies also include optimization of signal model shape parameters (Section 6.5.1), the choice of background functions (Section 6.5.2), spurious signal estimation (Section 6.5.2.1), as well as estimation of expected uncertainties (Section 6.7). These studies make use of generated MC samples, discussed in Section 3.6.

Several iterations of the analysis have been performed, incrementally incorporating the yearly datasets collected in Run 2. The published results and the respective sizes of the data subsets are listed in Table 6.1. More extended lists of ATLAS Higgs publications can be found in [265–267].

Table 6.1: Published Run 2 results of the ATLAS $H \to \gamma\gamma$ cross section analysis.

$\sqrt{s}$	Luminosity	Data set	Publications
13 TeV	$3.2\,\text{fb}^{-1}$	2015	ATLAS-CONF-2015-060 [268, 269]
13 TeV	$13.3\,\text{fb}^{-1}$	2015–2016	ATLAS-CONF-2016-067 [270, 271]
13 TeV	$36.1\,\text{fb}^{-1}$	2015–2016	ATLAS-CONF-2017-045, HIGG-2016-21 [272–274]
13 TeV	$79.8\,\text{fb}^{-1}$	2015–2017	ATLAS-CONF-2018-028 [275, 276]
13 TeV	$139.0\,\text{fb}^{-1}$	2015–2018	ATLAS-CONF-2019-029 [277, 278]

*Blinding is a measure typically taken in order to minimize bias. The problem is that, hypothetically, revealing all the details of collected data while analysis methodology is still being decided upon, can bias these choices and artificially inflate estimates of significance of the obtained results.

6.2 ATLAS dataset

The analysis results presented in this dissertation use the full Run 2 dataset with an integrated luminosity of 139 fb^{-1}. This number is slightly lower than the total LHC delivered luminosity of 156 fb^{-1} due to the efficiency of data taking, which is lowered by the trigger deadtime and the requirements for nominal performance of the detector subsystems. The data collection took place over 3 years, starting in 2015 and concluding in 2018. The dataset consists of proton-proton collision events with $\sqrt{s} = 13\,\text{TeV}$ and 25 ns bunch spacing. The amounts of data collected each year are listed in Table 6.2. The diphoton trigger efficiency for collection of the data relevant to the $H \to \gamma\gamma$ analysis is 98% [279].

Table 6.2: Yearly datasets making up the combined Run 2 ATLAS dataset. Estimates of luminosity and its uncertainty are taken from [280]. Numbers of events pertain to the inclusive fiducial region.

Year	Period	Luminosity	Luminosity uncertainty	Number of events
2015	D–J	3.2 fb^{-1}	2.1%	28 741
2016	A–L	32.9 fb^{-1}	2.2%	283 178
2017	B–K	44.3 fb^{-1}	2.4%	370 086
2018	B–Q	58.5 fb^{-1}	2.0%	496 082
Total		139.0 fb^{-1}	1.7%	1 178 087

Luminosity estimates at the LHC are based on measurements of several luminosity sensitive detectors. The primary luminosity detector is the LUCID-2 Cherenkov detector [281]. Its measurements are complemented by the ATLAS Beam Conditions Monitor (BCM) diamond detectors [282], and by offline measurements of the multiplicity of reconstructed charged particles, i.e. track counting, in randomly selected bunch crossings. The absolute calibration is determined using van der Meer [283] scans, performed under specially tailored low luminosity conditions. A calibration transfer procedure is used to extrapolate from the

low luminosity to the high luminosity regime, at which the data are taken [280]. During Run 2, the dedicated van der Meer runs were performed once a year. The methodology used to obtain the estimates of luminosity and its uncertainty, listed in Table 6.2, is discussed in [284]. Estimates of luminosity for the same dataset differ slightly from one round of the $H \to \gamma\gamma$ analysis to another due to continuing improvements in the assessment of the LHC luminosity and subsequent recalibrations.

6.3 Event and object selection

This section describes selection criteria for objects and events used in this analysis. The details of the selection criteria have slightly evolved between the analysis rounds. The respective publications, listed in Table 6.1, provide all the details. The criteria listed below correspond to the most recent analysis [277, 278]. Details of the reconstruction are discussed in Chapter 5.

6.3.1 Event preselection

Data and reconstructed MC events are first filtered through several general preselection criteria, to ensure data quality, before object-specific cuts, required for the analysis, are applied. The preselection criteria are listed below. The cutflow for the yearly datasets in shown in Table 6.3.

- Triggers (data only):
  - `HLT_g35_loose_g25_loose` (2015, 2016 data);
  - `HLT_g35_medium_g25_medium_L12EM20VH` (2017, 2018 data).

  These diphoton triggers require at least two reconstructed photons with E_{T} greater

than 35 (25) GeV for the leading* (subleading) photon. Loose photon identification requirements† were applied by this trigger in 2015–2016 and were tightened in 2017 to cope with a higher instantaneous luminosity. On average, the trigger has an efficiency greater than 98% for $H \to \gamma\gamma$ events that pass the diphoton event selection described in Section 6.3.2.

- Good Run List (data only):

  Events must belong to the luminosity blocks specified in the following run lists [286]. This requirement ensures that all the sub-detectors relevant for this analysis were fully operational.

  `data15_13TeV.periodAllYear_DetStatus-v89-pro21-02_Unknown`
  `_PHYS_StandardGRL_All_Good_25ns.xml`
  `data16_13TeV.periodAllYear_DetStatus-v89-pro21-01_DQDefects-00-02-04`
  `_PHYS_StandardGRL_All_Good_25ns.xml`
  `data17_13TeV.periodAllYear_DetStatus-v99-pro22-01_Unknown`
  `_PHYS_StandardGRL_All_Good_25ns_Triggerno17e33prim.xml`
  `data18_13TeV.periodAllYear_DetStatus-v102-pro22-04_Unknown`
  `_PHYS_StandardGRL_All_Good_25ns_Triggerno17e33prim.xml`

- Event Quality (data and MC):

  Standard ATLAS event cleaning based on the detector quality flags is applied. Events with data integrity errors in the calorimeters and incomplete events missing some detector information are rejected.

*Leading and subleading regarding photons and jets refers to p_{T} ordering. The leading photon or jet is the one with the highest p_{T} of all the objects of the same type in that event.

†See Table 1 in [285] for the definition of loose and tight photon identification requirements.

Table 6.3: Cutflow of event selection for the yearly datasets of ATLAS Run 2 data.

	2015			2016			2017			2018		
	Data yield	Total efficiency	Relative efficiency	Data yield	Total efficiency	Relative efficiency	Data yield	Total efficiency	Relative efficiency	Data yield	Total efficiency	Relative efficiency
N xAOD	1215682304	100.000%	100.000%	5130958848	100.000%	100.000%	5208373760	100.000%	100.000%	5607043072	100.000%	100.000%
N DxAOD	12737493	1.048%	1.048%	127609472	2.487%	2.487%	100062128	1.921%	1.921%	124560320	2.221%	2.221%
All events	12737493	1.048%	100.000%	127609472	2.487%	100.000%	100062128	1.921%	100.000%	124560320	2.221%	100.000%
No duplicates	12737493	1.048%	100.000%	127609440	2.487%	100.000%	100062024	1.921%	100.000%	124560320	2.221%	100.000%
GRL	12446557	1.024%	97.716%	124681352	2.430%	97.705%	97186944	1.866%	97.127%	123107840	2.196%	98.834%
Pass trigger	12194370	1.003%	97.974%	122364592	2.385%	98.142%	74383248	1.428%	76.536%	95320480	1.700%	77.428%
Detector DQ	12193188	1.003%	99.990%	122361008	2.385%	99.997%	74372296	1.428%	99.985%	95315520	1.700%	99.995%
Has PV	12193167	1.003%	100.000%	122361008	2.385%	100.000%	74372296	1.428%	100.000%	95315520	1.700%	100.000%
2 loose photons	3544155	0.292%	29.067%	36092436	0.703%	29.497%	20395000	0.392%	27.423%	26469698	0.472%	27.771%
e-γ ambiguity	3544155	0.292%	100.000%	36007060	0.702%	99.763%	20395000	0.392%	100.000%	26469698	0.472%	100.000%
Trigger match	2596133	0.214%	73.251%	26987322	0.526%	74.950%	11922093	0.229%	58.456%	16801656	0.300%	63.475%
Tight ID	373580	0.031%	14.390%	3668591	0.071%	13.594%	4589030	0.088%	38.492%	6371417	0.114%	37.921%
Isolation	150746	0.012%	40.352%	1461031	0.028%	39.825%	1845128	0.035%	40.207%	2477112	0.044%	38.879%
Relative p_{T} cuts	131166	0.011%	87.011%	1270619	0.025%	86.967%	1603480	0.031%	86.903%	2153889	0.038%	86.952%
$m_{\gamma\gamma} \in [105, 160]\,\mathrm{GeV}$	28741	0.002%	21.912%	283178	0.006%	22.287%	370086	0.007%	23.080%	496082	0.009%	23.032%

- Primary vertex (data and MC):

  At least one primary vertex is required to be reconstructed in the event. Only default reconstruction requirements are applied to this vertex, including consistency with the beam spot coordinate.

6.3.2 Photons

Fiducial cuts (object level):

- $p_{\mathrm{T}} > 25\,\mathrm{GeV}$;
- $|\eta| < 2.37$ excluding the crack region $1.37 < |\eta| < 1.52$.

Fiducial cuts (event level):

- $p_{\mathrm{T}}/m_{\gamma\gamma} > 0.35\,(0.25)$ for leading (subleading) photon;
- $m_{\gamma\gamma} \in [105, 160]\,\mathrm{GeV}$.

Events are required to have at least two photons passing the kinematic cuts. The two selected photons with the highest p_{T} are assumed to be coming from the Higgs decay and are used to redefine the primary vertex of the event using a neural network, which uses pointing information from the electromagnetic calorimeter [287]. The four-momenta of the two photons are corrected, so that they point to the diphoton primary vertex. The diphoton invariant mass is calculated using Eq. (6.2),

$$m_{\gamma\gamma} = \sqrt{2E_1E_2(1-\cos\theta)}. \tag{6.2}$$

Data and reco: Photons are required to pass cuts on the shape of the electromagnetic showers. At this stage of selection, the photons are referred to as loose [288]. Photons are calibrated using the latest Run 2 calibration corrections for the energy scale and resolution,

detailed in [289]. The photon identification cuts are performed using the latest Egamma* recommendations using an E_{T}-dependent identification detailed in [229]. A photon ambiguity requirement was implemented in Run 2 as a consequence of the increased electron-photon fake rate [215]. The rate was found to exceed 30% in the end-cap prior to introduction of the ambiguity requirement, which uses tracking information from the innermost pixel layers and IBL to separate electrons from converted photons.

The Higgs boson candidate photons must satisfy tight† shower shape requirements, as well as isolation criteria for tracks, `ptcone20` $< 0.05\,p_{\mathrm{T}}$, and calorimeter, `topoetcone20` $< 0.065\,p_{\mathrm{T}}$, using a cone of $\Delta R = 0.2$. Track isolation is always calculated from the selected primary vertex. The photon isolation efficiency is measured in data and MC using two independent methods: Single Photon and Radiative-Z. The methods are detailed in [290].

Particle level (MC): Photons are identified by requiring `PdgId = 22`, and must not be produced during hadronisation.

6.3.3 Jets

Fiducial cuts (object level):

- $p_{\mathrm{T}} > 30\,\mathrm{GeV}$, $p_{\mathrm{T}} > 25\,\mathrm{GeV}$ for VBF,
- $|\eta| < 4.4$.

Jets are rejected if they lie within $\Delta R < 0.4$ of a selected photon or $\Delta R < 0.2$ of a selected electron. Muons and neutrinos are not included in the clustering at particle level, because they do not leave significant energy deposits in the calorimeters and so do not enter the reconstruction level jet finding algorithm.

*Egamma refers to the electron and photon reconstruction working group.

†See Table 1 in [285] for the definition of loose and tight photon identification requirements.

Data and reco: A jet vertex tag (JVT) [252] cut is applied to reduce contamination from jets not originating from the selected primary vertex, i.e pileup jets. Jets with $p_{\mathrm{T}} < 120\,\mathrm{GeV}$ and $|\eta| < 2.5$ are required to pass the medium, JVT > 0.59, cut. A forward jet vertex tag (fJVT) [254–256] is used for jets with $p_{\mathrm{T}} < 60\,\mathrm{GeV}$ and $2.5 < |\eta| < 4.4$. This region is beyond the acceptance of the tracker. Therefore the fJVT algorithm uses timing and jet shape information in the calorimeter to reject pileup jets in the forward region. Qualifying jets are required to pass the medium fJVT cut.

Jets potentially originating from the decay of a b-hadron are identified with the help of a multivariate discriminant, which uses track impact parameters and secondary vertices information [291, 292]. The efficiency of the b-tagger is 70%, which is estimated using a $t\bar{t}$ control region. Data-driven correction factors are applied to the simulation such that the b-tagging efficiencies of jets originating from b quarks, c quarks, and the light quarks are consistent with the ones observed in the data [272].

Particle level (MC): Jets are considered to originate from a b-hadron, if there is one with $p_{\mathrm{T}} > 5\,\mathrm{GeV}$ within a cone of $\Delta R < 0.4$ around the jet.

6.3.4 Leptons

Fiducial cuts (object level):

- Electrons: $|\eta| < 2.47$ excluding the crack region $1.37 < |\eta| < 1.52$,
- Muons: $|\eta| < 2.7$.

Particle level (MC): Identified by requiring $|\texttt{PdgId}| \in \{\texttt{11}, \texttt{13}\}$.

6.3.5 Missing transverse energy

Particle level (MC): $E_{\mathrm{T}}^{\mathrm{miss}}$ is calculated as the 2D vector p_{T} sum of all neutrinos produced not during hadronization. Neutrinos are identified by requiring $|\texttt{PdgId}| \in \{12, 14, 16\}$.

6.4 Event categories and differential variables

The fiducial event category is the most inclusive one, as it contains all the diphoton events that pass the selection criteria described in Section 6.3, regardless of presence or absence of any other objects in the final state. Other event categories defined for the analysis consist of more exclusive fiducial regions, with discrete requirements for event topology or the presence of specific objects, and bins of the differential distributions.

6.4.1 Fiducial categories

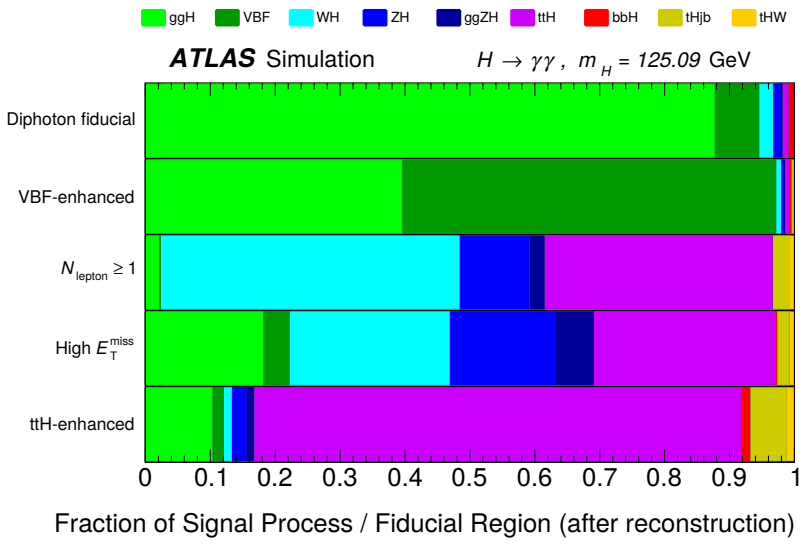

Figure 6.2: Expected composition of fiducial regions in terms of Higgs production modes.

6.4.1.1 VBF

A region enriched with vector boson fusion events is defined by requiring events to have at least two jets with a lowered transverse momentum cut of $p_{\mathrm{T}} > 25\,\mathrm{GeV}$. The two jets must have a wide separation in rapidity, $|\Delta y_{jj}| > 2.8$, and a dijet mass, $m_{jj} > 400\,\mathrm{GeV}$. The dijet system must be back-to-back to the diphoton, with azimuthal angle separation, $|\Delta\phi_{\gamma\gamma,jj}| > 2.6$. These criteria enhance the VBF fraction to 58% while reducing ggF to 39%. For comparison, the inclusive region composition is 88% ggF and only 7% VBF.

6.4.1.2 Lepton category

This category is defined by requiring at least one electron or muon,* $N_{\mathrm{lep}} \geq 1$. The presence of leptons selects the associated production modes. The composition of this region is 46% WH, 13% ZH, and 35% ttH.

6.4.1.3 Missing transverse energy

Large $E_{\mathrm{T}}^{\mathrm{miss}}$ is a potential signature for Higgs production in association with dark matter. The region is defined by $E_{\mathrm{T}}^{\mathrm{miss}} > 80\,\mathrm{GeV}$ and $p_{\mathrm{T}}^{\gamma\gamma} > 80\,\mathrm{GeV}$. SM events are expected to populate this region due to decays to neutrinos, as well as due to the effects of reconstruction efficiency and migration.

6.4.1.4 ttH

This region has an enhanced contribution from associated production with a top quark-antiquark pair, $t\bar{t}H$. The selection criteria require at least either three jets and one electron

*The definition of N_{lep} does not account for τ leptons, because they are difficult to reliably identify in the detector.

or muon, or four jets. At least one jet must be b-tagged in either case. The expected composition of the region is 75% $t\bar{t}H$ and 10% ggF.

6.4.2 Differential variables

Measurements of the Higgs boson production cross sections as functions of characteristic observables provide essential information for testing the fundamental properties of the Higgs field and our understanding of perturbative QCD. The variables studied can be broadly grouped into the following categories:

6.4.2.1 Higgs boson kinematics

Transverse momentum and rapidity describe the fundamental kinematics of the Higgs boson. Inclusive Higgs boson production is dominated by gluon fusion, with the Higgs boson transverse momentum predominantly balanced by soft gluons. The diphoton transverse momentum, $p_{\mathrm{T}}^{\gamma\gamma}$, is sensitive to the effective coupling of the Higgs to gluons in the ggF process, as well as to the Yukawa coupling to quarks. This provides the ability to test perturbative QCD modeling of ggF.

The low-p_{T} region of the $p_{\mathrm{T}}^{\gamma\gamma}$ distribution exhibits a Sudakov peak due to initial state radiation [293]. Therefore, this region is very sensitive to resummation effects. In addition, the low-p_{T} region can be used to set bounds on light quark Yukawa couplings [294, 295].

The high tail of the $p_{\mathrm{T}}^{\gamma\gamma}$ distribution is sensitive to the heaviest (top) quark mass.* Because boosted Higgs kinematics is sensitive to the masses of fermions participating in the production loop (Fig. 6.3), the high-p_{T} region may have a sensitivity to BSM particles. Also, the relative contribution of the non-resonant diphoton production decreases for larger $p_{\mathrm{T}}^{\gamma\gamma}$,

*See Appendix B for further discussion.

meaning that the high $p_{\mathrm{T}}^{\gamma\gamma}$ region of the phase space can provide a much purer sample of Higgs boson production events. The signal-to-background ratio reaches 1 around $p_{\mathrm{T}}^{\gamma\gamma} \approx 600\,\mathrm{GeV}$ and continues to improve at higher $p_{\mathrm{T}}^{\gamma\gamma}$. This is illustrated in Fig. B.2 in Appendix B.

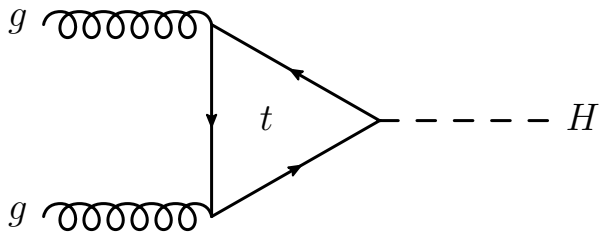

Figure 6.3: The largest contribution to the Higgs boson production at the LHC is from the gluon-gluon fusion process. At LO, the Higgs boson has an effective coupling to gluons via the loop diagram shown here. The effective coupling is sensitive to the mass of the fermion in the loop. As $\Gamma(H \to f\bar{f}) \propto m_f^2$, the partial width for $H \to t\bar{t}$ accounts for 99% of the combined width to all fermions.

The transverse momentum, $p_{\mathrm{T}}^{\gamma\gamma j}$, and mass, $m_{\gamma\gamma j}$, of the Higgs + the leading jet system complement the sensitivity to finite top quark mass and potential heavy BSM particles in high-$p_{\mathrm{T}}^{\gamma\gamma}$ region.

The rapidity, $\left|y_{\gamma\gamma}\right|$, distribution is sensitive to parton distribution functions and the modeling of gluon fusion, and can be used to probe the light quark Yukawa couplings [295]. The rapidity separation between the two photons, $\left|\Delta y_{\gamma\gamma}\right|$, is sensitive to the decay of the Higgs boson.

6.4.2.2 Jet activity

The multiplicity distribution for jets accompanying a Higgs boson allows a discrimination of different Higgs boson production mechanisms. The low multiplicity ($N_{\mathrm{jets}} = 0$ and 1) bins are dominated by gluon fusion. Medium multiplicity bins have increased contribution from VH (for $N_{\mathrm{jets}} \geq 1$) and from VBF (for $N_{\mathrm{jets}} \geq 2$). Associated production with top quarks, $t\bar{t}H$, is important for higher multiplicity bins (with $N_{\mathrm{jets}} \geq 3$). In addition, the jet

multiplicity is sensitive to QCD radiation, with real corrections producing additional jets. Both inclusive and exclusive jet multiplicities are measured, as well as multiplicities with different jet p_{T} thresholds, $N_{\mathrm{jets}}^{\geq 30\,\mathrm{GeV}}$ and $N_{\mathrm{jets}}^{\geq 50\,\mathrm{GeV}}$. The higher threshold p_{T}^{j} requirement changes the relative contributions of the different production processes. A requirement that jets have a threshold transverse momentum of 50 GeV or more enhances contributions from the Higgs boson production processes other than ggF, and reduces contamination due to pileup jets, but at the expense of a reduced number of selected events.

The distributions of transverse momentum and rapidity of the leading jets, and the H_{T}* probe the theoretical modeling of hard quark and gluon radiation. The invariant mass of the two leading jets, m_{jj}, is a useful discriminant for the VBF production.

6.4.2.3 Spin, charge conjugation, and parity

The polar angle, $\left|\cos\theta^{*}\right|$, between either of the two photons from the Higgs boson decay and the beam axis in the diphoton rest frame is sensitive to the spin of the Higgs boson. The rest frame of the Higgs boson, or the produced diphoton, is equivalent, in this case, to the Collins–Soper reference frame [293]. The angle $\left|\cos\theta^{*}\right|$ is also known as the helicity angle.

The azimuthal angle between the two leading jets, $\left|\Delta\phi_{jj}\right|$, when there are two or more jets present in the final state, is sensitive to the charge conjugation and parity properties of the Higgs boson, which affect its interactions with gluons in the ggF and the weak bosons in the VBF channels [296–299]. In such final states, the signed azimuthal separation between the two leading jets, $\Delta\phi_{jj,\mathrm{signed}}$, is sensitive to potential CP-violating effects originating from the interference between CP-even and CP-odd Lorentz structures.

*H_{T} is defined as the scalar sum of the magnitudes of the transverse momenta, p_{T}, of the final state particles produced in an event. The convention for this analysis is that $H_{\mathrm{T}}^{\mathrm{jets}}$ is the sum of only the jets' momenta, while H_{T} also includes the diphoton momentum, $p_{\mathrm{T}}^{\gamma\gamma}$.

6.4.2.4 VBF

Separations in rapidity and azimuth between the two leading jets, $|\Delta y_{jj}|$, $|\Delta\phi_{jj}|$, and $\Delta\phi_{jj,\text{signed}}$, and between the diphoton and dijet systems, $|\Delta y_{\gamma\gamma,jj}|$ and $|\Delta\phi_{\gamma\gamma,jj}|$ provide useful signatures to enhance the VBF process. The shapes of the distributions of these variables are different between VBF and ggF production. In vector boson fusion, the t-channel exchange of a W boson typically results in two high-p_{T} jets that are well separated in rapidity. Furthermore, the absence of any color flow between the two jets in VBF suppresses QCD radiation in the region between them. Therefore, the VBF $|\Delta\phi_{\gamma\gamma,jj}|$ distribution is steeper and more narrowly peaked near $|\Delta\phi_{\gamma\gamma,jj}| = \pi$.

6.4.2.5 Full list of the differential variables measured in this analysis

1. Transverse momentum of the diphoton system, $p_{\text{T}}^{\gamma\gamma}$.
2. Absolute rapidity of the diphoton system, $|y_{\gamma\gamma}|$.
3. Higgs boson helicity angle,

$$|\cos\theta^*| = \frac{\left|(E_{\gamma_1} + p_z^{\gamma_1})(E_{\gamma_2} - p_z^{\gamma_2}) - (E_{\gamma_1} - p_z^{\gamma_1})(E_{\gamma_2} + p_z^{\gamma_2})\right|}{m_{\gamma\gamma}\sqrt{m_{\gamma\gamma}^2 + p_{\text{T}\gamma\gamma}^2}}. \tag{6.3}$$

   This is the polar angle of the axis parallel to the two photons with respect to the beam axis in the Collins–Soper reference frame [293], or, equivalently, in the rest frame of the Higgs boson. Eq. (6.3) is valid in the laboratory reference frame.
4. The component of the diphoton transverse momentum, $\vec{p}_{\text{T}}^{\,\gamma\gamma}$, transverse to the diphoton thrust axis, $\hat{t}$, [300, 301]. The definition is illustrated in Fig. 6.4. The vector quantity

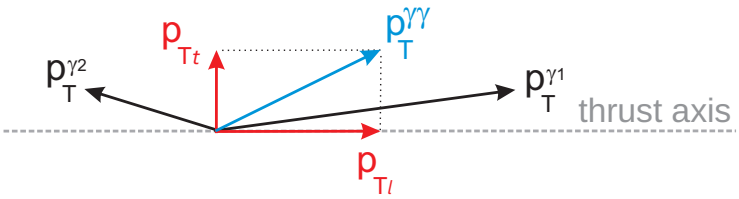

Figure 6.4: Sketch of the $\vec{p}_{\mathrm{Tt}}^{\gamma\gamma}$ definition [302].

can be expressed as

$$\vec{p}_{\mathrm{Tt}}^{\gamma\gamma} = \vec{p}_{\mathrm{T}}^{\gamma\gamma} - \left(\vec{p}_{\mathrm{T}}^{\gamma\gamma} \cdot \hat{t}\right) \hat{t}, \quad \text{where} \quad \vec{t} = \vec{p}_{\mathrm{T}}^{\gamma_1} - \vec{p}_{\mathrm{T}}^{\gamma_2}. \tag{6.4}$$

Only its magnitude is measured in this analysis, which is equal to

$$p_{\mathrm{Tt}}^{\gamma\gamma} = \left|\vec{p}_{\mathrm{T}}^{\gamma\gamma} \times \hat{t}\right| = \frac{2\left|p_x^{\gamma_1} p_y^{\gamma_2} - p_y^{\gamma_1} p_x^{\gamma_2}\right|}{\sqrt{(p_x^{\gamma_1} - p_x^{\gamma_2})^2 + (p_y^{\gamma_1} - p_y^{\gamma_2})^2}}. \tag{6.5}$$

5. Absolute rapidity separation of the two photons,

$$\left|\Delta y_{\gamma\gamma}\right| = \left|y_{\gamma_1} - y_{\gamma_2}\right|. \tag{6.6}$$

6. Number of jets with $p_{\mathrm{T}} \geq 30\,\mathrm{GeV}$, i.e. with nominal jet selection criteria, $N_{\mathrm{jets}}^{\geq 30\,\mathrm{GeV}}$.
7. Number of jets with $p_{\mathrm{T}} \geq 50\,\mathrm{GeV}$, $N_{\mathrm{jets}}^{\geq 50\,\mathrm{GeV}}$.
8. Leading jet transverse momentum, $p_{\mathrm{T}}^{j_1}$.
9. Subleading jet transverse momentum, $p_{\mathrm{T}}^{j_2}$.
10. Absolute leading jet rapidity, $\left|y_{j_1}\right|$.
11. Absolute subleading jet rapidity, $\left|y_{j_2}\right|$.

12. Scalar sum of the transverse momenta of jets,

$$H_{\mathrm{T}}^{\mathrm{jets}} = \sum_{j \in \mathrm{jets}} p_{\mathrm{T}j}. \tag{6.7}$$

13. Scalar sum of the transverse momenta of jets and the diphoton system,

$$H_{\mathrm{T}} = H_{\mathrm{T}}^{\mathrm{jets}} + p_{\mathrm{T}}^{\gamma\gamma}. \tag{6.8}$$

14. Transverse momentum of the diphoton and the leading jet system, $p_{\mathrm{T}}^{\gamma\gamma j}$.

15. Invariant mass of the diphoton and the leading jet system,

$$m_{\gamma\gamma j} = \sqrt{(p_{\gamma_1} + p_{\gamma_2} + p_{j_1})^2}. \tag{6.9}$$

16. Invariant mass of the system of the two leading jets,

$$m_{jj} = \sqrt{(p_{j_1} + p_{j_2})^2}. \tag{6.10}$$

17. Absolute rapidity separation of the two leading jets,

$$\left|\Delta y_{jj}\right| = \left|y_{j_1} - y_{j_2}\right|. \tag{6.11}$$

18. Absolute azimuthal separation between the two leading jets, $\left|\Delta\phi_{jj}\right|$.

19. Signed azimuthal separation between the two leading jets, $\Delta\phi_{jj,\mathrm{signed}}$.

    The angles are ordered according to the jets' rapidity.

20. Transverse momentum of the diphoton and two leading jets system, $p_{\mathrm{T}}^{\gamma\gamma jj}$.

21. Absolute rapidity separation between diphoton and dijet systems,

$$\left|\Delta y_{\gamma\gamma,jj}\right| = \left|y_{\gamma\gamma} - y_{jj}\right|. \tag{6.12}$$

22. Absolute azimuthal separation between diphoton and dijet systems, $\left|\Delta\phi_{\gamma\gamma,jj}\right|$.

23. Maximum beam-thrust-like variable [303],

$$\tau_1 = \max \tau_j, \text{ where } \tau_j = \frac{\sqrt{m_j^2 + p_{\mathrm{T}j}^2}}{2\cosh\left(y_j - y_{\gamma\gamma}\right)}. \tag{6.13}$$

24. Scalar sum of τ_j for all jets with $\tau_j > 8\,\mathrm{GeV}$, $\tau = \sum_j \tau_j$.

25. $p_{\mathrm{T}}^{\gamma\gamma}$ for $p_{\mathrm{T}}^{j} > 30, 40, 50, 60\,\mathrm{GeV}$.

26. $\left|y_{\gamma\gamma}\right|$ vs. $p_{\mathrm{T}}^{\gamma\gamma}$.

27. $p_{\mathrm{T}}^{\gamma_1}/m_{\gamma\gamma}$ and $p_{\mathrm{T}}^{\gamma_2}/m_{\gamma\gamma}$.

28. $(p_{\mathrm{T}}^{\gamma_1} + p_{\mathrm{T}}^{\gamma_2})/m_{\gamma\gamma}$ vs. $(p_{\mathrm{T}}^{\gamma_1} - p_{\mathrm{T}}^{\gamma_2})/m_{\gamma\gamma}$.

29. $p_{\mathrm{T}}^{\gamma\gamma j}$ vs. $p_{\mathrm{T}}^{\gamma\gamma}$.

30. τ_1 vs. $p_{\mathrm{T}}^{\gamma\gamma}$.

6.4.3 Binning

The binning of the measured differential distributions has to be chosen before the signal region, $m_{\gamma\gamma} \in [121, 129]\,\mathrm{GeV}$, is unblinded. This avoids potential bias that can be caused by accidental fluctuations of the observed numbers of events due to relatively low statistics, as well as limited detector resolution and efficiency. The binning optimization is performed using the estimated numbers of signal events from the MC and the background events from the data sidebands, $m_{\gamma\gamma} \in (105, 121) \cup (129, 160)\,\mathrm{GeV}$. Several criteria are taken into account

to make an optimal choice for the edges of the bins.

The signal significance in each bin needs to be sufficiently high. This helps reduce the uncertainty on the measured cross sections and on the shape of the distribution. The statistical model applied has a large number of free parameters, so fits that use small numbers of events can be poorly constrained. A minimum significance of 2σ per bin was chosen as a target value.

A common way to estimate signal significance is

$$Z = \frac{s}{\sqrt{s+b}}, \tag{6.14}$$

where s and b are the numbers of signal and background events respectively. The formula makes intuitive sense, as it gives the number of signal events in units of Poisson uncertainty of the total number of events. A more rigorous formula for estimation of significance has been proposed by Cowan and Gross [304],

$$Z = \sqrt{2\left((s+b)\log\left(1+\frac{s}{b}\right)-s\right)}. \tag{6.15}$$

The two equations yield comparable values, with the ones from Eq. (6.15) about 5% larger on average. Both prescriptions were implemented as a cross check.

Purity is another constraining factor for binning. It is a measure of the amount of event migration between bins due to detector effects. Purity is estimated by comparing the numbers of events predicted by MC before and after detector simulation and reconstruction. Specifically, purity is defined as the ratio between the total weight of events that populate the same bin at both levels, $n_{\text{truth \& reco}}$, and that of all events populating the bin after

reconstruction, n_{reco}, which also counts events that migrated into the bin,

$$\text{purity} = \frac{n_{\text{truth \& reco}}}{n_{\text{reco}}}. \tag{6.16}$$

A related measure of migration is efficiency, ϵ, which is the fraction of events' weight that remained in the same bin after reconstruction,

$$\epsilon = \frac{n_{\text{truth \& reco}}}{n_{\text{truth}}}. \tag{6.17}$$

A minimum purity and efficiency of 50% was chosen as the requirement.

Similar information can be obtained from a migration matrix, which is essentially a 2-dimensional histogram with values of the variable of interest at the particle-level on one axis, and at the detector level on the other. If scaled to the fraction of the total weight at detector (particle) level for each bin, the diagonal elements of the migration matrix give purities (efficiencies).

Other considerations in choosing the bin edges are as follows. Intuitive and easy to communicate values containing few significant figures are preferable. For example, 200 GeV instead of 203.5 GeV. Certain distributions are expected to be symmetric and require respective binning. Features in the shapes of distributions must not be obscured if they can be resolved. Binning that is too fine may adversely affect unfolding. For bin-by-bin unfolding, uniform correction factors are generally desired to avoid bias. Binnings used on sister analyses, namely the ATLAS $H \to 4\ell$ analysis and the analogous analyses done by the CMS collaboration, are taken into account to simplify the combination of results.

A web tool was developed by the author to simplify and automate exploration of possible

Table 6.4: Binning table produced by the web tool, showing quantities considered when choosing the appropriate binning for $p_{\mathrm{T}}^{\gamma\gamma}$, including significance, purity, and signal fractions.

bin	[121,129] sig	syst. unc. √∑w²	stat. unc. √sig	[105,121] L bkg	[129,160] R bkg	[121,129] bkg	syst. unc. from fit	stat. unc. √bkg	signif s/√(s+b)	signif Cowan	s/(s+b)	reco purity
[0,5)	259.68	0.22%	6.21%	34526	22124	10675.40	4.59%	0.97%	**2.48**	**2.50**	2.37%	84.32%
[5,10)	553.63	0.15%	4.25%	65599	41479	20339.20	3.63%	0.70%	**3.83**	**3.86**	2.65%	82.25%
[10,15)	593.88	0.14%	4.10%	70883	45007	22026.50	3.52%	0.67%	**3.95**	**3.98**	2.63%	81.39%
[15,20)	546.23	0.14%	4.28%	64439	42372	20210.40	3.61%	0.70%	**3.79**	**3.83**	2.63%	81.15%
[20,25)	478.96	0.15%	4.57%	54807	37674	17571.00	3.79%	0.75%	**3.57**	**3.60**	2.65%	81.05%
[25,30)	412.52	0.16%	4.92%	45083	32569	14862.10	4.03%	0.82%	**3.34**	**3.37**	2.70%	80.93%
[30,35)	353.40	0.17%	5.32%	37408	27564	12409.90	4.29%	0.90%	**3.13**	**3.16**	2.77%	80.64%
[35,45)	562.52	0.13%	4.22%	56874	44064	19434.20	3.64%	0.72%	**3.98**	**4.02**	2.81%	89.17%
[45,60)	589.72	0.12%	4.12%	54366	45195	19018.70	3.63%	0.73%	**4.21**	**4.25**	3.01%	91.92%
[60,80)	497.54	0.13%	4.48%	40512	36157	14740.20	3.97%	0.82%	**4.03**	**4.08**	3.27%	92.99%
[80,100)	310.40	0.15%	5.68%	18582	20851	7717.91	4.97%	1.14%	**3.46**	**3.51**	3.87%	92.58%
[100,120)	202.03	0.18%	7.04%	8867	10932	3664.58	6.31%	1.65%	**3.25**	**3.31**	5.22%	92.21%
[120,140)	141.21	0.20%	8.42%	4650	5822	1952.00	7.76%	2.26%	**3.09**	**3.16**	6.75%	91.79%
[140,170)	141.56	0.20%	8.40%	3335	4559	1480.12	8.46%	2.60%	**3.52**	**3.62**	8.73%	93.40%
[170,200)	87.85	0.24%	10.67%	1503	2202	685.42	10.55%	3.82%	**3.16**	**3.29**	11.36%	92.88%
[200,250)	80.51	0.25%	11.14%	1058	1567	479.03	11.64%	4.57%	**3.40**	**3.58**	14.39%	94.51%
[250,350)	57.19	0.29%	13.22%	593	849	254.88	13.39%	6.26%	**3.24**	**3.46**	18.33%	95.76%
[350,450)	15.44	0.54%	25.45%	122	182	63.19	17.97%	12.58%	**1.74**	**1.87**	19.63%	95.36%
[450,∞)	7.78	0.74%	35.85%	35	90	27.82	16.22%	18.96%	**1.30**	**1.41**	21.86%	96.72%

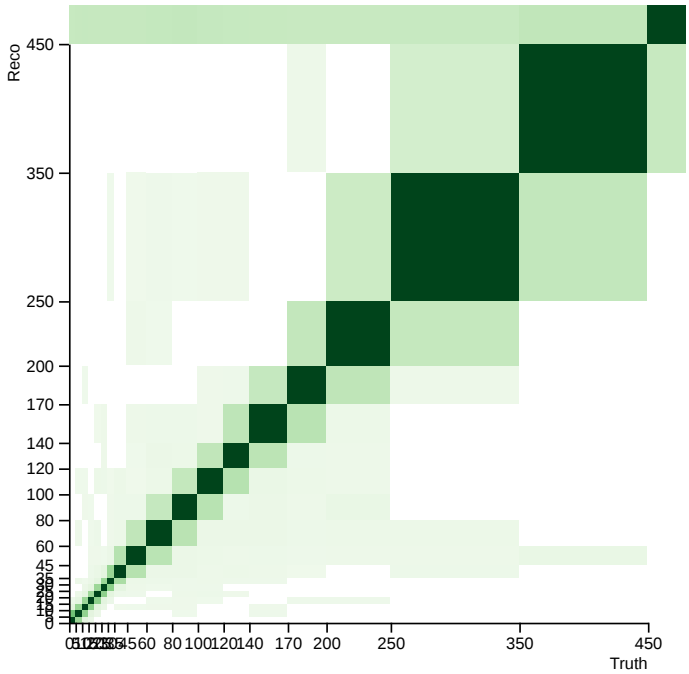

Figure 6.5: The migration matrix for division of the fiducial region into bins of $p_{\mathrm{T}}^{\gamma\gamma}$, produced by the binning web tool.

choices of binning for all variables of interest.* Table 6.4 and Fig. 6.5 show the estimates of significance, purity, and the migration matrix produced by the binning tool for $p_{\mathrm{T}}^{\gamma\gamma}$ with the full Run 2 dataset.

A data-driven estimate of the background in the signal region is used to calculate expected significance. This estimate is obtained by fitting an exponential of a second degree polynomial to the data sidebands and integrating the fitted function over $m_{\gamma\gamma} \in [121, 129]\,\mathrm{GeV}$. This functional form is chosen, because it generally has the best performance for background modeling, as discussed in Section 6.5.2.

6.5 Signal and background modeling

Given a data sample with a certain luminosity, a cross section measurement amounts to estimation of the number of signal events present in the sample, also called the signal yield. The application of the statistical procedure used to obtain the signal yield is referred to as the signal extraction. The general approach is to first choose appropriate models for signal and background and to study these models using the respective simulated MC samples. The two models are fitted to the MC in order to fix the nuisance parameters,† which are believed to be well modeled in MC and are not used in data-driven uncertainty estimation. The combined signal + background model is then fitted to the data. This final fit gives the sought-after signal yields, as well as their uncertainties. Uncertainties from other sources are modeled as extra nuisance parameters in the combined model.

In the present analysis, the $H \to \gamma\gamma$ signal yield is obtained from the Run 2 ATLAS

*The binning tool can be accessed at https://cern.ch/ivankp/hgam/?page=binning.

†Nuisance parameters are the parameters of a statistical model which are not of immediate interest for the specific analysis, but still need to be accounted for.

data by fitting the statistical model described below to the diphoton invariant mass ($m_{\gamma\gamma}$) spectrum using the extended unbinned maximum likelihood method [31].

6.5.1 Signal model

The $m_{\gamma\gamma}$ distribution for the signal process $pp \to H \to \gamma\gamma$ has a resonance peak at the Higgs mass, m_H. In the absence of interference with the $pp \to \gamma\gamma$ background process,* $m_{\gamma\gamma}$ is expected to be distributed according to a Breit–Wigner distribution, with a peak at m_H and, in the Standard Model, a narrow width of 4 MeV [28]. However, the distributions observed in data are smeared by effects of photon reconstruction from detector measurements, which broaden the signal distribution width to a few GeV. Because of this, the signal distribution is empirically modeled by a double-sided Crystal Ball function,† consisting of a Gaussian central part near the peak, smoothly transitioning to power-law functions at either tail. The analytic form of the function is given by Eq. (6.18),

$$\mathcal{S}(t) = \mathcal{N}_{\mathrm{s}} \cdot \begin{cases} e^{-t^2/2} & \text{if } -\alpha_{\mathrm{L}} \leq t \leq \alpha_{\mathrm{H}}, \\ e^{-\alpha_{\mathrm{L}}^2/2} \left[\left(R_{\mathrm{L}} - \alpha_{\mathrm{L}} - t \right) / R_{\mathrm{L}} \right]^{-n_{\mathrm{L}}} & \text{if } t < -\alpha_{\mathrm{L}}, \\ e^{-\alpha_{\mathrm{H}}^2/2} \left[\left(R_{\mathrm{H}} - \alpha_{\mathrm{H}} + t \right) / R_{\mathrm{H}} \right]^{-n_{\mathrm{H}}} & \text{if } t > \alpha_{\mathrm{H}}, \end{cases} \tag{6.18}$$

where $\mathcal{N}_{\mathrm{s}}$ is the normalization factor, $t = (m_{\gamma\gamma} - \mu)/\sigma$, $R = n/\alpha$, μ is the mean of the Gaussian, σ is the width of the Gaussian, $\alpha_{\mathrm{L,H}}$ determine at which points the Gaussian transitions to the power law, and $n_{\mathrm{L,H}}$ are the power law exponents. The function is illus-

*There, of course, is an interference between all channels for diphoton production, resonant or otherwise, because the initial and final states are the same. But the level of the interference is too small to affect this analysis.

†The function is named after the Crystal Ball experiment that ran at the Stanford Linear Accelerator Center in 1980s. The original version, first used there, had only the lower power law tail. See, for example [305].

trated in Fig. 6.6.

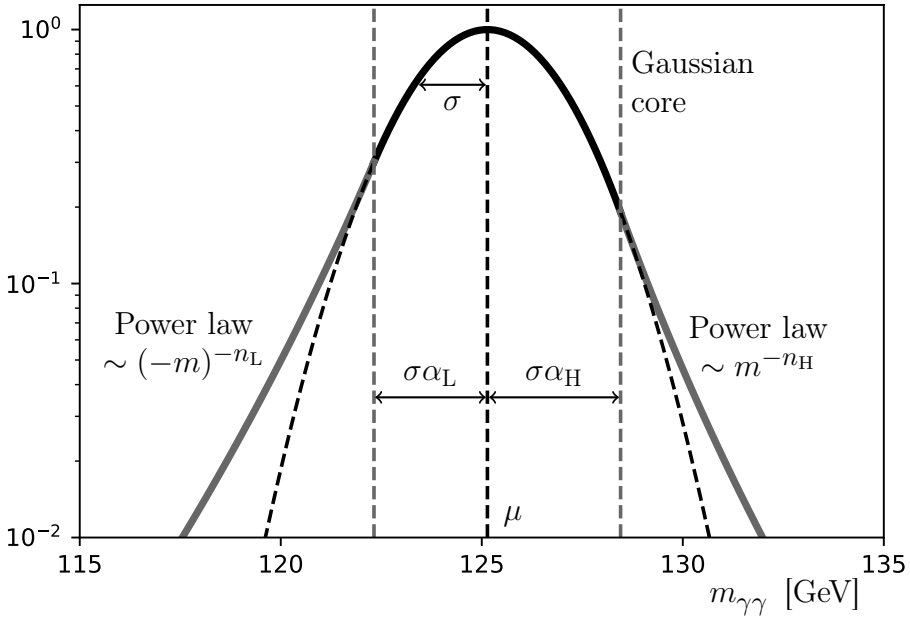

Figure 6.6: Example of a double-sided Crystal Ball function. Gaussian tails are drawn with dashed lines to illustrate the difference with the power law.

The shape parameters of the signal model are determined by fitting to the signal MC. As the MC samples are generated with $m_H = 125\,\mathrm{GeV}$, the mean parameter, μ, obtained from the fits, is shifted up by 90 MeV, to correct it to the experimental Higgs boson mass of 125.09 GeV, measured in Run 1 [306]. The MC signal fitting is done independently for each event category, using the unbinned maximum likelihood method. An example of a signal MC fit for the inclusive fiducial category is shown in Fig. 6.7.

The main uncertainties on the $m_{\gamma\gamma}$ signal shape can be categorized as energy scale and energy resolution. The photon energy scale uncertainty affects μ, shifting the position of the peak, and the photon energy resolution affects σ, broadening the width. The shifts introduced by these uncertainties are treated as constrained nuisance parameters. The uncertainty on the Higgs boson mass measured in Run 1, $(125.09 \pm 0.24)\,\mathrm{GeV}$ [306], is taken into account as an additional fixed nuisance parameter. The exact treatment of these sources

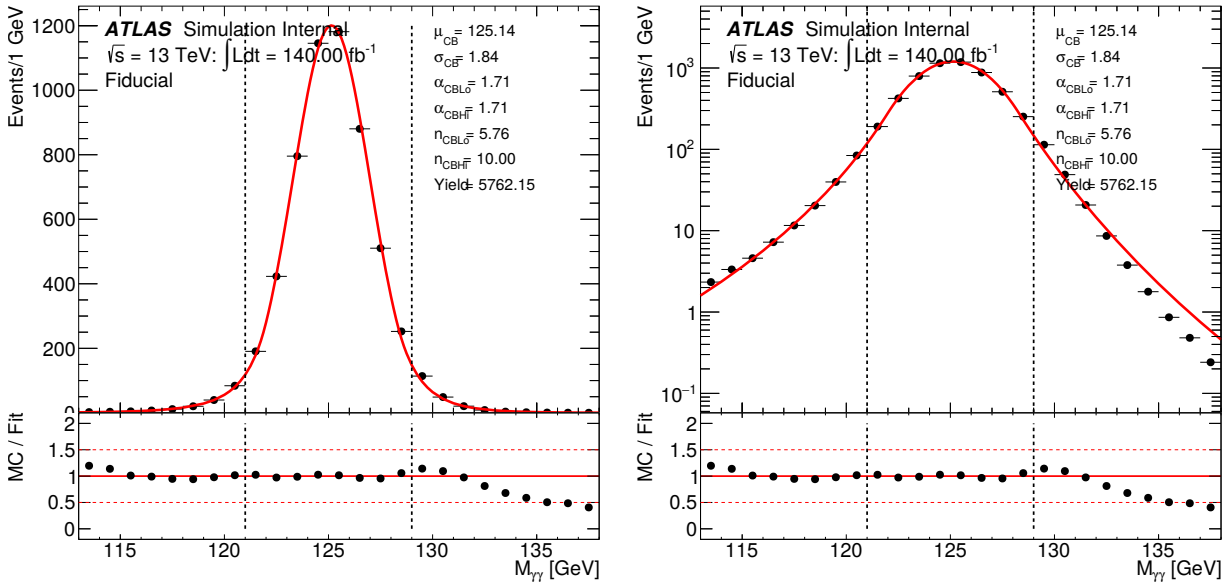

Figure 6.7: The MC signal fit for the inclusive fiducial event category drawn on a linear (left) or a logarithmic (right) vertical axis. The black dotted lines indicate the region used to estimate the spurious signal uncertainty.

of uncertainty is discussed in Section 6.5.3.

6.5.2 Background model

The main source of background for this analysis is non-resonant QCD diphoton production, from $gq \to \gamma\gamma$, $q\bar{q} \to \gamma\gamma$, and $gg \to \gamma\gamma$ processes. This is referred to as the irreducible background, because, aside from $m_{\gamma\gamma}$, these events individually bare no distinguishable characteristic from Higgs events. There is also reducible background from events with γ-jet and jet-jet final states, in which the jets are mistakenly reconstructed as photons. This background is reducible, because the amount of it present is depends on the detector performance. Fortunately, photon identification and isolation requirements reject most of these events, making the reducible background component relatively small, as can be seen in Fig. 6.8.

The background $m_{\gamma\gamma}$ distributions are non-resonant, and are modeled by a set of em-

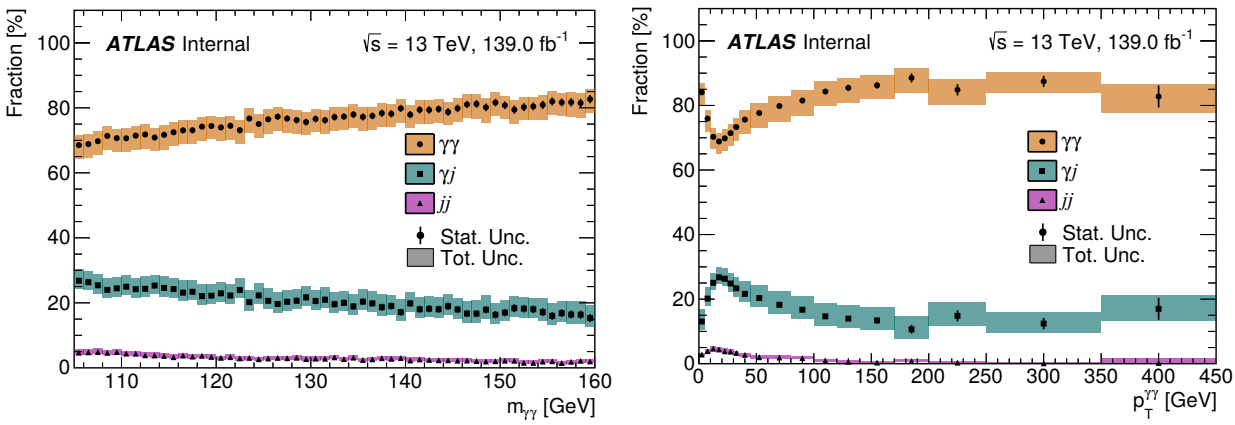

Figure 6.8: Background composition as a function of $m_{\gamma\gamma}$ (left) and $p_{\mathrm{T}\gamma\gamma}$ (right) [278] estimated using the 2×2D method [307, 308].

pirically chosen continuous, monotonically falling functions of one variable. A function is selected from the set independently for each event category using a spurious signal test complemented by an F-test. Three families of functions comprise the considered set: exponentials of polynomials, `ExpPoly`, Eq. (6.19), Bernstein polynomials, `Bern`, Eq. (6.20),* and power law functions, `Pow`, Eq. (6.21). An overall normalization factor is implied for each function. a_n and c_n are free parameters of the functions.†

$$\texttt{ExpPoly}_N(x) = \exp\left(\sum_{n=0}^{N} a_n x^n\right), \tag{6.19}$$

$$\texttt{Bern}_N(x) = \sum_{n=0}^{N} c_n \binom{N}{n} x^n (1-x)^{N-n}, \tag{6.20}$$

$$\texttt{Pow}_N(x) = \sum_{n=1}^{N} c_n x^{a_n}. \tag{6.21}$$

Only functions up to a certain order were considered. These are: `ExpPoly1` or `Exp`,

*The definition of `Bern` assumes function domain of $x \in [0, 1]$. The $m_{\gamma\gamma}$ values are transformed from $[105, 160]$ GeV accordingly before fitting.

†c_n are linear parameters, while a_n are not. `ExpPoly` can of course be fitted linearly in a binned fit to logarithms of the event counts in each bins. In the form the background functions are written in Eqs. (6.19) to (6.21), one of the parameters has to be eliminated for normalization when used in a likelihood fit.

`ExpPoly2`, `ExpPoly3`, `Bern3`, `Bern4`, `Bern5`, `Pow1` or `Pow`, and `Pow2`. The studies show that the best background model is given by `ExpPoly2` for most event categories. In this case, the background model can be written as

$$\mathcal{B}(m_{\gamma\gamma}) = \mathcal{N}_{\mathrm{b}} \cdot \exp\left(-\frac{m_{\gamma\gamma}}{a_1} - \frac{m_{\gamma\gamma}^2}{a_2}\right). \tag{6.22}$$

Background templates are created for the background studies. The primary reason for this approach is that for many event categories, the data do not contain a sufficient number of events to simultaneously constrain the functional form and the nuisance parameters of the background model. Therefore, the form of the background model cannot be selected by fitting directly to the data sidebands. Construction of templates allows efficient production of smooth test samples with high statistics, to improve the accuracy of background shape estimation, especially in low cross section regions with high p_{T} or jet multiplicity. Templates are also provide a way to add reducible background contributions to the MC, which are not simulated.

The irreducible component is obtained from the simulated SHERPA $\gamma\gamma$ sample, with events required to pass the nominal event selection. To determine the reducible γ-jet and jet-jet components' relative contributions, one signal and several control regions are defined by relaxing identification and/or isolation requirements for one or both photons. Reconstruction efficiencies are estimated for each region using MC. Combined with the respective event yields from data, a system of linear equations is formed, which is then solved to obtain the sought fractions of events with jets faking photons. This method is referred to as a double 2-dimensional, or 2×2D, sideband decomposition [307, 308].

An alternative approach to template construction, using a single-component reducible

background, was introduced in the 80 fb^{-1} analysis in 2018. This approach reduced the template shape uncertainty, which was hard to constrain with the original two-component approach, due to large uncertainties on the jj fraction. While both approaches produce distributions in agreement with the data sidebands, ignoring the jj contribution results in better agreement. See Appendix F in [276] and Appendix D in [278] for details.

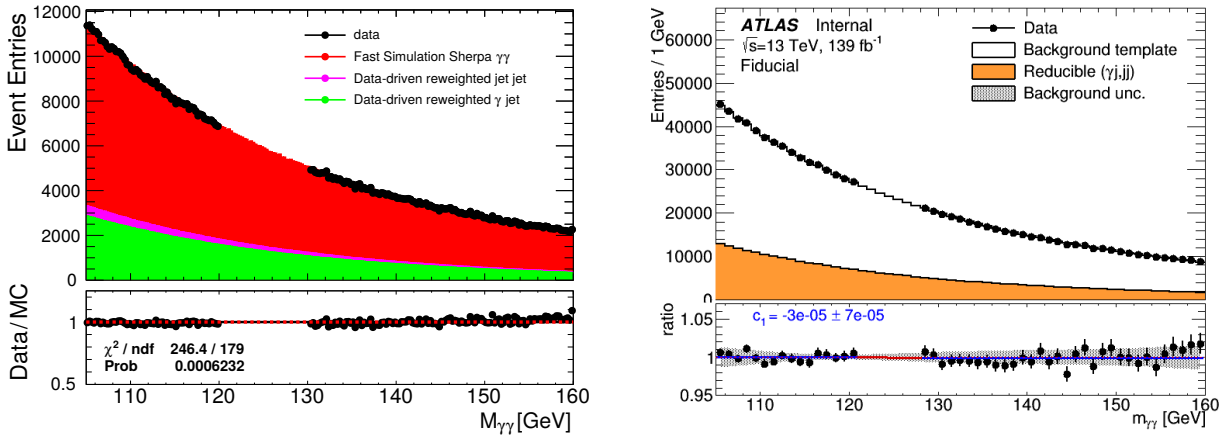

Figure 6.9: Comparison of the background templates to the data in sideband regions for the inclusive fiducial event category using the two-component (left) and one-component (right) reducible background model.

A smoothing procedure is applied in order to suppress statistical fluctuations. Gaussian process regression (GPR) with a Gibbs kernel and an additional custom error kernel has been used for template smoothing since the 2019 analysis. Prior to that, an exponential function or a second degree polynomial, depending on the event category, was fit to the fractions of reducible background. These smooth functions were used to reweight the SHERPA $\gamma\gamma$ events to produce templates including all background contributions. By contrast, GPR smoothing is applied after reweighting.

The templates are derived independently for each event category, and are normalized to data sidebands. All templates are validated for compatibility with the data sidebands with the help of a Pearson's χ^2 test.

6.5.2.1 Spurious signal

An empirically chosen modeling function can over- or underestimate the number of background events in the signal region. This defect can bias signal extraction, and is referred to as spurious signal. Dedicated spurious signal studies are conducted to minimize this effect. This is done by fitting the combined signal + background model to the background-only templates using each one of the background functions, independently for each event category. The fits are performed for different values of the peak $m_{\gamma\gamma}$, scanning the whole signal region, $m_{\gamma\gamma} \in [121, 129]$ GeV. The fitted number of signal events and its uncertainty, $N_{\rm sp} \pm \Delta_{\rm sp}$, are measures of the spurious signal bias. The most suitable function is selected according to the following prescription. First, any functions passing either of the following two criteria are selected:

- $N_{\rm sp} \pm n\Delta_{\rm sp}$ must be less than 20% of the background uncertainty, δS, or
- $N_{\rm sp} \pm n\Delta_{\rm sp}$ must be less than 10% of the expected number of signal events.

The criteria are applied with $n = 0$, then 1, then 2, until at least one function passes. The χ^2 probability of the fits is required to be greater than 1%, to veto parametrizations with accidentally small $N_{\rm sp}$. If multiple functions pass, the first tie breaker is the smallest number of degrees of freedom, and the second one is the smallest $N_{\rm sp}$.

6.5.2.2 F-test

Because data may contain features that do not exist in MC, it is important to test whether a selected background model has a sufficient number of degrees of freedom. To do so, the χ^2 of each selected function with respect to the histogram of data sidebands is compared to

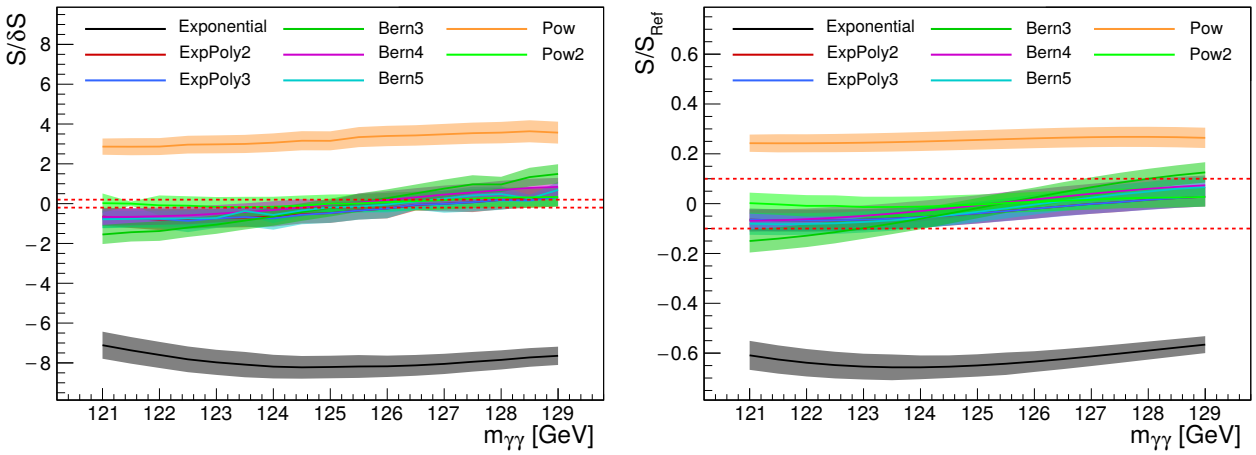

Figure 6.10: Results of the spurious signal test for the inclusive fiducial event category, showing the amount of fitted spurious signal S (referred to as N_{sp} in the text) relative to the background uncertainty δS (left) and relative to the expected signal yield S_{Ref} (right). S_{Ref} is obtained from fitting the signal model to the signal MC.

that of the function with the next higher number of parameters, usually in the same family.* This provides a measure of probability that the data follows the simpler model statistically significantly worse than a more complicated one.

The F-statistic is defined as

$$F_{1,2} = \frac{\frac{\chi_1^2 - \chi_2^2}{p_2 - p_1}}{\frac{\chi_2^2}{n - p_2}} = \frac{\Delta\chi^2}{\chi_2^2} \frac{\text{ndf}_2}{\Delta\text{ndf}}, \tag{6.23}$$

where p_i are the numbers of free parameters of the two function, n is the number of histogram bins, and $\text{ndf}_i = n - p_i$ are the numbers of degrees of freedom. The F-statistic follows the F-distribution (Fig. 6.11) uniquely specified by Δndf and ndf_2. The background model functions are required to pass the F-test with the probability $P > 0.05$, given by the integral of the F-distribution above the F-value. Otherwise, the respective higher order function is

*If a function fails the F-test, usually the function from the same family with one extra parameter is used instead. Exceptions include situations where a different function gives significantly smaller spurious signal, or two extra parameters would need to be added, as is the case for the `Pow` functions. For symmetric distributions, the same function is used on both sides. If the one on one side fails the F-test, the one on the other side is also substituted.

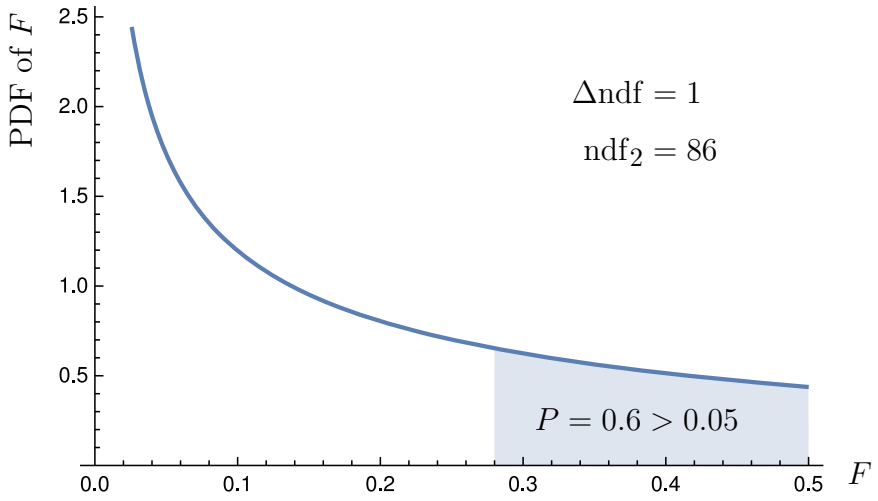

Figure 6.11: The F-distribution for $\Delta\text{ndf} = 1$ and $\text{ndf}_2 = 86$ corresponding to the F-test for the inclusive fiducial event category for the `ExpPoly2` background function and 0.5 GeV binning in $m_{\gamma\gamma}$. The highlighted area shows the integral of the distribution corresponding to the P-value.

used for the analysis instead.

6.5.3 Signal extraction

The signal yield, or the number of signal events present in the dataset, is obtained by performing an unbinned extended maximum likelihood fit of the statistical model to the data, using the likelihood function given in Eq. (6.24),

$$\mathcal{L}_{i\,\in\,\text{bins}} = \frac{e^{-\nu_i}}{n_i!} \prod_{\substack{j\,\in\,\text{events}\\ \text{in bin } i}} \left[\nu_i^{\text{sig}}\mathcal{S}\big({m_{\gamma\gamma}}^j\big|\boldsymbol{\theta}_i^{\text{sig}}\big) + \nu_i^{\text{bkg}}\mathcal{B}\big({m_{\gamma\gamma}}^j\big|\boldsymbol{\theta}_i^{\text{bkg}}\big)\right], \tag{6.24}$$

where the index j runs over the data events within the event category i. $\mathcal{S}$ and $\mathcal{B}$ are respectively the signal and background models. $\nu_i^{\text{sig, bkg}}$ and $\boldsymbol{\theta}_i^{\text{sig, bkg}}$ are the respective yields and vectors of nuisance parameters. For event categories corresponding to bins of a certain variable, for which differential analysis is performed, the likelihood fit is done simultaneously for all bins, indexed by i. The overall likelihood function is a product of the

likelihoods defined for the individual bins. The under- and overflow bins, or complementary categories, are also included in the fit, so that every fit is done using the whole dataset. n_i is the observed number of events in bin i, and $\nu_i = \nu_i^{\text{sig}} + \nu_i^{\text{bkg}}$ is the mean of the underlying Poisson distribution.

In order to obtain estimates of systematic uncertainties on the diphoton mass spectrum due to photon reconstruction, the signal model parameters, mean (μ) and width (σ), defined in Eq. (6.18), are adjusted to allow them to vary around their nominal values, determined and fixed by the fits to the nominal MC samples. Multiple linearly independent variations, indexed by k in the following discussion, are introduced for the μ and σ parameters to account for the different sources of uncertainty in photon reconstruction. The scales of these variations, δ_k, are set by the photon energy scale (PES) and resolution (PER) uncertainties, for the μ and σ, respectively. The δ_k are derived for the diphoton system from the single-photon PES and PER estimates, using systematic MC samples, as described in Section 6.7.1.1. Independent $\delta_{k,i}$ values are derived for each uncertainty component, k, and each event category, i.

The specific size of the variations is controlled by the respective nuisance parameters, θ_k. In this method, the optimization of these nuisance parameters is what propagates the photon reconstruction uncertainties into the diphoton spectrum model. To impose the uncertainty scales and to maintain linear independence of the k uncertainty components, multiplicative constraints, $\mathcal{C}_k$, are applied to the overall likelihood function, which can then be expressed as

$$\mathcal{L} = \prod_{i \in \text{bins}} \mathcal{L}_i \prod_k \mathcal{C}_k(\theta_k), \tag{6.25}$$

The constraints are all given the form of the standard normal p.d.f., evaluated at θ_k,

$$\mathcal{C}_k(\theta_k) = \text{Gaus}(\theta_k; 0, 1) = \frac{1}{\sqrt{2\pi}}\, e^{-\theta_k^2/2}. \tag{6.26}$$

Incorporation of the uncertainty scales into the expressions for the variations of the signal model parameters, rather than the constraints on the likelihood, is a convenient choice, because it enables this uniform definition of the constraints. Since likelihood constraints also define the expectation distributions for the nuisance parameters, the choice of the standard normal p.d.f. for the $\mathcal{C}_k$ makes the pulls* on the θ_k equal to the θ_k themselves. For simplicity, and to reduce the dimensionality of the fitted model, the value of each nuisance parameter, θ_k, is taken to be the same for every event category.

The variations applied to the signal model parameters are as follows:

- 1 symmetric variation is applied to the mean for the Higgs mass,

$$\mu(\theta_{m_H}) = m_H^{\text{nom}} \cdot (1 + \delta_{m_H} \cdot \theta_{m_H})\,, \tag{6.27}$$

with $m_H^{\text{nom}} = 125.09\,\text{GeV}$ and fractional uncertainty $\delta_{m_H} = 0.19\%$ obtained in Run 1 [306]. The nuisance parameter θ_{m_H} describes the deviation of m_H from its nominal value in units of its uncertainty. θ_{m_H} is constrained to one value for all bins in a distribution.

- 39 asymmetric variations are introduced to estimate photon energy scale (PES) systematic uncertainties on the mean parameter, μ,

$$\mu_i(\boldsymbol{\theta}^{\text{PES}}) = \mu_i^{\text{nom}} \cdot \prod_{k=1}^{N_{\text{PES}}} \begin{cases} 1 + \delta_{k,i}^{\text{PES},+} \cdot \theta_k^{\text{PES}}, & \theta_k^{\text{PES}} \geq 0 \\ 1 + \delta_{k,i}^{\text{PES},-} \cdot \theta_k^{\text{PES}}, & \theta_k^{\text{PES}} < 0 \end{cases}, \tag{6.28}$$

*The pull of a nuisance parameter θ is defined as $(\hat{\theta} - \theta_0)/\hat{\sigma}_\theta$. See Section 6.7.1.1 for further discussion.

where the single-source photon reconstruction uncertainties, $\delta_{k,i}^{\mathrm{PES},\pm}$, are derived independently for each event category i, while the nuisance parameters, θ_k^{PES}, are shared* between all i in the same fit. The procedure for derivation of $\delta_{k,i}^{\mathrm{PES},\pm}$ is discussed in Section 6.7.1.1.

- 9 asymmetric log-normal variations are introduced to estimate photon energy resolution (PER) systematic uncertainties on the width parameter, σ,

$$\sigma_i(\boldsymbol{\theta}^{\mathrm{PER}}) = \sigma_i^{\mathrm{nom}} \cdot \prod_{k=1}^{N_{\mathrm{PER}}} \begin{cases} \theta_k^{\mathrm{PER}} \cdot \exp\sqrt{\ln\left(1+\left(\delta_{k,i}^{\mathrm{PER},+}\right)^2\right)}, & \theta_k^{\mathrm{PER}} \geq 0 \\ \theta_k^{\mathrm{PER}} \cdot \exp\sqrt{\ln\left(1+\left(\delta_{k,i}^{\mathrm{PER},-}\right)^2\right)}, & \theta_k^{\mathrm{PER}} < 0 \end{cases}, \tag{6.29}$$

similarly to the PES variations. The reason for the use of log-normal PER variations is that resolution cannot be negative.

While the background function shape for each event category is chosen from the MC studies, the parameters of these functions float in the signal extraction fits, and, therefore, add to the total number of nuisance parameters. Thus, the total number of nuisance parameters in each signal extraction fit is $1 + N_{\mathrm{PES}} + N_{\mathrm{PER}} + \sum_i n_i^{\mathrm{bkg}}$, where n_i^{bkg} are the numbers of background function parameters for each bin. The parameters of interest are the two yields, $\nu_i^{\mathrm{sig,\,bkg}}$. These are not constrained to non-negative values. As an example, the fit for the inclusive fiducial category is show in Fig. 6.12.

Because an independent fit is performed to obtain a differential distribution for every variable of interest, the analysis produces multiple estimates of the total number of signal events. As a cross check, these are compared with each other, as show in Fig. 6.13. The individual estimates of the total number of signal events are found to agree with each other.

*The observed pulls for PES and PER nuisance parameters (see Fig. 6.18), were all found to be much smaller than 1 — the standard deviation of their expectation distribution — not soliciting a more detailed analysis with independent pulls for each bin.

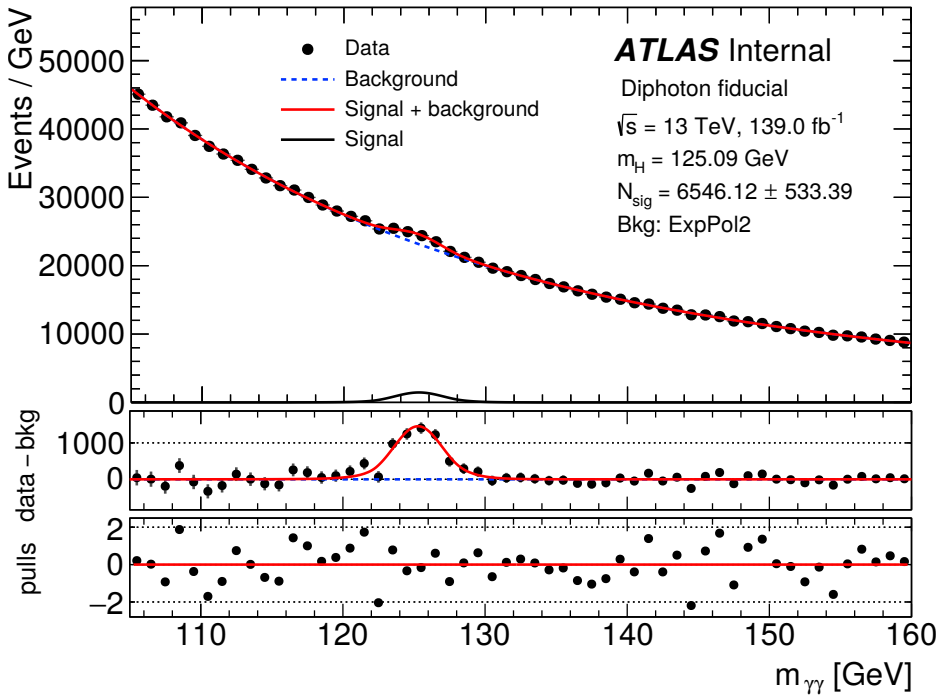

Figure 6.12: Signal extraction fit for the inclusive fiducial event category.

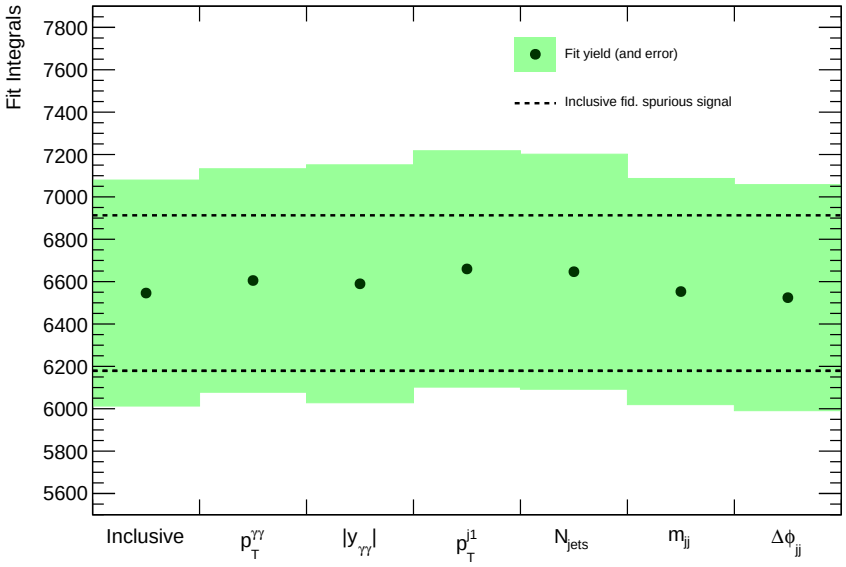

Figure 6.13: Comparison of the total signal yields obtained from independent fits for different combinations of event categories, i.e. different differential variables. Overflow bins are included in the fits. The inclusive fiducial spurious signal uncertainty is shown for reference.

The statistical model for this analysis is implemented using the `RooFit` [309] toolkit for data modeling. It is a part of the `ROOT` [310] data analysis framework developed at CERN. `RooFit` uses the `Minuit2` [311] minimization package for likelihood optimization and the `Minos` [312] algorithm for calculation of parameter errors. `Minos` profiles the log-likelihood function and follows it to the nearest points on either side of the maximum, at which its value decreases from the maximum by $\frac{1}{2}$, thus, in general, yielding asymmetric uncertainty estimates.

6.6 Correction for detector effects

In order to obtain cross section measurements that are independent of the particular experimental setup and can be meaningfully compared to results of other experiments and theoretical predictions, it is important to correct the cross sections obtained from signal yields for detector effects. There are many different sources of detector effects that can introduce systematic differences between true and measured distributions of observables. Examples include calibration, finite resolution, efficiencies, material non-uniformities, gaps in active detector elements, and operation conditions, such as pileup. It is worth noting, that these effects are also in general not constant in time, and hence throughout the dataset. The presence of these effects results in smearing of the observed distributions. Correction, then, is an inverse problem of deconvolution of the detector effects, which, in this context, is usually referred to as unfolding [31, 313].

This analysis uses the unfolding method of bin-by-bin correction factors. The correction factors enter the cross section calculation for each event category, i, as shown in Eq. (6.1)

repeated here:

$$\sigma_i = \frac{\nu_i^{\text{sig}}}{c_i \times L}. \tag{6.30}$$

The correction factors, c_i, account for detector inefficiency, as well as migrations across boundaries of event categories and accessible regions of phase space. The factors are obtained from MC, and are given by the ratio of reconstructed to truth events' weights selected for each category,

$$c_i = \frac{n_i^{\text{reco}}}{n_i^{\text{truth}}}, \quad n_i = \sum_s \frac{\sigma_s^{\text{SM}}}{N_s} n_{s,i}, \tag{6.31}$$

where n^{truth} is the weight of the selected truth, or particle-level, events, n^{reco} is the weight of the selected reconstructed, or detector-level, events. The weights obtained from each MC sample, s, are combined by adding them after reweighting by the ratio of the SM cross section for the respective process, σ_s^{SM}, and the total weight of all events in the sample, N_s. The relative weights of the MC samples, representing different production processes, can introduce model dependence into the correction factors. Fig. 6.14 shows correction factors from individual MC samples.

The performance of more sophisticated unfolding methods was studied, and is detailed in [314]. The list of methods considered includes:

1. correction factor method, or bin-by-bin unfolding, described above;
2. response matrix inversion method;
3. Bayesian iterative unfolding;
4. singular value decomposition (SVD) of the response matrix; and
5. iterative, dynamically stabilized (IDS) unfolding.

Appendix G in [278] includes comparisons between yield distributions unfolded using the first three methods, with the results agreeing within the uncertainties.

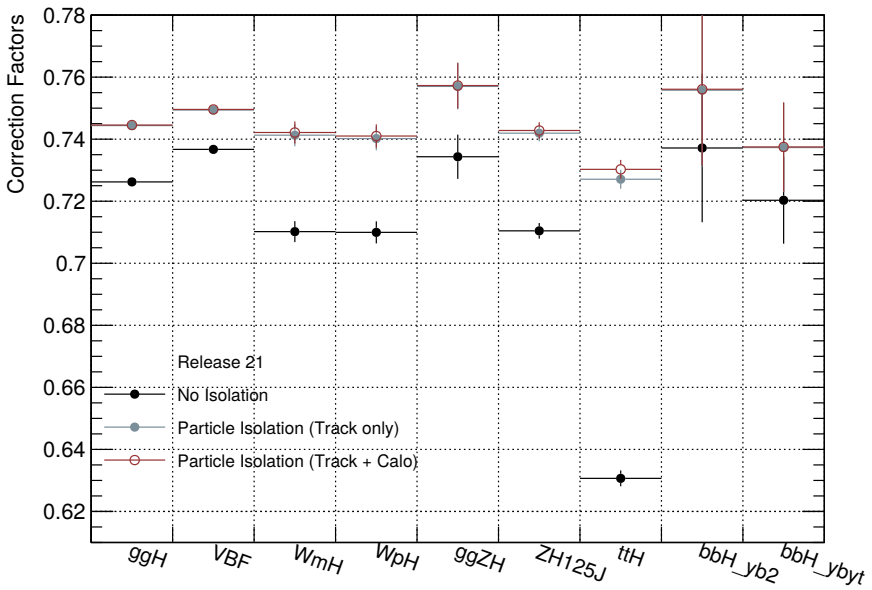

Figure 6.14: Inclusive fiducial correction factors from each production process MC. The values shown in black have no particle-level isolation applied and display a significant dependence on the production process. Values in green have particle-level track isolation applied. Values in red also have calorimeter isolation applied. The production mode dependence is reduced by isolation requirements. [231]

The method of correction factors is chosen as nominal because it is straight forward and suitable for limited statistics. And, while it can be biased, comparable or larger bias was estimated to be introduced by either of the regularized methods for this analysis with the available dataset. Though the matrix inversion method is theoretically unbiased, it can inflate uncertainties and, in worst case scenario, yield nonsensical estimator distributions.* The bias of the correction factor method is reduced by refraining from overly fine bins. This is confirmed by the approximately uniform correction factors derived.

*For a discussion of unfolding methods see Chapter 11 in [31]. The problem with the matrix inversion method is that, in general, a matrix may not have an inverse, or if it does, the solution may not be numerically stable.

6.7 Uncertainties

Corresponding to each factor in the equation for the measured cross section, Eq. (6.30), there are uncertainties associated with signal extraction, experimental uncertainties on luminosity estimates, and theoretical modeling uncertainties on correction factors. Statistical uncertainty is separated from the signal extraction uncertainty, obtained from fitting, with the help of likelihood profiling, as illustrated in Fig. 6.19. The spurious signal uncertainty is added into the signal extraction uncertainty in quadrature. All other sources of uncertainty, besides those on luminosity, correspond to the correction factor. Table 6.5 and Fig. 6.15 below summarize the uncertainties estimated within several event categories.

6.7.1 Signal extraction uncertainties

6.7.1.1 Signal modeling uncertainties

The main sources of uncertainty on the diphoton invariant mass distribution are the photon energy scale (PES), affecting the mode parameter of the signal model, μ, shifting the position of the distribution's peak, and photon energy resolution (PER), affecting the model's width parameter, σ, narrowing or broadening the distribution. These effects, as well as prior information on the Higgs mass from the Run 1 analysis [306], are included in the statistical model, as constrained pulls on the respective parameters, as discussed in Section 6.5.3.

The single-source photon reconstruction uncertainties, $\delta_{k,i}$, defined in Section 6.5.3, are derived using a full decorrelation scheme from single-photon PES and PER calibrations provided by the ATLAS Egamma group [289, 315]. The derived $\delta_{k,i}$ values for the inclusive category are listed in Table 6.6. The same set of values is also derived independently for each

Table 6.5: Breakdown of cross section uncertainties for the inclusive fiducial event category.

Statistics	6.9%
Signal extraction syst.	7.9%
Photon energy scale & resolution	4.6%
Background modeling (spurious signal)	6.4%
Correction factor	2.6%
Pile-up modeling	2.0%
Photon identification efficiency	1.2%
Photon isolation efficiency	1.1%
Trigger efficiency	0.5%
Theoretical modeling	0.5%
Photon energy scale & resolution	0.1%
Luminosity	1.7%
Total	11.0%

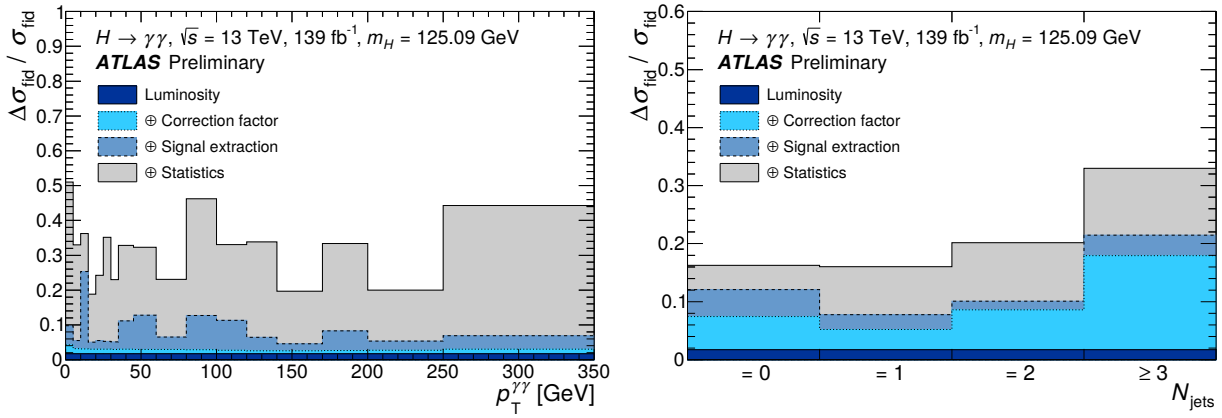

Figure 6.15: Component breakdown of the total uncertainty on the measured cross section in bins of $p_{\mathrm{T}}^{\gamma\gamma}$ and N_{jets}. These are stack plots, with consecutive components added in quadrature.

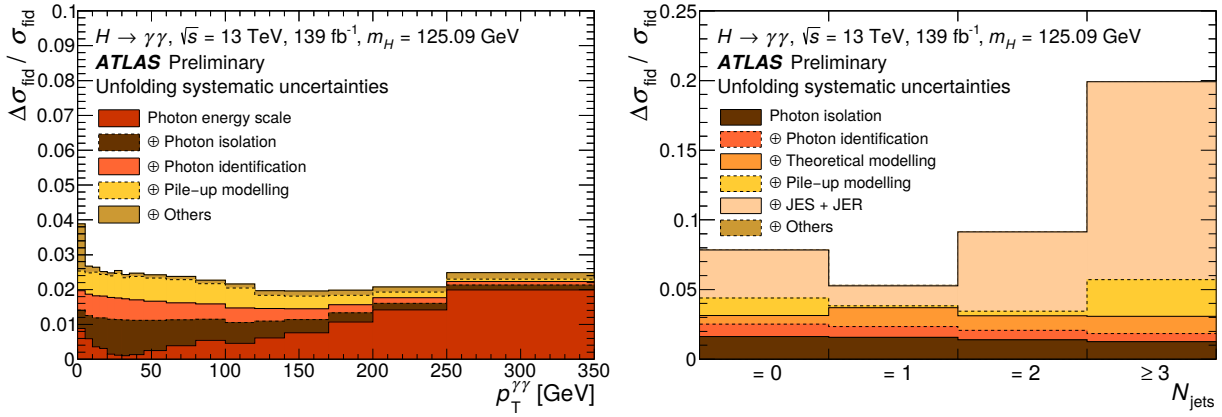

Figure 6.16: Further breakdown of the systematic correction factor component uncertainty on the measured cross section in bins of $p_{\mathrm{T}}^{\gamma\gamma}$ and N_{jets}. Only the largest contributions are explicitly shown. The rest are added as the other.

event category on the analysis. The derivation procedure consists of first generating signal MC samples for up and down variation of each calibration parameter. Only one parameter is varied from the nominal value in each sample. The respective diphoton uncertainties are then obtained from independent fits to the $m_{\gamma\gamma}$ distributions in each event category. The fitted function is the double-sided Crystal Ball function, given by Eq. (6.18), the same as what is used for the analysis signal model, but without the extra systematics nuisance parameters. The up and down variations in position of the $m_{\gamma\gamma}$ peak are taken as its asymmetric uncertainties due to PES sources, and, likewise, for variations of the $m_{\gamma\gamma}$ width due to PER sources. In other words, this procedure propagates single-photon PES and PER uncertainties to the respective ones for the diphoton mass spectrum. Fig. 6.17 shows the combined effects of simultaneous up and down variations independently for PES and PER.

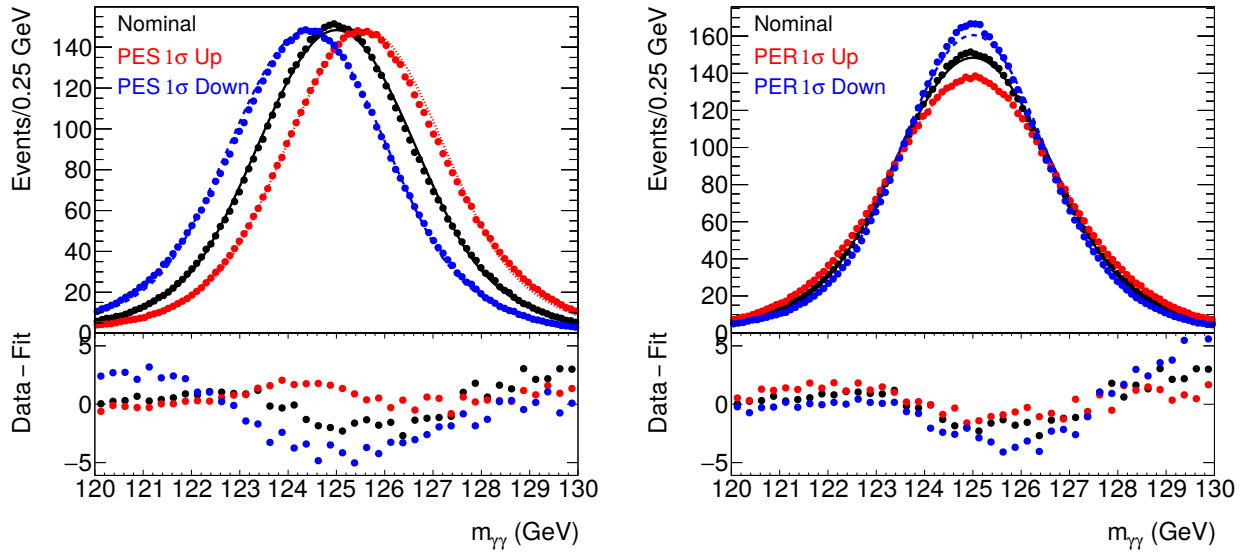

Figure 6.17: The effect of simultaneous variations of all photon calibrations on the diphoton mass spectrum, independently for PES (left) and PER (right).

Two important characteristics of constrained nuisance parameters are pulls and impacts. The pull is a dimensionless measure of the deviation of nuisance parameter θ from its expected

Table 6.6: List of derived relative PES/PER uncertainties, δ_k, that set the scales for the signal model nuisance parameters. The values listed are for the inclusive fiducial region.

Component	Down	Up	Component	Down	Up
EG_RESOLUTION_MATERIALCALO	0.0046218	0.0044663	EG_SCALE_MATCRYO__ETABN6	0.0000574	0.0000537
EG_RESOLUTION_MATERIALCRYO	0.0120173	0.0115940	EG_SCALE_MATCRYO__ETABN7	0.0001073	0.0001036
EG_RESOLUTION_MATERIALGAP	0.0065407	0.0059096	EG_SCALE_MATCRYO__ETABN8	0.0001025	0.0000991
EG_RESOLUTION_MATERIALIBL	0.0119270	0.0112591	EG_SCALE_MATCRYO__ETABN9	0.0000232	0.0000196
EG_RESOLUTION_MATERIALID	0.0377096	0.0362137	EG_SCALE_MATCRYO__ETABN10	0.0000116	0.0000081
EG_RESOLUTION_MATERIALPP0	0.0200846	0.0186260	EG_SCALE_MATCRYO__ETABN11	0.0000145	0.0000110
EG_RESOLUTION_PILEUP	0.0243305	0.0231763	EG_SCALE_MATCRYO_BARREL	0.0001552	0.0001467
EG_RESOLUTION_SAMPLINGTERM	0.0185316	0.0205275	EG_SCALE_MATCRYO_ENDCAP	0.0001513	0.0001453
EG_RESOLUTION_ZSMEARING	0.0509220	0.0708453	EG_SCALE_MATID__ETABN0	0.0001771	0.0001762
EG_SCALE_E4SCINTILLATOR__ETABN0	0.0000001	0.0000001	EG_SCALE_MATID__ETABN1	0.0001030	0.0001020
EG_SCALE_E4SCINTILLATOR__ETABN1	0.0000042	0.0000038	EG_SCALE_MATID__ETABN2	0.0001397	0.0001388
EG_SCALE_E4SCINTILLATOR__ETABN2	0.0000377	0.0000375	EG_SCALE_MATID__ETABN3	0.0000209	0.0000205
EG_SCALE_G4	0.0001301	0.0001297	EG_SCALE_MATPP0__ETABN0	0.0000608	0.0000599
EG_SCALE_L1GAIN	0.0004108	0.0004156	EG_SCALE_MATPP0__ETABN1	0.0001869	0.0001861
EG_SCALE_L2GAIN	0.0009825	0.0009792	EG_SCALE_PEDESTAL	0.0000778	0.0000800
EG_SCALE_LARCALIB__ETABN0	0.0007395	0.0007400	EG_SCALE_PS__ETABN0	0.0000728	0.0000751
EG_SCALE_LARCALIB__ETABN1	0.0002312	0.0002312	EG_SCALE_PS__ETABN1	0.0000548	0.0000569
EG_SCALE_LARELECCALIB	0.0000487	0.0000494	EG_SCALE_PS__ETABN2	0.0000575	0.0000598
EG_SCALE_LARELECUNCONV__ETABN0	0.0008510	0.0008523	EG_SCALE_PS__ETABN3	0.0000945	0.0000969
EG_SCALE_LARELECUNCONV__ETABN1	0.0003349	0.0003364	EG_SCALE_PS__ETABN4	0.0000407	0.0000429
EG_SCALE_LARUNCONVCALIB__ETABN0	0.0002951	0.0002933	EG_SCALE_PS__ETABN5	0.0000602	0.0000625
EG_SCALE_LARUNCONVCALIB__ETABN1	0.0000689	0.0000694	EG_SCALE_PS__ETABN6	0.0006191	0.0006314
EG_SCALE_MATCALO__ETABN0	0.0000415	0.0000409	EG_SCALE_PS__ETABN7	0.0000043	0.0000066
EG_SCALE_MATCALO__ETABN1	0.0000370	0.0000366	EG_SCALE_PS__ETABN8	0.0001084	0.0001108
EG_SCALE_MATCALO__ETABN2	0.0000315	0.0000312	EG_SCALE_PS_BARREL	0.0006396	0.0006529
EG_SCALE_MATCALO__ETABN3	0.0000527	0.0000529	EG_SCALE_PS_BARREL_B12	0.0006092	0.0006156
EG_SCALE_MATCALO__ETABN4	0.0000634	0.0000636	EG_SCALE_PS_ENDCAP	0.0001084	0.0001108
EG_SCALE_MATCALO__ETABN5	0.0000662	0.0000656	EG_SCALE_S12__ETABN0	0.0003040	0.0003067
EG_SCALE_MATCALO__ETABN6	0.0000596	0.0000589	EG_SCALE_S12__ETABN1	0.0003103	0.0003122
EG_SCALE_MATCALO__ETABN7	0.0000099	0.0000095	EG_SCALE_S12__ETABN2	0.0000001	0.0000001
EG_SCALE_MATCALO__ETABN8	0.0000275	0.0000270	EG_SCALE_S12__ETABN3	0.0003037	0.0003041
EG_SCALE_MATCALO__ETABN9	0.0000002	0.0000002	EG_SCALE_S12__ETABN4	0.0000001	0.0000001
EG_SCALE_MATCALO__ETABN10	0.0000002	0.0000002	EG_SCALE_TOPOCLUSTER_THRES	0.0000004	0.0000793
EG_SCALE_MATCALO__ETABN11	0.0000002	0.0000002	EG_SCALE_WTOTS1	0.0003596	0.0003587
EG_SCALE_MATCALO_BARREL	0.0001372	0.0001364	EG_SCALE_ZEESTAT	0.0000178	0.0000183
EG_SCALE_MATCALO_ENDCAP	0.0000292	0.0000286	EG_SCALE_ZEESYST	0.0009334	0.0009322
EG_SCALE_MATCRYO__ETABN0	0.0000293	0.0000287	PH_SCALE_CONVEFFICIENCY	0.0003389	0.0003413
EG_SCALE_MATCRYO__ETABN1	0.0000514	0.0000479	PH_SCALE_CONVFAKERATE	0.0001372	0.0001329
EG_SCALE_MATCRYO__ETABN2	0.0000463	0.0000427	PH_SCALE_CONVRADIUS	0.0001947	0.0001964
EG_SCALE_MATCRYO__ETABN3	0.0000773	0.0000736	PH_SCALE_LEAKAGECONV	0.0004426	0.0004358
EG_SCALE_MATCRYO__ETABN4	0.0000814	0.0000779	PH_SCALE_LEAKAGEUNCONV	0.0006540	
EG_SCALE_MATCRYO__ETABN5	0.0000506	0.0000471			

value θ_0 relative to its expected uncertainty, δ_θ,

$$\text{pull}(\theta) = \frac{\hat{\theta} - \theta_0}{\delta_\theta}. \tag{6.32}$$

A healthy situation is when the pull average is 0, with a standard deviation close to 1. If this is not the case, further investigation is required [316]. The impact is a measure of deviation of a parameter of interest ν with respect to variations of a nuisance parameter within the range of its uncertainty. This can be expressed as,

$$\text{impact}_\nu(\theta) = \Delta\nu^{\pm} = \hat{\hat{\nu}}_{\theta_0 \pm \delta_\theta} - \hat{\nu}, \tag{6.33}$$

where $\hat{\nu}$ is the parameter of interest estimated with θ floating, and $\hat{\hat{\nu}}_{\theta_0 \pm \delta_\theta}$ is the same parameter estimated with θ fixed to $\theta_0 \pm \delta_\theta$. As the name implies, the impact is a measure of the effect that optimization of a nuisance parameter has on a parameter of interest. Pulls are symmetric by definition, while impacts can be asymmetric.

As a cross check, the signal model nuisance parameters are ranked according to their impact on the signal yield, and the values and uncertainties of their pulls are compared before and after fitting, as shown in Fig. 6.18. The pre-fit pull values are, by design, all equal to 0 with uncertainty of 1. The post-fit pull values are obtained using the profile likelihood method, implemented in `Minos` [311, 312]. The pre-fit impacts are obtained from signal extraction with nuisance parameters fixed to their pre-fit values of 0. The post-fit impacts are obtained with nuisance parameters floating, i.e. with fitted nuisance parameters' values. Before the signal region is unblinded, the signal extraction fitting procedure is tested using Asimov datasets, which gives the expected values for the pulls and impacts. For

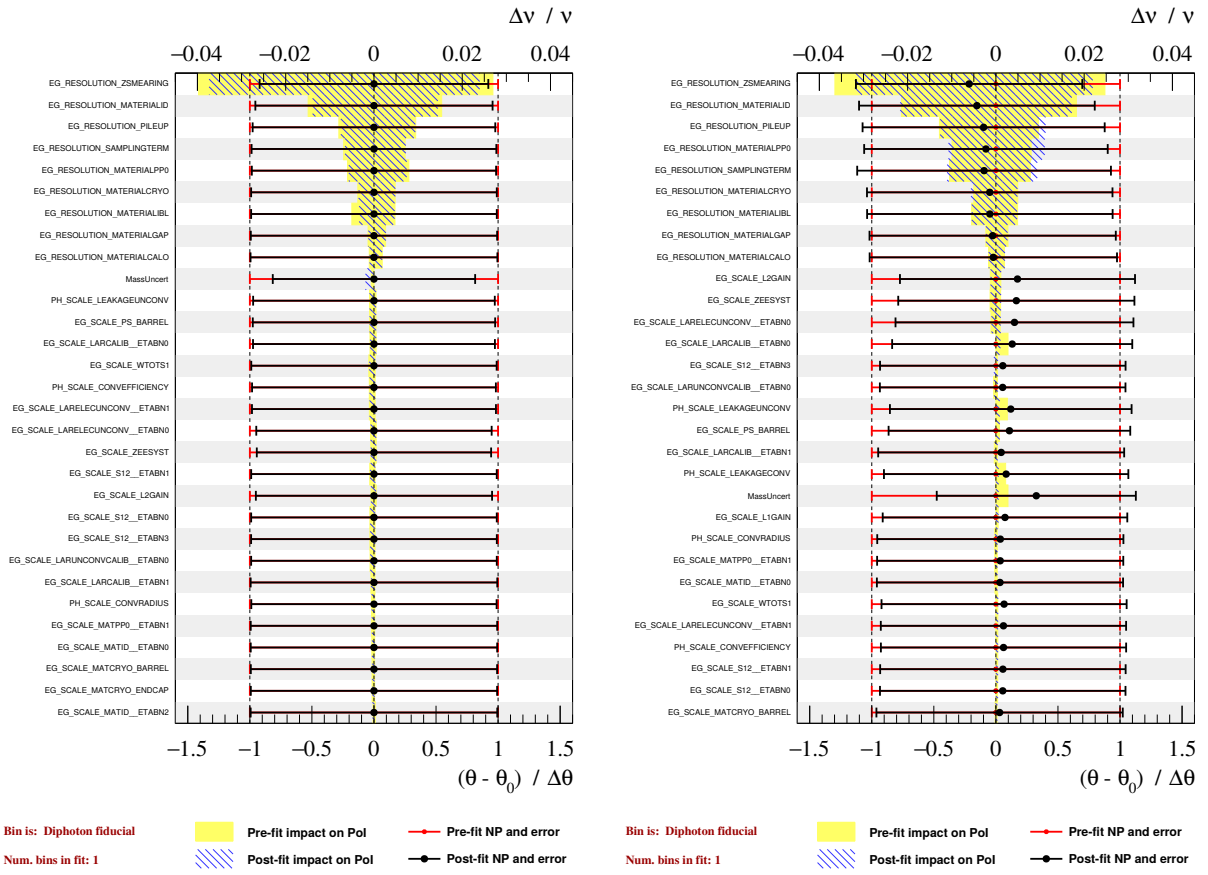

(a) Expected NP ranking.

(b) Observed NP ranking.

Figure 6.18: Expected and observed nuisance parameters' pre- and post-fit pulls and impacts for the inclusive fiducial category. The nuisance parameters (NP) are ranked by their impacts on the signal yield parameter of interest (PoI).

example, as can be seen in Fig. 6.18a, the Higgs mass nuisance parameter is expected to be underconstrained in the fits. The expected post-fit pulls have a mean of 0, because the Asimov data exactly follows the model distribution.

In order to separate the statistical and systematic components of the uncertainty on the extracted signal yield, the likelihood function is profiled for the signal yield parameter of interest with nuisance parameters floating or fixed to their optimal values, as shown in Fig. 6.19. By the standard prescription [31], the one standard deviation uncertainty range is given by the values of the parameter for which the quantity $-2 \log L$ increases by 1

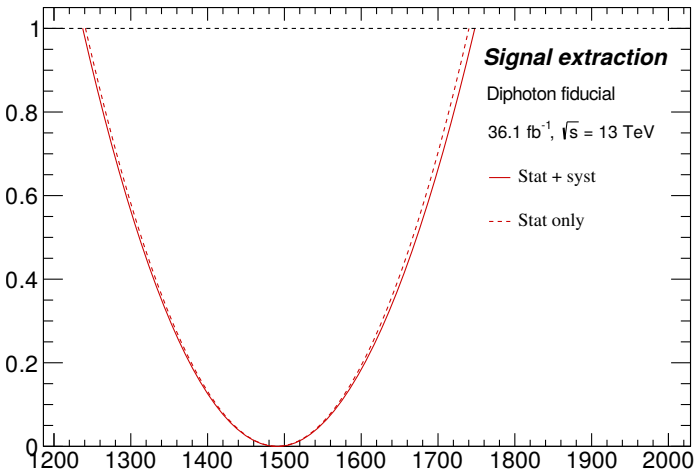

Figure 6.19: The likelihood profile for the signal yield in the inclusive fiducial event category. The combined statistical and systematic uncertainty is determined from the profile obtained with floating nuisance parameters, shown with a solid line. The statistical-only uncertainty is determined from the other, dashed, profile, for which the nuisance parameters are fixed to the best fit values.

from its minimum. The likelihood profile, obtained with floating nuisance parameters, gives the combined systematic and statistical uncertainty. The likelihood profile, constructed by fixing the nuisance parameters to their values at the global likelihood maximum, gives the statistical contribution to the uncertainty. The systematic uncertainty is then obtained by taking the quadrature difference between the total and the statistical-only uncertainty estimates. Comparisons between expected, obtained using Asimov datasets, and observed systematic and statistical uncertainties on signal yields are shown in Fig. 6.20.

6.7.1.2 Background modeling uncertainties

The uncertainty associated with the background modeling is estimated in the spurious signal studies. As discussed in Section 6.5.2.1, the spurious signal is the number of signal events obtained from fitting the signal + background model to the background-only MC templates. This quantity is used select the functional form of the background model applied in signal extraction. The contribution to the signal extraction uncertainty from the spurious

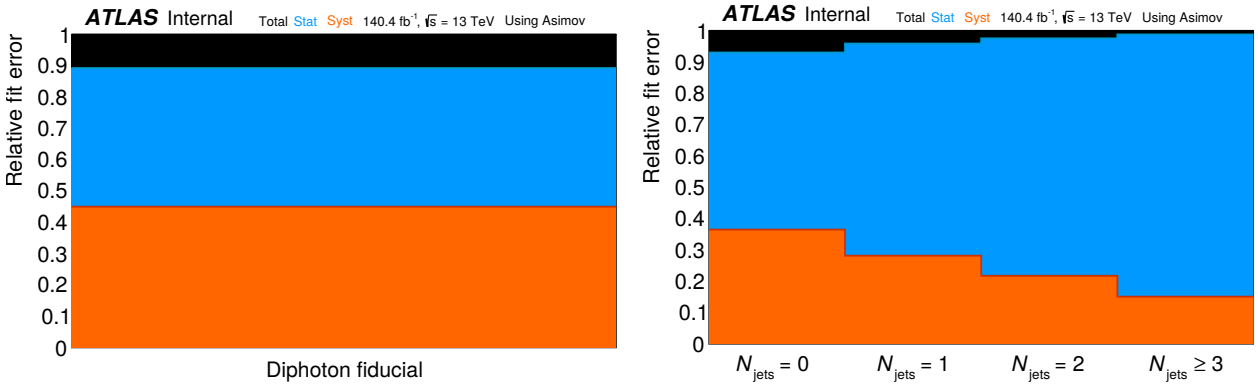

Figure 6.20: Expected systematic and statistical uncertainties on signal yield estimated using the Asimov method for inclusive fiducial event category and in bins of jet multiplicity.

signal is estimated by the maximum value of $N_{\text{sp}}/S_{\text{Ref}}$ obtained in the spurious signal scans over the signal region, where N_{sp} is the fitted number of spurious signal events, and S_{Ref} is the expected signal yield obtained from the signal MC. The spurious signal uncertainty is added in quadrature to the signal extraction uncertainty, after correcting S_{Ref} for the observed signal strength.

6.7.2 Theoretical modeling uncertainties

6.7.2.1 Signal composition uncertainty

In the computation of the correction factors, the events from each MC sample are weighted by the respective SM cross section, as shown in Eq. (6.31). Correction factors are thus affected by the uncertainties of the production modes' cross sections. Another related source of uncertainty is due to model dependence, which may be introduced, if the correction factors for different modes vary significantly. These uncertainties are estimated by varying the models' cross sections within the uncertainty bounds obtained experimentally in the couplings measurements in $H \to \gamma\gamma$ and $H \to 4\ell$ channels [317, 318]. The composition uncertainty bounds are determined by recomputing correction factors using simultaneous up

or down variations off all production mode cross sections.

6.7.2.2 Unfolding bias

A recursive technique is used to estimate the systematic uncertainty due to unfolding bias. The procedure consists of reweighting the signal MC, so that its $p_{\mathrm{T}}^{\gamma\gamma}$ and $\left|y_{\gamma\gamma}\right|$ distributions match more closely with the measured unfolded distributions. Correction factors are then derived again using the reweighted MC, and the uncertainty is estimated by the difference between the reweighted and original correction factors. The reweighting functions are derived by smoothing the ratio between the measured and MC distributions using a Gaussian kernel. The comparison between the original and reweighted distributions is shown in Fig. 6.21. Simultaneous reweighting with respect to both distributions can be applied because the two variables are largely uncorrelated.

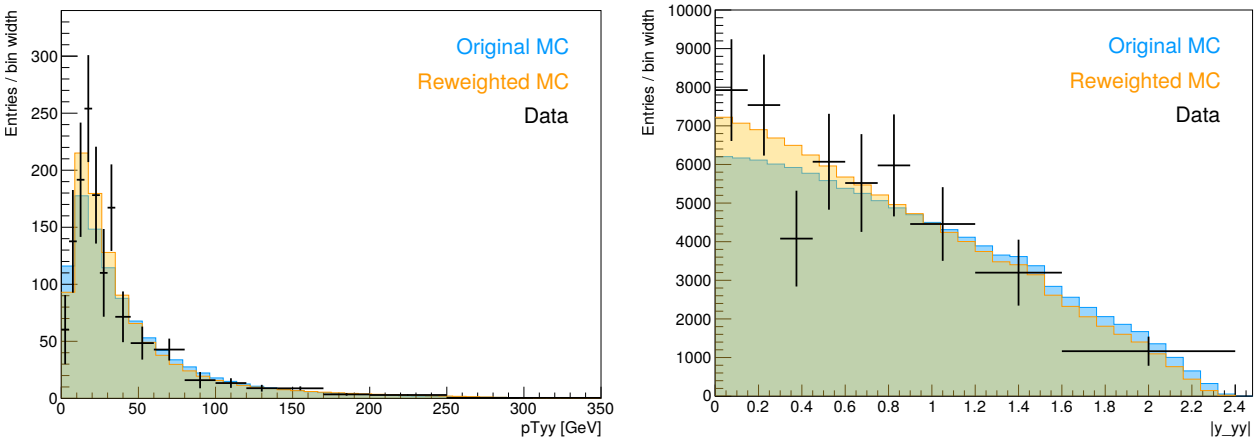

Figure 6.21: Original and reweighted $p_{\mathrm{T}}^{\gamma\gamma}$ (left) and $\left|y_{\gamma\gamma}\right|$ (right) MC distributions used in estimation of the unfolding bias uncertainty.

6.7.2.3 Event modeling

To simulate collision events, MC generators apply several algorithms to model different aspects of an event. This is discussed further in Chapter 3. Parton shower and underlying

event models convert inclusive parton-level MC to exclusive particle-level predictions. To estimate the uncertainty from these models, the correction factors derived from the nominal MC samples, produced using PYTHIA 8 [81, 319], are compared to those obtained using HERWIG 7 [320]. The two programs implement different algorithms for parton showers and modeling of non-perturbative effects of hadronization and multi-parton interactions. The difference between correction factors derived using PYTHIA or HERWIG, from gluon-fusion samples generated with POWHEG, is taken as the systematic uncertainty.

6.7.2.4 Dalitz events

The signal MC samples used in this analysis, produced with PYTHIA 8, include events with unstable off-shell photons. These, so called, Dalitz events, represent contributions from the $H \to \gamma\gamma^* \to \gamma f \bar{f}$ decay channel, where γ^* is an off-shell photon, and f is any charged fermion. These events constitute approximately 6% of the total number of generated events. They, however, are not considered a part of the fiducial volume, which requires a stable diphoton system. The Dalitz events are removed from particle-level distributions, and the remaining event are reweighted to maintain correct cross section. At the detector level, around 0.3% of the signal MC events that pass fiducial selection are Dalitz events. This fraction is approximately constant across the analyzed event categories. These events are not removed after reconstruction, but are corrected for by the unfolding. Dalitz decay branching ratio is not known very precisely, and different generators produce different fractions. Because of this, a conservative uncertainty of 100% is assigned to the Dalitz contribution, which results in an approximately 0.3% uncertainty on the correction factors.

6.7.3 Experimental uncertainties

6.7.3.1 Luminosity

Luminosity measurements are discussed in Section 6.2. Estimates of luminosity and its uncertainty, given in Table 6.2 are obtained using methods discussed in [280, 284], which are based on van der Meer [283] scans.

6.7.3.2 Trigger efficiency

The diphoton trigger efficiency is obtained using the bootstrap method in data [321], and using trigger matching in MC. The estimated efficiency is $99.16^{+0.23}_{-0.49}(\text{stat.})^{+0.34}_{-0.52}(\text{sys.})$ [279], which is in agreement with the predictions from simulations.

6.7.3.3 Vertex selection efficiency

Identification of the primary vertex is a part of the event selection criteria of this analysis. An estimate of the primary vertex selection efficiency is a part of the correction factor, and, thus, contributes to its uncertainty. For this analysis, the primary vertex is corrected using photon pointing information [215]. The primary vertex selection is one of the factors that impact the migration of events in an out of the fiducial region.

The vertex selection uncertainty is estimated by the difference between vertex selection efficiencies in data and MC using $Z \to ee$ events, ignoring electron tracks. The uncertainty is generally found to be $< 0.3\%$. The ratio of the efficiencies is used to increase the weights of the analysis MC events with $|z_{\text{reco}} - z_{\text{true}}| > 0.3\,\text{mm}$.

6.7.3.4 Photon selection

Photon identification efficiency Photon reconstruction and identification requirements are discussed in Section 5.2.3. The analysis selection criteria are listed in Section 6.3.2. A combination of three methods is used to estimate photon identification efficiency:

1. Photon tagging in $Z \to \ell\ell\gamma$ events, providing a very pure sample at lower p_{T};
2. Applying electron-to-photon mapping derived from MC to data $Z \to ee$ events; and
3. Using a sideband method, requiring to solve a linear system of equations, combined with track isolation as an additional discriminating variable.

The methods agree with each other within the statistical uncertainties.

Photon isolation efficiency Track and calorimeter isolation uncertainties are combined in quadrature. These are estimated using data, by shifting the respective isolation requirements.

Photon energy scale and resolution In addition to affecting the diphoton mass distribution, contributing to the signal yield uncertainty, accounted for in Section 6.7.1.1, photon reconstruction uncertainties contribute to event migration, both in an out of the fiducial volume and between bins. The migration contributes to the correction factor uncertainty, which is estimated from MC by simultaneously varying the PES and PER parameters up or down. The migration uncertainties, δ_{mig}, are given by

$$\delta_{\mathrm{mig}} = \frac{\alpha'}{\alpha} - 1, \quad \alpha^{(\prime)} = \frac{N_A^{(\prime)}}{N_A^{(\prime)} + N_B^{(\prime)}}, \tag{6.34}$$

where A and B are two event categories and primes denote the numbers of events obtained from simulations with varied PES and PER parameters [322].

6.7.3.5 Jet selection

Though the fiducial selection does not have any jet requirements, the jet-related event categories are affected by jet reconstruction.

Jet energy scale and resolution JES and JER uncertainties are estimated with the help of the transverse momentum balance technique, using $Z+\text{jets}$, $\gamma+\text{jets}$, and dijet events, as described in [323].

Jet vertex tagging efficiency The jet vertex tagging (JVT) algorithm, discussed in Section 5.3.5, is used to suppress pileup jets originating from additional interaction vertices. Selection criteria for both data and simulation require that central jets, within $|\eta| < 2.5$, pass a JVT cut. The JVT selection uncertainty contributes to the correction factor uncertainty, as false acceptance of pileup (PU) jets and false rejection of hard scatter (HS) jets can cause event migrations between bins of jet-dependent observables, especially at higher jet multiplicities. The JVT uncertainty is estimated by comparing the JVT selection efficiency in MC and in data sidebands [252]. The efficiency is given by the fraction of central jets passing the cut. In the simulation, a jet is defined as pileup if it has $p_{\mathrm{T}} > 10\,\mathrm{GeV}$ and is not matched to a particle-level jet within $\Delta R < 0.2$. Therefore, in MC, the efficiency can be obtained for both HS and PU jets independently, while only the combined efficiency for all central jets can be obtain from the data. The separate efficiencies for HS and PU jets in the data are estimated by scaling the combined efficiency to the HS and PU fractions from the MC. The JVT uncertainty is small for the HS jets, amounting at most to 0.3%. The uncertainties for PU jets is on the order of 2%. The residual pileup jet contamination is corrected for in the unfolding.

6.7.3.6 Pileup reweighting

The modeling of pileup is based on simulations of inelastic pp collisions. As discussed in Section 3.6, pileup reweighting is applied to the MC samples so that their distributions of the number of interactions per bunch crossing match that observed in the collected data. The reweighting impacts the correction factors. Pileup reweighting is varied to cover the uncertainty in the ratio between the predicted and measured inelastic cross section for events with the mass of the non-diffractive hadronic system greater than 13 GeV [324]. This effectively shifts the pileup distribution by ±3%, as shown in Fig. 6.22.

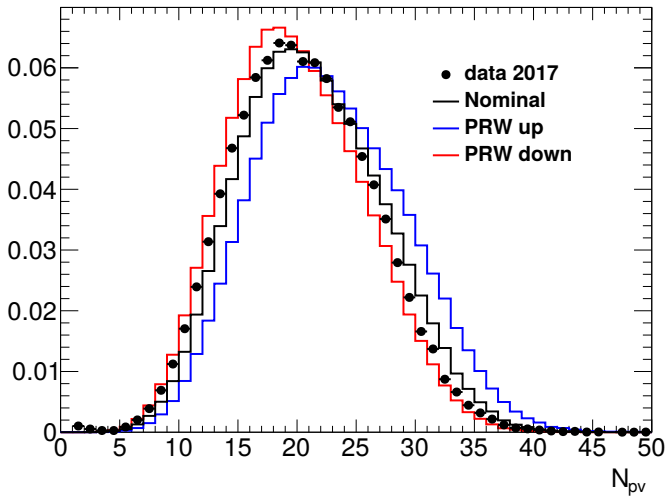

Figure 6.22: Effects of pileup reweighting variations on the distribution of the number of primary vertices, N_{pv}.

6.8 Results

6.8.1 Asimov closure tests

To cross check the analysis procedure, a mock analysis was performed using Asimov datasets instead of the data. These were built using a signal parametrization from MC, and

a background parametrization from data sidebands. The results are shown in Fig. 6.23. No biases were observed. This cross check also provides estimates of the expected statistical and systematic uncertainties from fitting and unfolding.

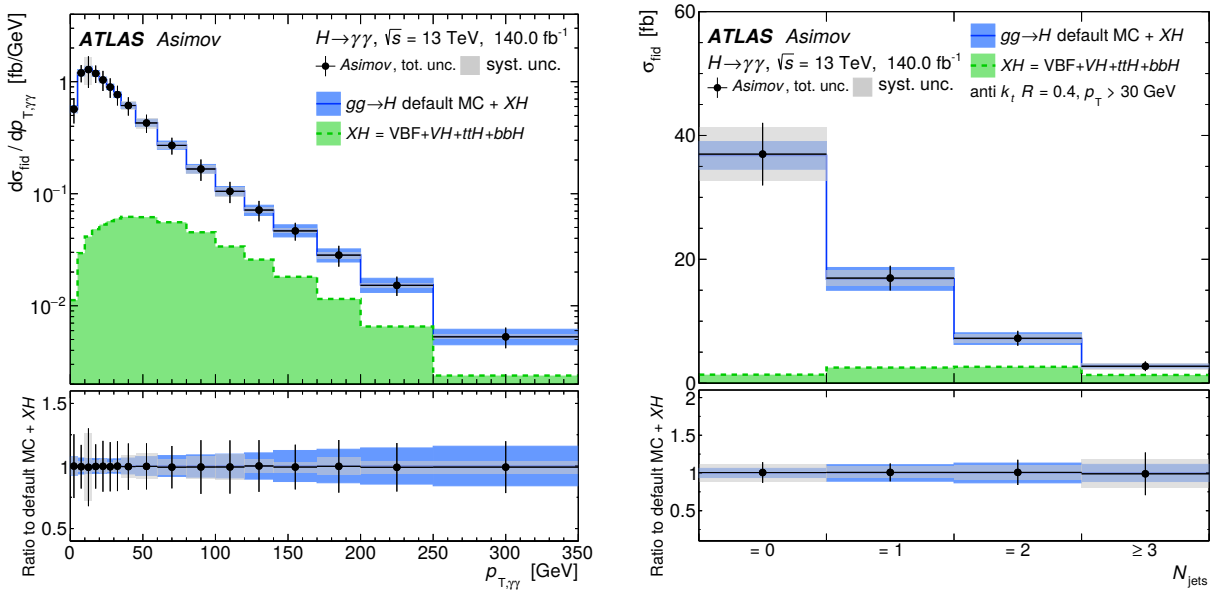

Figure 6.23: Cross checks of the analysis using Asimov datasets for diphoton transverse momentum (left) and jet multiplicity (right) distributions. The extracted cross section is compared to the particle-level MC.

In comparison to the 36 fb^{-1} results [272–274], the statistical uncertainty is reduced by almost a factor of 2, while the experimental systematic uncertainty is of the same order, with larger contributions from spurious signal uncertainty and jet systematics, due to higher pileup conditions. The experimental uncertainty is largely reduced in comparison to the 80 fb^{-1} measurements [275, 276], that used preliminary calibrations.

6.8.2 Unfolded cross sections and theory comparisons

The inclusive fiducial cross section for the $pp \to H \to \gamma\gamma$ process obtained in the most resent analysis using the complete Run 1 dataset is

$$\boxed{\sigma_{\text{fid}} = 65.2 \pm 4.5\,(\text{stat.}) \pm 5.6\,(\text{exp.}) \pm 0.3\,(\text{theory})\,\text{fb} \approx 65.2 \pm 7.2\,\text{fb}}, \quad (6.35)$$

which can be compared with the state-of-the-art Standard Model prediction of $63.5 \pm 3.3\,\text{fb}$, calculated to N^{3}LO in perturbative QCD [325]. The measured value agrees with the prediction within 1 standard deviation. The uncertainty on the measured cross section is dominated by the systematic uncertainties related to signal extraction, namely the photon energy resolution and the spurious signal.

The figures below show the measured differential cross sections and compare them to the nominal MC, as well as the state-of-the-art theoretical predictions discussed in Section 3.6. Note that all additional theoretical predictions provide cross sections only for the ggF process, and the summed cross section of other processes (XH, shown in light green) is added to them from the default MC.

The compatibility between the measured and default MC differential distributions was assessed using a χ^2 test, using the covariance matrix, constructed from the full set of measurement uncertainties, taking into account correlations between bins, as well as theoretical uncertainties on the SM prediction. Table 6.7 lists the p-values obtained in the χ^2 tests which indicate excellent agreement between data and MC for all observables measured in the 2019 analysis [277, 278].

Table 6.7: p-values from χ^2 tests for compatibility of the measured differential distributions with those predicted using the analysis MC, for the observables measured in the 2019 analysis [277, 278]. The tests used the full set of measurement uncertainties for the χ^2 computation.

Observable	$p_{\mathrm{T}}^{\gamma\gamma}$	$\lvert y_{\gamma\gamma}\rvert$	$p_{\mathrm{T}j_1}$	N_{jets}	$\Delta\phi_{jj,\mathrm{signed}}$	m_{jj}
$p(\chi^2)$	0.44	0.68	0.77	0.96	0.82	0.75

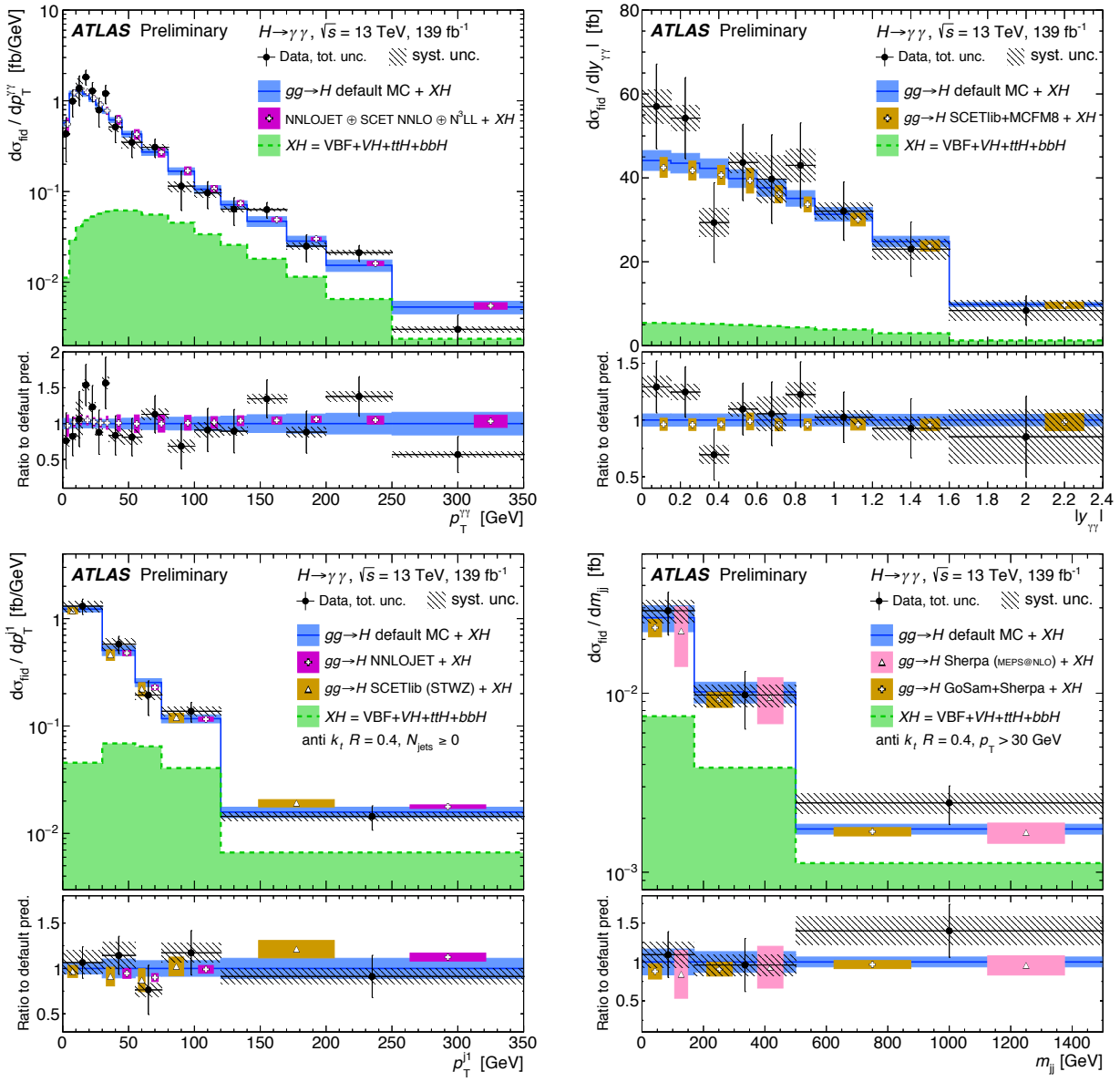

Figure 6.24: Fiducial differential cross section measurements for $p_{\mathrm{T}}^{\gamma\gamma}$, $|y_{\gamma\gamma}|$, $p_{\mathrm{T}}^{j_1}$, and m_{jj} done with $\int L = 139.0\,\mathrm{fb}^{-1}$ in 2019 [277, 278].

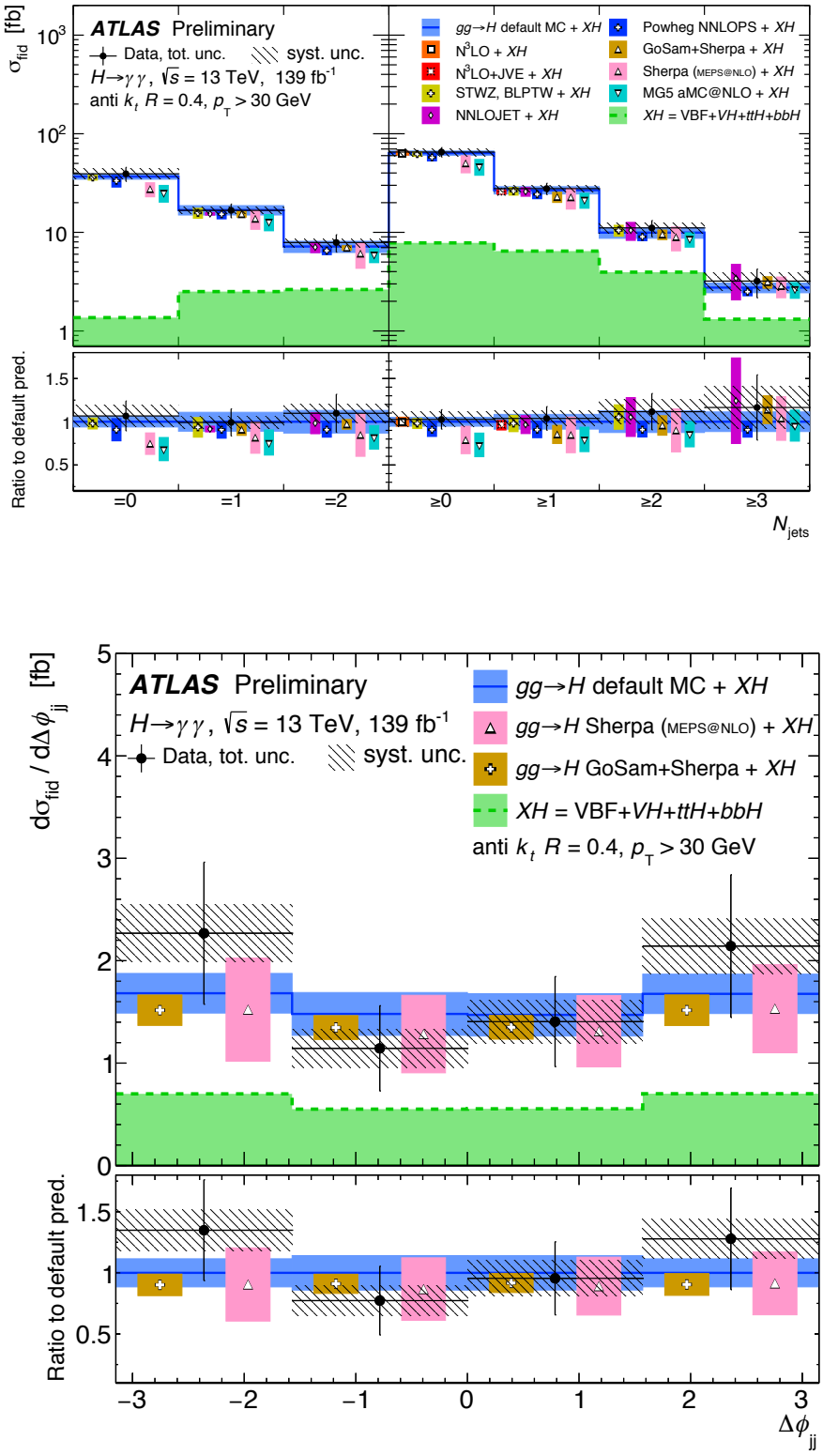

Figure 6.25: Fiducial differential cross section measurements for N_{jets} and $\Delta\phi_{jj}$ done with $\int L = 139.0\,\text{fb}^{-1}$ in 2019 [277, 278].

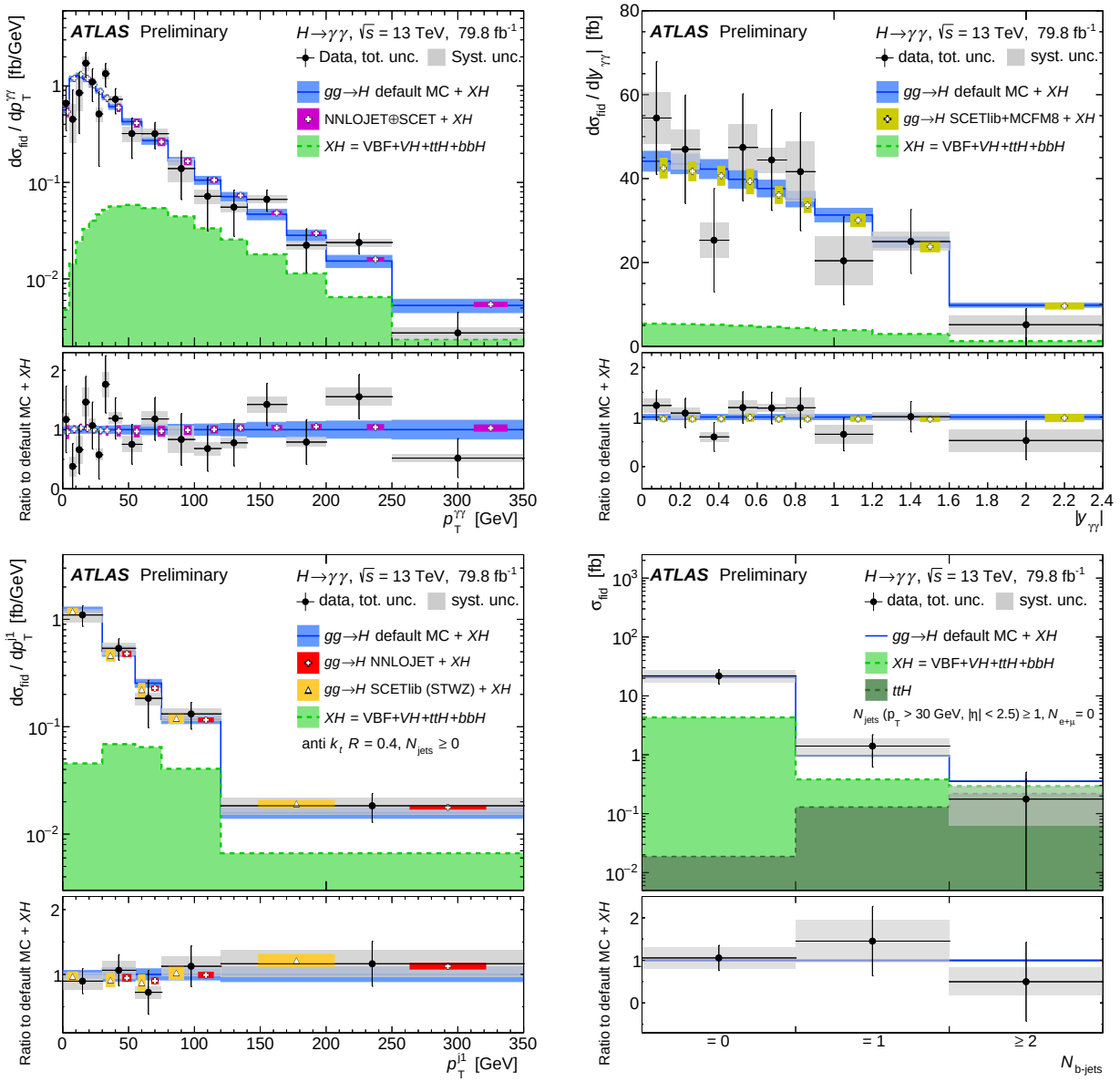

Figure 6.26: Fiducial differential cross section measurements for $p_{\mathrm{T}}^{\gamma\gamma}$, $|y_{\gamma\gamma}|$, $p_{\mathrm{T}}^{j_1}$, and $N_{b\text{-jets}}$ done with $\int L = 79.8\,\mathrm{fb}^{-1}$ in 2018 [275, 276].

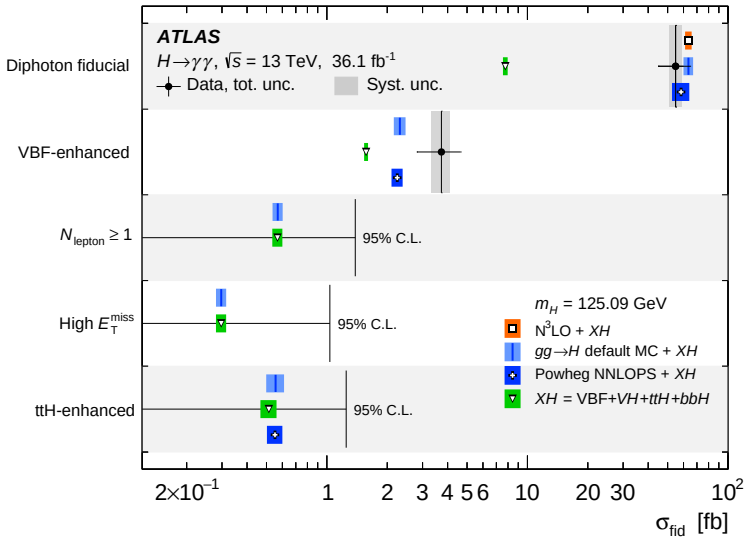

Figure 6.27: Fiducial differential cross section measurements for the fiducial event categories defined in Section 6.4.1 done with $\int L = 36.1\,\text{fb}^{-1}$ in 2017 [272–274].

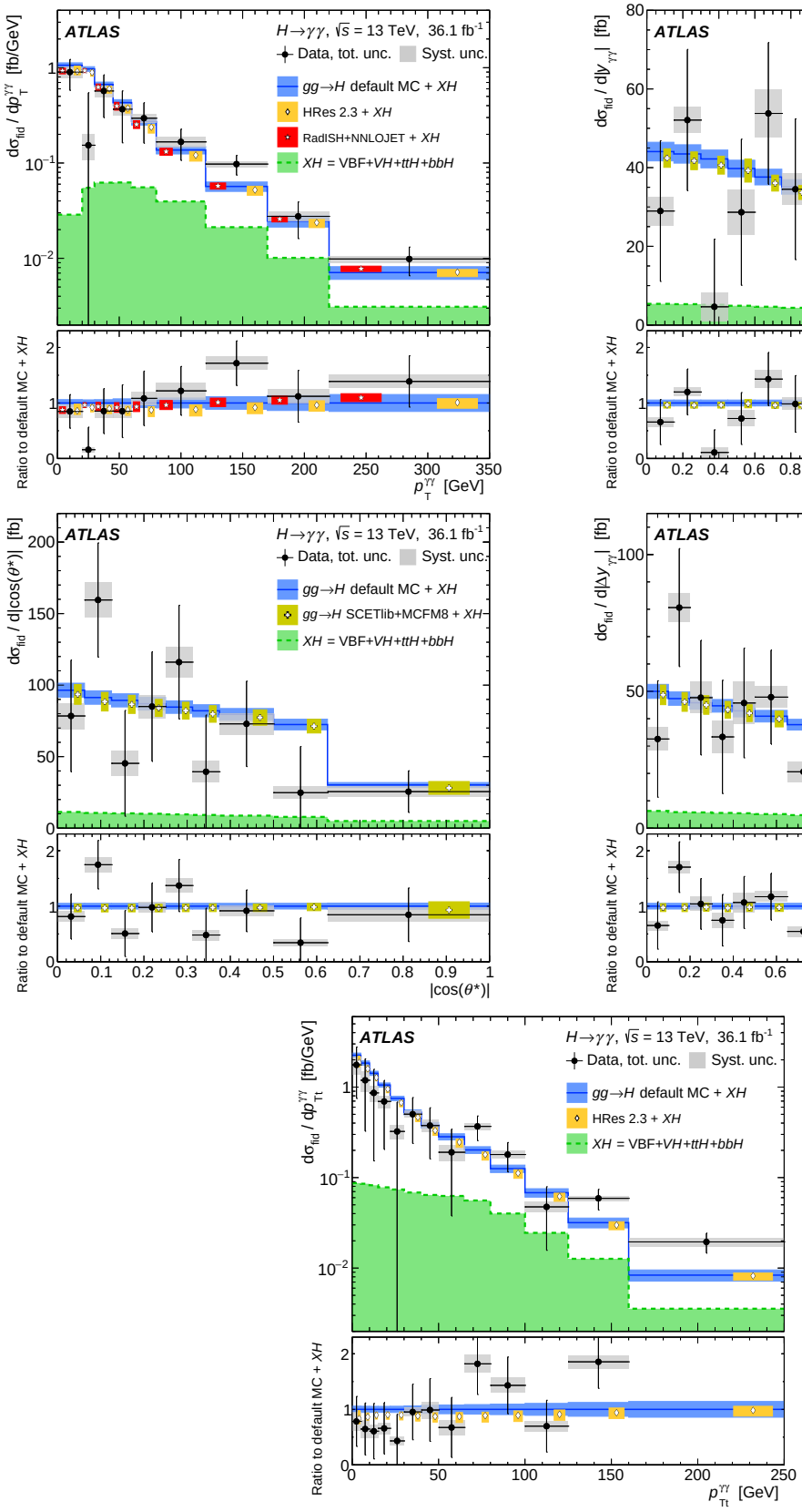

Figure 6.28: Fiducial differential cross section measurements for $p_{\mathrm{T}}^{\gamma\gamma}$, $|y_{\gamma\gamma}|$, $|\cos\theta^*|$, $|\Delta y_{\gamma\gamma}|$, and $p_{\mathrm{Tt}}^{\gamma\gamma}$ done with $\int L = 36.1\,\mathrm{fb}^{-1}$ in 2017 [272–274].

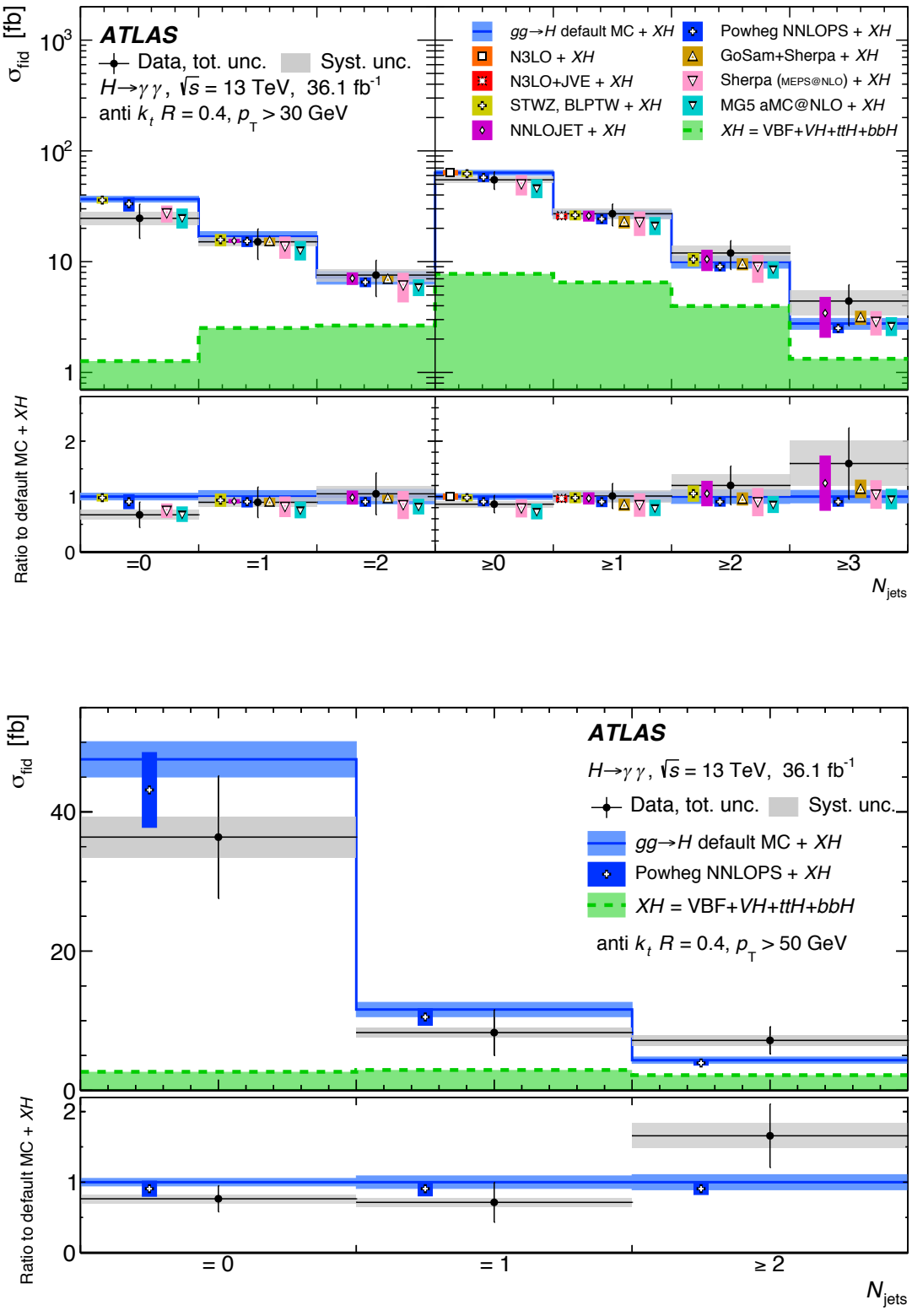

Figure 6.29: Fiducial differential cross section measurements for inclusive and exclusive jet multiplicities, N_{jets}, for $p_{\text{T}}^{j} > 30$ GeV (top) and for $p_{\text{T}}^{j} > 50$ GeV (bottom) done with $\int L = 36.1\,\text{fb}^{-1}$ in 2017 [272–274].

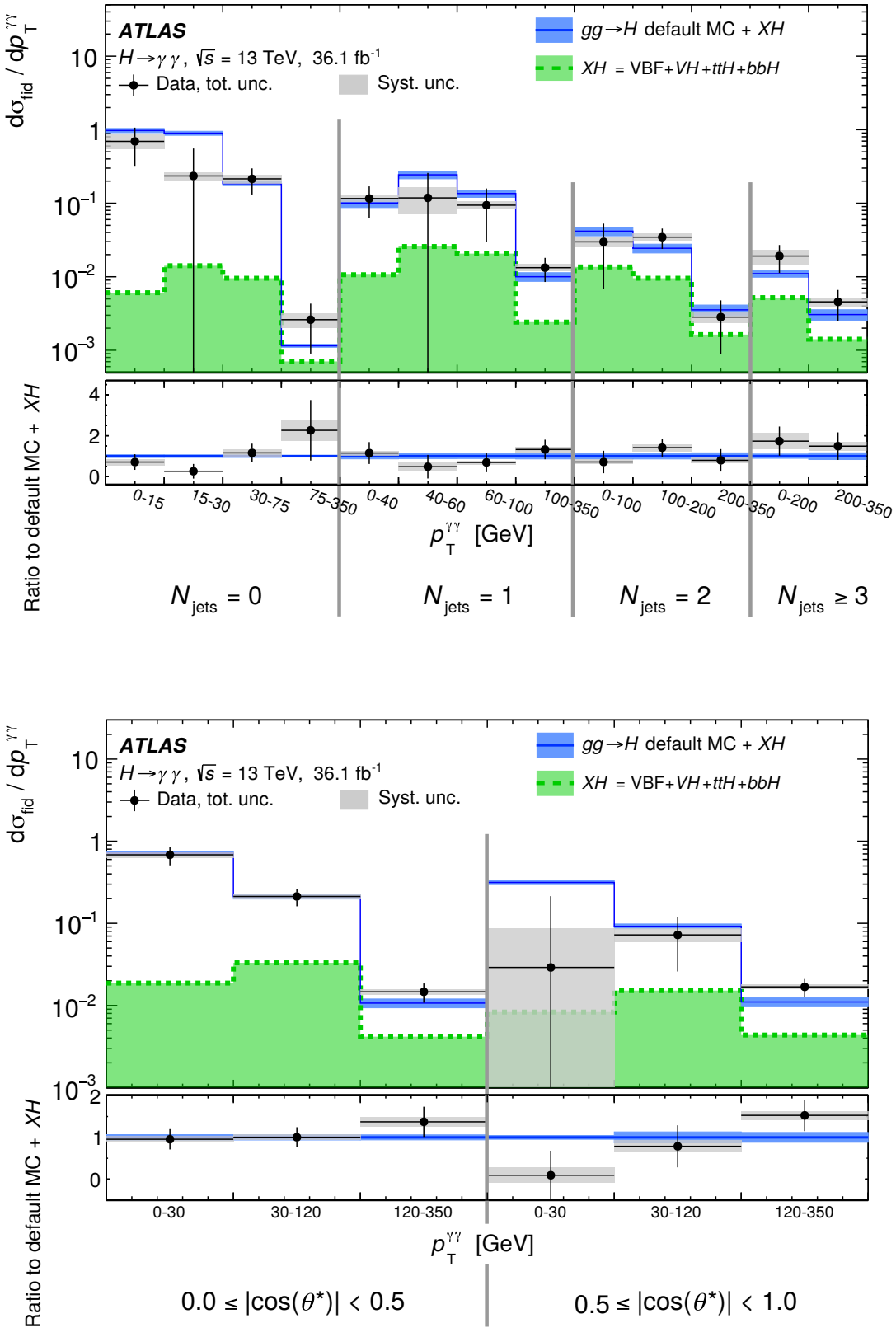

Figure 6.30: Fiducial double-differential cross section measurements for $p_{\mathrm{T}}^{\gamma\gamma}$ further subdivided in N_{jets} (top) and $|\cos\theta^*|$ (bottom) done with $\int L = 36.1\,\mathrm{fb}^{-1}$ in 2017 [272–274].

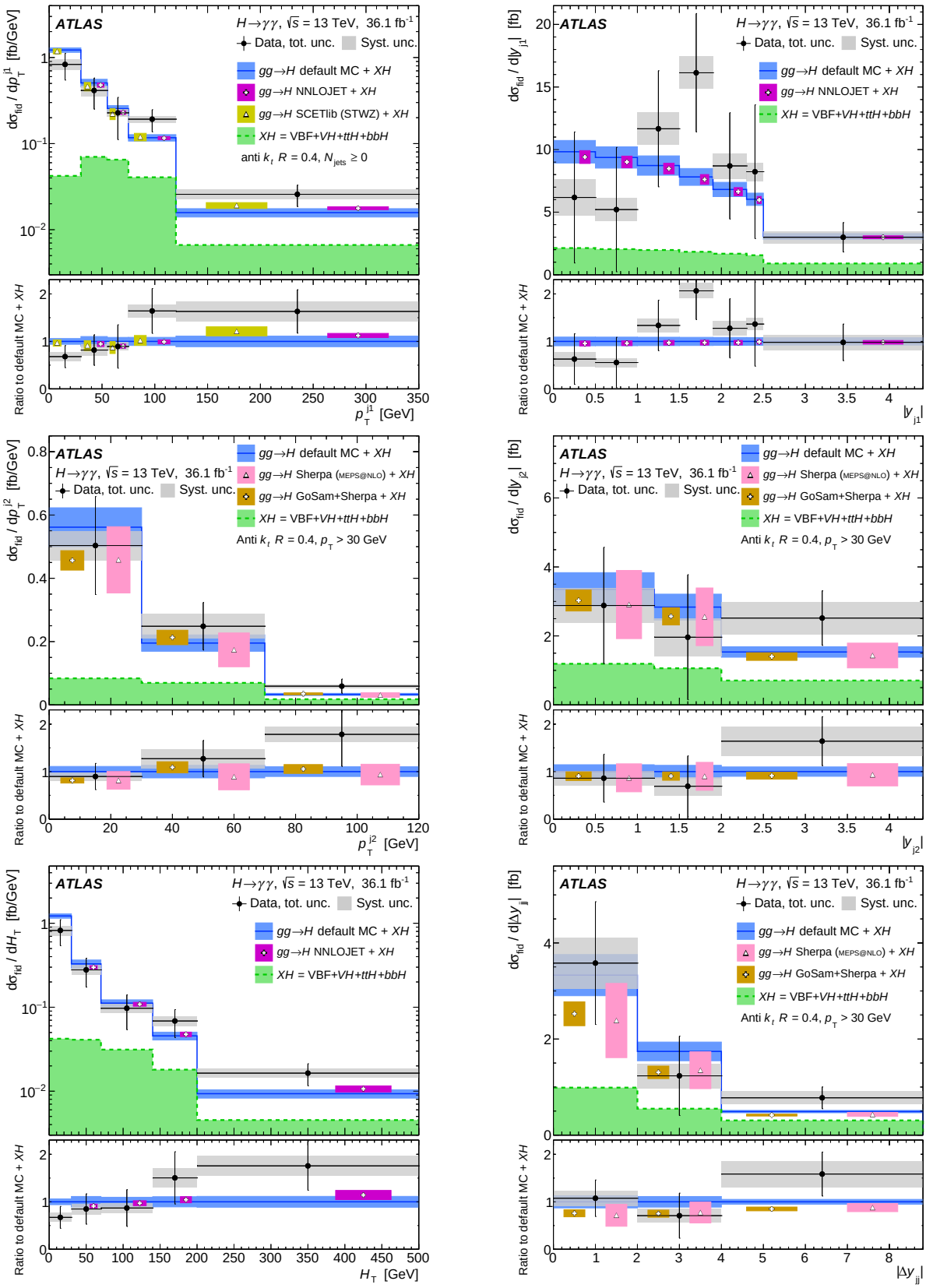

Figure 6.31: Fiducial differential cross section measurements for $p_{\mathrm{T}}^{j_1}$, $|y_{j_1}|$, $p_{\mathrm{T}}^{j_2}$, $|y_{j_2}|$, H_{T}, and $|\Delta y_{jj}|$ done with $\int L = 36.1\,\mathrm{fb}^{-1}$ in 2017 [272–274].

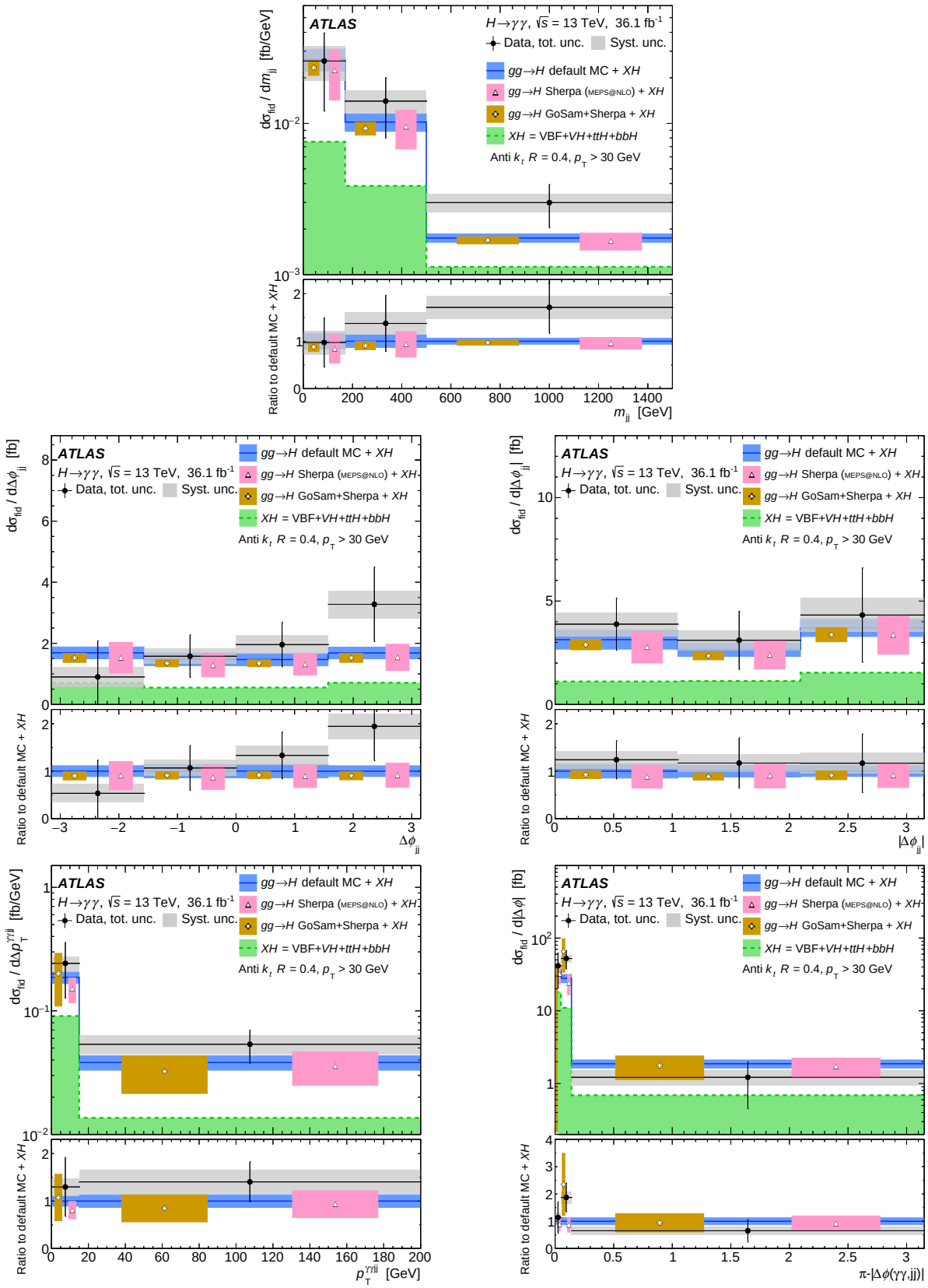

Figure 6.32: Fiducial differential cross section measurements for m_{jj}, $\Delta\phi_{jj}$, $|\Delta\phi_{jj}|$, $p_{\mathrm{T}}^{\gamma\gamma jj}$, and $|\Delta\phi_{\gamma\gamma,jj}|$ done with $\int L = 36.1\,\mathrm{fb}^{-1}$ in 2017 [272–274].

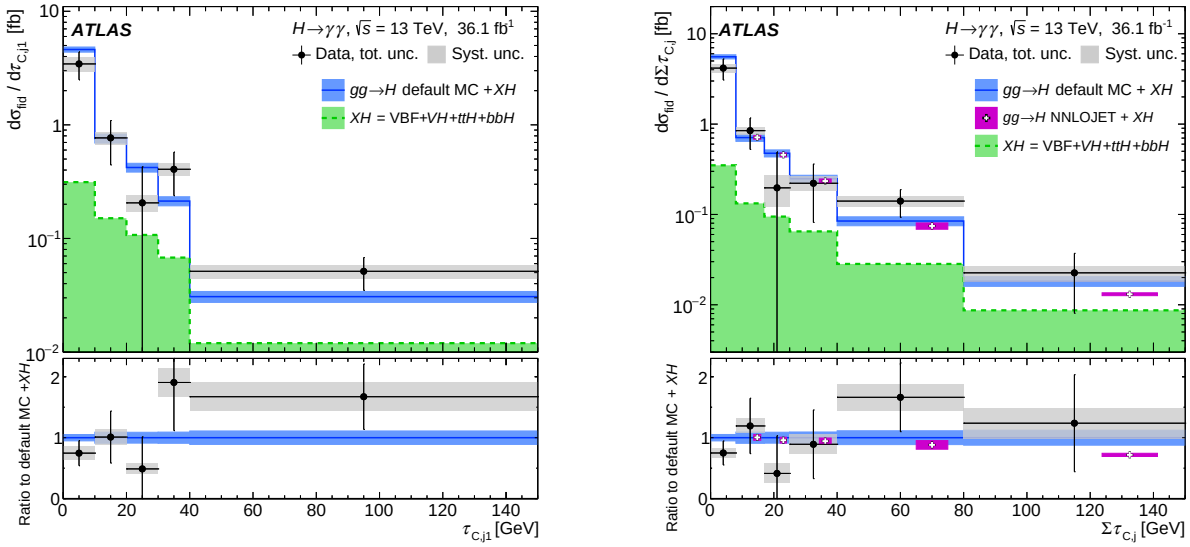

Figure 6.33: Fiducial differential cross section measurements for τ_1 and $\sum \tau_j$ done with $\int L = 36.1\,\text{fb}^{-1}$ in 2017 [272–274].

Chapter 7

Conclusion

This dissertation has presented the cross section measurements of the Higgs boson production process in the diphoton decay channel. The cross section measurements were obtained from a statistical analysis of the ATLAS data collected in the Run 2 of the LHC. The dataset is comprised of proton-proton collision events with the center-of-mass energy of $\sqrt{s} = 13\,\text{TeV}$. The integrated luminosity of the dataset amounted to $139.0 \pm 2.4\,\text{fb}^{-1}$ [280, 281]. Fiducial cross sections were measured in order to reduce model dependence by defining a fiducial phase space closely resembling the phase space of detector acceptance. The measurements were inclusive, in the sense that presence of additional objects such as jets and leptons was allowed in the selected events. Additional event categories were defined and analyzed to measure cross section as a function of jet multiplicity and lepton presence. Differential cross section measurements were performed for a number of variables that characterize kinematic and quantum properties of the Higgs boson. Care was taken in deriving the correction factors, estimating the uncertainties, and optimizing the binning of the differential distributions.

The inclusive fiducial cross section obtained from the latest analysis [277, 278], including the $H \to \gamma\gamma$ branching ratio, is

$$\sigma_{\text{fid}} = 65.2 \pm 4.5\,(\text{stat.}) \pm 5.6\,(\text{exp.}) \pm 0.3\,(\text{theory})\,\text{fb} \approx 65.2 \pm 7.2\,\text{fb}. \tag{7.1}$$

Its combined fractional uncertainty is 11%. The measured cross section can be compared with the most accurate Standard Model prediction of $63.5 \pm 3.3\,\text{fb}$, calculated at N^3LO in perturbative QCD [325]. The differential cross sections were presented in Section 6.8.2 and were compared to the state-of-the-art theoretical predictions. The analysis results are in excellent agreement with the SM predictions.

Extrapolation of the measured fiducial cross section to the full phase space for the Higgs boson production in the $H \to \gamma\gamma$ channel yields a value of $56.7^{+6.4}_{-6.2}\,\text{pb}$. For comparison, the total cross section from the ATLAS $H \to ZZ^* \to 4\ell$ analysis is $54.4^{+5.6}_{-5.4}\,\text{pb}$. The combination of the two measurements yields $56.1\,^{+4.5}_{-4.3} \pm 3.2\,(\text{stat.})\,^{+3.1}_{-2.8}\,(\text{sys.})\,\text{pb}$ [326]. The derived total cross sections are in good agreement with the SM prediction of $55.6 \pm 2.5\,\text{pb}$.

An updated $H \to \gamma\gamma$ cross section analysis, using the full Run 2 ATLAS dataset, including the full list of observables, is currently being prepared and is expected to be completed in 2021.

The future prospects for the analysis include improved measurements with the larger dataset that will be collected in the Run 3 of the LHC, and, further in the future, during the operation of the HL-LHC.

The high-p_{T} Higgs boson phase space is of particular interest for future analyses, as it provides a much higher purity sample of the Higgs boson production events relative to the irreducible diphoton background. With an increased integrated luminosity, this phase space will become more accessible and will be investigated more thoroughly.

APPENDICES

APPENDIX A

GoSam ntuples

A.1 GoSam ntuples

A considerable amount of computer resources is involved in generation of MC events. With data storage becoming more easily available, it is often more practical to store each generated event, rather than to fill histograms and immediately discard the events. The approach of saving the events affords more flexibility, especially in exploratory studies, as the saved events can be quickly iterated over to produce histograms for any desired combination of variables. Many parameters can be adjusted without rerunning the event generator, such as kinematic cuts, binning of the histograms, or definitions of observables and event categories. Depending on the saved information, even parameters of the cross section calculation or the physics assumptions can be modified by reweighting the events. The reduced turnover time allows to quickly explore a process of interest within a desired phase space. For complex processes with high multiplicity of final state particles or higher order calculations, reading saved events instead of generating them anew can be several orders of magnitude faster. Files containing MC events have colloquially acquired the name of ntuples. Ntuples typically contain the 4-momenta of the final state particles together with additional information, such as event weights and particle ids.

Through collaboration with the GoSam authors [106, 109, 327], we acquired a large

number* of GoSam ntuples for QCD production of Higgs boson and diphoton in association with 1, 2, or 3 jets. GoSam is a package that provides means for automated calculation of one-loop amplitudes for multi-particle processes in renormalizable quantum field theories. Though it is not a stand-along event generator, combined with Sherpa, GoSam pushed the frontier for the number of jets in the final state, calculated at matrix element level, rather than through parton shower, in differential cross section predictions. At the time they were generated, the Higgs + jets ntuples represented the result of the cutting edge calculations [328, 329].

The format of GoSam ntuples [330] was adopted from that of the earlier developed BlackHat+Sherpa ntuples [100, 107, 108, 331–333], which saw wide use, for example in the studies published in [334–340]. The ntuples are saved as `ROOT` [310] files, with one tree of single-value and array branches, representing variables describing weighted events. The file format is summarized in Table A.1. A set of ntuples for a given process, for example Higgs + 1 jet at $\sqrt{s} = 13\,\text{TeV}$, consists of a number of files, with multiple files corresponding to each NLO contribution type (B, RS, I, V) from the Catani–Seymour subtraction method.† Splitting sets of events into multiple files, typically containing a few million events, allows to easily run analysis programs in parallel, particularly on a computer cluster using a batch system, such as `HTCondor` [342]. Outputs of individual processing jobs can then be merged to obtain the full result.

Observables are computed by taking weighted averages of their values over events of the same type and adding the averages from each NLO contribution. This can be written as

*The amount of GoSam ntuples we have amassed consists of 21518 files in 88 sets, containing 5.9×10^{10} events, and occupying 18.6 TB of disk space. Special thanks for providing these goes to Gionata Luisoni and Nicolas Greiner.

†See Section 3.2 for the preliminary discussion.

Table A.1: Format of GoSam ROOT ntuples [330].

Name	Type	Description
t3	TTree	ROOT tree containing generated events.
id	Int_t	Event index number. Real emission entries and their associated counterterms share the same id.
ncount†	Int_t	Number of trials between the previous and current event during generation. The number of times an event should be counted.
nparticle	Int_t	Number of particles in the final state.
px, py, pz, E	Double_t[nparticle]*	Arrays of 4-momenta components of the final-state particles.
kf	Int_t[nparticle]	PDG [14] codes of the final-state particles.
weight	Double_t	Total weight of the entry.
weight2	Double_t	Correlated weight used for the RS contribution. Identical to weight for the B, V, and I contributions.
me_wgt	Double_t	Coefficient of the product of parton distribution functions in weight. For the B, V, and RS contributions, this is the squared matrix element multiplied by the phase space measure and the Jacobian from Sherpa's phase space mapping.
me_wgt2	Double_t	Coefficient of the PDFs product in weight2.
ps_wgt†	Double_t	Phase space weight.
x1, x2	Double_t	Fractions of hadron momentum carried by the incoming partons.
x1p, x2p	Double_t	Secondary momentum fractions used in integrated subtraction entries [333].
id1, id2	Int_t	PDG codes of the incoming partons.
id1p, id2p†	Int_t	PDG codes of incoming partons in subtraction events.
fac_scale	Double_t	Factorization scale used, $\mu_{F,0}$.
ren_scale	Double_t	Renormalization scale used, $\mu_{R,0}$.
nuwgt	Int_t	Number of additional weights.
usr_wgts	Double_t[nuwgt]	Additional weights needed to recompute entries' weights for different scale or PDF choices.
part	Char_t[2]	Type of contribution: B, V, I, or RS.
alphasPower	Char_t	Power of the strong coupling.
alphas	Double_t	α_s value used for this entry.

*In an older version, components of the 4-momenta were stored as Float_t instead of Double_t.
†Additional new branches introduced for the EDNtuples [341].

follows,

$$\langle \mathcal{O} \rangle = \sum_t \langle \mathcal{O} \rangle_t, \quad \langle \mathcal{O} \rangle_t = \frac{1}{N_t} \sum_{i \in t} w_i \mathcal{O}_i, \tag{A.1}$$

where $\mathcal{O}$ is an observable, $t \in \{\mathrm{B}, \mathrm{RS}, \mathrm{I}, \mathrm{V}\}$ represents a contribution type, i is the index of an event of type t, N_t is the number of events of type t, and w_i and $\mathcal{O}_i$ are the event weight and the value of the observable for the event i respectively. The sum $\sum w_i \mathcal{O}_i$ typically runs over events from multiple ntuple files. But, subsets of events of the same type can be used, if a shorter run time is preferred over statistical accuracy. Most often, the observable of interest is the cross section as a function of one or more variables that characterize the process, or, in other words, the joint distribution of the variables, which is represented by a histogram populated by the weighted events. In that case,

$$\mathcal{O}_i = \delta_i^b = i \in b, \tag{A.2}$$

where δ_i^b is a boolean variable, which is 1 if event i falls into bin b of the histogram and 0 otherwise. $\langle \mathcal{O} \rangle_b = \sigma_b$ is the total cross section in bin b, and the differential cross section is obtained by dividing σ_b by the bin width.

The statistical uncertainty is obtained by the standard prescription for MC integration,

$$\varepsilon_{\mathcal{O}} = \left[\sum_t \varepsilon_{\mathcal{O}_t}^2 \right]^{1/2}, \quad \varepsilon_{\mathcal{O}_t} = \frac{1}{\sqrt{N_t(N_t - 1)}} \left[\sum_{i \in t} \left(w_i \mathcal{O}_i \right)^2 - \frac{1}{N_t} \left(\sum_{i \in t} w_i \mathcal{O}_i \right)^2 \right]^{1/2}, \tag{A.3}$$

where statistically independent contributions from different types are added in quadrature, while within a type, the uncertainty is estimated using the equation for the unbiased sample variance. ε is used to represent uncertainty to avoid confusion with σ used for the cross section. An illustrative example is the case in which one wants to look at both exclusive

and inclusive distributions.* The value for $\langle\mathcal{O}\rangle_b$ in the inclusive histogram can simply be obtained by adding the $\langle\mathcal{O}\rangle_b$ in the exclusive one. But adding the $\varepsilon_{\mathcal{O}_b}$ in quadrature will not yield uncertainty estimates as accurate as following Eq. (A.3). For a large number of events, however, the difference may be insignificant, as the second term in the square brackets will vanish.

Another situation where statistical uncertainty needs to be handled carefully is in rebinning. If bins b_1 and b_2 need to be merged, the second term in Eq. (A.3) is the square of the sum, and will remain the same; but the first term is the sum of squares, which becomes

$$\sum_{i\in t}\left(w_i\delta_i^{b_1\cup b_2}\right)^2=\sum_{i\in t}\left(w_i\left(\delta_i^{b_1}\vee\delta_i^{b_2}\right)\right)^2=(w_1+w_2)^2=w_1^2+w_2^2+2w_1w_2, \tag{A.4}$$

where w_1 and w_2 are the cumulative weights in the respective bins.

There is an additional caveat concerning specifically the real emission (RS) ntuples. These ntuples are special in that any one of their events generally consists of more than one tree entry. Because of this, one must make the following substitution in Eq. (A.3):

$$\text{For RS ntuples:}\quad w_i\mathcal{O}_i\to\sum_{j\in i}w_j\mathcal{O}_j. \tag{A.5}$$

When filling histograms, the weights of the entries corresponding to the same event that fall into the same bin must be added before they are squared. The multiple entries correspond to different phase space configurations: a real emission configuration and counter-configurations. The latter correspond to the subtraction term that regulates the square

*The relationship between exclusive and inclusive distributions is the same as between p.d.f. and c.d.f., the later being the integral of the former. This terminology is typically used in discrete context, such as distributions of jet multiplicity. A histogram showing the exclusive distribution would, for example, contain a bin for $n = 2$, while the corresponding bin in the inclusive distribution would be for $n \geq 2$.

of the matrix element in the soft and collinear limits, where the unregulated matrix element diverges. The real emission configurations and subtraction counter-configurations are strongly anticorrelated. This means that simply adding their weights independently, as in Eq. (A.3), will grossly overestimate the statistical error. The estimated error would typically be of order the central value. Using these weights will, however, yield the correct central value, Eq. (A.1) [330]. The ntuples contain a second set of weights, `weight2` rather then `weight`, which allows to take the anticorrelation into account. The entries in the `ROOT` file corresponding to the same RS event are written consecutively and can be identified by the same event `id`. Because `weight2` = `weight` for B, I, and V type files, in practice, one should always use the `weight2` branch for histogramming.

A.2 Reweighting of ntuples

In order to evaluate the validity of QCD predictions, it is important to explore their dependence on the choice of scales and PDFs. A very convenient feature of the GoSam ntuples is that they save information required to modify scales and PDFs of existing events, avoiding the need to generate the events anew. This is done by reweighting the events according to the prescription [330] described below. The prescription varies depending on the NLO contribution type the event represents. In the following, variables written in `monospace` font refer to the ntuple branches listed in Table A.1. The indices of branch arrays start at zero, as in `C`.

A.2.1 Born and real-subtraction contributions

For B and RS type events, the new weight, w, is given by

$$n = \texttt{alphasPower}, \tag{A.6a}$$

$$w = \texttt{me\_wgt2}\, f_1(\texttt{id1}, \texttt{x1}, \mu_\mathrm{F})\, f_2(\texttt{id2}, \texttt{x2}, \mu_\mathrm{F})\, \frac{\alpha_\mathrm{s}(\mu_\mathrm{R})^n}{\texttt{alphas}^n}. \tag{A.6b}$$

The PDFs of the interacting partons are denoted f_1 and f_2. They depend on the respective parton type (`id1`, `id2`), momentum fraction (`x1`, `x2`), and the new factorization scale, μ_F. For the LHC, both f_1 and f_2 are proton PDFs. α_s is the strong coupling, running with respect to the renormalization scale, μ_R.* n is the power of the strong coupling and depends on the number of emitted jets.

If the factorization scale and the PDFs don't need to be changed, α_s contains the whole renormalization scale dependence, and reweighting can be simplified to

$$\text{If } \mu_\mathrm{F} = \texttt{fac\_scale}, \quad w = \texttt{weight2}\, \frac{\alpha_\mathrm{s}(\mu_\mathrm{R})^n}{\texttt{alphas}^n}. \tag{A.7}$$

Conversely, if α_s and μ_R need no variation,

$$\text{If } \mu_\mathrm{R} = \texttt{ren\_scale}, \quad w = \texttt{me\_wgt2}\, f_1(\texttt{id1}, \texttt{x1}, \mu_\mathrm{F})\, f_2(\texttt{id2}, \texttt{x2}, \mu_\mathrm{F}). \tag{A.8}$$

Note, that for the Born contribution, but not for the real-subtraction, `weight` and `weight2`, and likewise `me_wgt` and `me_wgt2` are equal. Reweighting has to be done for every entry of RS type events.

*The value of α_s at different renormalization scale values can be found using `LHAPDF` [73] by calling the `LHAPDF::PDF::alphasQ()` function.

A.2.2 Virtual contributions

The treatment of V type events is similar to that of B and RS, except that the matrix element has an explicit dependence on μ_R. In dimensional regularization, this dependence arises from the introduction of a scale to give the coupling g the required dimension, $g \to g\mu^\epsilon$, along with the $\overline{\mathrm{MS}}$ ultraviolet subtraction that replaces the bare coupling g_0 with the physical coupling $g(\mu_\mathrm{R})$ [330].

$$n = \texttt{alphasPower}, \tag{A.9a}$$

$$l = \log\left(\frac{\mu_\mathrm{R}^2}{\texttt{ren\_scale}^2}\right), \tag{A.9b}$$

$$\omega_0 = \texttt{me\_wgt} + l\,\texttt{usr\_wgts[0]} + \frac{l^2}{2}\,\texttt{usr\_wgts[1]}, \tag{A.9c}$$

$$w = \omega_0\, f_1(\texttt{id1}, \texttt{x1}, \mu_\mathrm{F})\, f_2(\texttt{id2}, \texttt{x2}, \mu_\mathrm{F})\, \frac{\alpha_\mathrm{s}(\mu_\mathrm{R})^n}{\texttt{alphas}^n}. \tag{A.9d}$$

If μ_R is not changed, the scale-changing logarithm in Eq. (A.9b) vanishes together with the additional terms in Eq. (A.9c) and Eq. (A.9d) simplifies to the Born case.

A.2.3 Integrated subtraction contributions

Reweighting computation for the I type events is the most complicated. It requires 16 additional weights (`usr_wgt[2]`, …, `usr_wgt[17]`), computed from the virtual pole coefficients and other quantities extracted from the Catani–Seymour subtraction formalism [51]. Discussion of the meaning of the `me_wgt` and `usr_wgts` terms can be found in [330].

$$n = \texttt{alphasPower}, \tag{A.10a}$$

$$l = \log\left(\frac{\mu_{\mathrm{R}}^2}{\texttt{ren\_scale}^2}\right), \tag{A.10b}$$

$$\omega_0 = \texttt{me\_wgt} + l\,\texttt{usr\_wgts[0]} + \frac{l^2}{2}\,\texttt{usr\_wgts[1]}, \tag{A.10c}$$

$$\omega_i = \texttt{usr\_wgt}[i+1] + \texttt{usr\_wgts}[i+9]\,\log\left(\frac{\mu_{\mathrm{F}}^2}{\texttt{fac\_scale}^2}\right), \tag{A.10d}$$

$$\begin{aligned} m = {} & \omega_0\, f_1(\texttt{id1}, \texttt{x1}, \mu_{\mathrm{F}})\, f_2(\texttt{id2}, \texttt{x2}, \mu_{\mathrm{F}}) \\ & + f_2(\texttt{id2}, \texttt{x2}, \mu_{\mathrm{F}}) \sum_{j=1}^{4} f_1^{(j)}(\texttt{id1}, \texttt{x1}, \texttt{x1p}, \mu_{\mathrm{F}})\, \omega_j \\ & + f_1(\texttt{id1}, \texttt{x1}, \mu_{\mathrm{F}}) \sum_{j=1}^{4} f_2^{(j)}(\texttt{id2}, \texttt{x2}, \texttt{x2p}, \mu_{\mathrm{F}})\, \omega_{j+4} \end{aligned} \tag{A.10e}$$

$$w = m\,\frac{\alpha_{\mathrm{s}}(\mu_{\mathrm{R}})^n}{\texttt{alphas}^n}, \tag{A.10f}$$

where

$$f_p^{(1)}(i, x, x', \mu_{\mathrm{F}}) = \begin{cases} p = \text{quark}: & f_p(i, x, \mu_{\mathrm{F}}), \\ p = \text{gluon}: & \sum_{q \in \text{quarks}} f_p(i, x, \mu_{\mathrm{F}}), \end{cases} \tag{A.11a}$$

$$f_p^{(2)}(i, x, x', \mu_{\mathrm{F}}) = \begin{cases} p = \text{quark}: & f_p(i, x/x', \mu_{\mathrm{F}})/x', \\ p = \text{gluon}: & \sum_{q \in \text{quarks}} f_p(q, x/x', \mu_{\mathrm{F}})/x', \end{cases} \tag{A.11b}$$

$$f_p^{(3)}(p, x, x', \mu_{\mathrm{F}}) = f_p(g, x, \mu_{\mathrm{F}}), \tag{A.11c}$$

$$f_p^{(4)}(p, x, x', \mu_{\mathrm{F}}) = f_p(g, x/x', \mu_{\mathrm{F}})/x'. \tag{A.11d}$$

A.3 GoSam distributions with uncertainties

The reweighting formalism described in Section A.2 was used to assess the uncertainty of GoSam predicted distributions for many observables relevant for the Higgs + jets production at the LHC, such as those provided for the $H \to \gamma\gamma$ cross section analysis. Here, several distributions with estimated MC statistics, scale, and PDF uncertainties are shown with finer binning for reference. These distribution were prepared similarly to the ones used for comparisons with the $H \to \gamma\gamma$ analysis results, but are different in several ways.

The distributions given below were prepared using NLO GoSam ntuple sets for Higgs boson + 1, 2, and 3 jets production in proton-proton collisions at $\sqrt{s} = 13\,\text{TeV}$. The calculation was done in the Higgs effective field theory (HEFT) approximation, corresponding to the infinite top quark mass limit, $m_t \to \infty$. The ntuples were reweighted using the $\hat{H}''_{\text{T}}$ central scale, defined in Eq. (3.6), and the CT14nlo PDF set [25]. The scale uncertainty was estimated using the 7-point variation scheme, and the PDF uncertainties using the Hessian method. The events were only simulated at the parton level, and include neither hadronization nor Higgs boson decays. Electroweak effects are also not included. As these predictions do not include Higgs boson decays, no branching ratio factors or cuts on the possible decay products, such as photons, were applied. Typically, the diphoton branching ratio of 2.27×10^{-3}, in combination with the photon cuts listed in Section 6.3.2, reduces the cross section by a factor of approximately 10^{-3}, from the pb to the fb level. The AntiKt jet clustering algorithm was applied to the final state partons, with the radius parameters, $R = 0.4$. The typical ATLAS jet cuts of $p_{\text{T}} > 30\,\text{GeV}$ and $\eta < 4.4$ were applied to the clustered jets.

Fig. A.1 shows the predicted cross section as a function of jet multiplicity. The GoSam

NLO calculations are technically inclusive with respect to the additional radiation. The real-subtraction ntuples contain an additional final state parton, and histograms populated without an explicit cut, requiring the number of jets to be strictly equal to the nominal number of final state partons, estimate inclusive distributions. The values of the first three bins in the exclusive jet multiplicity distribution in Fig. A.1 were obtained from the Higgs boson + 1, 2, and 3 jets ntuples respectively, with the strict multiplicity cut applied. The same bins in the inclusive distribution differ in that they also include the events from the respective sets with the additional jet from the real correction. The last bin in both distributions is populated only by the events from the Higgs boson + 3 jets set, which contain the additional fourth jet due to the real correction.

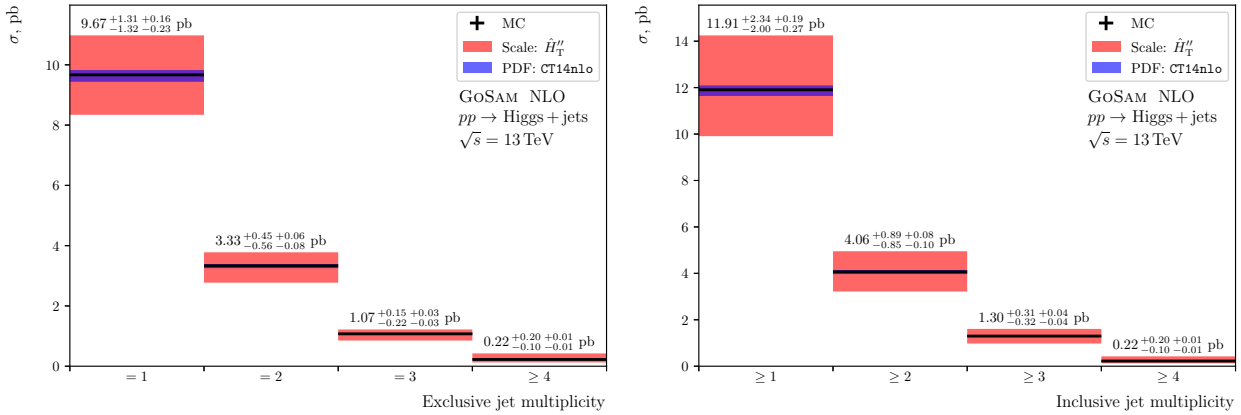

Figure A.1: GoSam NLO predictions for jet multiplicity distributions. The cross section in each of the first three bins was calculated using the set of ntuples corresponding to the respective number of jets. The last bin represents the additional radiation due to the real correction to the process with 3 nominal jets.

The figures below show the predictions for the distributions of observables related to the kinematics of the Higgs boson and jets.

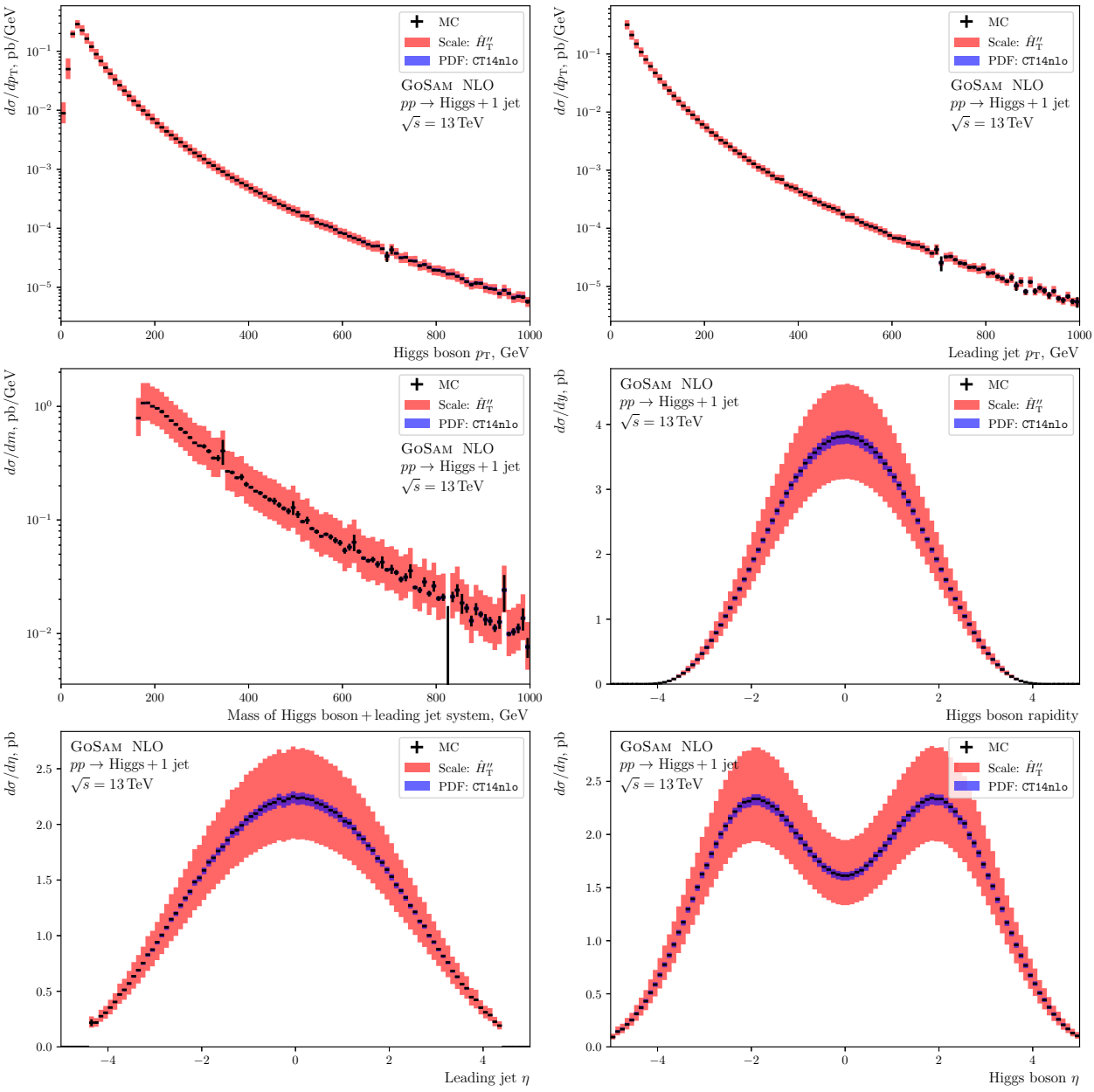

Figure A.2: GoSam NLO predictions for distributions of observables in Higgs boson + 1 jet events.

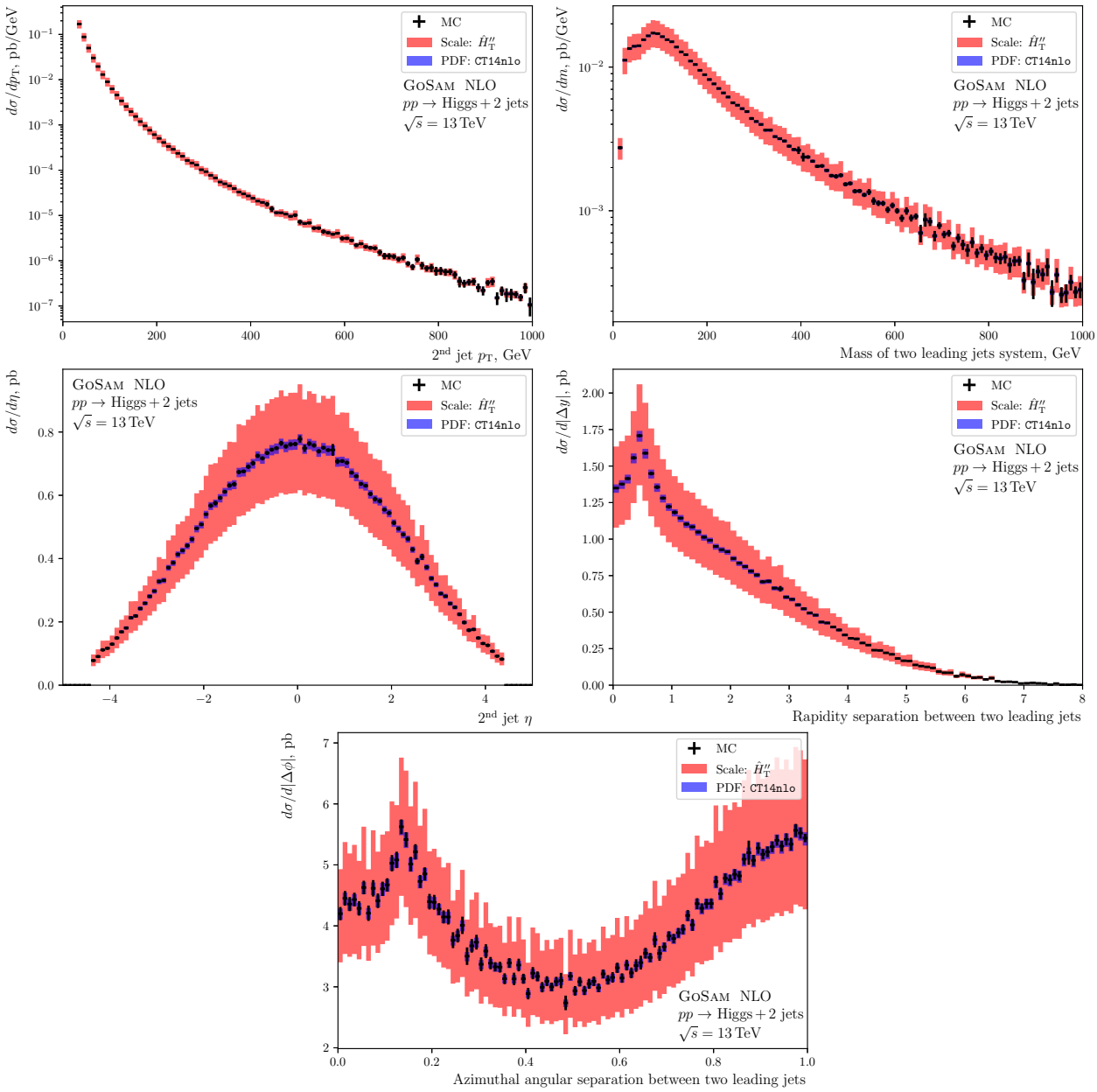

Figure A.3: GoSam NLO predictions for distributions of observables in Higgs boson + 2 jets events.

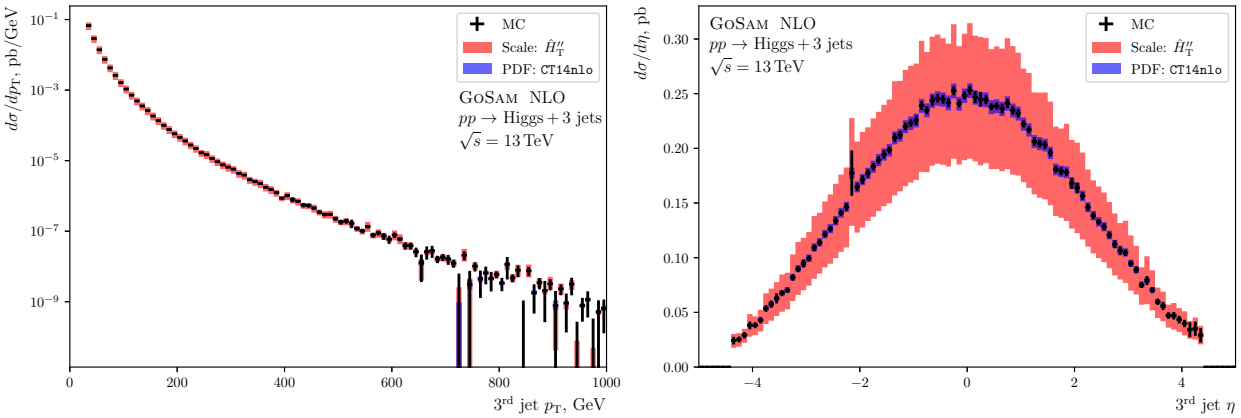

Figure A.4: GoSam NLO predictions for distributions of observables in Higgs boson + 3 jets events.

APPENDIX B

Effects of finite top quark mass in Higgs boson production

B.1 Higgs effective field theory

A technique commonly used in calculations of the Higgs boson production is the effective field theory (EFT) approximation,* whereby an effective coupling of the Higgs boson to gluons is derived by taking the infinite limit of the mass of the heavy virtual quark involved in the loop mediating the interaction. The EFT approximation reduces the number of loops in the relevant Feynman diagrams by 1, which results in a substantial reduction in complexity of the scattering amplitude expressions. This simplification is especially important for fixed order matrix element calculations in processes involving additional QCD radiation, i.e. jets. Due to the coupling of the Higgs boson to fermions being proportional to the fermion's mass, $-im_f/v$, over 99% of the effective coupling of the Higgs boson to gluons is accounted for by the top quark loop.

The EFT approximation has its range of validity over the phase space of the process. The most obvious limitation is that when the partonic $\sqrt{s}$ reaches $2m_t$, there is enough energy for the virtual top quark to go on shell. In other words, the loop can be resolved,

*In this context, the Higgs effective field theory is also commonly abbreviated as HEFT. [343]

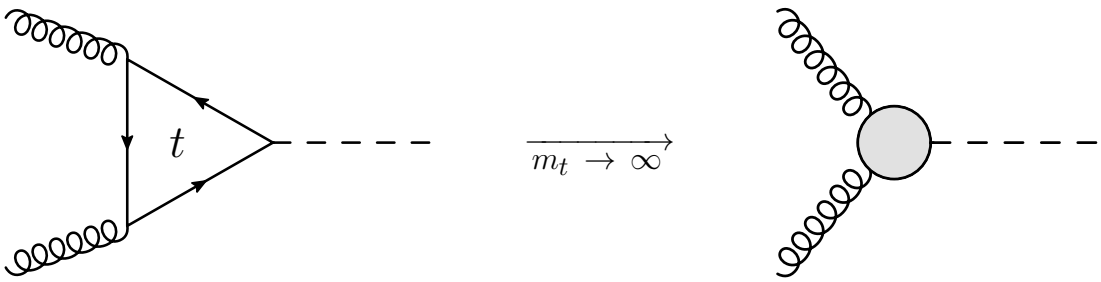

Figure B.1: Using effective field theory (EFT), an effective coupling of the Higgs boson to gluons can be derived by taking the limit $m_t \to \infty$. This approach simplifies calculations by reducing the number of loops, but the approximation is only valid for $p_{\mathrm{T}}^{H} \lesssim 2m_t \approx 350\,\mathrm{GeV}$.

and the assumption that the m_t is large relative to the energy scale of the process becomes invalid. The operating energy of the LHC is sufficient to obtain high-p_{T} events outside the validity range of the EFT, and the $H \to \gamma\gamma$, as well as other, analyses have begun exploring this regime. As the integrated luminosity of the LHC will continue to increase, and larger datasets will expand the volume of accessible phase space, it is important to understand the limitations of the EFT approach. Conversely, exploring beyond the range of validity of the EFT may provide interesting physics insights. Understanding of the impact of the Higgs boson production via a fermionic loop with a finite mass propagator on the kinematics of the Higgs + jets events can provide new approaches not only to directly observe the top quark loop, but also to search for hypothetical BSM particles that could potentially participate in the loop, as well as to examine our understanding of QCD and the interactions of the Higgs boson.

Although the first calculations of the Higgs boson + jets production, incorporating the full mass dependence, were done at the end of the '80s, general purpose MC event generation, including the finite top mass effects, has become available only more recently, in particular with the help of GoSam [341]. The technology to include the finite m_t in fixed-order Higgs boson production calculations has been developed for events with up to one jet at NLO [344]

and up to 3 jets at LO. GoSam provides event generation with finite m_t at LO for 1, 2, or 3 jets. The limiting factor in pushing the finite m_t calculations to NLO is the complexity of the required virtual corrections, with the Feynman diagrams explicitly containing the additional fermionic loop. Using both EFT and finite m_t sets of GoSam ntuples,* we performed a number of comparisons in order to investigate areas of discrepancy, as well as possible measurable effects due to the finite value of the mass of the top quark.

Some of the first effects we were able to quantify with the help of the GoSam ntuples were the range of validity of the HEFT and the degree of its discrepancy with the cross section predictions that include the full mass dependence. This comparison is illustrated in Fig. B.2, which shows differential cross section distributions for diphoton production as functions of the diphoton p_{T} for resonant production via the Higgs boson, calculated using both EFT and the finite m_t (mtop) approaches, as well as non-resonant QCD diphoton production for events with at least one hadronic jet. The HEFT is valid to within approximately 10% for $p_{\mathrm{T}}^H < 225\,\mathrm{GeV}$. At higher p_{T}^H, the fractional discrepancy continues to rise as a power law, reaching a factor of 10 around 1 TeV.

In addition, the comparisons to the diphoton background show that within the signal region of the fiducial phase space for the $H \to \gamma\gamma$ analysis, for the diphoton transverse momentum above 500 GeV, the signal-to-background ratio becomes close to or better than 1. With the increased integrated luminosity of the future LHC runs, the $H \to \gamma\gamma$ analysis will be able to take full advantage of a high purity sample of Higgs events at high transverse momentum.

*The GoSam ntuples, discussed in Appendix A, were provided to us by our colleagues, theorists of the GoSam collaboration [106, 109, 327]. The events in the samples used for the studies discussed in Appendix B were generated at LO, using 5-flavor CT10 PDFs [66], with the $\mu_{\mathrm{F}} = \mu_{\mathrm{R}} = \hat{H}'_{\mathrm{T}}/2$ dynamic scales (see Section 3.4), and, unless otherwise stated, represent proton collisions at $\sqrt{s} = 13$ TeV. The event were simulated only at parton level. The partons were clustered using the AntiKt4 algorithm and the standard ATLAS jet cuts of $p_{\mathrm{T}} > 30\,\mathrm{GeV}$ and $\eta < 4.4$ were applied.

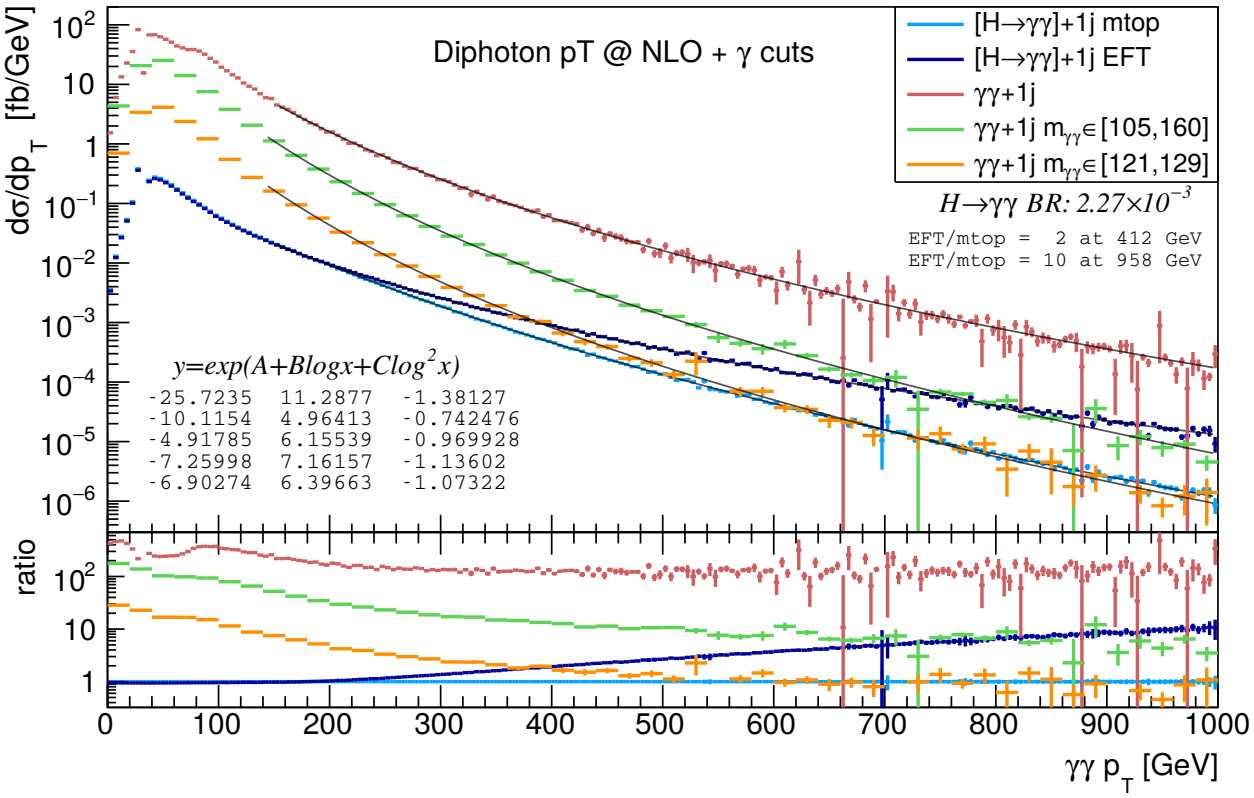

Figure B.2: Comparison of diphoton transverse momentum distributions, generated using GoSam ntuples [106, 330], for $(H \to \gamma\gamma) + 1$ jet produced in gluon fusion with (mtop) and without (EFT) accounting for the finite value of the top quark mass. The former is obtained by reweighting the later by the ratio of the respective distributions at LO. Also shown are distributions for the background diphoton production. The distributions include photon and jet cuts on p_{T} and η used in the $H \to \gamma\gamma$ analysis.

B.2 Finite top quark mass effects in Higgs boson + jets production

Subsequently, we used the GoSam ntuples to investigate the invariant mass distribution of the Higgs boson + the leading jet system (Hj). The comparisons of the histograms from the EFT and finite m_t LO ntuples are shown in Figs. B.5 and B.6 for Higgs boson + at least 1 jet (H1j) and 2 jets (H2j) respectively. The ratio of the finite m_t to the EFT cross section, plotted on the right hand side, clearly shows a resonance-like structure, with the peak near $m_{Hj} = 2m_t$, marked by the vertical gray line. We conjecture this distinction to be due to the finite m_t calculation accounting for the resonant behavior, expected when the top quark in the loop has energy sufficient to be on-shell.

Although selection based on the initial state partons cannot be done in experimental data, it can be instructive to consider in a MC study. Plots of the m_{Hj} distributions in H1j events (Fig. B.5) for the specific initial states support our interpretation of the feature observed in the ratio plots. Fig. B.3 shows representative triangle diagrams contributing to the H1j process with the specific initial state partons. The diagram for the qq initial state clearly explains why the effect observed in this case is much more pronounced, as the qq initial state enables both the Higgs boson and the gluon jet to be produced directly from the quark loop. The same is possible for the gg initial state, but requires a box diagram shown

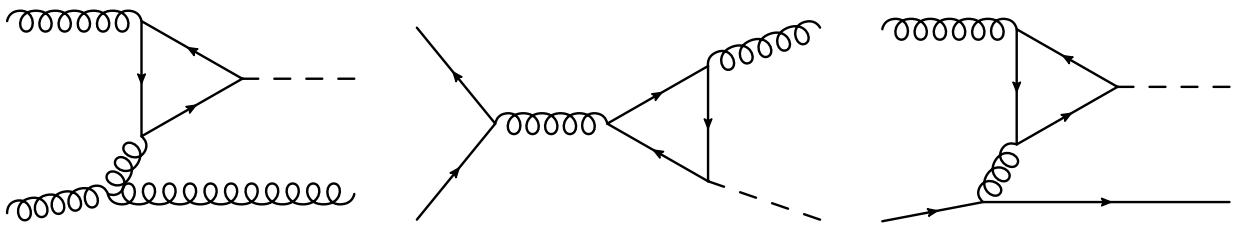

Figure B.3: Representative Feynman diagrams containing a quark triangle loop that contribute to the Higgs boson + 1 jet process for the gg, qq, and gq initial states.

in Fig. B.4. However, the amplitude for this process is suppressed by the allowed helicity combinations. This explains why the effect is less pronounced for the gg than for the qq initial state.

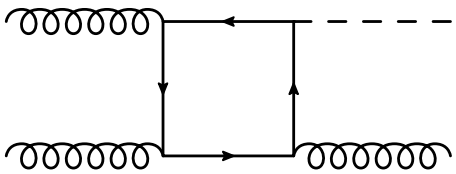

Figure B.4: A Feynman diagram containing a quark box loop that contributes to the Higgs boson + 1 jet process for the gg initial state.

For the Higgs boson production with 2 jets, the effect is reduced for the qq initial state, appears for the gq, and is consistent for gg. Evidently, at the higher jet multiplicity, events with the gg initial state are the ones primarily affected by the finite m_t. This is good news for a potential future experimental measurement, as the gg initial state contributes the main fraction of the cross section.

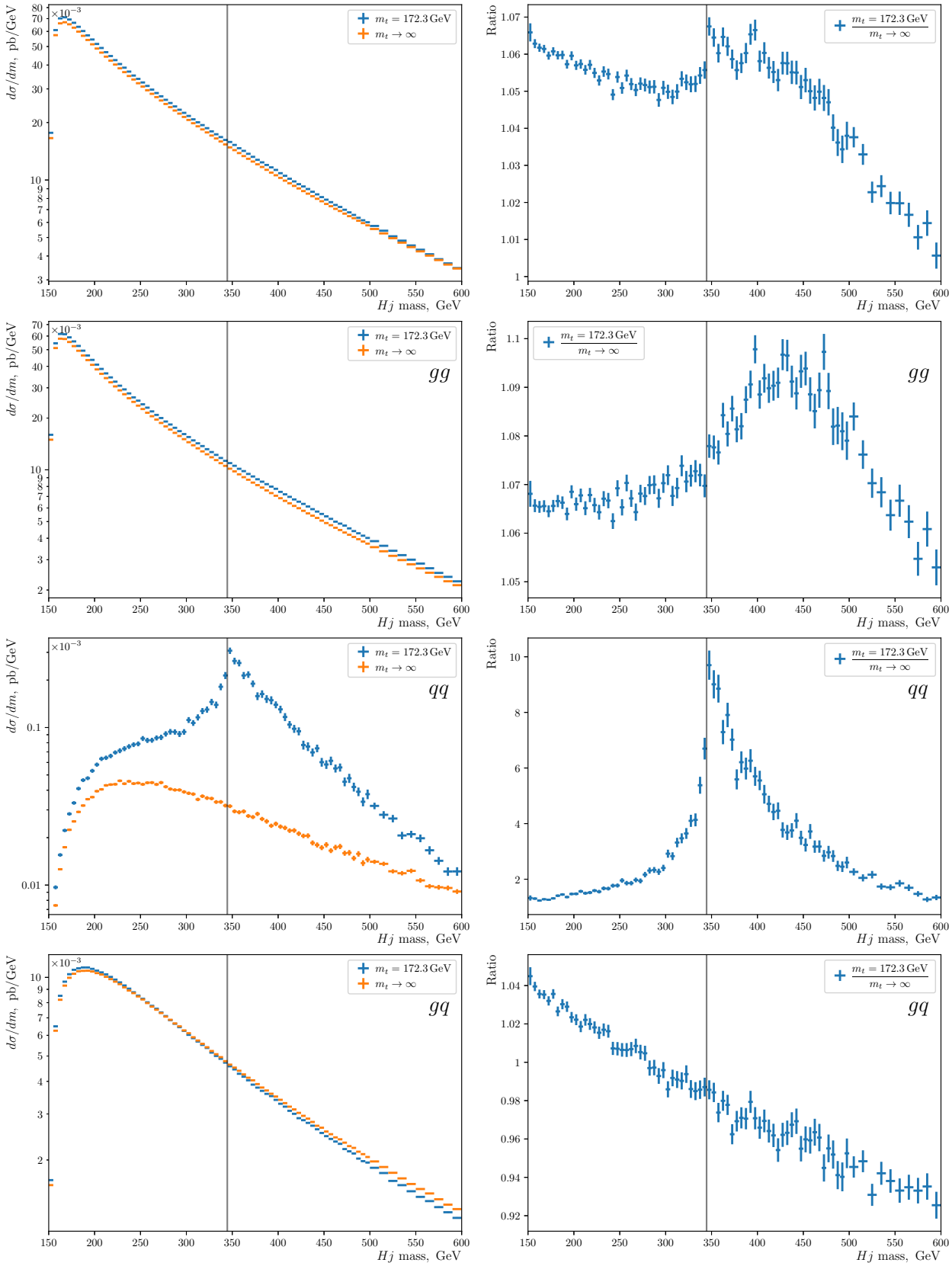

Figure B.5: Distributions of the mass of the Higgs boson + the leading jet system produced using EFT and finite m_t LO GoSam ntuples for Higgs boson + at least 1 jet production. gg, qq, and gq labels indicate the initial state partons.

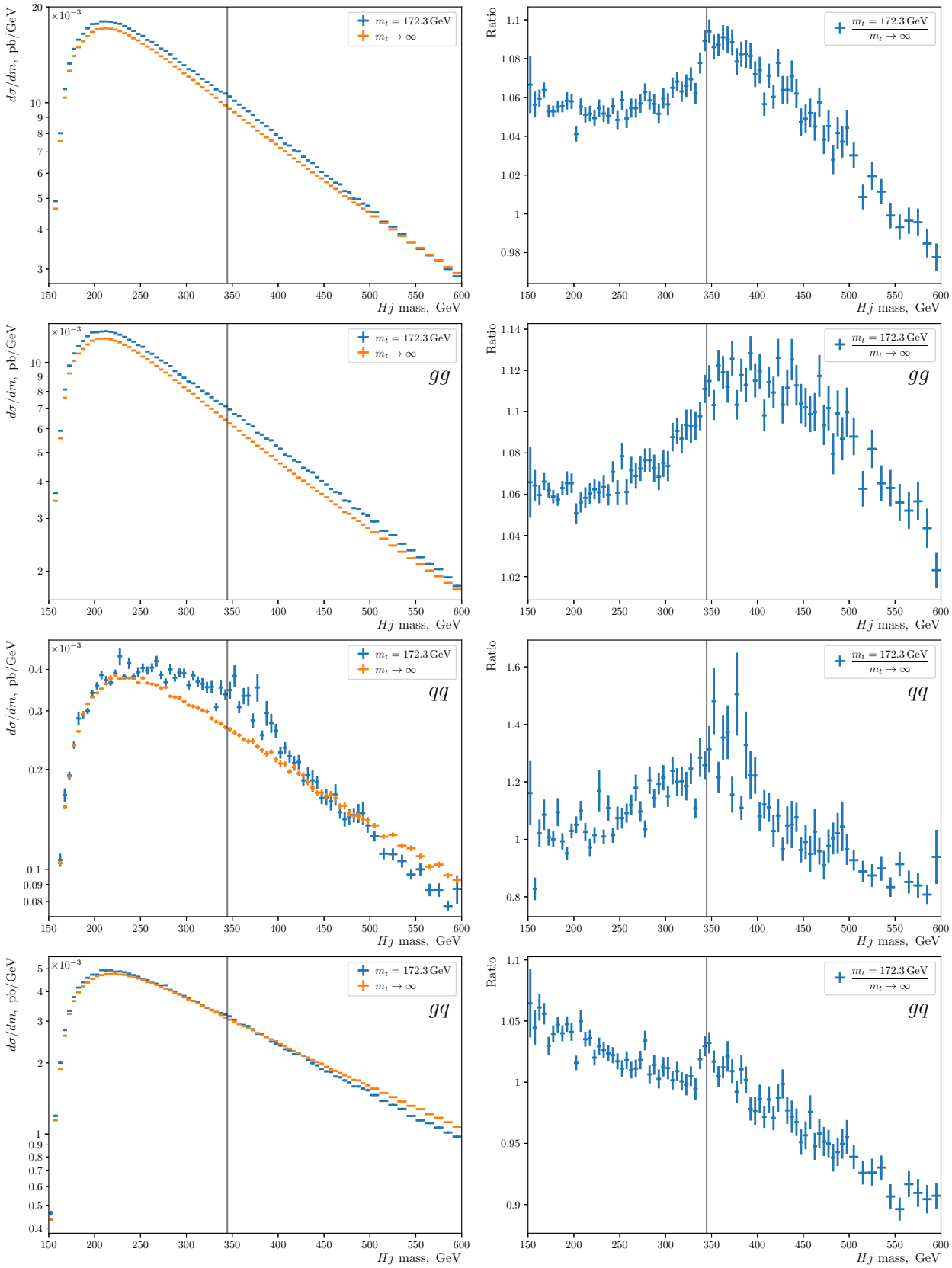

Figure B.6: Distributions of the mass of the Higgs boson + the leading jet system produced using EFT and finite m_t LO GoSam ntuples for Higgs boson + at least 2 jets production. gg, qq, and gq labels indicate the initial state partons.

Besides the distributions shown in Fig. B.6, we further investigated the finite m_t effects on the process of Higgs boson production with 2 jets. Using the additional jet in the H2j events as a handle on the Hj kinematics, we studied the behavior of the m_{Hj} distribution as a function of $p_{\mathrm{T}}^{j_2}$. Fig. B.7 shows these distributions for a specific slice in $p_{\mathrm{T}}^{j_2}$. A particular enhancement due to restriction to a $p_{\mathrm{T}}^{j_2}$ interval can be seen for the gg initial state. We also observed a trend for the magnitude of the effect to increase at larger $p_{\mathrm{T}}^{j_2}$. However, beyond $p_{\mathrm{T}}^{j_2} \gtrsim 500\,\mathrm{GeV}$, m_{Hj} values at or below $2m_t$ become inaccessible kinematically.

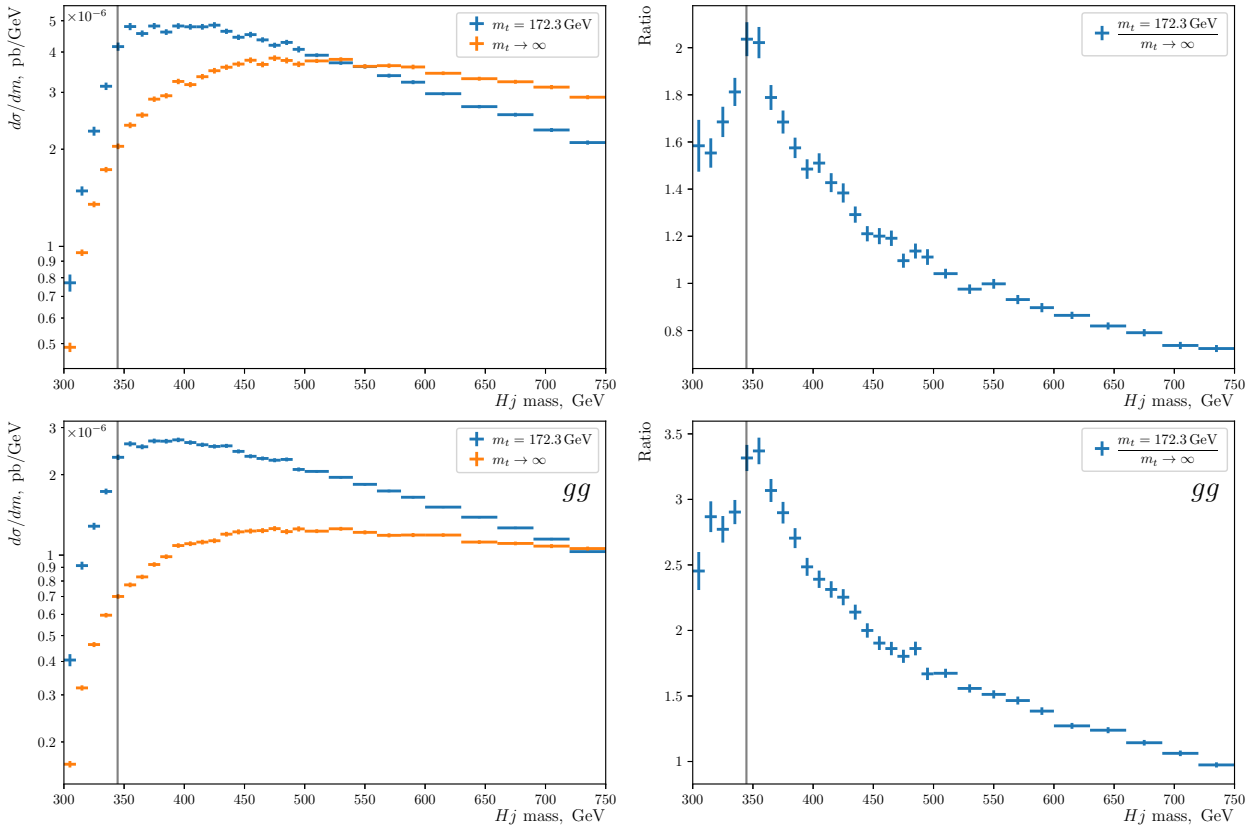

Figure B.7: Distributions of the mass of the Higgs boson + the leading jet system for a specific slice in the subleading jet's transverse momentum, $p_{\mathrm{T}}^{j2} \in [268, 311)\,\mathrm{GeV}$.

Seeing that the transverse momentum of the subleading jet (an experimentally observable quantity) allowed us to isolate a region of phase space where the effect of the finite m_t was more pronounced, we attempted to further understand the effect in the context of H2j

events, with the goal to identify potential observables with enhanced sensitivity to the finite m_t effects, which could provide a basis for a future experimental analysis.

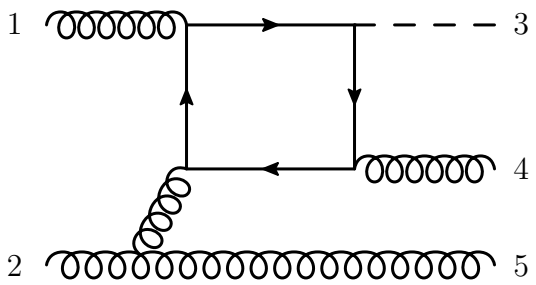

Figure B.8: A representative Feynman diagram for the Higgs boson production with 2 jets from the gg initial state.

Fig. B.8 shows a typical box diagram contributing to the H2j process with the gg initial state. As the Higgs boson is a scalar particle, in order for the incoming (1 and 2) and the outgoing (4 and 5) gluons to each have helicity ± 1, the virtual gluon must have helicity 0, and hence large virtuality.* The virtuality is given by the kinematic invariant corresponding to the t-channel-like interaction of the virtual gluon, t_{25}, defined in Eq. (B.1). Similarly to the previous case, where the finite m_t effect was enhanced for the qq initial state in the H1j process, we would like to consider the mass of the system of the Higgs boson and the jet emitted from the quark loop, which would be equal to the $\sqrt{s_{34}}$.

$$t_{25} = -(k_2 - k_5)^2, \quad s_{34} = (k_3 + k_4)^2. \tag{B.1}$$

However, at the cross section level, a jet cannot be strictly identified as either particle 4 or 5, as the diagram in Fig. B.8 interferes with the one in which legs 4 and 5 are crossed. The same is true for legs 1 and 2. To investigate the relationship between the virtuality t_{25}

*The process illustrated in Fig. B.8 is kinematically similar to that to which the so-called effective W approximation has been applied in the past [345]. Here, a virtual gluon is involved in a scattering process rather than a vector boson.

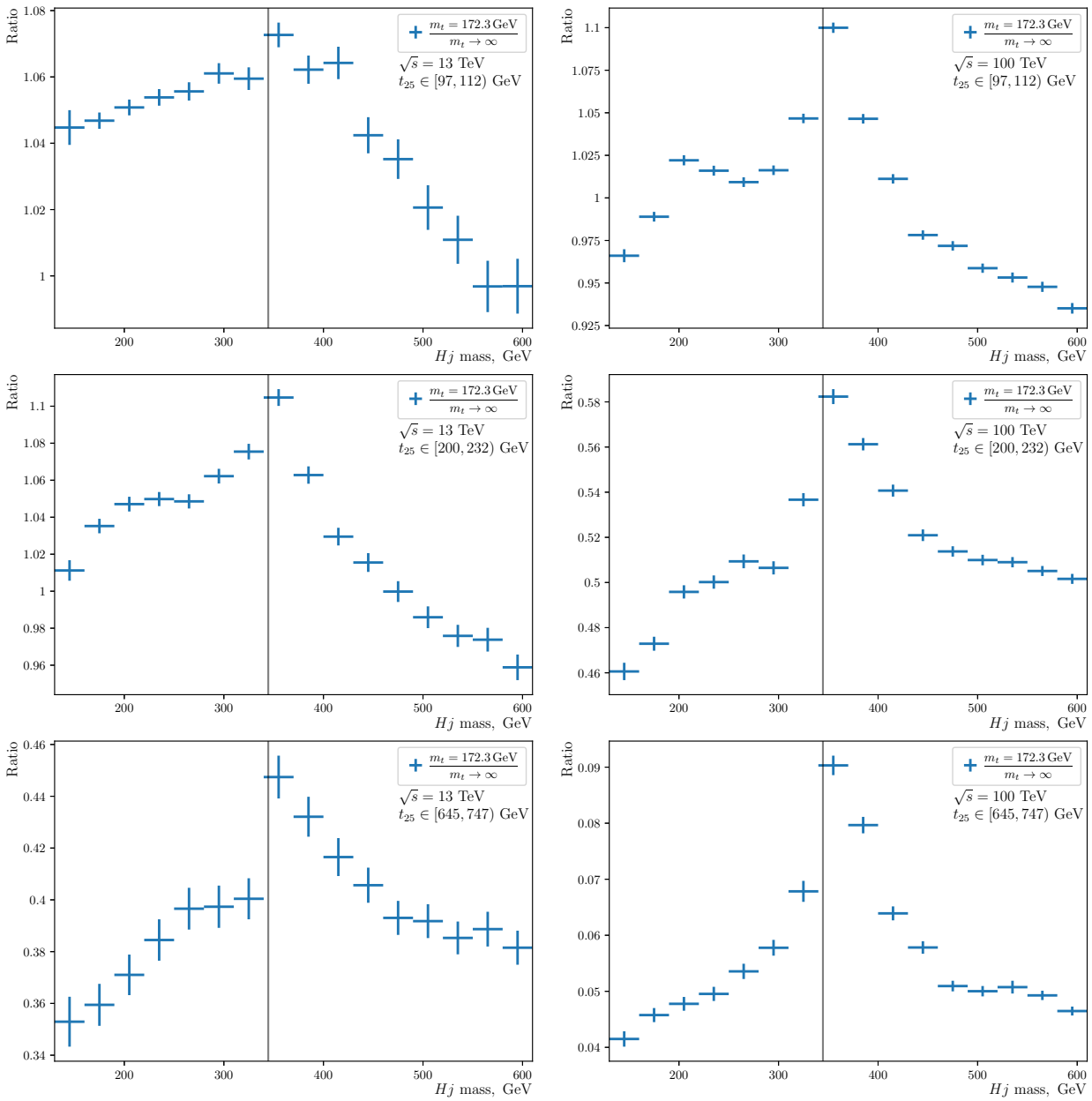

Figure B.9: Ratios of the distributions of the invariant mass of the Higgs boson and the leading jet system from full and effective theory GoSam calculations within intervals of the virtuality variable, t_{25}, for proton-proton $\sqrt{s} = 13$ (left) and 100 (right) GeV.

and how pronounced the finite m_t effect is, we used the following kinematic rules to improve the degree of correlation between the selected particles and the legs of the diagram:

- assign 4 to the leading jet;
- assign 1 and 2 such that $\Delta\theta_{25} < \Delta\theta_{15}$.

Ratios of the obtained distributions are shown in Fig. B.9 for 13 and 100 TeV collisions. Indeed, the size of the peak relative to the adjacent values increases for larger values of t_{25}, especially for $\sqrt{s} = 100\,\text{TeV}$. Although, t_{25} cannot be measured experimentally, these results support our conjecture.

Following these studies, our colleague, Kirtimaan Mohan, proposed a systematic way to identify singularities potentially responsible for resonant effects in the $gg \to Hgg$ process. Using Landau conditions, he compiled a list of all possible invariants that can appear as factors in the denominators of the relevant amplitude expressions. The list of these invariants is given bellow, with the following shorthand convention:

$$s_{ij} = (k_i + k_j)^2, \quad t_{ij} = (k_i - k_j)^2, \tag{B.2}$$

where indices i and j refer to the legs of the diagram in Fig. B.8. As before, for the analysis using the ntuples, index 4 is assigned to the leading jet, and index 5 to the subleading one.

Triangle diagrams:

$$x_0^3 = m_h^2 - 4m_t^2 - s_{12} + s_{45} - t_{23} \tag{B.3}$$

$$x_1^3 = s_{34} - 4m_t^2 \tag{B.4}$$

$$x_2^3 = m_h^2 - 4m_t^2 + s_{12} - s_{34} - s_{45} \tag{B.5}$$

$$x_3^3 = s_{45} - 4m_t^2 \tag{B.6}$$

$$x_4^3 = s_{12} - 4m_t^2 \tag{B.7}$$

$$x_5^3 = 4m_t^2 + s_{12} - s_{34} + t_{15} \tag{B.8}$$

$$x_6^3 = 4m_t^2 + s_{45} + t_{15} - t_{23} \tag{B.9}$$

$$x_7^3 = m_h^2 - 4m_t^2 - s_{34} + t_{15} - t_{23} \tag{B.10}$$

$$x_8^3 = m_h^2 \Big(s_{12}s_{45} - 2m_t^2(s_{12} + s_{45})\Big) + m_h^4 m_t^2 + m_t^2(s_{12} - s_{45})^2 \tag{B.11}$$

$$x_9^3 = m_h^2 \Big(2m_t^2(s_{12} - s_{34} + s_{45} + 2t_{15} - t_{23}) + (s_{12} - s_{34} + t_{15})(s_{45} + t_{15} - t_{23})\Big) \tag{B.12}$$
$$+ m_h^4 m_t^2 + m_t^2(s_{12} - s_{34} - s_{45} + t_{23})^2$$

$$x_{10}^3 = t_{15}m_h^4 + m_t^2(s_{34} + t_{23})^2 - m_h^2 t_{15}(4m_t^2 + s_{34} - t_{15} + t_{23}) \tag{B.13}$$

Box diagrams, double cut:

$$x_0^4 = s_{12} - 4m_t^2 \tag{B.14}$$

$$x_1^4 = s_{34} - 4m_t^2 \tag{B.15}$$

$$x_2^4 = m_h^2 - 4m_t^2 + s_{12} - s_{34} - s_{45} \tag{B.16}$$

$$x_3^4 = s_{45} - 4m_t^2 \tag{B.17}$$

$$x_4^4 = 4m_t^2 + s_{45} + t_{15} - t_{23} \tag{B.18}$$

$$x_5^4 = 4m_t^2 - t_{23} \tag{B.19}$$

$$x_6^4 = 4m_t^2 + s_{12} - s_{34} + t_{15} \tag{B.20}$$

$$x_7^4 = m_h^2 - 4m_t^2 - s_{12} + s_{45} - t_{23} \tag{B.21}$$

$$x_8^4 = m_h^2 - 4m_t^2 - s_{34} + t_{15} - t_{23} \tag{B.22}$$

$$x_9^4 = -x_7^4 \tag{B.23}$$

Box diagrams, triple cut:

$$x_{10}^4 = m_h^2 \Big(s_{12}s_{45} - 2m_t^2(s_{12} + s_{45})\Big) + m_t^2 m_h^4 + m_t^2(s_{12} - s_{45})^2 \tag{B.24}$$

$$x_{11}^4 = m_h^2 \Big(2m_t^2(s_{12} - s_{34} + s_{45} + 2t_{15} - t_{23}) + (s_{12} - s_{34} + t_{15})(s_{45} + t_{15} - t_{23})\Big) \tag{B.25}$$
$$+ m_t^2 m_h^4 + m_t^2(s_{12} - s_{34} - s_{45} + t_{23})^2$$

$$x_{12}^4 = m_t^2(s_{34} + t_{23})^2 - m_h^2 t_{15}(m_h^2 - 4m_t^2 - s_{34} + t_{15} - t_{23}) \tag{B.26}$$

Box diagrams, quadruple cut:

$$x_{13}^4 = (s_{12} - s_{34})(m_h^2 - s_{34}) + s_{45}(s_{34} - 4m_t^2) \tag{B.27}$$

$$x_{14}^4 = 4m_t^2(s_{34} - s_{12})(m_h^2 - s_{34}) + s_{34}s_{45}(s_{34} - 4m_t^2) \tag{B.28}$$

$$x_{15}^4 = 2m_h^2\left(2m_t^2(s_{12} - s_{34}) + s_{45}(s_{12} - s_{34} - s_{45})\right) - 4m_t^2 s_{34}(s_{12} - s_{34} - s_{45}) \tag{B.29}$$
$$- s_{45}\left(m_h^4 + (s_{12} - s_{34} - s_{45})^2\right)$$

$$x_{16}^4 = 4m_t^2 m_h^2(s_{45} + t_{15}) + 4m_t^2 t_{23}(s_{12} - s_{34} - s_{45}) - t_{23}^2(s_{12} - s_{34} + t_{15}) \tag{B.30}$$

$$x_{17}^4 = m_h^2(s_{45} + t_{15}) - 4m_t^2(s_{12} - s_{34} + t_{15}) + t_{23}(s_{12} - s_{34} - s_{45}) \tag{B.31}$$

$$x_{18}^4 = \left(2m_h^2 + (s_{12} - s_{34} - s_{45})\right)(s_{12} - s_{34} - s_{45})(s_{12} - s_{34} + t_{15}) \tag{B.32}$$
$$- 4m_t^2\left(m_h^2(s_{45} + t_{15}) + t_{23}(s_{12} - s_{34} - s_{45})\right) + m_h^4(s_{12} - s_{34} + t_{15})$$

$$x_{19}^4 = 4m_t^2\left(m_h^2 t_{15} + (s_{12} - s_{34} - s_{45})(s_{12} - s_{45} + t_{23})\right) \tag{B.33}$$
$$- t_{15}(m_h^2 - s_{12} + s_{45} - t_{23})^2$$

$$x_{20}^4 = t_{15}(m_h^2 - 4m_t^2) + (s_{12} - s_{34} - s_{45})(s_{12} - s_{45} + t_{23}) \tag{B.34}$$

$$x_{21}^4 = 4m_t^2\left(m_h^2 t_{15} + (s_{12} - s_{34} - s_{45})(s_{12} - s_{45} + t_{23})\right) \tag{B.35}$$
$$- t_{15}(m_h^2 + s_{12} - s_{34} - s_{45})^2$$

$$x_{22}^4 = m_h^2(4m_t^2 t_{15} - t_{23}^2) + t_{23}^2(s_{34} - t_{15} + t_{23}) - 4m_t^2 s_{34} t_{23} \tag{B.36}$$

$$x_{23}^4 = m_h^2(t_{15} - 4m_t^2) + 4m_t^2(s_{34} - t_{15} + t_{23}) - s_{34}t_{23} \tag{B.37}$$

$$x_{24}^4 = 4m_t^2(m_h^2 t_{15} - s_{34}t_{23}) - s_{34}^2(m_h^2 - s_{34} + t_{15} - t_{23}) \tag{B.38}$$

$$x_{25}^4 = (s_{45} + t_{15} - t_{23})\left(m_h^4 - 2m_h^2(s_{12} - s_{45} + t_{23}) + (s_{12} - s_{45} + t_{23})^2\right) \tag{B.39}$$
$$+ 4m_t^2\left(s_{34}(s_{12} - s_{45} + t_{23}) - m_h^2(s_{12} + t_{15})\right)$$

$$x_{26}^4 = m_h^2(s_{12} + t_{15}) - 4m_t^2(s_{45} + t_{15} - t_{23}) - s_{34}(s_{12} - s_{45} + t_{23}) \tag{B.40}$$

$$x_{27}^4 = 4m_t^2 m_h^2(s_{12} + t_{15}) - 4m_t^2 s_{34}(s_{12} - s_{45} + t_{23}) - s_{34}^2(s_{45} + t_{15} - t_{23}) \tag{B.41}$$

$$x_{28}^4 = (s_{12} - s_{45} + t_{23}) \Big(s_{12}(s_{12} - s_{45} + t_{23} - 2m_h^2) - 4m_t^2 t_{23} \Big) \tag{B.42}$$
$$+ m_h^4 s_{12} - 4m_t^2 m_h^2 (s_{12} + t_{15})$$

$$x_{29}^4 = 4m_t^2 m_h^2 (t_{23} - s_{45}) - 4m_t^2 t_{23}(s_{12} - s_{45} + t_{23}) + s_{12} t_{23}^2 \tag{B.43}$$

$$x_{30}^4 = m_h^2 (s_{45} - t_{23}) - 4m_t^2 s_{12} + t_{23}(s_{12} - s_{45} + t_{23}) \tag{B.44}$$

Histograms of the distributions of the x observables listed above revealed that only 4 of them are kinematically allowed to have both positive and negative values near zero. Of those, $x_1^3 = x_1^4 \sim s_{34}$ corresponds to the Hj invariant mass, $x_3^3 = x_3^4 \sim s_{45}$ corresponds to the dijet invariant mass, $x_4^3 = x_0^4 \sim s_{12}$ corresponds to the invariant mass of the initial state partons, and $x_2^3 = x_2^4$ is a linear combination of the three preceding variables.

B.3 Conclusion

Our study of the effects of the finite mass of the top quark on the production of the Higgs boson with jets using GoSam MC is still ongoing. We have clearly demonstrated that effects are expected to be present, e.g. resulting in resonance-like deviations from the EFT predictions in the Hj mass distribution near $m_{Hj} = 2m_t$. We have also been able to associate these effects with certain aspects of the interactions comprising the production process, in particular with the virtual off-shell gluon exchange between an incoming parton and the quark loop in the $gg \to Hgg$ interaction. Going forward, we hope to better identify regions of phase space where the finite m_t effects are enhanced, and to define these regions in terms of observables that can be used to perform an experimental measurement in the future.

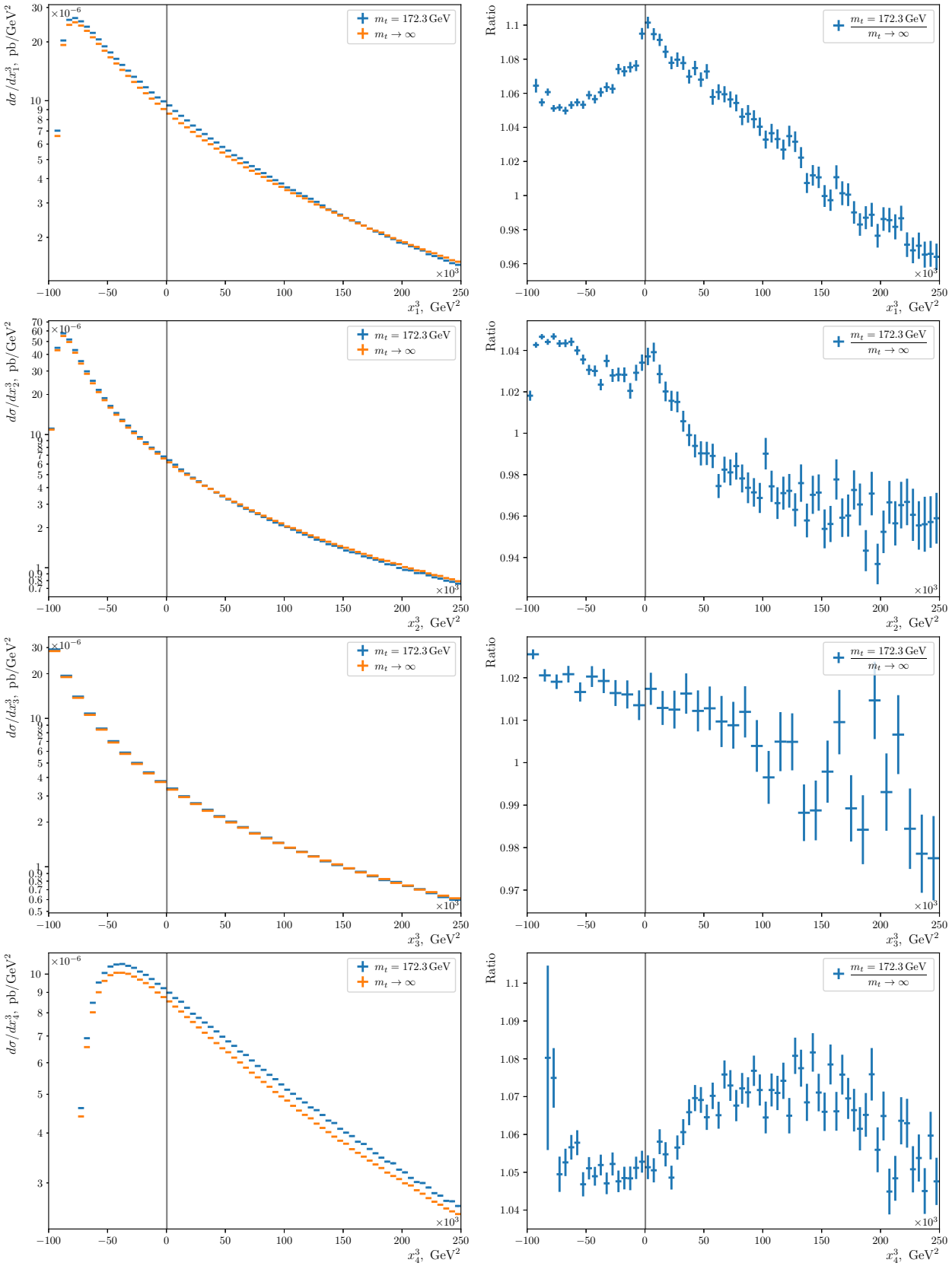

Figure B.10: Distributions of the kinematic invariants that can appear in the denominators of amplitude expressions for the $gg \to Hgg$ process and lead to singularities.

APPENDIX C

TileCal upgrade work

The MSU ATLAS group has been involved in the design and construction of the Tile hadronic calorimeter (TileCal) from its inception. Continuing MSU participation on TileCal, I worked on a number of projects related to the Phase-II upgrade, in preparation for the High-Luminosity LHC. A part of this work was done in fulfillment of the authorship requirements for the ATLAS collaboration. The Tile calorimeter is the main device on ATLAS used for jet reconstruction. Its continued operation is essential for the future of all analyses looking at processes that contain jets in the final state. This includes the Higgs boson cross section analysis presented in this dissertation, as many key observables, such as the VBF cross section, rely on measurements of jets.

C.1 Phase-II upgrade

For high energy collider experiments, whose lifetime spans decades, research and development is always an on-going process that does not stop after continuous operation has been established. Detector components age because of intense radiation levels, old components become obsolete, and spare parts become unavailable, while new approaches are developed, that promise to improve detector performance and reliability. These factors alone would solicit continued work on upgrading the detector systems. Additionally, experience from operation of the collider shows ways to increase delivered luminosity. Increasing the rate of

data collection comes with certain challenges, such as a larger number of collisions per bunch crossing and an increase in both pileup and the radiation doses that the detector components are going to be expected to withstand.

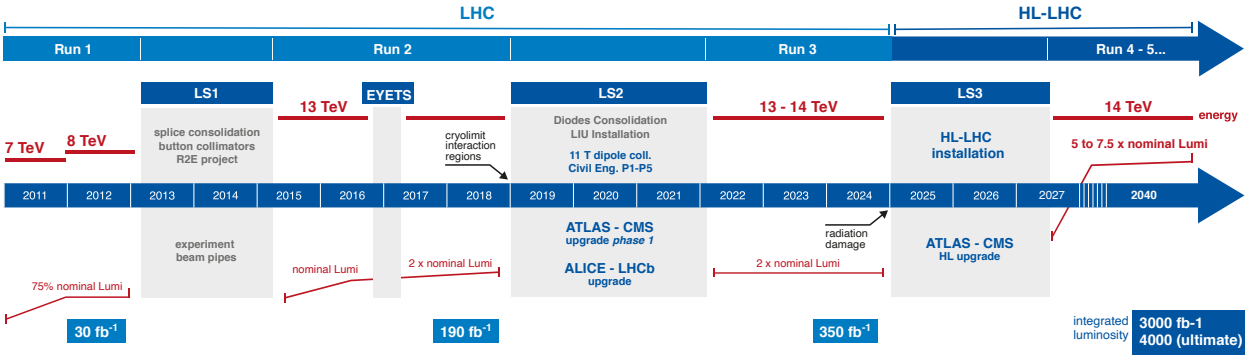

Figure C.1: Current LHC operation and upgrade timeline [346].

Fig. C.1 shows the timeline of the past and planned LHC operation and upgrade stages. The data from $\sqrt{s} = 13$ TeV proton-proton collisions, used in the analysis presented in this dissertation, was collected in the Run 2 period from 2015 to 2018. The LHC has now entered the second long shutdown (LS2), during which Phase-I ATLAS upgrades are being installed. After the Phase-I upgrades are complete, the LHC will collect additional data at its current capacity in Run 3, before entering the third long shutdown (LS3). The major Phase-II upgrades planned to be installed during LS3 will enable the High-Luminosity LHC (HL-LHC) [347] to deliver instantaneous luminosity over a factor of 5 larger than the LHC's nominal. Continued HL-LHC operation is expected to last for many years, in order to achieve an integrated luminosity of over $3000\,\mathrm{fb}^{-1}$, and will require an improved radiation tolerance for many detector components. The Phase-II ATLAS upgrades [348–350] will allow the detector to cope with data collection at the increased rate in the much more intense collision environment. A major upgrade of TileCal electronics is being developed for the Phase-II.

As discussed in Section 4.5.2.1, TileCal modules are made of plastic scintillator tiles inter-

leaved with steal absorber plates. The scintillation light, produced in the tiles by interactions with the passing particles, is read out via wavelength shifting fibers by photomultiplier tubes, housed inside the support girder of every module. The modules are arranged in a cylindrically symmetric configuration with 4 sections, each made up of 64 modules. The two central sections (LBA & LBC) make up the Long Barrel. The other two form the Extended Barrels (EBA & EBC). Positioning of the Tile calorimeter within ATLAS is shown in Fig. 4.14 on page 97. Configuration of the modules is illustrated in Fig. 4.17 on page 106. Fig. C.2 below shows photographs of the modules before installation. The hollow girder at the base of each module houses a drawer that contains PMTs and their control and readout electronics. When the detector is open for maintenance, the drawers can be pulled out of the girders, while the modules can remain in place. The on-detector electronics transmist digitized readings from

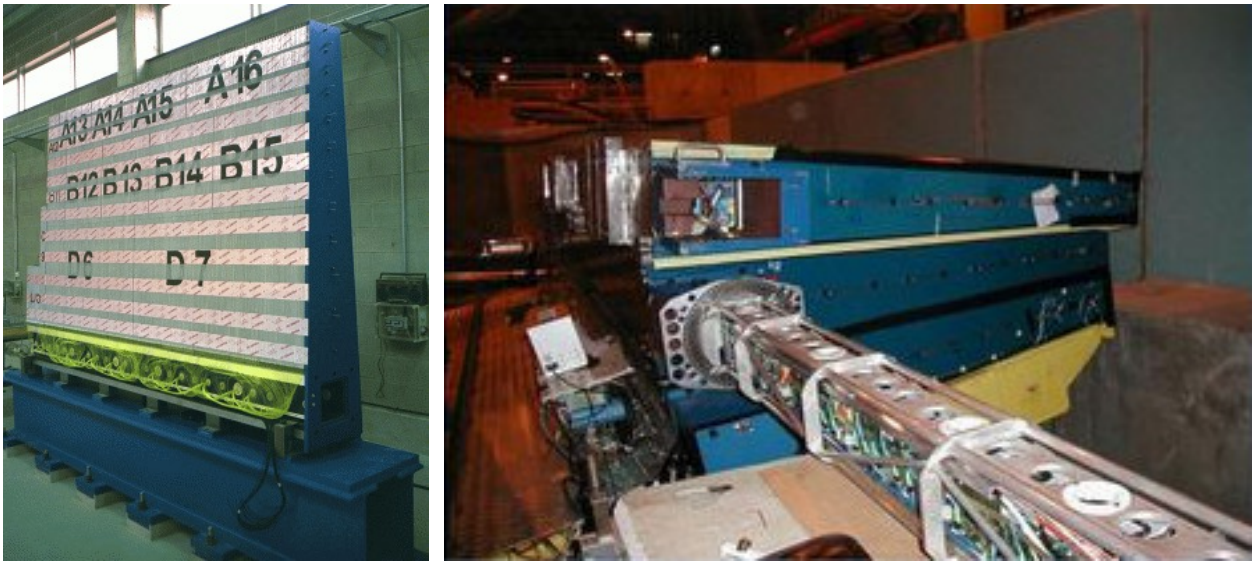

Figure C.2: Photographs of TileCal modules [351]. Left: An Extended Barrel module. Module cells are labeled on the flat side. Bundles of yellow-green wavelength-shifting fibers can be seen at the bottom of the module. The opening at the bottom of the module is where the drawer housing the PMTs and on-detector electronics is inserted. Tight bundles of fibers are threaded through holes along the bottom of the module and are fitted against the PMTs' photocathodes. Right: Drawer electronics being inserted into a module. Not yet connected ends of the Cs calibration system tubes can be seen along the narrow blue side of the modules.

the PMTs to and receives power and operation commands from the ATLAS counting room in USA15.

The present TileCal electronics was designed in the late 1990s, using technologies available at the time. Maintenance of the legacy systems is becoming increasingly difficult as its components age and become obsolete. The output bandwidth and radiation tolerance are also not suited for high luminosity operation. The HL upgrade of TileCal therefore involves a full replacement of the on- and off-detector electronics systems with modern technologies, in order to provide improved trigger performance, higher resolution read-out, and better radiation tolerance. Detailed descriptions of the legacy and upgrade systems can be found in the respective technical design reports [185] and [352].

A conceptual schematic of the existing legacy TileCal electronics is shown in Fig. C.3. A Super Drawer spanning the whole module is divided into two drawers, each containing 4 digitizer boards. The digitizers receive analog signals from the front-end boards (FEB), called 3-in-1 cards [353], that control and read out the PMTs. There is one FEB for every PMT. The digitized PMT readings are transmitted to the back-end system called the Read-Out Driver (ROD). Independently of the digitizers, signals for the Level 1 triggers (L1Calo) are processed by analog adders (indicated by Σ on the diagram), which are also located in the electronics drawers. Separate lines are used for communication with the triggers, the Detector Control System (DCS), and the ROD.

The Phase-II electronics has a different structure, the diagram for which is shown in Fig. C.4. The new Super Drawer is divided into 4 mini-drawers, each containing a Main board (MB), a Daughter board (DB), and a dedicated high-voltage (HV) board. The FEBs will be connected to the Main board. All communication between the on- and off-detector electronics goes through the GigaBit (GBT) fiber-optic connection between the Daughter

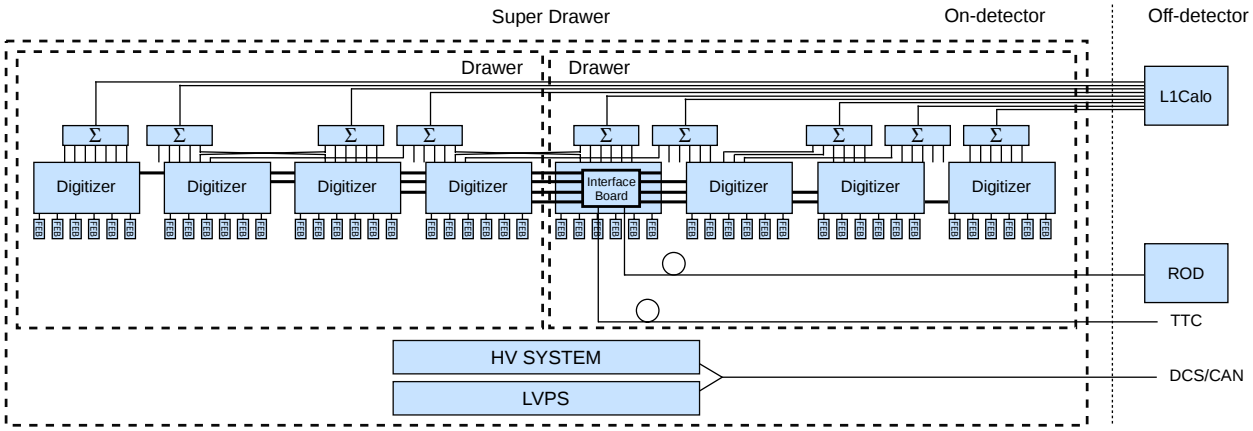

Figure C.3: Diagram of the legacy TileCal electronics.

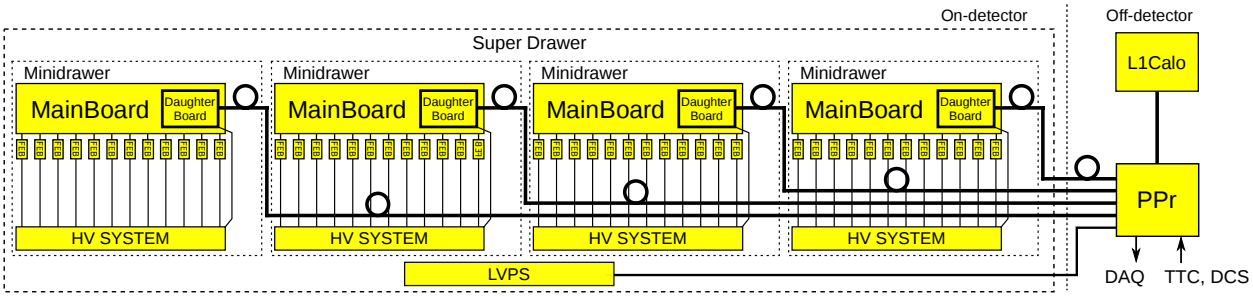

Figure C.4: Diagram of the Phase-II TileCal electronics.

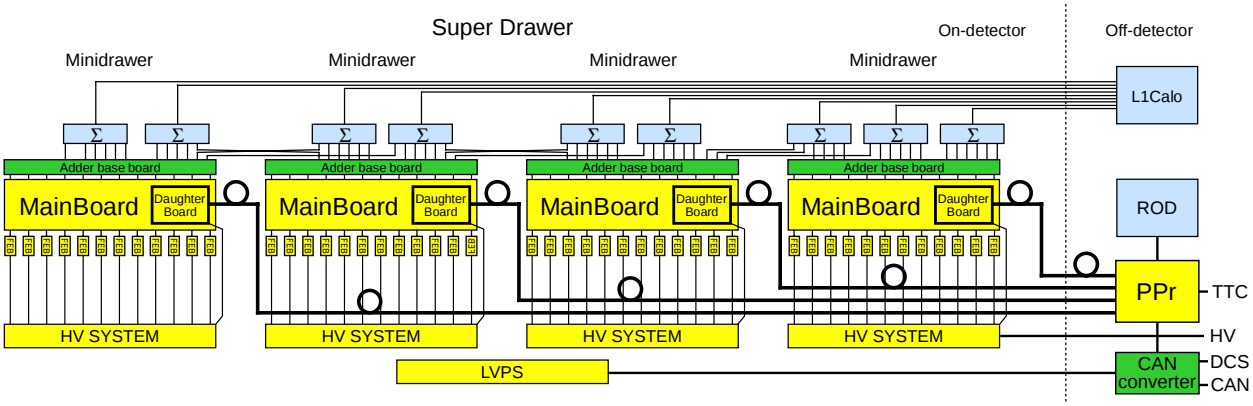

Figure C.5: Diagram of the hybrid Phase-I Demonstrator TileCal electronics.

boards and the PreProcessor (PPr). The PPr provides a centralized back-end interface. It takes over the functionality of the ROD, and also serves as the connection point to the TileCal electronics for the data acquisition (DAQ), the Timing, Trigger and Control (TTC), the detector control (DCS), and the L1Calo systems. The new GBT connection will dramatically improve the communication speed and bandwidth. With the downlinks running at 4.8 Gbps and the uplinks at 9.6 Gbps, PPr and DB registers, holding data and control messaged, can be synchronized every 25 ns, with the same frequency as the event rate of the LHC proton collisions. The subdivision of the Super Drawer into 4 mini-drawers instead of 2 drawers, will make maintenance work in the cavern more convenient. Each mini-drawer will be essentially autonomous and will be connected directly to the low-voltage power suppy (LVPS) and the PPr.

In order to test the upgrade electronics before the Phase-II design is finalized, a hybrid system, called the Demonstrator, has been developed. As shown in Fig. C.5, includes elements of both the legacy and the upgrade electronics to provide interoperability with the currently installed back-end and trigger systems. A photograph of a Demonstrator mini-drawer is shown in Fig. C.6. A drawer containing the Demonstrator electronics has already been installed on the detector during the current long shutdown (LS2). During the development of the Demonstrator, 3 competing designs of the FEB were considered: an upgraded version of the 3-in-1 cards [354], and two ASIC-based solutions, called FATALIC [355] and QIE [356]. Eventually, the new version of 3-in-1 was selected as the main upgrade candidate.

An integral part of any electronics is the power delivery system. The TileCal on-board electronics requires low-voltage (LV) power for control and read-out systems and high-voltage (HV) power for the PMTs. Remote control of both LV and HV power systems is necessary for operation. The value of high voltage supplied to the PMTs has to be dynamically

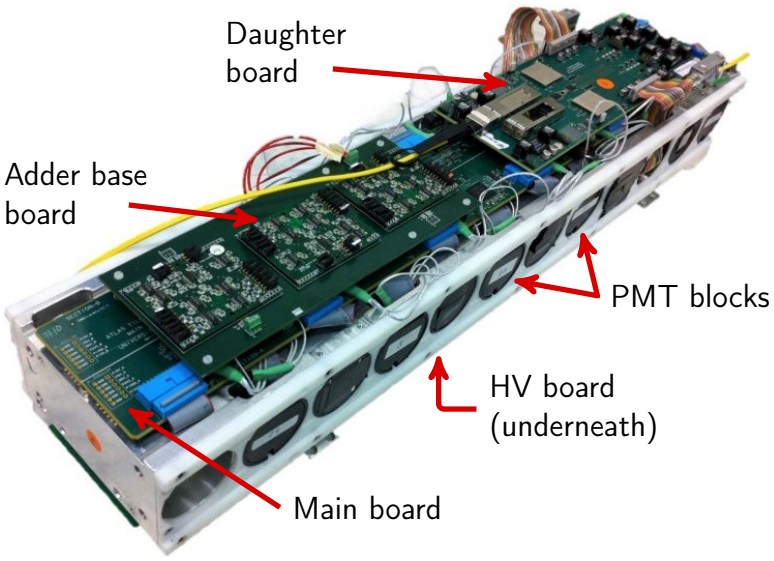

Figure C.6: Photograph of a Demonstrator mini-drawer with the electronics components labeled.

adjusted, depending on the signal level from the respective calorimeter cells, for the PMTs to remain near the operation point in order to provide accurate measurements. Also, the relative calibration of the signal from tiles within each cell has to maintained, which is done by adjusting the PMTs' gain with the HV supplied to them. Stable low voltage has to be supplied to the control and read-out electronics. In case of failure, the LV has to be shut off, to either prevent a potential short circuit from affecting still-operational components, or to reboot the drawer electronics, which often allows a resumption of regular operation.

The projects described in Sections C.2 and C.3 contributed to the upgrade developments for TileCal on-detector power supply systems. The projects described in Sections C.4 and C.5 are related to calibration and testing of the upgrade hardware and firmware.

C.2 HVOpto firmware

The high voltage (HV) supply system for the TileCal has been redesigned for the Phase-II upgrade with two solutions: HV remote and HV internal. With the HV remote, individual adjusted voltages are supplied from an off-detector source to each PMT. This requires one or two (for the extended and long barrel modules respectively) 100 m long multi-conductor cables per module connecting to dedicated off-detector control crates housed in USA15. The HV internal only requires a single constant bulk HV supplied to each module. A dedicated HV control board, called HVOpto, adjusts the supplied bulk HV for each PMT as needed. Each mini-drawer contains its own HVOpto board, located on the opposite side of the drawer, as illustrated in Figs. C.7 and C.8. HVOpto specifications can be found in [357].

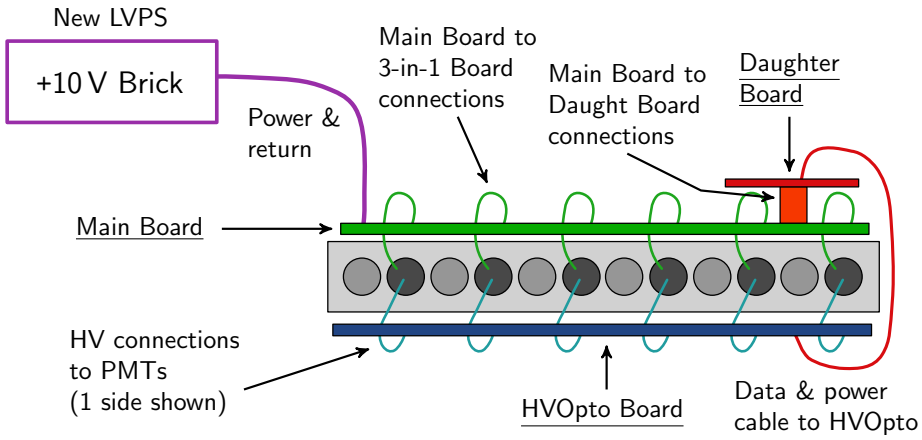

Figure C.7: Diagram illustrating location of the Main, Daughter, and HVOpto boards, as well as the PMTs, in a mini-drawer [357].

The basic configuration of an HVOpto board is as follows. Each HV control circuit contains a digital-to-analog converter (DAC), an analog-to-digital converter (ADC), a pass switch, and analog control circuitry that incorporates optical isolation between the LV control and monitoring, and the HV side that supplies voltage to the PMTs. The optical isolation helps reduce ground loops that might introduce noise into the system, since the bulk HV

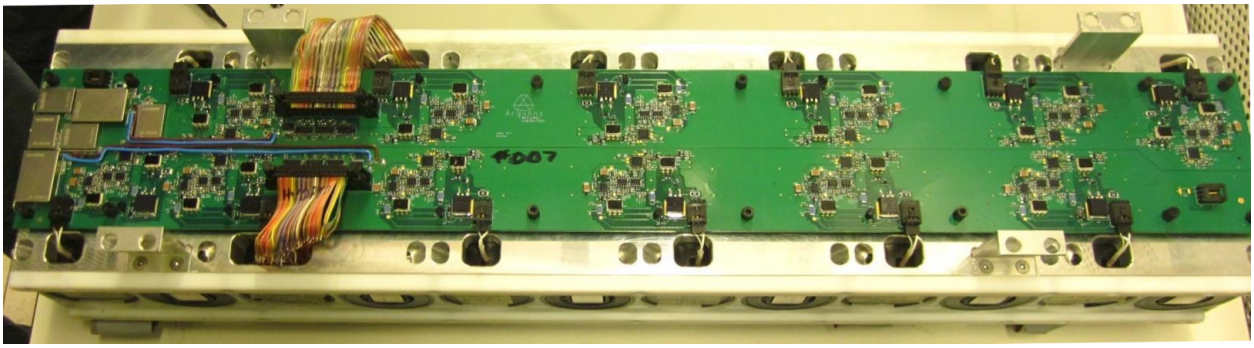

Figure C.8: Photograph of an HVOpto board mounted on a mini-drawer. The circuits for 12 channels, 6 on each side, can be seen as clusters of components. The two ribbon cables provide SPI bus communication with the Daughter board on the other side of the mini-drawer.

supplies reside in USA15. The control circuits produce an output HV that is derived from the HV input, with the output proportional to the DAC voltage, up to a maximum equal to the input voltage. The output HV is monitored by the ADC, using a voltage divider to step the voltage down to a level that can be processed by the LV circuits. A single HVOpto board contains 12 channel circuits – one for each mini-drawer PMT. 4 HVOpto boards share one input HV, as only one is supplied per module.

The ADC and DAC are incorporated into a single chip, MAX1329 [358], one for each HV control channel. In addition to setting the PMT voltages, HVOpto provides monitoring capabilities. With the help of the MAX chip, it is able to continuously monitor the reference and PMT voltages as well as the board temperature. The digital interface to the chip uses Serial Peripheral Interface (SPI) [359], which is a 4-wire serial interface with a write serial data line (`MOSI`), a read serial data line (`MISO`), a slave select line (`nSS`), and a serial clock (`SCLK`) sourced by the master. In this design, the MAX chips are slaves and the Daughter board plays the role of the master. For robustness, the SPI connection is implemented using Low-voltage differential signal (LVDS) lines. In order to provide direct means to shut off HV input, an additional single-ended line (`HV_Enable`) is added to the bus, which has to be

held high for an optically isolated switch to remain in the on position. An HVOpto board is divided into two halves, with each controlling the voltage for PMTs oriented in the same direction inside the mini-drawer. The two halves communicate with the Daughter board via independent SPI buses, with 6 MAX chips per bus. The independent slave SPI configuration is used, so each channel has its own `nSS` and `HV_Enable` lines.

The Daughter board is an FPGA based device, using Kintex7 `XC7K160T-2FFG676` FPGA chips. In order to communicate with HVOpto, the SPI protocol needed to be implemented in the FPGA firmware of the Daughter board written in the VHDL language.* The primary purpose of the HVOpto component of the DB firmware is to provide an interface via which commands to request changes of specific PMT voltages or readings of voltages and temperatures can be sent to the MAX chips operating the HVOpto channels. These commands can be issued either by the DB or be received via the GBT link from the PPr and then delivered to the HVOpto via the SPI connection.

The HVOpto firmware component is essentially a converter that encodes and decodes DB command registers and sends the respective messages over the SPI to read or write data to the MAX chips. The component is implemented as a finite state machine illustrated in Fig. C.9. Before integration into the DB firmware project, the HVOpto component was developed using

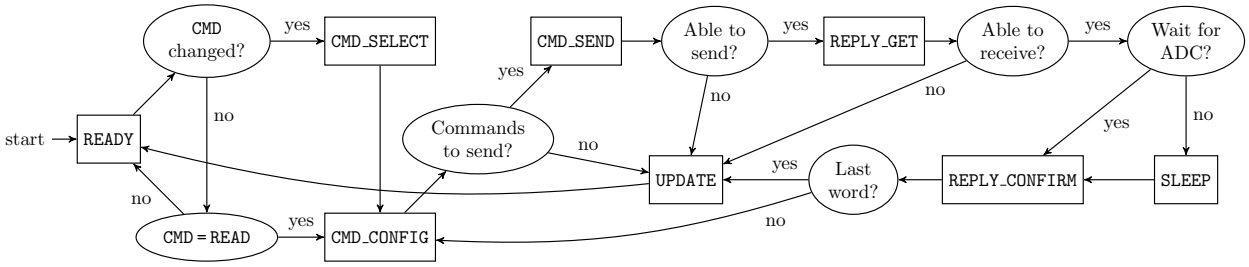

Figure C.9: Finite state machine of the HVOpto component of the Daughter board firmware.

*VHDL (VHSIC-HDL, Very High Speed Integrated Circuit Hardware Description Language) is a hardware description language used for programming FGPA (field-programmable gate array) chips. When the VHDL firmware is uploaded to an FPGA, the logic gates inside are connected in such a way that the chip behaves like the described circuit.

a Xilinx Atlys prototyping board and a single-channel HVOpto test board. A photograph of the setup is shown in Fig. C.10. The developmental version of the firmware with its

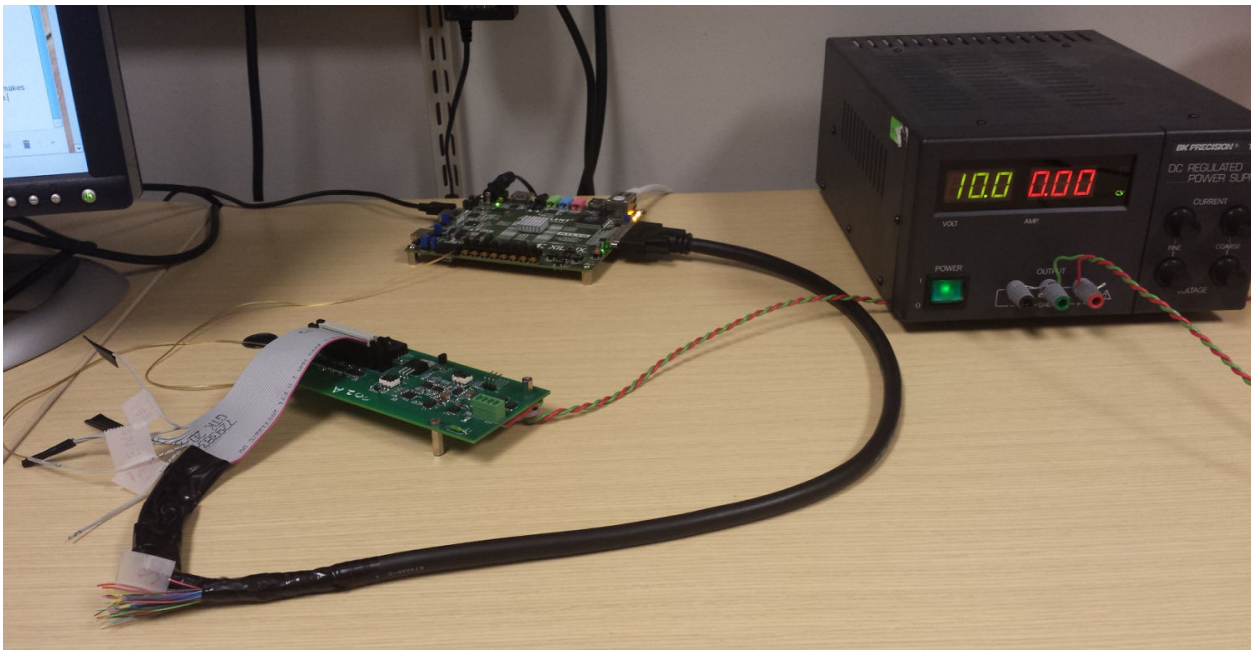

Figure C.10: Photograph of the electronics setup used for development of the HVOpto FPGA firmware component for the TileCal mini-drawer Daughter board. Shown are a Xilinx Atlys prototyping board, a single-channel HVOpto test board, and a LV power supply.

documentation can be found in the CERN Git repository [360]. Porting of the firmware to the DB project was done in collaboration with the TileCal colleagues. A complete technical report can be found in [361].

C.3 Low voltage system monitoring upgrade

Experience from operation of the TileCal in Run 1 of the LHC demonstrated that the LV control and monitoring system did not provide sufficient diagnostic information. Moreover, the existing monitoring system was based on a now outdated custom board which is not sufficiently radiation tolerant to reliably work on HL-LHC. These factors demanded development of a new solution for LV control and monitoring for the TileCal on-detector

electronics. A study to assess the status of the current system, develop a set of requirements for the upgrade, and propose possible upgrade solutions was conducted by me in collaboration with TileCal experts at Argonne National Laboratory. The outcome of the study was a written report documenting the requirements for the low voltage monitoring upgrade of the ATLAS hadronic calorimeter [362]. Presented in the following are an overview of the TileCal LV system, a summary of the major findings of the conducted study, an outline of the proposed requirements, and a discussion of the present developments for the upgrade.

The TileCal LV supply system is a part of the on-detector electronics. It consists of the finger Low Voltage Power Supplies (fLVPS), with one located at the outer end of every module drawer. An fLVPS contains 8 DC-DC converter "bricks", that take 200 V input from USA15 and output voltages* needed for the on-detector electronics, and a monitoring system comprised of two circuit boards: ELMB and its motherboard. Picture of an open fLVPS are show in Fig. C.11.

The LVPS used during the Run 1 of the LHC, which were produced with the original brick design [363] and installed in 2007, exhibited a linear increase in the number of trips with respect to integrated luminosity. While most of the trips were not debilitating and the affected modules could be brought back online, the recovery process took time (~ 2 min to power-cycle the module) and sometimes required human intervention. The increasing amount of TileCal modules' deadtime had to be addressed to continue effective operation in the future. Prior to my involvement in the project, the bricks were redesigned [364] and a LV monitoring system was introduced [365, 366]. The revised brick design considerably reduced the frequency of trips in Run 2 and the added monitoring system successfully identifies LVPS

*The present system requires bricks to supply different voltages: from -15 V to $+15$ V. The Phase-II upgrade system contains identical bricks, with $+10$ V output.

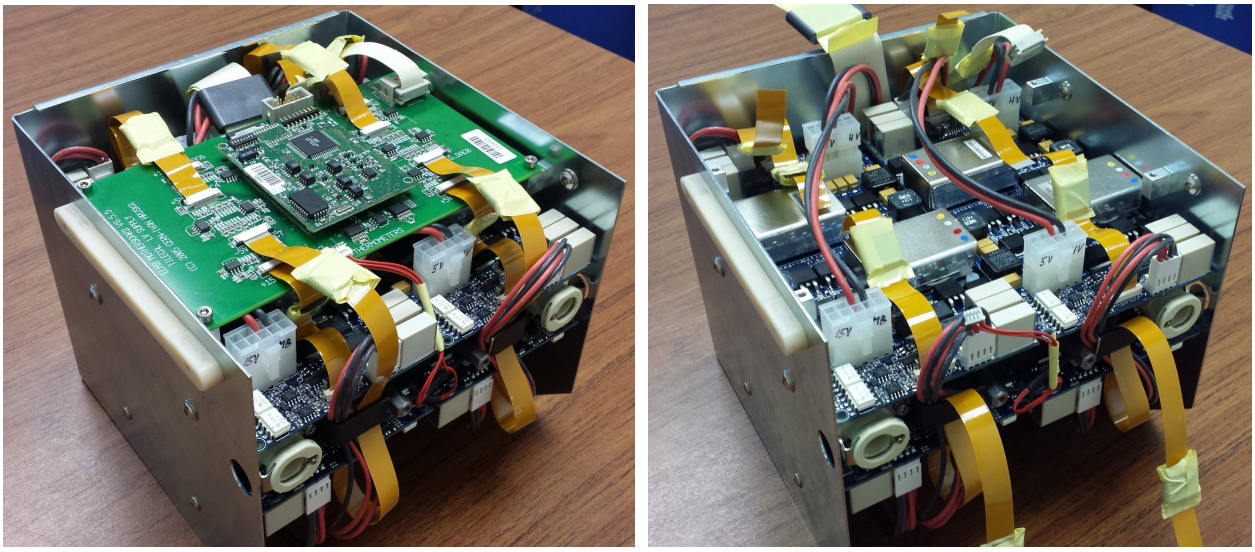

Figure C.11: Photograph of a TileCal finger Low Voltage Power Supply (fLVPS). The green circuit boards of the ELMB and its motherboard can be seen on the left photo. On the right photon, the ELMB and motherboard are removed. The blue circuit boards belong to the DC-DC converter bricks.

trips. However, due to limited sampling frequency, the existing monitoring system did not provide sufficient information to diagnose causes of failure. Because of this, a wholesale approach was implemented to power cycle the entire module after any trip. Power cycling is time consuming and module inactivity reduced the detector's hermeticity and data taking efficiency for events involving jets, which adversely affects analyses of processes such as Higgs production through VBF or with high transverse momentum. As was found, most trips don't require full power cycling to resume operation. An improved control and monitoring system should be able to automatically identify the type of failure and take the appropriate measures.

The existing LV monitoring system [365] is based on the Embedded Local Monitoring Board (ELMB), developed at CERN as an all-purpose slow monitoring solution. It's last revision, ELMB128 [367–369], shown in Fig. C.12, was developed in 2003. As such, it contains no longer replaceable components. ELMB128 utilized a single-channel ADC limited by circuit components to a maximum sampling rate of 30 sps, shared among up to 64 multiplexed

input signals. And while it is sufficiently radiation tolerant to operate on TileCal even through Run 3, it cannot be relied on during the future high-luminosity runs.

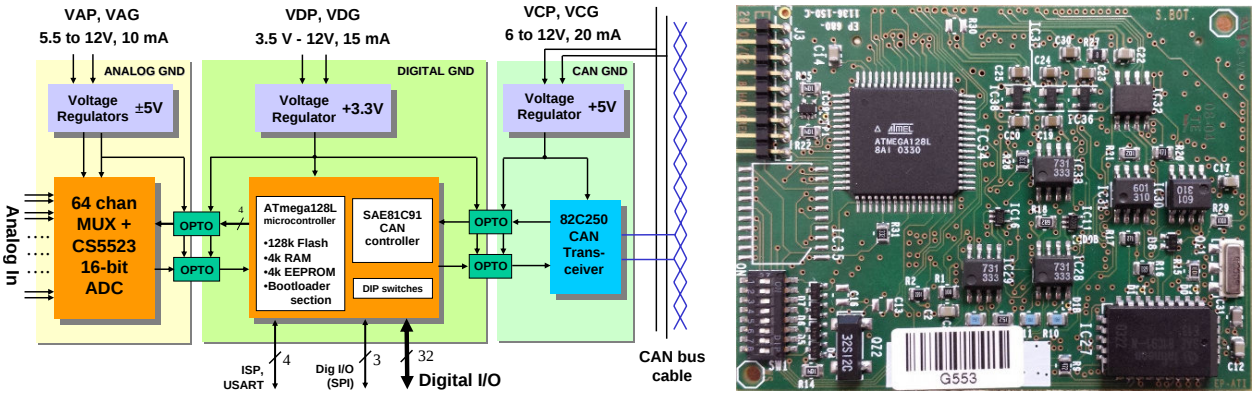

Figure C.12: ELMB128. Its block diagram [367] is shown on the left and its photograph on the right. The dimensions of the circuit board are 50×67 mm.

The studies I conducted at Argonne National Laboratory showed that analysis of transient behavior of output current from the bricks is a viable way to distinguish several types of failure. In order to do so, a minimum required sampling rate of 2 ksps was estimated. The possibility of upgrading ELMB128 by component replacement to improve its sampling rate and radiation tolerance was considered, but was not found feasible. The details can be found in the report [362]. The considerations presented there were incorporated into the Technical Design Report for the Phase-II Upgrade of the ATLAS Tile Calorimeter [352].

Following the LV monitoring upgrade report [362], development started to provide a modern replacement for the ELMB. Widespread use of the ELMB in slow-control system at the LHC means that the best solution would be to design a fully backwards compatible board. Unfortunately, after different solutions were considered, it became apparent that it would not be possible to simultaneously maintain backward compatibility and to satisfy the increased requirements for radiation tolerance and throughput. Three parallel development paths were agreed upon to produce new ELMB versions that meet requirements of different

groups of users. The first design, called ELMB2, is backward compatible with the current ELMB. The second design, called ELMB++ GBT-SCA [370], based on radiation hard ASICs is aimed to satisfy the highest requirements with respect to radiation. And a third design, called ELMB++ FPGA, is composed only of commercial off-the-shelf components and would have the highest data throughput [371].

Continuing MSU's contribution to the development and operation TileCal, the MSU group was tasked with production and design of the new ELMB2 Mother-board for the fLVPS [372].

C.4 Cs calibration firmware

Three calibration and monitoring systems are implemented on TileCal [185, 373]. The charge injection system is designed to calibrate the relative pulse response of the readout electronics for all PMTs and to monitor its variations over time. The laser system is used to check the PMTs' linearity, for studies of pulse saturation recovery, in calorimeter timing, and also for debugging and diagnostics tests. The cesium calibration system is implemented to determine the quality of the optical response of each calorimeter cell, to adjust the PMTs' HV to equalize the response from all cells, and to monitor it over time [374, 375].

The Cs calibration system, schematically illustrated in Fig. C.13, works in the following way. Every TileCal module is equipped with a hollow tube that passes perpendicularly through every scintillator tile. A 5.6×11.5 mm capsule, containing an 8 mCi sample of Cs^{137}, can travel through the 6 mm tube to provide a temporary source of γ radiation. The capsule is moved through the tube using water as the hydraulic fluid driven by a pump located in the hydraulic crate off the detector. When calibration runs are not performed,

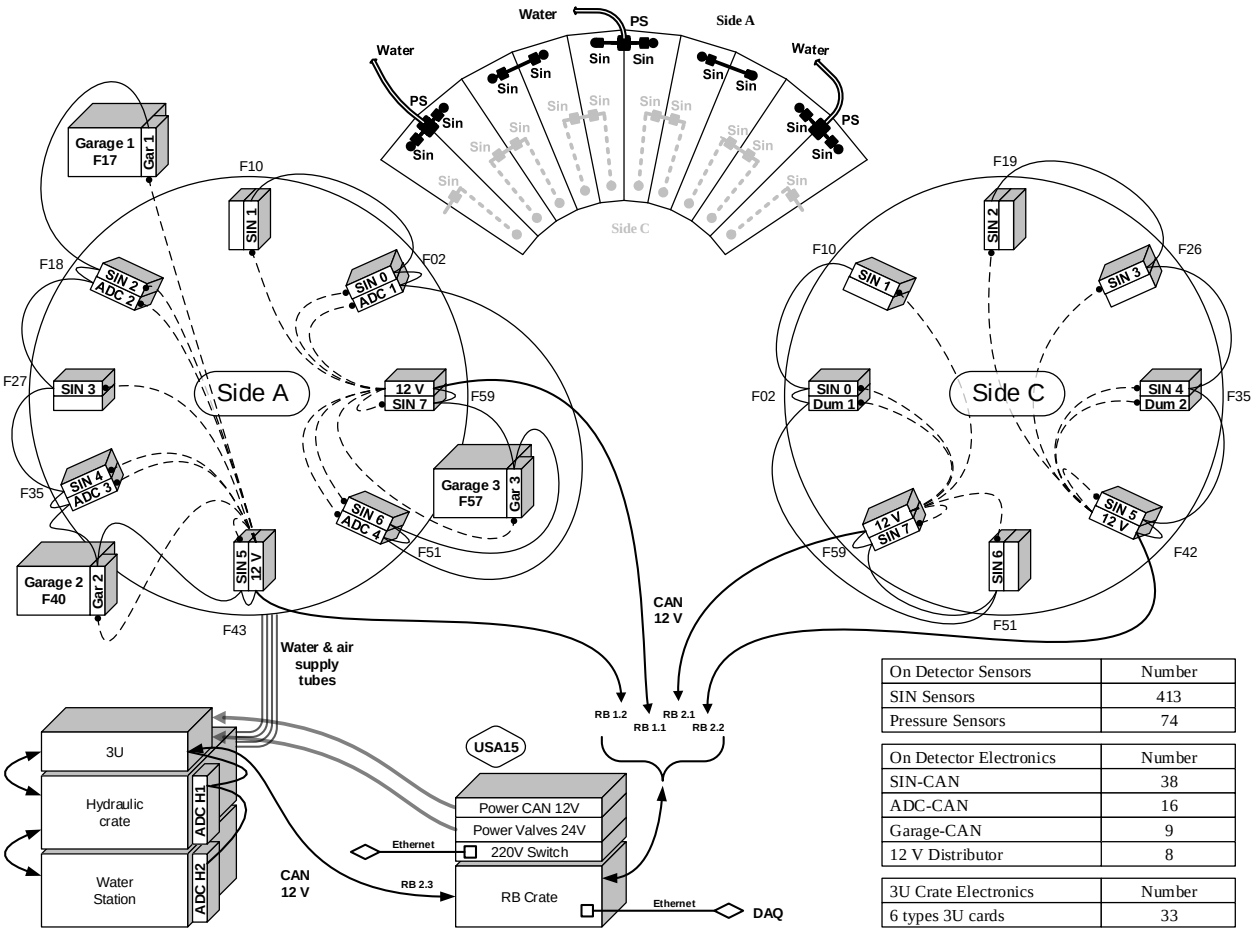

On Detector Sensors	Number
SIN Sensors	413
Pressure Sensors	74

On Detector Electronics	Number
SIN-CAN	38
ADC-CAN	16
Garage-CAN	9
12 V Distributor	8

3U Crate Electronics	Number
6 types 3U cards	33

Figure C.13: Diagram of the TileCal cesium calibration system [375].

the capsules are housed in garage compartments mounted on every TileCal barrel. Multiple modules are connected together and are serviced by one garage. Inductance sensors, labeled SIN, are used to track the capsule's position in the system. Calibration runs are controlled by electronics boards also located in the garages.

An example of Cs calibration data is shown in Fig. C.14. The horizontal axis effectively shows the position of the capsule within the cell and the vertical axis shows integrated signal from the PMTs. The source-induced current is measured approximately every 3 mm, giving 6 points per tile, the tile spacing being about 18 mm. What emerges is a picture of the relative response of the scintillator tiles, with each tooth on the plot corresponding to the amount of

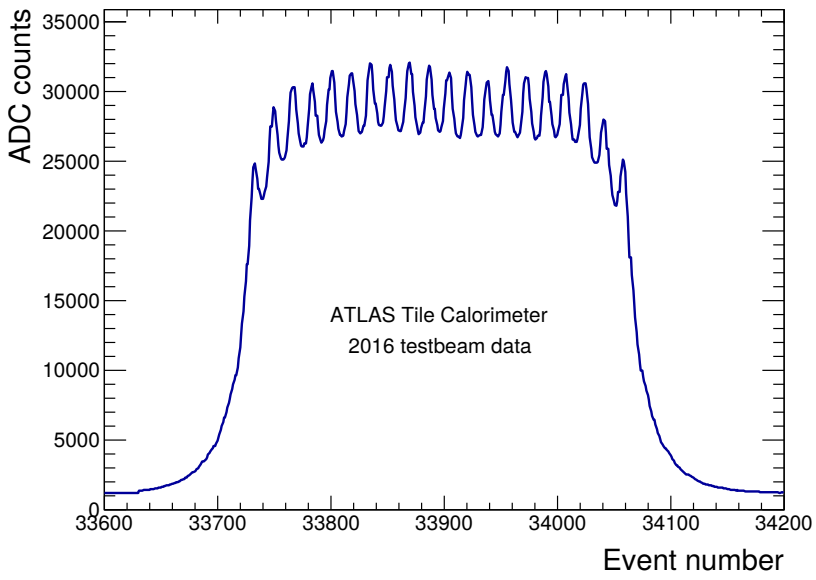

Figure C.14: Cs scan data collected during a testbeam in 2016 using the Demonstrator electronics [349]. The plot shows the response of the tiles in the BC6 cell of the module. Each peak corresponds to the Cs source passing though a tile.

signal from a particular tile. The tiles' response can then be equalized by adjusting the HV delivered to the PMTs thereby calibrating their gain. Cs scans allow to evaluate single-tile response to within 2%. That leads to the tile row mean response accuracy close to 0.6%, and 0.3% for the cell average.

As part of the Phase-II upgrade, communication between DCS and the Cs boards will be routed through the Daughter boards. One of the upgrade projects that I worked on was the development of the required component for the Daughter board FPGA firmware [376]. This VHDL firmware component implements communication between the DB and the Cs boards via SPI protocol using LVDS lines. A test bench setup used in the development of the firmware is shown in Fig. C.15.

When a Cs scan begins, the Cs board runs a program installed on its microcontroller. The program controls the hydraulic system, the release, tracking, and parking of the Cs capsule in the garage compartment, as well as data collection. During the scan, the Cs

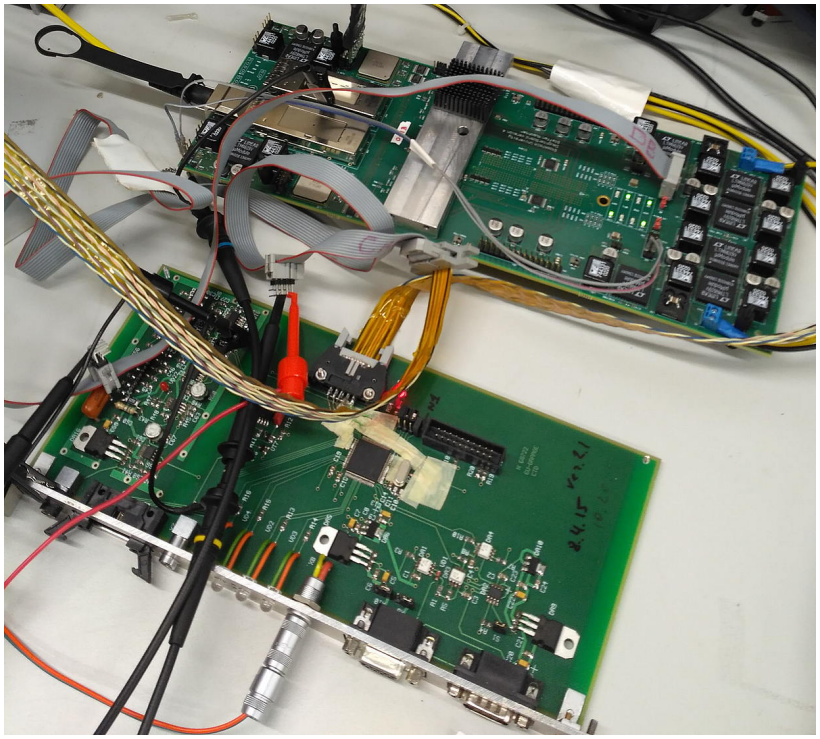

Figure C.15: Photograph of the electronics setup used for development of the Cs calibration system (bottom board) FPGA firmware component for the TileCal mini-drawer Daughter board (top board).

board collects and transmits information about the scan. With the Cs board operating the scans, the natural setup for the SPI protocol is for the Cs board to act as a master and for the DB to be a slave device. However, the Cs board needs to receive commands to start or abort a scan. In order to allow this, the SPI protocol was slightly modified, and the slave select (`nSS`) line was changed to a request (`nREQ`) line, to enable the DB to request clock cycles and initialize communication. Only one Cs board is installed for each garage, so only some Daughter boards need to connect to one. This one-to-one connection makes the modification of the SPI protocol possible. With every transmission, a message from the Cs board is stored in the `cs_status` register on the DB, and the contents of the `cs_command` DB register are transmitted to the Cs board. A new time stamp is written to the `cs_timestamp` register upon the completion of every transaction. The DB lowers the

`nREQ` line, when a different value is written into the `cs_command` register by the PPr. The values of the DB registers are automatically and periodically copied to the PPr. This update rate is much faster then the communication between the DB and the Cs board, so there will be no apparent synchronization delay.

Communication was successfully tested with a version 4 Daughter board [376]. The firmware was later used during the testbeam to collect calibration data, shown in Fig. C.14.

C.5 Testbeam

Before any new hardware can be installed on ATLAS, its readiness for deployment has to be verified. For detector components and electronics this includes studies that use particle beams to simulate data collection under realistic operation conditions. Such tests are colloquially referred to as the testbeam and are carried out at a dedicated cite at CERN on the Prévessin campus, where the SPS beam can be redirected via the H8 beam line for use in fixed-target experiments. With different components of the TileCal readout electronics chain developed by independent teams in different countries, testbeam studies allow to evaluate the joint operation of the whole system and to test for problems that are difficult to identify in a test-bench environment.

From 2015 to 2017 a number of testbeam campaigns was carried out to study the performance and stability of the full chain of TileCal Phase-II upgrade electronics [377–379]. A diagram of the test setup is shown in Fig. C.16. Response and calibration were tested for different types of particles at different energies. The testbeam facility can provide beams of muons, positrons, or hadrons, all of which were used. To identify the particle species at energies below 50 GeV, two Cherenkov counters and a muon hodoscope were placed in the

path of the particle beam. The additional instruments included trigger scintillators, used in coincidence to signal passing of the beam, and wire chambers, which provided position measurements of the beam with respect to the modules. 5 modules were used in the tests, arranged as shown in Fig. C.17. The modules were placed on a mobile table to allow their orientation to be changed with respect to the beam. Different versions of electronics, listed in Table C.1, were installed on different modules to run comparative tests.

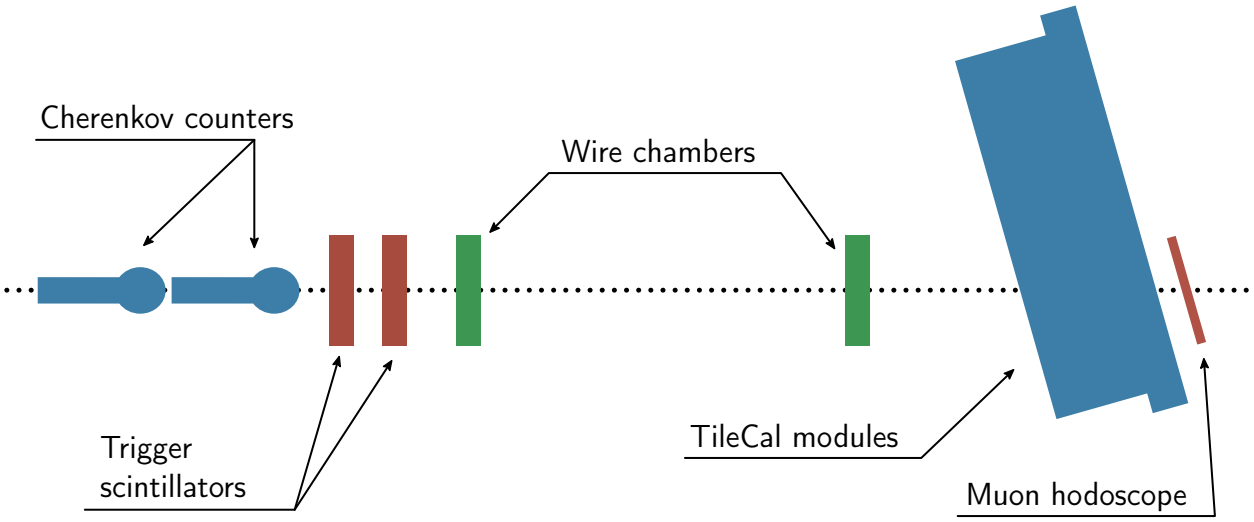

Figure C.16: TileCal Demonstrator testbeam setup [379]. The beam direction is from left to right.

The testbeam results demonstrated good performance of the new electronics and agreement of its calibrated measurements with the legacy system and simulations [380]. I participated in the testbeam activities in 2016, including firmware debugging, writing a program for positioning of the mobile table, and taking data collection shifts in August of that year. The data shown in Fig. C.14 was collected at the testbeam in 2016 using the firmware I developed for communication between the DB and the Cs calibration boards.

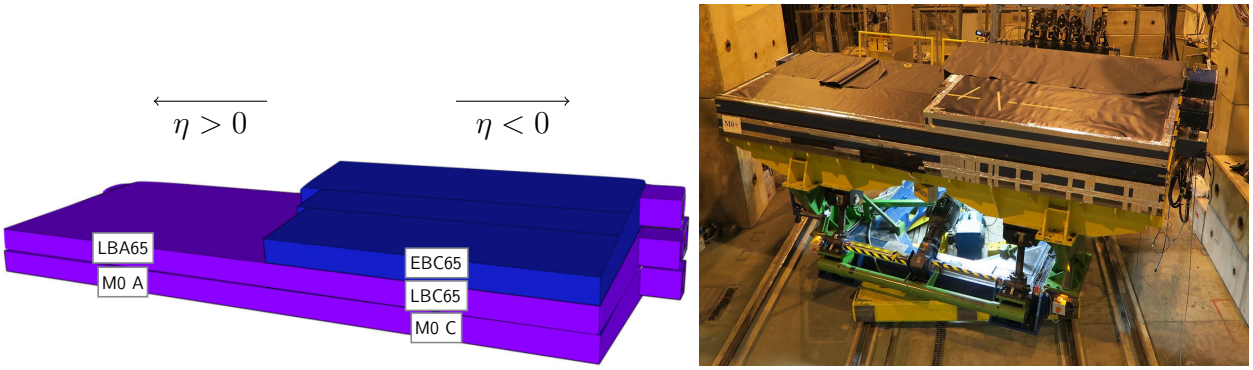

Figure C.17: Left: Diagram of TileCal modules' arrangement for the testbeam [379]. Right: Photograph of the modules positioned on the mobile table in the testbeam area [381].

Table C.1: Configuration of modules and electronics during the October 2016 testbeam period [349].

				Superdrawer LEGACY			
				EB65 - C side			
MD#4 QIE	MD#3 QIE	MD#2 FATALIC	MD#1 FATALIC	MD#1 3in1	MD#2 3in1	MD#3 3in1	MD#4 3in1
HVOpto	HVOpto	HVRemote	HVRemote	HVRemote	HVOpto	HVOpto	HVRemote
LB65 - A side				LB65 - C side			
Superdrawer LEGACY				Superdrawer LEGACY			
Module 0 - A side				Module 0 - C side			

BIBLIOGRAPHY

BIBLIOGRAPHY

[1] ATLAS Collaboration. "Observation of a new particle in the search for the Standard Model Higgs boson with the ATLAS detector at the LHC". *Phys. Lett. B* **716** (Aug. 2012), 1–29. DOI: 10.1016/j.physletb.2012.08.020. arXiv: 1207.7214. CDS: 1471031 (on pp. 2, 87, 145).

[2] CMS Collaboration. "Observation of a new boson at a mass of 125 GeV with the CMS experiment at the LHC". *Phys. Lett. B* **716** (Aug. 2012), 30. DOI: 10.1016/j.physletb.2012.08.021. arXiv: 1207.7235. CDS: 1471031 (on pp. 2, 145).

[3] D. J. Griffiths. *Introduction to Quantum Mechanics*. 2005. ISBN: 978-0-13-111892-8 (on p. 5).

[4] M. E. Peskin and D. V. Schroeder. *An Introduction to Quantum Field Theory*. 1995. ISBN: 978-0-201-50397-5 (on pp. 6, 15, 17, 18).

[5] J. D. Wells. "The Once and Present Standard Model of Elementary Particle Physics" (2019). arXiv: 1911.04604 (on p. 7).

[6] "Standard Model of Elementary Particles". Oct. 2019. URL: https://commons.wikimedia.org/wiki/File:Standard_Model_of_Elementary_Particles.svg (on p. 8).

[7] A. Zee. *Quantum Field Theory in a Nutshell*. 2003. ISBN: 978-0-691-01019-9 (on p. 9).

[8] "Understanding gauge fields as connections on a principal G-bundle". URL: https://physics.stackexchange.com/a/295846/81346 (on p. 19).

[9] F. Englert and R. Brout. "Broken Symmetry and the Mass of Gauge Vector Mesons". *Phys. Rev. Lett.* **13** (Aug. 1964), 321–323. DOI: 10.1103/PhysRevLett.13.321 (on p. 22).

[10] P. W. Higgs. "Broken Symmetries and the Masses of Gauge Bosons". *Phys. Rev. Lett.* **13** (Oct. 1964), 508–509. DOI: 10.1103/PhysRevLett.13.508 (on p. 22).

[11] G. S. Guralnik, C. R. Hagen, and T. W. B. Kibble. "Global Conservation Laws and Massless Particles". *Phys. Rev. Lett.* **13** (Nov. 1964), 585–587. DOI: 10.1103/PhysRevLett.13.585 (on p. 22).

[12] V. L. Ginzburg and L. D. Landau. "Towards theory of superconductivity". *JETP* **20** (1950), 1064 (on p. 22).

[13] M. Shifman. "ITEP Lectures in Particle Physics". 1995. arXiv: hep-ph/9510397 (on p. 30).

[14] M. Tanabashi et al., Particle Data Group. "Review of Particle Physics". *Phys. Rev. D* **98** (Aug. 2018), 030001. DOI: 10.1103/PhysRevD.98.030001 (on pp. 30, 32, 46, 216).

[15] J. Campbell, J. Huston, and F. Krauss. *The Black Book of Quantum Chromodynamics: A Primer for the LHC Era*. 2018. ISBN: 978-0-19-965274-7 (on pp. 31, 48, 49, 53).

[16] J. C. Collins, D. E. Soper, and G. Sterman. "Factorization of Hard Processes in QCD". *Adv. Ser. Direct. High Energy Phys.* **5** (July 1989), 1–91. DOI: 10.1142/9789814503266_0001. arXiv: hep-ph/0409313 (on p. 33).

[17] J.-W. Chen et al. "Lattice calculation of parton distributions" (May 2018). arXiv: 1803.04393 (on p. 33).

[18] C. Alexandrou et al. "Lattice calculation of parton distributions". *Phys. Rev. D* **92** (July 2015), 014502. DOI: 10.1103/PhysRevD.92.014502 (on p. 33).

[19] C. Alexandrou et al. "Updated lattice results for parton distributions". *Phys. Rev. D* **96** (July 2017), 014513. DOI: 10.1103/PhysRevD.96.014513 (on p. 33).

[20] Y. L. Dokshitser. "Calculation of structure functions of deep-inelastic scattering and e^+-e^- annihilation by perturbation theory in quantum chromodynamics". *JETP* **46**.4 (Oct. 1977), 641 (on p. 34).

[21] V. N. Gribov and L. N. Lipatov. "Deep inelastic *e-p* scattering in perturbation theory". *Sov. J. Nucl. Phys.* **15** (1972), 438–450 (on p. 34).

[22] G. Altarelli and G. Parisi. "Asymptotic Freedom in Parton Language". *Nucl. Phys. B* **126** (1977), 298–318. DOI: 10.1016/0550-3213(77)90384-4 (on p. 34).

[23] A. D. Martin and M. G. Ryskin. "The photon PDF of the proton". *Eur. Phys. J. C* **74**.9 (Sept. 2014), 3040. DOI: 10.1140/epjc/s10052-014-3040-y. arXiv: 1406.2118 (on p. 34).

[24] V. Bertone et al. "On the Impact of Lepton PDFs". *JHEP* 11 (2015), 194. DOI: 10.1007/JHEP11(2015)194. arXiv: 1508.07002. CDS: 2047948 (on p. 34).

[25] S. Dulat et al. "New parton distribution functions from a global analysis of quantum chromodynamics". *Phys. Rev. D* **93** (Feb. 2016), 033006. DOI: 10.1103/PhysRevD.93.033006. arXiv: 1506.07443 (on pp. 34, 61, 223).

[26] D. d'Enterria. "Higgs physics at the Future Circular Collider. Higgs physics at the Future Circular Collider". *PoS* **282**.ICHEP2016 (Jan. 2017), 434. DOI: 10.22323/1.282.0434. arXiv: 1701.02663. CDS: 2241951 (on p. 36).

[27] "Higgs cross sections for HL-LHC and HE-LHC". URL: https://twiki.cern.ch/twiki/bin/view/LHCPhysics/HiggsEuropeanStrategy (on p. 36).

[28] LHC Higgs Cross Section Working Group. *Handbook of LHC Higgs Cross Sections: 3. Higgs Properties*. 2013. DOI: 10.5170/CERN-2013-004. arXiv: 1307.1347. CDS: 1559921 (on pp. 37, 65, 67, 169).

[29] ATLAS Collaboration. "Identification of boosted Higgs bosons decaying into b-quark pairs with the ATLAS detector at 13 TeV". *Eur. Phys. J. C* **79**.10 (Oct. 2019), 836. DOI: 10.1140/epjc/s10052-019-7335-x. CDS: 2680245 (on p. 37).

[30] LHC Higgs Cross Section Working Group. *Handbook of LHC Higgs Cross Sections: 4. Deciphering the Nature of the Higgs Sector*. 2017. DOI: 10.23731/CYRM-2017-002. arXiv: 1610.07922. CDS: 2227475 (on pp. 37, 69, 72).

[31] G. Cowan. *Statistical Data Analysis*. 1998. ISBN: 978-0-19-850155-8 (on pp. 40, 169, 182, 184, 190).

[32] S. Höche. "Introduction to parton-shower event generators" (2014). arXiv: 1411.4085 (on pp. 43, 44).

[33] Z. Nagy and D. E. Soper. "What is a parton shower?" *Phys. Rev. D* **98** (July 2018), 014034. DOI: 10.1103/PhysRevD.98.014034. arXiv: 1705.08093 (on p. 43).

[34] D. Kar. *Experimental Particle Physics*. 2019. ISBN: 978-0-7503-2110-5. DOI: 10.1088/2053-2563/ab1be6 (on pp. 44, 46, 53).

[35] A. Buckley et al. "General-purpose event generators for LHC physics". *Phys. Rep.* **504**.5 (July 2011), 145–233. DOI: 10.1016/j.physrep.2011.03.005. arXiv: 1101.2599 (on p. 44).

[36] J. C. Collins. "Sudakov Form Factors". *Adv. Ser. Direct. High Energy Phys.* **5** (July 1989), 573–614. DOI: 10.1142/9789814503266_0006. arXiv: hep-ph/0312336 (on p. 44).

[37] S. Höche, D. Reichelt, and F. Siegert. "Momentum conservation and unitarity in parton showers and NLL resummation". *JHEP* 01 (Jan. 2018), 118. DOI: 10.1007/JHEP01(2018)118. arXiv: 1711.03497 (on p. 45).

[38] M. Dasgupta et al. "Parton Showers beyond Leading Logarithmic Accuracy". *Phys. Rev. Lett.* **125** (July 2020), 052002. DOI: 10.1103/PhysRevLett.125.052002. arXiv: 2002.11114 (on p. 45).

[39] B. Andersson et al. "Parton fragmentation and string dynamics". *Phys. Rep.* **97**.2 (1983), 31–145. DOI: 10.1016/0370-1573(83)90080-7 (on p. 45).

[40] B. Andersson. *The Lund Model*. Cambridge Monographs on Particle Physics, Nuclear Physics and Cosmology. 1998. ISBN: 978-0-511-52436-3. DOI: 10.1017/CBO9780511524363 (on p. 45).

[41] G. Marchesini and B. R. Webber. "Simulation of QCD jets including soft gluon interference". *Nucl. Phys. B* **238**.1 (1984), 1–29. DOI: 10.1016/0550-3213(84)90463-2. CDS: 143716 (on p. 45).

[42] B. R. Webber. "A QCD model for jet fragmentation including soft gluon interference". *Nucl. Phys. B* **238**.3 (1984), 492–528. DOI: 10.1016/0550-3213(84)90333-X. CDS: 147786 (on p. 45).

[43] G. Marchesini and B. R. Webber. "Monte Carlo simulation of general hard processes with coherent QCD radiation". *Nucl. Phys. B* **310**.3 (1988), 461–526. DOI: 10.1016/0550-3213(88)90089-2. CDS: 184684 (on p. 45).

[44] S. Agostinelli et al. "Geant4 — a simulation toolkit". *NIM A* **506**.3 (2003), 250–303. DOI: 10.1016/S0168-9002(03)01368-8. CDS: 602040 (on pp. 45, 66).

[45] R. Field. "Min-Bias and the Underlying Event at the LHC" (2011). arXiv: 1110.5530 (on p. 45).

[46] R. Boughezal et al. "Higgs boson production in association with a jet at NNLO using jettiness subtraction". *Phys. Lett. B* **748** (2015), 5–8. DOI: 10.1016/j.physletb.2015.06.055. arXiv: 1505.03893 (on p. 47).

[47] G. P. Salam. "Perturbative QCD for the LHC" (2011). arXiv: 1103.1318 (on p. 47).

[48] Z. Bern et al. "The NLO multileg working group: summary report" (2008). arXiv: 0803.0494 (on p. 47).

[49] J. Huston. "The new Les Houches high precision wish list". Aug. 2014. URL: https://indico.cern.ch/event/334268/ (on p. 47).

[50] S. Catani and M. H. Seymour. "The dipole formalism for the calculation of QCD jet cross sections at next-to-leading order". *Phys. Lett. B* **378**.1 (1996), 287–301. DOI: 10.1016/0370-2693(96)00425-X. arXiv: hep-ph/9602277 (on p. 50).

[51] S. Catani and M. H. Seymour. "A general algorithm for calculating jet cross sections in NLO QCD". *Nucl. Phys. B* **485**.1 (1997), 291–419. DOI: 10.1016/S0550-3213(96)00589-5. arXiv: hep-ph/9605323 (on pp. 50, 221).

[52] S. Frixione, Z. Kunszt, and A. Signer. "Three-jet cross sections to next-to-leading order". *Nucl. Phys. B* **467**.3 (1996), 399–442. DOI: 10.1016/0550-3213(96)00110-1. arXiv: hep-ph/9512328 (on p. 50).

[53] S. Frixione. "A general approach to jet cross sections in QCD". *Nucl. Phys. B* **507**.1 (1997), 295–314. DOI: 10.1016/S0550-3213(97)00574-9. arXiv: hep-ph/9706545 (on p. 50).

[54] S. Frixione, P. Nason, and C. Oleari. "Matching NLO QCD computations with parton shower simulations: the POWHEG method". *JHEP* 11 (2007), 070. DOI: 10.1088/1126-6708/2007/11/070. arXiv: 0709.2092 (on pp. 51, 53, 65).

[55] S. Frixione and B. R. Webber. "Matching NLO QCD computations and parton shower simulations". *JHEP* 06 (June 2002), 029. DOI: 10.1088/1126-6708/2002/06/029. arXiv: hep-ph/0204244 (on p. 52).

[56] S. Frixione et al. "NLO QCD corrections in HERWIG++ with MC@NLO". *JHEP* 01 (Jan. 2011), 053. DOI: 10.1007/JHEP01(2011)053. arXiv: 1010.0568 (on p. 52).

[57] M. L. Mangano, M. Moretti, and R. Pittau. "Multijet matrix elements and shower evolution in hadronic collisions: $Wb\bar{b}+n$-jets as a case study". *Nucl. Phys. B* **632**.1 (2002), 343–362. DOI: 10.1016/S0550-3213(02)00249-3. arXiv: hep-ph/0108069 (on p. 52).

[58] S. Catani et al. "QCD Matrix Elements + Parton Showers". *JHEP* 11 (Nov. 2001), 063. DOI: 10.1088/1126-6708/2001/11/063. arXiv: hep-ph/0109231 (on p. 53).

[59] F. Krauss. "Matrix Elements and Parton Showers in Hadronic Interactions". *JHEP* 08 (Aug. 2002), 015. DOI: 10.1088/1126-6708/2002/08/015. arXiv: hep-ph/0205283 (on p. 53).

[60] L. Lönnblad. "Correcting the Colour-Dipole Cascade Model with Fixed Order Matrix Elements". *JHEP* 05 (May 2002), 046. DOI: 10.1088/1126-6708/2002/05/046. arXiv: hep-ph/0112284 (on p. 53).

[61] M. Kaku. *Quantum Field Theory: A modern introduction*. 1993. ISBN: 978-0-19-507652-3 (on p. 56).

[62] G. 't Hooft. "Dimensional regularization and the renormalization group". *Nucl. Phys. B* **61** (1973), 455–468. DOI: 10.1016/0550-3213(73)90376-3 (on p. 57).

[63] S. Weinberg. "New Approach to the Renormalization Group". *Phys. Rev. D* **8** (Nov. 1973), 3497–3509. DOI: 10.1103/PhysRevD.8.3497 (on p. 57).

[64] J. Huston. "Scale dependence for inclusive and non-inclusive cross sections". Jan. 2013. URL: https://indico.cern.ch/event/226756/contributions/1535641/ (on p. 58).

[65] J. Huston. "Lessons from Measurements of $W/Z/H$ + jets production". Mar. 2017. URL: https://indico.cern.ch/event/555452/contributions/2495869/ (on p. 58).

[66] H.-L. Lai et al. "New parton distributions for collider physics". *Phys. Rev. D* **82** (Oct. 2010), 074024. DOI: 10.1103/PhysRevD.82.074024. arXiv: 1007.2241 (on pp. 61, 230).

[67] T.-J. Hou et al. "New CTEQ global analysis of quantum chromodynamics with high-precision data from the LHC" (2019). arXiv: 1912.10053 (on p. 61).

[68] R. D. Ball et al., NNPDF Collaboration. "QCD matrix elements + parton showers. The NLO case". *JHEP* 04 (2015), 040. DOI: 10.1007/JHEP04(2015)040 (on pp. 61, 68).

[69] S. Forte and S. Carrazza. "Parton distribution functions" (2020). arXiv: 2008.12305 (on p. 61).

[70] J. Pumplin et al. "Collider inclusive jet data and the gluon distribution". *Phys. Rev. D* **80** (July 2009), 014019. DOI: 10.1103/PhysRevD.80.014019. arXiv: 0904.2424 (on p. 61).

[71] J. Pumplin et al. "Uncertainties of predictions from parton distribution functions II: The Hessian method". *Phys. Rev. D* **65** (Dec. 2001), 014013. DOI: 10.1103/PhysRevD.65.014013. arXiv: hep-ph/0101032 (on p. 61).

[72] J. Pumplin. "Data set diagonalization in a global fit". *Phys. Rev. D* **80** (Aug. 2009), 034002. DOI: 10.1103/PhysRevD.80.034002. arXiv: 0904.2425 (on p. 61).

[73] A. Buckley et al. "LHAPDF6: parton density access in the LHC precision era". *Eur. Phys. J. C* **75**.3 (Mar. 2015). DOI: 10.1140/epjc/s10052-015-3318-8. arXiv: 1412.7420 (on pp. 61, 220).

[74] ATLAS Collaboration. "The ATLAS Simulation Infrastructure". *Eur. Phys. J. C* **70**.3 (2010), 823–874. DOI: 10.1140/epjc/s10052-010-1429-9. arXiv: 1005.4568. CDS: 1267853 (on pp. 64, 68).

[75] R. D. Ball et al. "Parton distributions with LHC data". *Nucl. Phys. B* **867**.2 (2013), 244–289. DOI: 10.1016/j.nuclphysb.2012.10.003. arXiv: 1207.1303. CDS: 1460337 (on p. 64).

[76] ATLAS Collaboration. "The Pythia 8 A3 tune description of ATLAS minimum bias and inelastic measurements incorporating the Donnachie-Landshoff diffractive model". ATL-PHYS-PUB-2016-017. Aug. 2016. CDS: 2206965 (on p. 64).

[77] K. Hamilton et al. "NNLOPS simulation of Higgs boson production". *JHEP* 10 (2013), 222. DOI: 10.1007/JHEP10(2013)222. arXiv: 1309.0017 (on p. 65).

[78] P. Nason. "A New Method for Combining NLO QCD with Shower Monte Carlo Algorithms". *JHEP* 11 (2004), 040. DOI: 10.1088/1126-6708/2004/11/040. arXiv: hep-ph/0409146 (on p. 65).

[79] S. Alioli et al. "A general framework for implementing NLO calculations in shower Monte Carlo programs: the POWHEG BOX". *JHEP* 06 (2010), 043. DOI: 10.1007/JHEP06(2010)043. arXiv: 1002.2581 (on p. 65).

[80] J. Butterworth et al. "PDF4LHC recommendations for LHC Run II". *J. Phys. G* **43**.2 (Jan. 2016), 023001. DOI: 10.1088/0954-3899/43/2/023001. arXiv: 1510.03865. CDS: 2059563 (on pp. 65, 69).

[81] T. Sjöstrand, S. Mrenna, and P. Skands. "A Brief Introduction to PYTHIA 8.1". *Comput. Phys. Commun.* **178**.11 (2008), 852–867. DOI: 10.1016/j.cpc.2008.01.036. arXiv: 0710.3820 (on pp. 65, 194).

[82] ATLAS Collaboration. "Measurement of the Z/γ^* boson transverse momentum distribution in pp collisions at $\sqrt{s} = 7$ TeV with the ATLAS detector". *JHEP* 09 (2014), 145. DOI: 10.1007/JHEP09(2014)145. arXiv: 1406.3660. CDS: 1708940 (on p. 66).

[83] A. Djouadi, J. Kalinowski, and M. Spira. "HDECAY: a program for Higgs boson decays in the Standard Model and its supersymmetric extension". *Comput. Phys. Commun.* **108**.1 (1998), 56–74. DOI: 10.1016/S0010-4655(97)00123-9. arXiv: hep-ph/9704448 (on p. 66).

[84] M. Spira. "QCD Effects in Higgs Physics". *Fortschr. Phys.* **46**.3 (1998), 203–284. DOI: 10.1002/(SICI)1521-3978(199804)46:3<203::AID-PROP203>3.0.CO;2-4. arXiv: hep-ph/9705337. CDS: 326141 (on p. 66).

[85] A. Djouadi, M. M. Muhlleitner, and M. Spira. "Decays of supersymmetric particles: The Program SUSY-HIT (SUspect-SdecaY-Hdecay-InTerface)". *Acta Phys. Polon. B* **38** (2007), 635–644. arXiv: hep-ph/0609292 (on p. 66).

[86] A. Djouadi et al. "HDECAY: Twenty++ years after". *Comput. Phys. Commun.* **238** (2019), 214–231. DOI: 10.1016/j.cpc.2018.12.010. arXiv: 1801.09506 (on p. 66).

[87] A. Bredenstein et al. "Radiative corrections to the semileptonic and hadronic Higgs-boson decays $H \to WW/ZZ \to 4$ fermions". *JHEP* 02 (2007), 080. DOI: 10.1088/1126-6708/2007/02/080. arXiv: hep-ph/0611234 (on p. 66).

[88] A. Bredenstein et al. "Precise predictions for the Higgs-boson decay $H \to WW/ZZ \to 4$ leptons". *Phys. Rev. D* **74** (July 2006), 013004. DOI: 10.1103/PhysRevD.74.013004. arXiv: hep-ph/0604011 (on p. 66).

[89] A. Bredenstein et al. "Precision calculations for the Higgs decays $H \to ZZ/WW \to 4$ leptons". *Nucl. Phys. B* **160** (2006). Proceedings of the 8th DESY Workshop on Elementary Particle Theory, 131–135. DOI: 10.1016/j.nuclphysbps.2006.09.104. arXiv: hep-ph/0607060 (on p. 66).

[90] K. Hamilton et al. "NNLOPS simulation of Higgs boson production". *JHEP* 10 (2013), 222. DOI: 10.1007/JHEP10(2013)222. arXiv: 1309.0017 (on pp. 66, 69).

[91] K. Hamilton, P. Nason, and G. Zanderighi. "MINLO: Multi-scale Improved NLO". *JHEP* 10 (2012), 155. DOI: 10.1007/JHEP10(2012)155. arXiv: 1206.3572 (on p. 66).

[92] G. Bozzi et al. "Transverse-momentum resummation and the spectrum of the Higgs boson at the LHC". *Nucl. Phys. B* **737**.1 (2006), 73–120. DOI: 10.1016/j.nuclphysb.2005.12.022. arXiv: hep-ph/0508068 (on p. 66).

[93] P. Nason and C. Oleari. "NLO Higgs boson production via vector-boson fusion matched with shower in POWHEG". *JHEP* 02 (2010), 037. DOI: 10.1007/JHEP02(2010)037. arXiv: 0911.5299 (on p. 67).

[94] E. Bothmann et al. "Event Generation with Sherpa 2.2". *SciPost Phys.* **7**.3 (2019), 34. DOI: 10.21468/SciPostPhys.7.3.034. arXiv: 1905.09127 (on p. 67).

[95] S. Schumann and F. Krauss. "A parton shower algorithm based on Catani–Seymour dipole factorisation". *JHEP* 03 (2008), 038. DOI: 10.1088/1126-6708/2008/03/038. arXiv: 0709.1027 (on pp. 68, 69).

[96] S. Höche et al. "A critical appraisal of NLO+PS matching methods". *JHEP* 09 (2012), 049. DOI: 10.1007/JHEP09(2012)049 (on p. 68).

[97] S. Höche et al. "QCD matrix elements + parton showers. The NLO case". *JHEP* 09 (2013), 027. DOI: 10.1007/JHEP09(2012)049 (on p. 68).

[98] S. Catani et al. "QCD Matrix Elements + Parton Showers". *JHEP* 11 (2001), 063. DOI: 10.1088/1126-6708/2001/11/063 (on p. 68).

[99] S. Höche et al. "QCD matrix elements and truncated showers". *JHEP* 05 (2009), 053. DOI: 10.1088/1126-6708/2009/05/053 (on p. 68).

[100] T. Gleisberg et al. "Event generation with SHERPA 1.1". *JHEP* 02 (Feb. 2009), 007. DOI: 10.1088/1126-6708/2009/02/007. arXiv: 0811.4622 (on pp. 69, 70, 215).

[101] S. Höche et al. "A critical appraisal of NLO+PS matching methods". *JHEP* 09 (Sept. 2012), 049. DOI: 10.1007/JHEP09(2012)049. arXiv: 1111.1220 (on p. 69).

[102] S. Höche et al. "QCD matrix elements + parton showers: The NLO case". *JHEP* 04 (Apr. 2013), 027. DOI: 10.1007/JHEP04(2013)027. arXiv: 1207.5030 (on p. 69).

[103] S. Höche and M. Schönherr. "Uncertainties in next-to-leading order plus parton shower matched simulations of inclusive jet and dijet production". *Phys. Rev. D* **86** (Nov. 2012), 094042. DOI: 10.1103/PhysRevD.86.094042. arXiv: 1208.2815 (on p. 69).

[104] J. Campbell et al. "MCFM — Monte Carlo for FeMtobarn processes". URL: https://mcfm.fnal.gov (on p. 69).

[105] N. Greiner et al. "Phenomenological analysis of Higgs boson production through gluon fusion in association with jets". *JHEP* 1 (Jan. 2016), 169. DOI: 10.1007/JHEP01(2016)169. arXiv: 1506.01016 (on p. 69).

[106] G. Cullen et al. "GoSam-2.0: a tool for automated one-loop calculations within the Standard Model and beyond". *Eur. Phys. J. C* **74**.8 (Aug. 2014), 3001. DOI: 10.1140/epjc/s10052-014-3001-5. arXiv: 1404.7096 (on pp. 69, 70, 214, 230, 231).

[107] F. Krauss, R. Kuhn, and G. Soff. "AMEGIC++ 1.0, A Matrix Element Generator In C++". *JHEP* 02 (2002), 044. DOI: 10.1088/1126-6708/2002/02/044. arXiv: hep-ph/0109036 (on pp. 69, 215).

[108] T. Gleisberg and S. Höche. "Comix, a new matrix element generator". *JHEP* 12 (2008), 039. DOI: 10.1088/1126-6708/2008/12/039. arXiv: 0808.3674 (on pp. 69, 215).

[109] G. Cullen et al. "Automated one-loop calculations with GoSam". *Eur. Phys. J. C* **72**.3 (Mar. 2012). DOI: 10.1140/epjc/s10052-012-1889-1. arXiv: 1111.2034 (on pp. 70, 214, 230).

[110] D. de Florian et al. "Higgs boson production at the LHC: transverse momentum resummation effects in the $H \to \gamma\gamma$, $H \to WW \to l\nu l\nu$ and $H \to ZZ \to 4l$ decay

modes". *JHEP* 06 (June 2012), 132. DOI: 10.1007/JHEP06(2012)132. arXiv: 1203.6321 (on p. 70).

[111] M. Grazzini and H. Sargsyan. "Heavy-quark mass effects in Higgs boson production at the LHC". *JHEP* 09 (Sept. 2013), 129. DOI: 10.1007/JHEP09(2013)129. arXiv: 1306.4581 (on p. 70).

[112] X. Chen et al. "Precise QCD predictions for the production of Higgs + jet final states". *Phys. Lett. B* **740** (2015), 147–150. DOI: 10.1016/j.physletb.2014.11.021. arXiv: 1408.5325 (on p. 71).

[113] P. F. Monni, E. Re, and P. Torrielli. "Higgs Transverse-Momentum Resummation in Direct Space". *Phys. Rev. Lett.* **116** (June 2016), 242001. DOI: 10.1103/PhysRevLett.116.242001. arXiv: 1604.02191 (on p. 71).

[114] X. Chen et al. "NNLO QCD corrections to Higgs boson production at large transverse momentum". *JHEP* 10 (Oct. 2016), 066. DOI: 10.1007/JHEP10(2016)066. arXiv: 1607.08817 (on p. 71).

[115] M. A. Ebert, J. K. L. Michel, and F. J. Tackmann. "Resummation improved rapidity spectrum for gluon fusion Higgs production". *JHEP* 05 (May 2017), 088. DOI: 10.1007/JHEP05(2017)088. arXiv: 1702.00794 (on p. 71).

[116] "SCETlib Home". URL: http://scetlib.desy.de (on pp. 71, 72).

[117] R. Boughezal et al. "Color-singlet production at NNLO in MCFM". *Eur. Phys. J. C* **77**.1 (Dec. 2016), 7. DOI: 10.1140/epjc/s10052-016-4558-y. arXiv: 1605.08011 (on p. 71).

[118] J. R. Gaunt et al. "N-jettiness subtractions for NNLO QCD calculations". *JHEP* 09 (Sept. 2015), 058. DOI: 10.1007/JHEP09(2015)058. arXiv: 1505.04794 (on p. 71).

[119] I. W. Stewart et al. "Jet p_{T} resummation in Higgs production at NNLL$'$ + NNLO". *Phys. Rev. D* **89** (Mar. 2014), 054001. DOI: 10.1103/PhysRevD.89.054001. arXiv: 1307.1808 (on p. 72).

[120] X. Chen et al. "Precise QCD description of the Higgs boson transverse momentum spectrum". *Phys. Lett. B* **788** (2019), 425–430. DOI: 10.1016/j.physletb.2018.11.037. arXiv: 1805.00736 (on p. 72).

[121] R. Boughezal et al. "Combining resummed Higgs predictions across jet bins". *Phys. Rev. D* **89** (Apr. 2014), 074044. DOI: 10.1103/PhysRevD.89.074044. arXiv: 1312.4535 (on p. 72).

[122] A. Banfi et al. "Jet-vetoed Higgs cross section in gluon fusion at $N^3LO + NNLL$ with small-R resummation". *JHEP* 04 (Apr. 2016), 049. DOI: 10.1007/JHEP04(2016)049. arXiv: 1511.02886 (on p. 72).

[123] J. Alwall et al. "The automated computation of tree-level and next-to-leading order differential cross sections, and their matching to parton shower simulations". *JHEP* 07 (July 2014), 079. DOI: 10.1007/JHEP07(2014)079. arXiv: 1405.0301 (on p. 73).

[124] R. Frederix et al. "Heavy-quark mass effects in Higgs plus jets production". *JHEP* 08 (Aug. 2016), 006. DOI: 10.1007/JHEP08(2016)006. arXiv: 1604.03017 (on p. 73).

[125] R. V. Harlander, H. Mantler, and M. Wiesemann. "Transverse momentum resummation for Higgs production via gluon fusion in the MSSM". *JHEP* 11 (Nov. 2014), 116. DOI: 10.1007/JHEP11(2014)116. arXiv: 1409.0531 (on p. 73).

[126] L. Evans and P. Bryant. "LHC Machine". *JINST* **3**.08 (Aug. 2008), S08001. DOI: 10.1088/1748-0221/3/08/S08001. CDS: 1129806 (on pp. 74, 75).

[127] ATLAS Collaboration. "The ATLAS Experiment at the CERN Large Hadron Collider". *JINST* **3**.08 (Aug. 2008), S08003. DOI: 10.1088/1748-0221/3/08/S08003. CDS: 1129811 (on pp. 74, 91, 94, 96, 102, 103, 106–109, 115).

[128] CMS Collaboration. "The CMS experiment at the CERN LHC". *JINST* **3**.08 (Aug. 2008), S08004. DOI: 10.1088/1748-0221/3/08/S08004. CDS: 1129810 (on p. 74).

[129] LHCb Collaboration. "The LHCb Detector at the LHC". *JINST* **3**.08 (Aug. 2008), S08005. DOI: 10.1088/1748-0221/3/08/S08005. CDS: 1129809 (on p. 74).

[130] ALICE Collaboration. "The ALICE experiment at the CERN LHC". *JINST* **3**.08 (Aug. 2008), S08002. DOI: 10.1088/1748-0221/3/08/S08002. CDS: 1129812 (on p. 75).

[131] TOTEM Collaboration. "The TOTEM Experiment at the CERN Large Hadron Collider". *JINST* **3**.08 (Aug. 2008), S08007. DOI: 10.1088/1748-0221/3/08/S08007. CDS: 1129807 (on p. 75).

[132] LHCf Collaboration. "The LHCf detector at the CERN Large Hadron Collider". *JINST* **3**.08 (Aug. 2008), S08006. DOI: 10.1088/1748-0221/3/08/S08006. CDS: 1129808 (on p. 75).

[133] MoEDAL Collaboration. "The physics programme of the MoEDAL experiment at the LHC". *Int. J. Mod. Phys. A* **29**.23 (Sept. 2014), 1430050. DOI: 10.1142/S0217751X14300506. arXiv: 1405.7662. CDS: 1705285 (on p. 75).

[134] E. Mobs. "The CERN accelerator complex. Complexe des accélérateurs du CERN". Aug. 2018 (on p. 76).

[135] J. Coupard. "LHC underground and access system". Feb. 2020. URL: https://edms.cern.ch/document/1001086/ (on p. 77).

[136] C. Fluder et al. "The Development of the Control System for the Cryogenics in the LHC Tunnel". CERN-ATS-2011-012. Jan. 2011. CDS: 1357569 (on p. 77).

[137] O. S. Brüning et al. *LHC Design Report. The LHC Main Ring*. Vol. 1. CERN Yellow Reports: Monographs. 2004. DOI: 10.5170/CERN-2004-003-V-1. CDS: 782076 (on pp. 75, 79, 82).

[138] O. S. Brüning et al. *LHC Design Report. The LHC Infrastructure and General Services*. Vol. 2. CERN Yellow Reports: Monographs. 2004. DOI: 10.5170/CERN-2004-003-V-2. CDS: 815187 (on p. 75).

[139] M. Benedikt et al. *LHC Design Report. The LHC Injector Chain*. Vol. 3. CERN Yellow Reports: Monographs. 2004. DOI: 10.5170/CERN-2004-003-V-3. CDS: 823808 (on pp. 75, 80).

[140] "Taking a closer look at LHC: RF cavities". URL: https://www.lhc-closer.es/taking_a_closer_look_at_lhc/0.rf_cavities (on p. 78).

[141] "LHC parameters". URL: https://www.lhc-closer.es/taking_a_closer_look_at_lhc/1.lhc_parameters (on p. 79).

[142] L. Arnaudon et al. "Linac4 Technical Design Report". CERN-AB-2006-084. Dec. 2006. CDS: 1004186 (on p. 79).

[143] F. Blas et al. "Conversion of the PS complex as LHC proton pre-injector". In: *Proceedings of the 1997 Particle Accelerator Conference*. Vol. 1. 1997, pp. 973–975. DOI: 10.1109/PAC.1997.749899. CDS: 328735 (on p. 80).

[144] M. Benedikt and G. Métral. "Cycling of the PS complex and the SPS analysis and possibilities for optimisation". CERN-AB-Note-2004-061. Aug. 2004. CDS: 789153 (on p. 80).

[145] C. Hill, K. Prelec, and M. Weiss. "Design of the preinjector for the CERN RFQ2 project". CERN-PS-88-72-HI. 1988. CDS: 193345 (on p. 79).

[146] R. Bailey and P. Collier. "Standard Filling Schemes for Various LHC Operation Modes". LHC-PROJECT-NOTE-323. Sept. 2003. CDS: 691782 (on p. 81).

[147] "LHC Programme Coordination: Filling Schemes". URL: https://lpc.web.cern.ch/cgi-bin/fillingSchemeTab.py (on p. 81).

[148] K. Yurkewicz. "Protecting the LHC from itself". *Symmetry magazine* (Dec. 2007). URL: https://www.symmetrymagazine.org/article/december-2007/protecting-the-lhc-from-itself (on p. 82).

[149] W. Herr and B. Muratori. "Concept of luminosity" (2006). DOI: 10.5170/CERN-2006-002.361. CDS: 941318 (on p. 83).

[150] ATLAS Collaboration. "Luminosity Public Results Run 2". URL: https://twiki.cern.ch/twiki/bin/view/AtlasPublic/LuminosityPublicResultsRun2 (on pp. 83, 85).

[151] ATLAS Collaboration. "Measurement of the total cross section from elastic scattering in pp collisions at $\sqrt{s} = 8$ TeV with the ATLAS detector". *Phys. Lett. B* **761** (2016), 158. DOI: 10.1016/j.physletb.2016.08.020. arXiv: 1607.06605. CDS: 2201004 (on p. 84).

[152] ATLAS Collaboration. "Measurement of the Inelastic Proton-Proton Cross Section at $\sqrt{s} = 13$ TeV with the ATLAS Detector at the LHC". *Phys. Rev. Lett.* **117** (Oct. 2016), 182002. DOI: 10.1103/PhysRevLett.117.182002. CDS: 2159578 (on p. 84).

[153] J. Pequenão. "Computer generated image of the whole ATLAS detector". CERN-GE-0803012. Mar. 2008. CDS: 1095924 (on p. 88).

[154] ATLAS Collaboration. *ATLAS calorimeter performance: Technical Design Report*. Technical Design Report ATLAS CERN-LHCC-96-040. 1996. CDS: 331059 (on p. 89).

[155] A. Hoecker. "Radiation Simulation Public Results". URL: https://twiki.cern.ch/twiki/bin/view/AtlasPublic/RadiationSimulationPublicResults (on p. 90).

[156] S. Baranov et al. "Estimation of Radiation Background, Impact on Detectors, Activation and Shielding Optimization in ATLAS". ATL-GEN-2005-001. Jan. 2005. CDS: 814823 (on p. 90).

[157] J. Pequenão. "Computer generated image of the ATLAS inner detector". CERN-GE-0803014. Mar. 2008. CDS: 1095926 (on p. 91).

[158] ATLAS Collaboration. *ATLAS inner detector: Technical Design Report, 1*. Technical Design Report ATLAS CERN-LHCC-97-016. 1997. CDS: 331063 (on p. 90).

[159] ATLAS Collaboration. "ATLAS pixel detector electronics and sensors". *JINST* **3** (2008), P07007. DOI: 10.1088/1748-0221/3/07/P07007. CDS: 1119279 (on p. 92).

[160] N. Wermes and G. Hallewel. *ATLAS pixel detector: Technical Design Report*. Technical Design Report ATLAS CERN-LHCC-98-013. 1998. CDS: 381263 (on p. 92).

[161] M. S. Alam et al. "The ATLAS silicon pixel sensors". *NIM A* **456**.3 (2001), 217–232. DOI: 10.1016/S0168-9002(00)00574-X. CDS: 683924 (on p. 92).

[162] E. Galyaev, ATLAS Collaboration. "Results from the Commissioning of the ATLAS Pixel Detector with Cosmic data" (2009). arXiv: 0910.0847. CDS: 1211070 (on p. 93).

[163] J. Pequenão. "Computer generated images of the Pixel, part of the ATLAS inner detector". CERN-GE-0803013. Mar. 2008. CDS: 1095925 (on p. 93).

[164] H. Pernegger. "The Pixel Detector of the ATLAS experiment for LHC Run-2". *JINST* **10**.06 (June 2015), C06012. DOI: 10.1088/1748-0221/10/06/C06012. CDS: 1985432 (on p. 93).

[165] M. Capeans et al. "ATLAS Insertable B-Layer Technical Design Report". CERN-LHCC-2010-013. Sept. 2010. CDS: 1291633 (on p. 93).

[166] J. N. Jackson, ATLAS SCT Collaboration. "The ATLAS semiconductor tracker (SCT)". *NIM A* **541**.1 (2005). Development and Application of Semiconductor Tracking Detectors, 89–95. DOI: 10.1016/j.nima.2005.01.043. CDS: 908854 (on p. 94).

[167] ATLAS Collaboration. "Operation and performance of the ATLAS semiconductor tracker. Operation and performance of the ATLAS semiconductor tracker". *JINST* **9** (Apr. 2014), P08009. DOI: 10.1088/1748-0221/9/08/P08009. arXiv: 1404.7473. CDS: 1698966 (on p. 94).

[168] ATLAS TRT Collaboration. "The ATLAS TRT Barrel Detector". *JINST* **3**.02 (Feb. 2008), P02014. DOI: 10.1088/1748-0221/3/02/P02014. CDS: 1094548 (on p. 95).

[169] ATLAS TRT Collaboration. "The ATLAS TRT end-cap detectors". *JINST* **3**.10 (Oct. 2008), P10003. DOI: 10.1088/1748-0221/3/10/P10003. CDS: 1151338 (on p. 95).

[170] ATLAS TRT Collaboration. "The ATLAS Transition Radiation Tracker (TRT) proportional drift tube: design and performance". *JINST* **3**.02 (Feb. 2008), P02013. DOI: 10.1088/1748-0221/3/02/P02013. CDS: 1094549 (on p. 95).

[171] A. Romaniouk. "MEPhI, Elementary Particle Physics, ATLAS TRT (Transition Radiation Tracker)". URL: http://particle.mephi.ru/en/research/atlas/trt/ (on p. 95).

[172] University of Pennsylvania. "Transition Radiation Tracker - TRT". URL: http://www.hep.upenn.edu/atlas/trt/ (on p. 96).

[173] J. Pequenão. "Computer Generated image of the ATLAS calorimeter". CERN-GE-0803015. Mar. 2008. CDS: 1095927 (on p. 97).

[174] ATLAS Collaboration. *Expected Performance of the ATLAS Experiment - Detector, Trigger and Physics*. CERN-OPEN-2008-020. 2008. arXiv: 0901.0512. CDS: 1125884 (on p. 101).

[175] B. Aubert et al. "Construction, assembly and tests of the ATLAS electromagnetic barrel calorimeter". *NIM A* **558**.2 (2006), 388–418. DOI: 10.1016/j.nima.2005.11.212. CDS: 883909 (on p. 101).

[176] S. Akhmadaliev et al. "Results from a new combined test of an electromagnetic liquid argon calorimeter with a hadronic scintillating-tile calorimeter". *NIM A* **449**.3 (2000), 461–477. DOI: 10.1016/S0168-9002(00)00153-4. CDS: 457163 (on p. 101).

[177] B. Dowler et al. "Performance of the ATLAS hadronic end-cap calorimeter in beam tests". *NIM A* **482**.1 (2002), 94–124. DOI: 10.1016/S0168-9002(01)01338-9. CDS: 684257 (on p. 101).

[178] J. P. Archambault et al. "Energy calibration of the ATLAS Liquid Argon Forward Calorimeter". *JINST* **3**.02 (Feb. 2008), P02002. DOI: 10.1088/1748-0221/3/02/P02002. CDS: 1094554 (on p. 101).

[179] ATLAS Collaboration. *ATLAS liquid-argon calorimeter: Technical Design Report*. Technical Design Report ATLAS CERN-LHCC-96-041. 1996. CDS: 331061 (on pp. 101, 107).

[180] P. Krieger. "The ATLAS liquid argon calorimeter: construction, integration, commissioning and performance from selected particle beam test results". In: *IEEE NSS/MIC*. 2005, pp. 1029–1033. DOI: 10.1109/NSSMIC.2005.1596428. CDS: 1015504 (on pp. 101, 103).

[181] M. Aleksa and M. Diemoz. "Discussion on the electromagnetic calorimeters of ATLAS and CMS". ATL-LARG-PROC-2013-002. May 2013. CDS: 1547314 (on p. 101).

[182] M. L. Andrieux et al. "Construction and test of the first two sectors of the ATLAS barrel liquid argon presampler". *NIM A* **479**.2 (2002), 316–333. DOI: 10.1016/S0168-9002(01)00943-3 (on p. 101).

[183] S. S. Arfaoui. "The ATLAS liquid argon calorimeter high-voltage system: commissioning, optimisation, and LHC relative luminosity measurement". PhD Diss., U. de la Méditerranée – Aix-Marseille II, Oct. 2011, p. 54. URL: https://tel.archives-ouvertes.fr/tel-00658194 (on p. 102).

[184] D. Gillberg. "Performance of the ATLAS Forward Calorimeters in First LHC Data". *J. Phys. Conf. Ser.* **293** (Apr. 2011), 012041. DOI: 10.1088/1742-6596/293/1/012041. CDS: 1280675 (on p. 102).

[185] ATLAS Collaboration. *ATLAS tile calorimeter: Technical Design Report*. CERN-LHCC-96-042. 1996. CDS: 331062 (on pp. 104, 248, 259).

[186] M. J. Varanda. "The tile hadronic calorimeter for the ATLAS experiment". *IEEE Trans. Nucl. Sci.* **48**.3 (June 2001), 367–371. DOI: 10.1109/23.940082 (on p. 104).

[187] ATLAS TileCal Collaboration. "The ATLAS hadronic tile calorimeter: from construction toward physics". *IEEE Trans. Nucl. Sci.* **53**.3 (June 2006), 1275–1281. DOI: 10.1109/TNS.2006.872628 (on p. 104).

[188] ATLAS TileCal Collaboration. "Design, Construction and Installation of the ATLAS Hadronic Barrel Scintillator-Tile Calorimeter". ATL-TILECAL-PUB-2008-001, ATL-COM-TILECAL-2007-019. Nov. 2007. CDS: 1071921 (on p. 104).

[189] Tile Calorimeter Collaboration. "The optical instrumentation of the ATLAS Tile Calorimeter". *JINST* **8**.01 (Jan. 2013), P01005. DOI: 10.1088/1748-0221/8/01/P01005. CDS: 1073936 (on p. 104).

[190] K. Anderson et al. "TileCal: The Hadronic Section of the Central ATLAS Calorimeter". *Int. J. Mod. Phys. A* **25** (Jan. 2012). DOI: 10.1142/S0217751X10049360. CDS: 1221848 (on p. 105).

[191] D. M. Gingrich. "Construction, assembly and testing of the ATLAS hadronic end-cap calorimeter". *JINST* **2**.05 (May 2007), P05005. DOI: 10.1088/1748-0221/2/05/P05005 (on p. 107).

[192] J. Pequenão. "Computer generated image of the ATLAS Muons subsystem". CERN-GE-0803017. Mar. 2008. CDS: 1095929 (on p. 110).

[193] ATLAS Collaboration. *ATLAS muon spectrometer: Technical Design Report*. Technical Design Report ATLAS CERN-LHCC-97-022. 1997. CDS: 331068 (on pp. 110, 112).

[194] S. Palestini. "The muon spectrometer of the ATLAS experiment". *Nucl. Phys. B Proc. Suppl.* **125** (2003). Innovative Particle and Radiation Detectors, 337–345. DOI: 10.1016/S0920-5632(03)91013-9 (on p. 110).

[195] S. Aefsky et al. "The Optical Alignment System of the ATLAS Muon Spectrometer Endcaps". *JINST* **3**.11 (Nov. 2008), P11005. DOI: 10.1088/1748-0221/3/11/P11005 (on p. 111).

[196] F. Bauer et al. "Construction and Test of MDT Chambers for the ATLAS Muon Spectrometer". *NIM A* **461**.17 (2001). DOI: 10.1016/S0168-9002(00)01156-6. arXiv: 1604.02000 (on p. 111).

[197] Y. Arai et al. "ATLAS Muon Drift Tube Electronics". *JINST* **3**.09 (Sept. 2008), P09001. DOI: 10.1088/1748-0221/3/09/P09001 (on p. 111).

[198] ATLAS Collaboration. *ATLAS magnet system: Technical Design Report*. Technical Design Report ATLAS CERN-LHCC-97-018. 1997. CDS: 338080 (on pp. 114, 115).

[199] J. J. Goodson. "Search for Supersymmetry in States with Large Missing Transverse Momentum and Three Leptons including a Z-Boson". PhD Diss., Stony Brook U., May 2012. CDS: 1449722 (on p. 115).

[200] W. Panduro Vazquez, ATLAS Collaboration. "The ATLAS Data Acquisition System in LHC Run 2". *J. Phys. Conf. Ser.* **898** (Oct. 2017), 032017. DOI: 10.1088/1742-6596/898/3/032017. CDS: 2244345 (on p. 116).

[201] Y. Nakahama. "The ATLAS Trigger System: Ready for Run-2". *J. Phys. Conf. Ser.* **664**.8 (Dec. 2015), 082037. DOI: 10.1088/1742-6596/664/8/082037. CDS: 2015211 (on p. 116).

[202] M. zur Nedden. "The LHC Run 2 ATLAS trigger system: design, performance and plans". *JINST* **12**.03 (Mar. 2017), C03024. DOI: 10.1088/1748-0221/12/03/C03024 (on p. 116).

[203] ATLAS Collaboration. "Approved Plots DAQ". URL: https://twiki.cern.ch/twiki/bin/view/AtlasPublic/ApprovedPlotsDAQ (on p. 117).

[204] ATLAS Collaboration. "Operation of the ATLAS trigger system in Run 2" (2020), 1–60. DOI: 10.3204/PUBDB-2020-03029. arXiv: 2007.12539. CDS: 2725146 (on p. 116).

[205] S. M. Weber, ATLAS Collaboration. "Operation and Performance of the ATLAS Level-1 Calorimeter and Topological Triggers in Run 2". *PoS* **314**.EPS-HEP2017 (2017), 806. DOI: 10.22323/1.314.0806. CDS: 2287401 (on p. 116).

[206] W. Buttinger. "The ATLAS Level-1 Trigger System". *J. Phys. Conf. Ser.* **396**.1 (Dec. 2012), 012010. DOI: 10.1088/1742-6596/396/1/012010. CDS: 1456546 (on p. 117).

[207] R. Achenbach et al. "The ATLAS Level-1 Calorimeter Trigger". *JINST* **3**.03 (Mar. 2008), P03001. DOI: 10.1088/1748-0221/3/03/P03001. CDS: 1080560 (on p. 117).

[208] ATLAS Collaboration. "Performance of the ATLAS muon triggers in Run 2". *JINST* **15**.09 (Sept. 2020), P09015. DOI: 10.1088/1748-0221/15/09/P09015. arXiv: 2004.13447. CDS: 2716326 (on p. 117).

[209] E. Simioni et al. "Upgrade of the ATLAS Level-1 Trigger with event topology information". *J. Phys. Conf. Ser.* **664**.8 (Dec. 2015), 082052. DOI: 10.1088/1742-6596/664/8/082052. CDS: 2016644 (on p. 117).

[210] R. Simoniello, ATLAS Collaboration. "The ATLAS Level-1 Topological Processor: from design to routine usage in Run-2". In: *IEEE NSS/MIC*. 2018. DOI: 10.1109/NSSMIC.2018.8824280. CDS: 2649959 (on p. 117).

[211] J. Glatzer. "Operation of the Upgraded ATLAS Level-1 Central Trigger System". *J. Phys. Conf. Ser.* **664**.8 (Dec. 2015), 082013. DOI: 10.1088/1742-6596/664/8/082013. CDS: 2016347 (on p. 117).

[212] "The ATLAS Data Acquisition and High Level Trigger system". *JINST* **11**.06 (June 2016), P06008. DOI: 10.1088/1748-0221/11/06/p06008. CDS: 2255808 (on p. 118).

[213] J. Pequenão. "Event Cross Section in a computer generated image of the ATLAS detector." CERN-GE-0803022. Mar. 2008. CDS: 1096081 (on p. 120).

[214] J. Pequenão and P. Schaffner. "How ATLAS detects particles: diagram of particle paths in the detector". CERN-EX-1301009. Jan. 2013. CDS: 1505342 (on p. 120).

[215] J. Adelman et al. "Supporting note: Selection and performance for the $H \to \gamma\gamma$ and $H \to Z\gamma$ analyses, Spring 2017". ATL-COM-PHYS-2017-357. Apr. 2017. CDS: 2258158 (on pp. 121, 125, 132, 154, 195).

[216] ATLAS Collaboration. "Particle Identification Performance of the ATLAS Transition Radiation Tracker". ATLAS-CONF-2011-128. Sept. 2011. CDS: 1383793 (on p. 122).

[217] R. Frühwirth. "Application of Kalman filtering to track and vertex fitting". *NIM A* **262**.2 (1987), 444–450. DOI: 10.1016/0168-9002(87)90887-4 (on p. 122).

[218] T. Cornelissen et al. "Concepts, Design and Implementation of the ATLAS New Tracking (NEWT)". ATL-SOFT-PUB-2007-007. Mar. 2007. CDS: 1020106 (on pp. 122–124).

[219] T. G. Cornelissen et al. "The global χ^2 track fitter in ATLAS". *J. Phys. Conf. Ser.* **119**.3 (July 2008), 032013. DOI: 10.1088/1742-6596/119/3/032013. CDS: 1176901 (on pp. 122, 127, 143).

[220] M. Limper. "Track and vertex reconstruction in the ATLAS inner detector". PhD Diss., U. of Amsterdam, NIKHEF, Oct. 2009. CDS: 1202457 (on p. 122).

[221] H. Gray. "Track reconstruction in the ATLAS experiment". Joint Experimental Particle and Astroparticle seminar of UZH and ETH, Zurich. 2016. URL: https://indico.cern.ch/event/504284/ (on p. 122).

[222] A. Strandlie and R. Frühwirth. "Adaptive multitrack fitting". *Comput. Phys. Commun.* **133**.1 (2000), 34–42. DOI: 10.1016/S0010-4655(00)00166-1 (on p. 123).

[223] ATLAS Collaboration. "Performance of the ATLAS Inner Detector Track and Vertex Reconstruction in the High Pile-Up LHC Environment". ATLAS-CONF-2012-042. Mar. 2012. CDS: 1435196 (on p. 124).

[224] ATLAS Collaboration. "Electron reconstruction and identification in the ATLAS experiment using the 2015 and 2016 LHC proton-proton collision data at $\sqrt{s} = 13$ TeV". *Eur. Phys. J. C* **79** (Aug. 2019), 639. DOI: 10.1140/epjc/s10052-019-7140-6. arXiv: 1902.04655. CDS: 2657964 (on p. 126).

[225] ATLAS Collaboration. "Electron and photon reconstruction and performance in ATLAS using a dynamical, topological cell clustering-based approach". ATL-PHYS-PUB-2017-022. Dec. 2017. CDS: 2298955 (on p. 126).

[226] ATLAS Collaboration. "Electron and photon energy calibration with the ATLAS detector using LHC Run 1 data". *Eur. Phys. J. C* **74**.10 (Oct. 2014), 3071. DOI: 10.1140/epjc/s10052-014-3071-4. arXiv: 1407.5063. CDS: 1744017 (on p. 126).

[227] W. Lampl et al. "Calorimeter Clustering Algorithms: Description and Performance". ATL-LARG-PUB-2008-002. Apr. 2008. CDS: 1099735 (on pp. 126, 132).

[228] ATLAS Collaboration. "Improved electron reconstruction in ATLAS using the Gaussian Sum Filter-based model for bremsstrahlung". ATLAS-CONF-2012-047. May 2012. CDS: 1449796 (on p. 128).

[229] N. Proklova et al. "Measurements of Photon efficiencies in pp collision data collected in 2015, 2016 and 2017 at $\sqrt{s} = 13$ TeV with the ATLAS detector". ATL-COM-PHYS-2018-1604. Nov. 2018. CDS: 2647979 (on pp. 130, 131, 154).

[230] C. Anastopoulos et al. "Electron identification and efficiency measurements in 2017 data". ATL-COM-PHYS-2018-1727. Jan. 2019. CDS: 2652163 (on p. 130).

[231] A. Tarek. "Measurement of Higgs boson production cross sections in the diphoton channel with the full ATLAS Run-2 data and constraints on anomalous Higgs boson interactions". PhD Diss., Paris Diderot U., Sept. 2019. CDS: 2696211 (on pp. 130, 131, 184).

[232] J. Saxon. "Discovery of the Higgs Boson, Measurements of its Production, and a Search for Higgs Boson Pair Production". PhD Diss., U. of Pennsylvania, July 2014. CDS: 1746004 (on p. 131).

[233] A. J. Larkoski, I. Moult, and B. Nachman. "Jet substructure at the Large Hadron Collider: A review of recent advances in theory and machine learning". *Phys. Rep.*

841 (2020), 1–63. DOI: 10.1016/j.physrep.2019.11.001. arXiv: 1709.04464 (on p. 131).

[234] R. Kogler et al. "Jet substructure at the Large Hadron Collider". *Rev. Mod. Phys.* **91**.4 (Dec. 2019), 045003. DOI: 10.1103/RevModPhys.91.045003. arXiv: 1803.06991. CDS: 2641634 (on p. 131).

[235] S. Marzani, G. Soyez, and M. Spannowsky. *Looking Inside Jets: An Introduction to Jet Substructure and Boosted-object Phenomenology*. ISBN: 978-3-03-015709-8. DOI: 10.1007/978-3-030-15709-8. arXiv: 1901.10342. CDS: 2678317 (on p. 131).

[236] ATLAS Collaboration. "Topological cell clustering in the ATLAS calorimeters and its performance in LHC Run 1". *Eur. Phys. J. C* **77**.7 (July 2017), 490. DOI: 10.1140/epjc/s10052-017-5004-5. arXiv: 1603.02934. CDS: 2138166 (on p. 132).

[237] ATLAS Collaboration. "Jet reconstruction and performance using particle flow with the ATLAS Detector". *Eur. Phys. J. C* **77**.7 (July 2017), 466. DOI: 10.1140/epjc/s10052-017-5031-2. arXiv: 1703.10485 (on pp. 132, 133).

[238] R. Atkin. "Review of jet reconstruction algorithms". *J. Phys. Conf. Ser.* **645** (Oct. 2015), 12008. DOI: 10.1088/1742-6596/645/1/012008 (on p. 132).

[239] M. Cacciari, G. P. Salam, and G. Soyez. "The anti-kt jet clustering algorithm". *JHEP* 04 (2008), 063. DOI: 10.1088/1126-6708/2008/04/063. arXiv: 0802.1189 (on pp. 132, 135, 136).

[240] ATLAS Collaboration. *ATLAS detector and physics performance: Technical Design Report, 1*. Technical Design Report ATLAS CERN-LHCC-99-014. 1999. CDS: 391176 (on p. 133).

[241] ATLAS Collaboration. "A measurement of single hadron response using data at $\sqrt{s} = 8$ TeV with the ATLAS detector". ATL-PHYS-PUB-2014-002. Mar. 2014. CDS: 1668961 (on p. 133).

[242] S. Catani et al. "New clustering algorithm for multijet cross sections in e^+e^- annihilation". *Phys. Lett. B* **269**.3 (1991), 432–438. DOI: 10.1016/0370-2693(91)90196-W (on p. 135).

[243] Y. L. Dokshitzer et al. "Better jet clustering algorithms". *JHEP* 08 (1997), 001. DOI: 10.1088/1126-6708/1997/08/001. arXiv: hep-ph/9707323 (on p. 135).

[244] M. Wobisch and T. Wengler. "Hadronization Corrections to Jet Cross Sections in Deep-Inelastic Scattering". In: *Monte Carlo generators for HERA physics*. DESY-PROC-1999-02. Dec. 1999, pp. 270–279. arXiv: hep-ph/9907280 (on p. 135).

[245] M. Cacciari, G. P. Salam, and G. Soyez. "FastJet user manual". *Eur. Phys. J. C* **72**.3 (Mar. 2012), 1896. DOI: 10.1140/epjc/s10052-012-1896-2. arXiv: 1111.6097 (on p. 135).

[246] M. Cacciari and G. P. Salam. "Dispelling the N^3 myth for the k_t jet-finder". *Phys. Lett. B* **641**.1 (2006), 57–61. DOI: 10.1016/j.physletb.2006.08.037. arXiv: hep-ph/0512210 (on p. 135).

[247] S. Argyropoulos et al. "Pile-up subtraction and suppression for jets in ATLAS". ATL-COM-PHYS-2013-251. Mar. 2013. CDS: 1522015 (on p. 137).

[248] T. Barillari et al. "Local Hadronic Calibration". ATL-LARG-PUB-2009-001-2. June 2008. CDS: 1112035 (on p. 137).

[249] ATLAS Collaboration. "Jet energy scale measurements and their systematic uncertainties in proton-proton collisions at $\sqrt{s}$ = 13 TeV with the ATLAS detector". *Phys. Rev. D* **96** (Oct. 2017), 072002. DOI: 10.1103/PhysRevD.96.072002. arXiv: 1703.09665. CDS: 2257300 (on p. 138).

[250] ATLAS Collaboration. "Jet global sequential corrections with the ATLAS detector in proton-proton collisions at $\sqrt{s} = 8$ TeV". ATLAS-CONF-2015-002. Mar. 2015. CDS: 2001682 (on p. 138).

[251] D. W. Miller, A. Schwartzman, and D. Su. "Jet-Vertex Association Algorithm". ATL-COM-PHYS-2008-008. Jan. 2008. CDS: 1082880 (on p. 139).

[252] ATLAS Collaboration. "Tagging and suppression of pileup jets with the ATLAS detector". ATLAS-CONF-2014-018. May 2014. CDS: 1700870 (on pp. 139–141, 155, 197).

[253] K. G. Tomiwa. "Performance of Jet Vertex Tagger in suppression of pileup jets and $E_{\mathrm{T}}^{\mathrm{miss}}$ in ATLAS detector". *J. Phys. Conf. Ser.* **802** (Jan. 2017), 012012. DOI: 10.1088/1742-6596/802/1/012012 (on pp. 139, 140).

[254] A. Schwartzman, M. H. Klein, and F. Rubbo. "Identification and rejection of pileup jets in the forward region with the ATLAS detector". ATL-COM-PHYS-2016-710. July 2016. CDS: 2158916 (on pp. 141, 142, 155).

[255] ATLAS Collaboration. "Identification and rejection of pile-up jets at high pseudo-rapidity with the ATLAS detector". *Eur. Phys. J. C* **77**.9 (Sept. 2017), 580. DOI: 10.1140/epjc/s10052-017-5081-5. arXiv: 1705.02211. CDS: 2262419 (on pp. 141, 155).

[256] ATLAS Collaboration. "Forward jet vertex tagging using the particle flow algorithm". ATL-PHYS-PUB-2019-026. July 2019. CDS: 2683100 (on pp. 141, 155).

[257] ATLAS Collaboration. "Muon reconstruction performance of the ATLAS detector in proton-proton collision data at $\sqrt{s} = 13$ TeV". *Eur. Phys. J. C* **76**.5 (May 2016), 292. DOI: 10.1140/epjc/s10052-016-4120-y. arXiv: 1603.05598. CDS: 2139897 (on pp. 143, 144).

[258] N. Vranješ. "Muon reconstruction in ATLAS and CMS". LHC France. Apr. 2013. URL: https://indico.in2p3.fr/event/6838/contributions/39638/ (on p. 143).

[259] ATLAS Collaboration. "Performance of missing transverse momentum reconstruction for the ATLAS detector in the first proton-proton collisions at $\sqrt{s} = 13$ TeV". ATL-PHYS-PUB-2015-027. July 2015. CDS: 2037904 (on p. 144).

[260] A. Hrynevich. "ATLAS jet and missing energy reconstruction, calibration and performance in LHC Run-2". *JINST* **12**.06 (June 2017), C06038. DOI: 10.1088/1748-0221/12/06/C06038. CDS: 2263777 (on p. 144).

[261] ATLAS Collaboration. "Performance of missing transverse momentum reconstruction with the ATLAS detector using proton-proton collisions at $\sqrt{s} = 13$ TeV". *Eur. Phys. J. C* **78**.11 (Nov. 2018), 903. DOI: 10.1140/epjc/s10052-018-6288-9. arXiv: 1802.08168. CDS: 2305380 (on p. 144).

[262] ATLAS Collaboration. "Measurements of Higgs boson production and couplings in diboson final states with the ATLAS detector at the LHC". *Phys. Lett. B* **726**.1 (2013), 88–119. DOI: 10.1016/j.physletb.2013.08.010. arXiv: 1307.1427. CDS: 1559924 (on p. 145).

[263] ATLAS Collaboration. "Measurements of the Higgs boson production and decay rates and coupling strengths using *pp* collision data at $\sqrt{s} = 7$ and 8 TeV in the ATLAS experiment". *Eur. Phys. J. C* **76** (2016), 6. DOI: 10.1140/epjc/s10052-015-3769-y. arXiv: 1507.04548. CDS: 2034254 (on p. 145).

[264] F. Tackmann et al. "Simplified template cross sections". LHCHXSWG-DRAFT-INT-2016-006. Mar. 2016. CDS: 2138079 (on p. 146).

[265] Higgs Working Group, ATLAS Collaboration. "HGamma public results and supporting documentation". URL: https://twiki.cern.ch/twiki/bin/viewauth/AtlasProtected/HSG1notes (on p. 148).

[266] ATLAS Collaboration. "Higgs Public Results". URL: https://twiki.cern.ch/twiki/bin/view/AtlasPublic/HiggsPublicResults (on p. 148).

[267] ATLAS Collaboration. "ATLAS Experiment — public results". URL: https://twiki.cern.ch/twiki/bin/view/AtlasPublic/PublicConfigurableTestPageHIGG (on p. 148).

[268] S. Laplace et al., ATLAS Collaboration. "Measurement of the Higgs boson production cross section at 7, 8 and 13 TeV center-of-mass energies in the $H \to \gamma\gamma$ channel with the ATLAS detector". ATLAS-CONF-2015-060. Dec. 2015. CDS: 2114826. URL: https://atlas.web.cern.ch/Atlas/GROUPS/PHYSICS/CONFNOTES/ATLAS-CONF-2015-060/ (on p. 148).

[269] F. U. Bernlochner et al., ATLAS Collaboration. "Measurement of the fiducial cross section of the Higgs boson in the diphoton decay channel using 13 TeV *pp* data". ATL-COM-PHYS-2015-1244. Oct. 2015. CDS: 2056804 (on p. 148).

[270] ATLAS Collaboration. "Measurement of fiducial, differential and production cross sections in the $H \to \gamma\gamma$ decay channel with 13.3 fb^{-1} of 13 TeV proton-proton collision data with the ATLAS detector". ATLAS-CONF-2016-067. Aug. 2016. CDS: 2206210. URL: https://atlas.web.cern.ch/Atlas/GROUPS/PHYSICS/CONFNOTES/ATLAS-CONF-2016-067/ (on p. 148).

[271] F. U. Bernlochner et al., ATLAS Collaboration. "Measurement of the fiducial and differential cross sections of the Higgs boson in the diphoton decay channel using 2015/2016 13 TeV *pp* data". ATL-COM-PHYS-2016-433. May 2016. CDS: 2150683 (on p. 148).

[272] ATLAS Collaboration. "Measurements of Higgs boson properties in the diphoton decay channel with 36.1 fb^{-1} *pp* collision data at the center-of-mass energy of 13 TeV with the ATLAS detector". ATLAS-CONF-2017-045. July 2017. CDS: 2273852. URL: https://atlas.web.cern.ch/Atlas/GROUPS/PHYSICS/CONFNOTES/ATLAS-CONF-2017-045/ (on pp. 148, 155, 199, 204–210).

[273] ATLAS Collaboration. "Measurements of Higgs boson properties in the diphoton decay channel with 36 fb^{-1} of *pp* collision data at $\sqrt{s} = 13$ TeV with the ATLAS detector". *Phys. Rev. D* **98** (Sept. 2018), 052005. DOI: 10.1103/PhysRevD.98.052005. arXiv: 1802.04146. URL: https://atlas.web.cern.ch/Atlas/GROUPS/PHYSICS/PAPERS/HIGG-2016-21/ (on pp. 148, 199, 204–210).

[274] F. U. Bernlochner et al., ATLAS Collaboration. "Measurement of fiducial and differential cross sections in the $H \to \gamma\gamma$ decay channel with 36 fb^{-1} of 13 TeV proton-proton collision data with the ATLAS detector". ATL-COM-PHYS-2017-145. Feb. 2016. CDS: 2252597 (on pp. 148, 199, 204–210).

[275] ATLAS Collaboration. "Measurements of Higgs boson properties in the diphoton decay channel using 80 fb^{-1} of *pp* collision data at $\sqrt{s} = 13$ TeV with the ATLAS detector". ATLAS-CONF-2018-028. July 2018. CDS: 2628771. URL: https://atlas.web.cern.ch/Atlas/GROUPS/PHYSICS/CONFNOTES/ATLAS-CONF-2018-028/ (on pp. 148, 199, 203).

[276] L. Brenner et al., ATLAS Collaboration. "Measurement of fiducial and differential cross sections in the $H \to \gamma\gamma$ decay channel with 80 fb^{-1} of 13 TeV proton–proton collision data with the ATLAS detector". ATL-COM-PHYS-2018-202. Mar. 2018. CDS: 2306798 (on pp. 148, 174, 199, 203).

[277] ATLAS Collaboration. "Measurements and interpretations of Higgs-boson fiducial cross sections in the diphoton decay channel using 139 fb^{-1} of pp collision data at $\sqrt{s} = 13$ TeV with the ATLAS detector". ATLAS-CONF-2019-029. July 2019. CDS: 2682800. URL: https://atlas.web.cern.ch/Atlas/GROUPS/PHYSICS/CONFNOTES/ATLAS-CONF-2019-029/ (on pp. 148, 150, 200–202, 211).

[278] J. Adelman et al., ATLAS Collaboration. "Measurement of fiducial and differential cross sections in the $H \to \gamma\gamma$ decay channel with 140 fb^{-1} of 13 TeV proton–proton collision data with the ATLAS detector". ATL-COM-PHYS-2019-035. Jan. 2019. CDS: 2654897 (on pp. 148, 150, 172, 174, 183, 200–202, 211).

[279] T. Min et al. "Selection and performance for the $H \to \gamma\gamma$ 2018 analyses using 2015+16+17 pp collision data at $\sqrt{s} = 13$ TeV with the ATLAS detector". ATL-COM-PHYS-2018-250. Mar. 2018. CDS: 2309522 (on pp. 149, 195).

[280] ATLAS Collaboration. "Luminosity determination in pp collisions at $\sqrt{s} = 13$ TeV using the ATLAS detector at the LHC". ATLAS-CONF-2019-021. June 2019. CDS: 2677054 (on pp. 149, 150, 195, 211).

[281] G. Avoni et al. "The new LUCID-2 detector for luminosity measurement and monitoring in ATLAS". *JINST* **13**.07 (July 2018), P07017. DOI: 10.1088/1748-0221/13/07/P07017. CDS: 2633501 (on pp. 149, 211).

[282] V. Cindro et al. "The ATLAS Beam Conditions Monitor". *JINST* **3**.02 (Feb. 2008), P02004. DOI: 10.1088/1748-0221/3/02/P02004. CDS: 1094819 (on p. 149).

[283] S. van der Meer. "Calibration of the effective beam height in the ISR". CERN-ISR-PO-68-31. ISR-PO-68-31. 1968. CDS: 296752 (on pp. 149, 195).

[284] ATLAS Collaboration. "Improved luminosity determination in pp collisions at $\sqrt{s} = 7$ TeV using the ATLAS detector at the LHC". *Eur. Phys. J. C* 73 (2013), 2518. DOI: 10.1140/epjc/s10052-013-2518-3. arXiv: 1302.4393. CDS: 1517411 (on pp. 150, 195).

[285] ATLAS Collaboration. "Measurement of the photon identification efficiencies with the ATLAS detector using LHC Run 2 data collected in 2015 and 2016". *Eur. Phys. J. C* **79**.3 (Mar. 2019), 205. DOI: 10.1140/epjc/s10052-019-6650-6. arXiv: 1810.05087. CDS: 2643391 (on pp. 151, 154).

[286] A. Taffard. "Good Run Lists For Analysis Run 2". URL: https://twiki.cern.ch/twiki/bin/viewauth/AtlasProtected/GoodRunListsForAnalysisRun2#Recommendations_for_the_Goo_Run (on p. 151).

[287] ATLAS Collaboration. "Measurement of Higgs boson production in the diphoton decay channel in pp collisions at center-of-mass energies of 7 and 8 TeV with the ATLAS detector". *Phys. Rev. D* **90** (Dec. 2014), 112015. DOI: 10.1103/PhysRevD.90.112015. arXiv: 1408.7084 (on p. 153).

[288] ATLAS Collaboration. "Measurement of the photon identification efficiencies with the ATLAS detector using LHC Run-1 data". *Eur. Phys. J. C* **76**.12 (2016), 666. DOI: 10.1140/epjc/s10052-016-4507-9. arXiv: 1606.01813 (on p. 153).

[289] ATLAS Collaboration. "Electron and photon energy calibration with the ATLAS detector using 2015–2016 LHC proton-proton collision data". *JINST* **14**.03 (Mar. 2019), P03017. DOI: 10.1088/1748-0221/14/03/P03017. arXiv: 1812.03848 (on pp. 154, 185).

[290] M. J. Alconada Verzini et al. "Measurement of electron and photon isolation efficiencies in Run2". ATL-COM-PHYS-2018-1529. Nov. 2018. CDS: 2646265 (on p. 154).

[291] ATLAS FTAG Working Group. "Expected performance of the ATLAS b-tagging algorithms in Run-2". ATL-PHYS-PUB-2015-022. July 2015. CDS: 2037697 (on p. 155).

[292] ATLAS FTAG Working Group. "Optimisation of the ATLAS b-tagging performance for the 2016 LHC Run". ATL-PHYS-PUB-2016-012. June 2016. CDS: 2160731 (on p. 155).

[293] J. C. Collins, D. E. Soper, and G. F. Sterman. "Transverse momentum distribution in Drell–Yan pair and W and Z boson production". *Nucl. Phys. B* **250** (1985), 199–224. DOI: 10.1016/0550-3213(85)90479-1. CDS: 153460 (on pp. 158, 160, 161).

[294] F. Bishara et al. "Constraining Light-Quark Yukawa Couplings from Higgs Distributions". *Phys. Rev. Lett.* **118** (Mar. 2017), 121801. DOI: 10.1103/PhysRevLett.118.121801. arXiv: 1606.09253 (on p. 158).

[295] Y. Soreq, H. X. Zhu, and J. Zupan. "Light quark Yukawa couplings from Higgs kinematics". *JHEP* 12 (2016), 045. DOI: 10.1007/JHEP12(2016)045. arXiv: 1606.09621 (on pp. 158, 159).

[296] T. Plehn, D. Rainwater, and D. Zeppenfeld. "Determining the Structure of Higgs Couplings at the CERN Large Hadron Collider". *Phys. Rev. Lett.* **88** (Jan. 2002), 051801. DOI: 10.1103/PhysRevLett.88.051801. arXiv: hep-ph/0105325 (on p. 160).

[297] G. Klämke and D. Zeppenfeld. "Higgs plus two jet production via gluon fusion as a signal at the CERN LHC". *JHEP* 04 (2007), 052. DOI: 10.1088/1126-6708/2007/04/052. arXiv: hep-ph/0703202 (on p. 160).

[298] J. R. Andersen, K. Arnold, and D. Zeppenfeld. "Azimuthal angle correlations for Higgs boson plus multi-jet events". *JHEP* 06 (2010), 091. DOI: 10.1007/JHEP06(2010)091. arXiv: 1001.3822 (on p. 160).

[299] M. J. Dolan et al. "Constraining CP-violating Higgs sectors at the LHC using gluon fusion". *Phys. Rev. D* **90** (Oct. 2014), 073008. DOI: 10.1103/PhysRevD.90.073008. arXiv: 1406.3322 (on p. 160).

[300] M. Vesterinen and T. R. Wyatt. "A novel technique for studying the Z boson transverse momentum distribution at hadron colliders". *NIM A* **602**.2 (2009), 432–437. DOI: 10.1016/j.nima.2009.01.203 (on p. 161).

[301] OPAL Collaboration. "Search for anomalous production of di-lepton events with missing transverse momentum in e^+e^- collisions at $\sqrt{s} = 161$ and 172 GeV". *Eur. Phys. J. C* **4**.1 (1998), 47–74. DOI: 10.1007/PL00021655. arXiv: hep-ex/9710010 (on p. 161).

[302] ATLAS Collaboration. "Search for the Standard Model Higgs boson in the diphoton decay channel with $4.9\,\mathrm{fb}^{-1}$ of ATLAS data at $\sqrt{s} = 7\,\mathrm{TeV}$". ATLAS-CONF-2011-161. Dec. 2011. CDS: 1406356 (on p. 162).

[303] I. W. Stewart, F. J. Tackmann, and W. J. Waalewijn. "Factorization at the LHC: From parton distribution functions to initial state jets". *Phys. Rev. D* **81** (May 2010), 094035. DOI: 10.1103/PhysRevD.81.094035. arXiv: 0910.0467 (on p. 164).

[304] G. Cowan and E. Gross. "Discovery significance with statistical uncertainty in the background estimate". In: *ATLAS Statistics Forum*. May 2008. URL: https://www.pp.rhul.ac.uk/~cowan/stat/notes/SigCalcNote.pdf (on p. 165).

[305] M. Oreglia. "A Study of the Reactions $\psi' \to \gamma\gamma\psi$". PhD Diss., Stanford U., SLAC, 1980. URL: http://inspirehep.net/record/158483 (on p. 169).

[306] ATLAS and CMS Collaborations. "Combined Measurement of the Higgs Boson Mass in pp Collisions at $\sqrt{s} = 7$ and 8 TeV with the ATLAS and CMS Experiments". *Phys. Rev. Lett.* **114** (May 2015), 191803. DOI: 10.1103/PhysRevLett.114.191803. arXiv: 1503.07589 (on pp. 170, 179, 185).

[307] ATLAS Collaboration. "Measurements of fiducial and differential cross sections for Higgs boson production in the diphoton decay channel at $\sqrt{s} = 8$ TeV with ATLAS". *JHEP* 01 (2012), 086. DOI: 10.1007/JHEP01(2013)086. arXiv: 1211.1913 (on pp. 172, 173).

[308] ATLAS Collaboration. "Measurement of the isolated diphoton cross section in pp collisions at $\sqrt{s} = 7$ TeV with the ATLAS detector". *Phys. Rev. D* **85** (Jan. 2012), 012003. DOI: 10.1103/PhysRevD.85.012003. arXiv: 1107.0581 (on pp. 172, 173).

[309] W. Verkerke and D. P. Kirkby. "The `RooFit` toolkit for data modeling". In: *13th International Conference for Computing in High-Energy and Nuclear Physics (CHEP 2003)*. C0303241. Mar. 2003, pp. 186–189. arXiv: physics/0306116. URL: http://inspirehep.net/record/621398 (on p. 182).

[310] I. Antcheva et al. "`ROOT` — A `C++` framework for petabyte data storage, statistical analysis and visualization". *Comput. Phys. Commun.* **180**.12 (2009), 2499–2512. DOI: 10.1016/j.cpc.2009.08.005 (on pp. 182, 215).

[311] F. James and M. Roos. "Minuit — a system for function minimization and analysis of the parameter errors and correlations". *Comput. Phys. Commun.* **10**.6 (1975), 343–367. DOI: 10.1016/0010-4655(75)90039-9 (on pp. 182, 189).

[312] W. T. Eadie et al. *Statistical methods in experimental physics*. 1971, pp. 204–205. ISBN: 978-0-444-10117-4 (on pp. 182, 189).

[313] G. Cowan. "A survey of unfolding methods for particle physics". In: *Advanced Statistical Techniques in Particle Physics*. C0203181. Mar. 2002, pp. 248–257. URL: http://inspirehep.net/record/599644/ (on p. 182).

[314] F. U. Bernlochner et al., ATLAS Collaboration. "$H \to \gamma\gamma$ fiducial and differential cross section measurement: Unfolding Support Documentation for the 2017 Paper". ATL-COM-PHYS-2017-533. May 2017. CDS: 2262458 (on p. 183).

[315] ATLAS Collaboration. "Electron and photon performance measurements with the ATLAS detector using the 2015–2017 LHC proton-proton collision data". *JINST* **14**.12 (Dec. 2019), P12006. DOI: 10.1088/1748-0221/14/12/P12006. arXiv: 1908.00005. CDS: 2684552 (on p. 185).

[316] E. Gross. "Practical Statistics for High Energy Physics". In: *CERN Yellow Report: 2017 European School of High-Energy Physics*. Vol. 3. 2018, p. 199. DOI: 10.23730/CYRSP-2018-003.199 (on p. 189).

[317] ATLAS and CMS Collaborations. "Measurements of the Higgs boson production and decay rates and constraints on its couplings from a combined ATLAS and CMS analysis of the LHC pp collision data at $\sqrt{s} = 7$ and 8 TeV". *JHEP* 08 (2016), 045. DOI: 10.1007/JHEP08(2016)045. arXiv: 1606.02266. CDS: 2158863 (on p. 192).

[318] A. Gabrielli et al. "Combined measurement of the differential cross sections in the $H \to \gamma\gamma$ and the $H \to ZZ^* \to 4\ell$ decay channels in pp collisions at 13 TeV with ATLAS". ATL-COM-PHYS-2017-1526. Oct. 2017. CDS: 2287483 (on p. 192).

[319] T. Sjöstrand, S. Mrenna, and P. Skands. "PYTHIA 6.4 Physics and Manual". *JHEP* 05 (2006), 026. DOI: 10.1088/1126-6708/2006/05/026. arXiv: hep-ph/0603175 (on p. 194).

[320] J. Bellm et al. "Herwig 7.0/Herwig++ 3.0 release note". *Eur. Phys. J. C* **76**.4 (2016), 196. DOI: 10.1140/epjc/s10052-016-4018-8. arXiv: 1512.01178 (on p. 194).

[321] ATLAS Collaboration. "Performance of the ATLAS Electron and Photon Trigger in p-p Collisions at $\sqrt{s} = 7$ TeV in 2011". ATLAS-CONF-2012-048. May 2012. CDS: 1450089 (on p. 195).

[322] N. L. Martinez, R. Turra, et al. "Mass measurement in the $H \to \gamma\gamma$ channel: Supporting documentation for the Mass Paper". ATL-COM-PHYS-2014-018. Jan. 2014. CDS: 1642851 (on p. 196).

[323] ATLAS Collaboration. "Jet Calibration and Systematic Uncertainties for Jets Reconstructed in the ATLAS Detector at $\sqrt{s} = 13$ TeV". ATL-PHYS-PUB-2015-015. July 2015. CDS: 2037613 (on p. 197).

[324] ATLAS Collaboration. "Measurement of the Inelastic Proton-Proton Cross Section at $\sqrt{s} = 13$ TeV with the ATLAS Detector at the LHC". *Phys. Rev. Lett.* **117** (2016), 182002. DOI: 10.1103/PhysRevLett.117.182002. arXiv: 1606.02625 (on p. 198).

[325] C. Anastasiou et al. "Higgs Boson Gluon-Fusion Production in QCD at Three Loops". *Phys. Rev. Lett.* **114** (May 2015), 212001. DOI: 10.1103/PhysRevLett.114.212001. arXiv: 1503.06056 (on pp. 200, 212).

[326] ATLAS Collaboration. "Combined measurement of the total and differential cross sections in the $H \to \gamma\gamma$ and the $H \to ZZ^* \to 4\ell$ decay channels at $\sqrt{s} = 13$ TeV with the ATLAS detector". In: *EPS-HEP2019*. ATLAS-COM-CONF-2019-049. July 2019. CDS: 2681143 (on p. 212).

[327] "GoSam – Hepforge". URL: https://gosam.hepforge.org (on pp. 214, 230).

[328] H. van Deurzen et al. "NLO QCD corrections to the production of Higgs plus two jets at the LHC". *Phys. Lett. B* **721**.1 (2013), 74–81. DOI: 10.1016/j.physletb.2013.02.051. arXiv: 1301.0493 (on p. 215).

[329] G. Cullen et al. "Next-to-Leading-Order QCD Corrections to Higgs Boson Production Plus Three Jets in Gluon Fusion". *Phys. Rev. Lett.* **111** (Sept. 2013), 131801. DOI: 10.1103/PhysRevLett.111.131801. arXiv: 1307.4737 (on p. 215).

[330] Z. Bern et al. "Ntuples for NLO events at hadron colliders". *Comput. Phys. Commun.* **185**.5 (2014), 1443–1460. DOI: 10.1016/j.cpc.2014.01.011. arXiv: 1310.7439 (on pp. 215, 216, 219, 221, 231).

[331] C. F. Berger et al. "Automated implementation of on-shell methods for one-loop amplitudes". *Phys. Rev. D* **78** (Aug. 2008), 036003. DOI: 10.1103/PhysRevD.78.036003. arXiv: 0803.4180 (on p. 215).

[332] T. Gleisberg et al. "SHERPA 1.α, a proof-of-concept version". *JHEP* 02 (2004), 056. DOI: 10.1088/1126-6708/2004/02/056. arXiv: hep-ph/0311263 (on p. 215).

[333] T. Gleisberg and F. Krauss. "Automating dipole subtraction for QCD NLO calculations". *Eur. Phys. J. C* **53**.3 (Dec. 2007), 501–523. DOI: 10.1140/epjc/s10052-007-0495-0. arXiv: 0709.2881 (on pp. 215, 216).

[334] C. F. Berger et al. "Precise predictions for $W + 3$ jet production at hadron colliders". *Phys. Rev. Lett.* **102** (June 2009), 222001. DOI: 10.1103/PhysRevLett.102.222001. arXiv: 0902.2760 (on p. 215).

[335] C. F. Berger et al. "Next-to-leading order QCD predictions for $W + 3$-jet distributions at hadron colliders". *Phys. Rev. D* **80** (Oct. 2009), 074036. DOI: 10.1103/PhysRevD.80.074036. arXiv: 0907.1984 (on p. 215).

[336] C. F. Berger et al. "Next-to-leading order QCD predictions for $Z, \gamma^* + 3$-jet distributions at the Tevatron". *Phys. Rev. D* **82** (Oct. 2010), 074002. DOI: 10.1103/PhysRevD.82.074002. arXiv: 1004.1659 (on p. 215).

[337] C. F. Berger et al. "Precise predictions for $W + 4$-jet production at the Large Hadron Collider". *Phys. Rev. Lett.* **106** (Mar. 2011), 092001. DOI: 10.1103/PhysRevLett.106.092001. arXiv: 1009.2338 (on p. 215).

[338] H. Ita et al. "Precise predictions for Z-boson $+ 4$-jet production at hadron colliders". *Phys. Rev. D* **85** (Feb. 2012), 031501. DOI: 10.1103/PhysRevD.85.031501. arXiv: 1108.2229 (on p. 215).

[339] Z. Bern et al. "Driving missing data at next-to-leading order". *Phys. Rev. D* **84** (Dec. 2011), 114002. DOI: 10.1103/PhysRevD.84.114002. arXiv: 1106.1423 (on p. 215).

[340] Z. Bern et al. "Four-jet Production at the Large Hadron Collider at Next-to-Leading Order in QCD". *Phys. Rev. Lett.* **109** (July 2012), 042001. DOI: 10.1103/PhysRevLett.109.042001. arXiv: 1112.3940 (on p. 215).

[341] N. Greiner et al. "Full mass dependence in Higgs boson production in association with jets at the LHC and FCC". *JHEP* 01 (2017), 091. DOI: 10.1007/JHEP01(2017)091. arXiv: 1608.01195 (on pp. 216, 229).

[342] D. Thain, T. Tannenbaum, and M. Livny. "Distributed computing in practice: the Condor experience." *Concurr. Comput.* **17**.2-4 (2005), 323–356. DOI: 10.1002/cpe.938 (on p. 215).

[343] F. Wilczek. "Decays of Heavy Vector Mesons into Higgs Particles". *Phys. Rev. Lett.* **39** (Nov. 1977), 1304. DOI: 10.1103/PhysRevLett.39.1304 (on p. 228).

[344] S. P. Jones, M. Kerner, and G. Luisoni. "Next-to-Leading-Order QCD Corrections to Higgs Boson Plus Jet Production with Full Top-Quark Mass Dependence". *Phys. Rev. Lett.* **120** (Apr. 2018), 162001. DOI: 10.1103/PhysRevLett.120.162001 (on p. 229).

[345] S. Dawson. "The effective W approximation". *Nucl. Phys. B* **249**.1 (1985), 42–60. DOI: 10.1016/0550-3213(85)90038-0 (on p. 237).

[346] "High Luminosity LHC Project website". URL: https://project-hl-lhc-industry.web.cern.ch/content/project-schedule (on p. 246).

[347] G. Apollinari et al. *High-Luminosity Large Hadron Collider (HL-LHC): Preliminary Design Report*. CERN Yellow Reports: Monographs. 2015. DOI: 10.5170/CERN-2015-005. CDS: 2116337 (on p. 246).

[348] ATLAS Collaboration. "ATLAS Phase-II Upgrade Scoping Document". CERN-LHCC-2015-020. LHCC-G-166. Sept. 2015. CDS: 2055248 (on p. 246).

[349] F. Carrió Argos. "Development of Readout Electronics for the ATLAS Tile Calorimeter at the HL-LHC". PhD Diss., U. of Valencia, 2017. URL: http://roderic.uv.es/handle/10550/60981 (on pp. 246, 261, 265).

[350] E. Valdés Santurio. "Development of the read-out link and control board for the ATLAS Tile Calorimeter Upgrade". PhD Diss., Stockholm U., 2019. URL: https://inspirehep.net/literature/1768300 (on p. 246).

[351] "ATLAS TileCal Pictures Archive". URL: http://tilecal.web.cern.ch/tilecal/Pictures/ (on p. 247).

[352] ATLAS Collaboration. "Technical Design Report for the Phase-II Upgrade of the ATLAS Tile Calorimeter". CERN-LHCC-2017-019. ATLAS-TDR-028. Sept. 2017. CDS: 2285583 (on pp. 248, 258).

[353] K. Anderson et al. "Design of the front-end analog electronics for the ATLAS tile calorimeter". *NIM A* **551**.2 (2005), 469–476. DOI: 10.1016/j.nima.2005.06.048 (on p. 248).

[354] F. Tang et al. "Design of the front-end readout electronics for ATLAS tile calorimeter at the sLHC". In: *2010 17th IEEE-NPSS Real Time Conference*. May 2010, pp. 1–5. URL: https://ieeexplore.ieee.org/document/5750382 (on p. 250).

[355] S. Angelidakis et al. "FATALIC: a fully integrated electronics readout for the ATLAS tile calorimeter at the HL-LHC". ATL-TILECAL-PROC-2018-005. June 2018. CDS: 2626873 (on p. 250).

[356] A. Baumbaugh et al. "QIE10: a new front-end custom integrated circuit for high-rate experiments". *JINST* **9**.01 (Jan. 2014), C01062. DOI: 10.1088/1748-0221/9/01/C01062 (on p. 250).

[357] G. Drake. "Specifications for the HV_Opto Control Board V1.0 for the ATLAS TileCal Demonstrator Project". Nov. 2013. URL: https://tilecal.web.cern.ch/tilecal/DemonstratorReview/HVPS/131111_atlas_tilecal_upgrade_hvopto_spec.pdf (on p. 252).

[358] *MAX1329/MAX1330 datasheet. 12-/16-Bit DASs with ADC, DACs, DPIOs, APIOs, Reference, Voltage Monitors, and Temp Sensor*. URL: https://datasheets.maximintegrated.com/en/ds/MAX1329.pdf (on p. 253).

[359] "Serial Peripheral Interface". URL: https://en.wikipedia.org/wiki/Serial_Peripheral_Interface (on p. 253).

[360] I. Pogrebnyak. "HV-Opto firmware development project for the Atlys testboard". URL: https://gitlab.cern.ch/ivankp/HVOptoAtlys (on p. 255).

[361] I. B. Belean et al. "Firmware Prototype for HVopto slow control in TileCal Phase-II Upgrade". ATL-COM-TILECAL-2019-014. Mar. 2019. CDS: 2666886 (on p. 255).

[362] I. Pogrebnyak et al. "Requirements for the Low Voltage Monitoring Upgrade of ATLAS Hadronic Calorimeter". ATL-COM-TILECAL-2015-067. Sept. 2015. CDS: 2055254 (on pp. 256, 258).

[363] I. Hruska. "Radiation-Tolerant Custom Made Low Voltage Power Supply System for ATLAS/TileCal Detector". In: *Topical Workshop on Electronics for Particle Physics*. CERN. Sept. 2007, pp. 369–373. DOI: 10.5170/CERN-2007-007. CDS: 1038085 (on p. 256).

[364] G. Drake et al. "An Upgraded Front-End Switching Power Supply Design for the ATLAS TileCAL Detector of the LHC". ATL-TILECAL-PROC-2011-015. Nov. 2011. CDS: 1398264 (on p. 256).

[365] G. Arabidze et al. "Detector Control System of Tile Calorimeter Low Voltage Power Supplies System". ATL-TILECAL-INT-2012-001. Feb. 2012. CDS: 1421617 (on pp. 256, 257).

[366] S. Chekanov, S. Norberg, and J. Proudfoot. "Offline LVPS trip monitoring. Software implementation". ATL-COM-TILECAL-2011-020. July 2011. CDS: 1366335 (on p. 256).

[367] H. Boterenbrood and B. I. Hallgren. "The Development of Embedded Local Monitor Board (ELMB)". ATL-DAQ-2003-053. Oct. 2003. DOI: 10.5170/CERN-2003-006.331. CDS: 690030 (on pp. 257, 258).

[368] "ELMB128 CERN website". URL: http://elmb.web.cern.ch/ELMB/ELMBhome.html (on p. 257).

[369] "ELMB128 ATLAS website". URL: http://atlas.web.cern.ch/Atlas/GROUPS/DAQTRIG/DCS/ELMB/elmb128.html (on p. 257).

[370] A. Caratelli et al. "The GBT-SCA, a radiation tolerant ASIC for detector control and monitoring applications in HEP experiments". *JINST* **10**.03 (Mar. 2015), C03034. DOI: 10.1088/1748-0221/10/03/C03034 (on p. 259).

[371] K. S. Nicpon et al. "The Embedded Local Monitor Board upgrade proposals". *PoS* **343**.TWEPP2018 (2019), 034–039. DOI: 10.22323/1.343.0034. CDS: 2710377 (on p. 259).

[372] J. Huston and D. Shooltz. "ELMB2_MB: The Embedded Local Monitoring Board Motherboard for the Tile Calorimeter Low Voltage Power Supply System". Sept. 2019. URL: https://edms.cern.ch/document/2227463 (on p. 259).

[373] J. Carvalho. "Calibration and monitoring of the ATLAS Tile calorimeter". ATL-TILECAL-PUB-2006-007. July 2006. CDS: 973861 (on p. 259).

[374] E. Starchenko et al. "Cesium monitoring system for ATLAS Tile Hadron Calorimeter". *NIM A* **494**.1 (2002), 381–384. DOI: 10.1016/S0168-9002(02)01507-3. CDS: 685349 (on p. 259).

[375] G. Blanchot et al. "The Cesium Source Calibration and Monitoring System of the ATLAS Tile Calorimeter: Design, Construction and Results". *JINST* **15**.03 (Mar. 2020), P03017. DOI: 10.1088/1748-0221/15/03/P03017. arXiv: 2002.12800. CDS: 2714024 (on pp. 259, 260).

[376] O. Solovyanov et al. "Tile Cs Sensors readout upgrade: ideas, results and plans". Presented at the Tile Week Upgrade Session. Oct. 2016. URL: https://indico.cern.ch/event/573823/contributions/2325787/ (on pp. 261, 263).

[377] "TileCal Phase-II upgrade project twiki". URL: https://twiki.cern.ch/twiki/bin/view/Atlas/TileCalUpgradePhaseII (on p. 263).

[378] "TileCal Testbeam Analysis twiki page". URL: https://twiki.cern.ch/twiki/bin/view/Atlas/TileCalTestbeamAnalysis (on p. 263).

[379] "TileCal Testbeam Analysis 2016 twiki page". URL: https://twiki.cern.ch/twiki/bin/view/Atlas/TileCalTestbeamAnalysis2016 (on pp. 263–265).

[380] E. Valdés Santurio and M. Oreglia, ATLAS Collaboration. "Beam Tests on the ATLAS Tile Calorimeter Demonstrator Module". ATL-TILECAL-PROC-2018-001. June 2018. DOI: 10.1016/j.nima.2018.10.066. CDS: 2624587 (on p. 264).

[381] A. Valero, ATLAS Tile Calorimeter System. "Data acquisition and processing in the ATLAS tile calorimeter phase-II upgrade demonstrator". *J. Phys. Conf. Ser.* **898**.3 (Oct. 2017), 032012. DOI: 10.1088/1742-6596/898/3/032012. CDS: 2243768 (on p. 265).